Dissertation
submitted to the
Combined Faculty of Natural Sciences and Mathematics
of Heidelberg University, Germany
for the degree of
Doctor of Natural Sciences

Put forward by
M.Sc. Benedikt Frey
born in: Grünstadt

Oral examination: 22. June 2021

Landau-Zener spectroscopy of bulk glasses

Referees: Prof. Dr. Christian Enss
Prof. Dr. Heinz Horner

Within the thesis at hand, for the first time a measurement technique was developed and established to perform the Landau-Zener spectroscopy of atomic tunneling systems (TSs) in bulk glasses at very low temperatures. Superconducting bridge-type micro-resonators with the sample as substrate were developed that allow a microwave drive under dynamic bias conditions. Beyond dielectric equilibrium measurements, extensively conducted in the past, the novel setup allows to perform measurements in non-equilibrium (Landau-Zener dynamics), which enables a comprehensive study of TSs in bulk glasses with a single device. As sample the borosilicate glass N-BK7 was used which was well-characterized in previous studies and is therefore well-suited for the validation of the setup. Non-equilibrium loss-measurements revealed an average dipole moment of $p = 1.5\,\mathrm{D}$ for the sample, which yields a TS density of $P_0 = 6.46 \times 10^{45}\,\mathrm{J^{-1}m^{-3}}$. A relaxation from the non-equilibrium loss back to the steady-state compatible with a one-phonon process was observed. In two-tone spectroscopy measurements a selective saturation of TSs could be demonstrated and detected through a modified dielectric function. Therewith, a lower limit for the average TS dephasing rate of $\tau_2 \gtrsim 10\,\mu\mathrm{s}$ was determined. In combination with implemented detailed numerical simulations, the Landau-Zener spectroscopy of bulk glasses provides a new way of systematic TS characterization in amorphous materials at very low temperatures.

Landau-Zener Spektroskopie von Gläsern

Im Rahmen dieser Arbeit wurde erstmalig eine Messmethodik zur Landau-Zener Spektroskopie von atomaren Tunnelsystemen (TS) in Gläsern bei tiefen Temperaturen entwickelt und eingesetzt. Hierfür wurden supraleitende mikrostrukturierte Brückenresonatoren mit der Probe als Substrat verwendet, welche neben der Anregung durch elektrische Hochfrequenzfelder ein dynamisches elektrisches Vorspannen des Resonators ermöglichen. Neben der in der Vergangenheit umfassend durchgeführten dielektrischen Messungen im Gleichgewicht erlaubt dieser neuartige Aufbau durch die induzierte Landau-Zener Dynamik auch Nicht-Gleichgewichtsmessungen, was eine umfassende Untersuchung von TS in Gläsern mit einer einzigen Apparatur ermöglicht. Das in früheren Messungen bereits ausführlich untersuchte Borosilikatglas N-BK7 wurde als Probe verwendet und eignet sich damit gut zur Validierung des neuen Aufbaus. Aus Nicht-Gleichgewichtsmessungen des Verlusts wurde ein mittleres Dipolmoment der Probe von $p = 1{,}5\,\mathrm{D}$ bestimmt, woraus sich eine TS Dichte von $P_0 = 6{,}46 \cdot 10^{45}\,\mathrm{J^{-1}m^{-3}}$ bestimmen ließ. Eine mit Ein-Phonon Prozessen vereinbare Relaxation des Nicht-Gleichgewichtsverlust zurück zu seinem Gleichgewichtswert konnte zudem beobachtet werden. In Zwei-Ton Spektroskopie Messungen konnten selektiv TS gesättigt werden, was anhand von Änderungen der dielektrischen Funktion nachweisbar war. Daraus konnte eine untere Grenze für die TS Dephasierungszeit von $\tau_2 \gtrsim 10\,\mu\mathrm{s}$ ermittelt werden. Die Kombination der Landau-Zener Spektroskopie mit durchgeführten detaillierten nummerischen Simulationen stellen einen neuen Weg zur systematischen Untersuchung von TS in amorphen Festkörper bei sehr tiefen Temperaturen dar.

Contents

1. Introduction

It has been 50 years now since Zeller and Pohl [Zel71] published their work on the anomalous low temperature properties of amorphous solids where they unambiguously revealed a fundamental disparity between the thermal properties of insulating glasses and their crystalline counterparts below 1 K. Moreover, not only on a qualitative level but also quantitatively, very similar results between amorphous solids of different classes were found. It is not surprising that these findings quickly attracted attention from experimental and theoretical side, and a new research field in solid-state physics was formed. A lot of efforts have been made over the last decades to establish and improve the understanding of amorphous solids at low temperatures. However, up to now – besides a phenomenological description – the question about the microscopic origin for the anomalous low temperature behavior of amorphous solids remains open. A major difficulty for the theoretical description of amorphous solids lies in their structural disorder.

In contrast to ideal crystals, amorphous solids, such as insulating bulk glasses, which are used in this thesis and can be fabricated, for example, through rapid cooling of a melt, do not possess any long-range order. In fact, the chemical bonding provides a certain short-range order, however, statistical variations of the bonding angles eventually lead to a structural disordering [Ell84, Sch91, Vog92]. The periodicity of an ideal crystal allows the definition of a unit cell, whereby the description of the solid composed of $\sim 10^{23}$ atoms is condensed to a few parameters. However, this important concept in solid-state physics is not readily applicable to amorphous solids, and their description is often restricted to less powerful statistical methods. Because of the absence of a periodic lattice in amorphous solids, also the treatment of phonons as elementary excitations of the lattice only makes sense at large phonon-wavelengths, where the solid can be considered as a continuum, independently from its microscopic structure. At low temperatures, these long-wavelength phonons determine the thermal properties of crystalline solids, which are successfully described within the Debye model [Deb12]. Since long-wavelength phonons are also present in amorphous solids, it was assumed that the Debye model should be a valid description of the low temperature properties of amorphous solids as well. Therefore, it was all the more surprising when the measurements of Zeller and Pohl revealed a considerable deviating behavior of the specific heat and the thermal conductivity. The heat capacity showed an almost linear dependence on temperature, instead of the cubic one proposed by the Debye model, and the thermal conductivity was several orders of magnitude smaller and showed a weaker temperature dependency compared to the crystalline counterpart.

These observations pointed towards the existence of localized low-energy excitations in amorphous solids which contribute to the heat capacity even at very low temperatures where phononic contributions have already died out. Thermal phonons scatter at these additional excitations in amorphous solids, leading to a significant reduction of the thermal conductivity. Independently, Anderson *et al.* [And72] and Phillips [Phi72] provided a phenomenological description where they identified the low-energy excitations as atomic tunneling systems, which occur as broadly distributed two-level states that determine the low temperature properties of glasses. Besides explaining the already mentioned thermal properties [Zel71, Las75, Ste76, Poh85], this model is also quite successful in describing many other properties of amorphous solids at low temperatures like dielectric [vS77, Fro77, Ens89, Rog97, VR98, Luc14] or acoustic [Cla94, Rau95, Cla00, Fef08] susceptibility measurements and the ultrasonic absorption [Hun72, Hun77]. Nowadays, this model is commonly accepted as foundation for describing amorphous solids at low temperatures and is typically referred to as the *standard tunneling model.*

Alongside its general success in describing the low temperature properties of amorphous solids, deviations observed from the predicted behavior have raised questions concerning the standard tunneling model's integrity and led to several extensions over time. On the one hand these extensions target to modify the underlying tunneling system distribution function [Dou80, Ens89], but also interactions between tunneling systems, which become relevant at low temperatures, were discussed and incorporated into the model [Bla77, Bur95, Ens97, Nal04]. The importance of nuclear electric quadrupole moments as constituent of a tunneling systems could be demonstrated in measurements of dielectric polarization echo decays [Wür02, Baz08, Bar13], which could also explain the unexpected magnetic field dependency of the echo amplitude [Lud02] and the dielectric function [Str98, Woh01]. Moreover, dielectric measurements at low frequencies of glasses containing elements with large nuclear quadrupole moments revealed a novel relaxation channel for tunneling systems via the nuclear spin bath [Luc14, Luc16], which is the subject of current research and scientific discussion.

Beyond these topical questions and the unexplained question concerning the microscopic nature of the two-level states, tunneling systems recently attracted high scientific interested due to their deteriorative effects on the performance of superconducting quantum devices. In these experiments they appear as a major origin for noise [Nei13, Bur14b, Pal14] and decoherence [Mar05, Ku05, Mü19]. Improving coherence times for state-of-the-art solid-state qubits addresses the avoidance of tunneling systems and therefore requires a substantial understanding of them. On the other hand, the strong coupling of tunneling systems to these devices opens a whole new experimental way to examine tunneling systems. Spectroscopy of single tunneling systems strongly coupled to a qubit was performed under modifying the two-level system's energy with an applied strain or electric field [Gra12, Lis19], which allowed, for example, to directly observe interactions between tunneling systems [Lis15, Mei18].

In the thesis at hand, we investigate tunneling systems with another novel spectroscopy method by the use of superconducting micro-resonators with a bridge-type capacitor geometry. These resonators allow to probe tunneling systems with a microwave electric field, while an electric bias field provides a dynamic control of the two-level systems' energies. In an earlier experiment by Khalil *et al.* [Kha14] studying amorphous thin films it was observed that sweeping the bias field induces tunneling systems to perform Landau-Zener transitions. This results in an enhanced dielectric loss due to an effective suppression of the tunneling system saturation through the non-equilibrium Landau-Zener population control. The goal of this thesis is to demonstrate and establish this Landau-Zener spectroscopy method for bulk glasses by direct processing planar superconducting micro-resonators on a substrate which is the sample itself. Performing the Landau-Zener spectroscopy with bulk glasses allows us to extensively study microscopic properties of tunneling systems in these materials, like their dipole moment, relaxation times, or the distribution of two-level systems, through a single device. Transferring this measurement technique to a larger range of accessible materials enables to revisit well-characterized materials with new non-equilibrium techniques in order to establish a more conclusive picture about tunneling states in amorphous solids. This will hopefully give an important contribution to resolve the long-standing question concerning the nature of two-level systems in amorphous materials – "always present but never identified" [Dou80].

This thesis is structured as follows:

Chapter 2 provides the essential theoretical background for understanding the measurements performed in the thesis at hand. It starts with a short introduction about the structure of glass before the anomalous low temperature properties of glasses are discussed within the standard tunneling model. Particular emphasis is put on the interaction of tunneling systems with high-frequency electric fields and the non-equilibrium dielectric loss induced by Landau-Zener transitions.

In chapter 3 we introduce a simulation framework which was implemented to model the complex dielectric response of tunneling systems under multi-tone excitations and dynamic biasing conditions. The random nature of the tunneling system ensemble is mapped with a Monte Carlo approach. We discuss the time evolution of single tunneling systems and the response of the tunneling system ensemble on more elaborated aspects arising from the Landau-Zener dynamics of tunneling systems.

The experimental setup for performing the Landau-Zener spectroscopy at very low temperatures is discussed in chapter 4. We present the different bridge-type resonators used within this thesis and explain the applied protocols for extracting the dielectric function out of the recorded resonance spectra.

Chapter 5 starts with the characterization of the bridge-type resonators. In dielectric equilibrium measurements the novel resonators are compared to previous measurements. From a comparison with the standard tunneling model information about the distribution of tunneling systems can be drawn. The results of the Landau-Zener spectroscopy are given in Section 5.3, which is combined in Section 5.4 with a two-tone measurement scheme by applying additional off-resonant microwave pump tones to the resonator.

The thesis ends with a summary of the obtained results and an outlook for future experiments.

2. Theory

This chapter provides the essential theoretical background for understanding the measurements performed in the thesis at hand. After a short introduction about the general structure of glass, the discussion is specified on the anomalous low temperature properties of glasses. As an underlying model for the description of the low temperature behavior of glasses the so-called standard tunneling model is introduced, in particular with regard to its impact on the dielectric low temperature properties. The chapter ends with the discussion of the non-equilibrium dielectric loss, induced by tunneling systems undergoing Landau-Zener transitions, in the presence of a rapidly swept large electric bias field.

2.1 Structure of glass

If a melt is cooled down slowly below its melting point T_m, the atoms will eventually start to nucleate and crystallize in a periodic structure. At T_m the melt then undergoes a first order phase transition and solidifies as a crystal, which appears as an abrupt volume drop in the V-T diagram as shown in Figure 2.1. On the other hand a glass can be formed by a rapid cooling of the melt. In this case below T_m no solidification occurs initially since the mobility of the atoms is sufficiently limited to prevent an arrangement in a crystal lattice. One speaks of a supercooled melt,

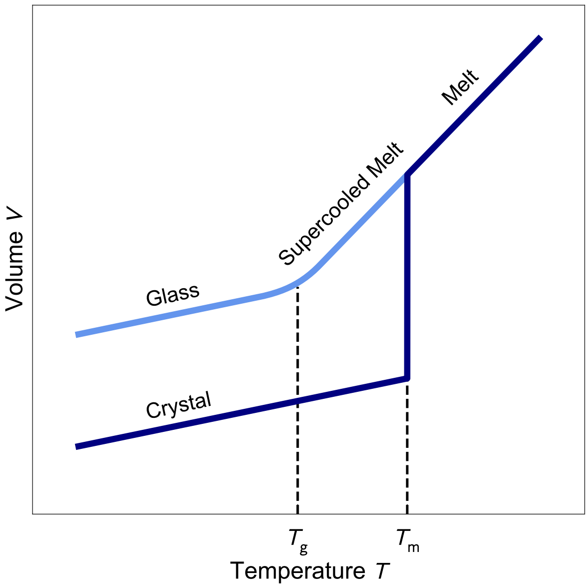

Figure 2.1: Schematic illustration of the change in volume under cooling of a melt. A rapid cooling of the melt results in a solidification into a glass at T_g, while on the other hand a crystal can be formed at T_m under slow cooling, which is thermodynamically the more stable state, and therefore has a lower volume. Adapted from [Sch91].

which is typically associated with a strongly increased viscosity of the material with decreasing temperature [Vog92]. Further cooling increases the viscosity so much that the thermodynamic equilibrium (crystal) cannot be reached, and the melt solidifies vitreously. This transition emerges as a continuous kink in the V-T diagram. The corresponding temperature is called the glass transformation temperature T_g, but it should be noted that, as this is a continuous transition, one should rather speak of a transformation range [Sch91]. By means of viscosity, the transformation temperature T_g can be defined as the temperature range where the viscosity η lies between $10^{12}\,\mathrm{Pa\,s} < \eta < 10^{13.5}\,\mathrm{Pa\,s}$. The occurrence of a transformation into a glass strongly depends on the cooling rate. While some materials form a glass under almost all circumstances, other materials like metals require cooling rates of up to $10^6\,\mathrm{K\,s^{-1}}$ [Wan04]. The glass transformation in general is a very complex phenomenon, and up to now there exists no complete picture that can fully describe the processes involved during the glass transformation. It shows similarities to a second order phase transition, but cannot be interpreted as a phase transition in the classical sense since there is no transition between two equilibrium states during the glass formation [Sch91].

First attempts to specify the structure of glasses were made by performing X-ray diffraction measurements. Figure 2.2 shows such a measurement where the diffraction pattern of quartz glass is compared to its crystalline counterpart. Both materials have the same chemical composition (SiO_2) but originate from a different manufacturing process as explained above. In contrast to the quartz crystal, where the observed discrete diffraction pattern arises from the periodic lattice, the quartz glass features a broad diffuse peak. From this divergent outcome it was concluded that glasses should be non-crystalline solids, or in other words possess an amorphous

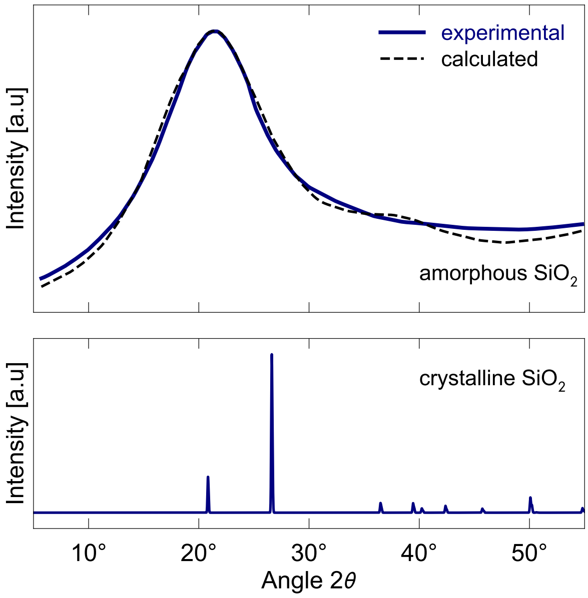

Figure 2.2: Comparison of X-ray diffraction measurements of quartz glass (amorphous SiO_2) (top) and quartz crystal (crystalline SiO_2) (bottom). While the periodic atomic arrangement of the crystal leads to sharp diffraction peaks, the lack of a long-range order results in a broad diffuse peak for the glass. Data from [War34] and [Laf15].

structure [Sel25]. The term ‘glass’ is typically used for materials originating from melt quenching, which is the manufacturing process of the used sample in this thesis. However, there exist several techniques to prepare a material into its amorphous state. For example, a common method is to create thin amorphous films by using sputter deposition. When talking about the structure of an amorphous material, one needs to differentiate between the used preparation techniques, as there is no reason to assume the same structure occurring from different preparation processes [Ell84]. Although strictly speaking a glass is a subgroup of the class of amorphous solids, both terms will be used equivalently here. When speaking of glasses or amorphous solids in the following, we will imply bulk glasses.

The first satisfactory picture of the glass structure goes back to 1932 by Zachariasen with his random network theory [Zac32]. As a requirement for a material to form a stable amorphous structure, he claimed that its internal energy should only slightly exceed the energy of the crystalline phase. Moreover, the inter-atomic interactions in the glass and the crystal should be approximately the same. Therefore, Zachariasen assumed that, as in crystals, the elementary base units of oxide-glasses – which were only known back then – are formed by oxygen polyhedra. In contrast to crystals the relative orientation between these polyhedra, which share corners with each other, is not fixed but varies. Therefore, in glasses only a short-range order appears, but no long-range order establishes and thus the periodicity is lost [Ell84]. The constraint of a low internal energy leads to certain selection rules that need to be fulfilled for a glassforming chemical compound. With these postulated rules, Zachariasen was able to explain why certain materials tend to be good glassformers, and others are not. For example SiO_2, which is the main constituent of most oxide glasses, is a good glassformer. It is composed out of SiO_4-tetrahedra with oxygen atoms sitting at the corners, and the silicon atom located in the center. A two-dimensional projection of crystalline and amorphous SiO_2 is shown in Figure 2.3. An exemplary SiO_4-tetrahedron is marked red for both cases, whereby only three oxygen atoms are shown in this projection because the fourth oxygen atom sits in the drawing plane above or below the silicon atom. While the crystalline modification is composed out of identical SiO_4-tetrahedra, in the amorphous case the bonding angles slightly vary from atom to atom. Heavily skewed chemical bonds can be avoided at the same time, and therefore an internal energy similar to the crystal is maintained. Consequently, SiO_2 is able to arrange in a continuous random network, whereby rings of different sizes are formed.

By using this picture for the structure of a glass, Warren [War34] was able to explain and reproduce the observed X-ray diffraction pattern of quartz glass (see Figure 2.2), which confirmed the random network theory of glasses. A direct observation of the two-dimensional structure of amorphous SiO_2 was achieved by Lichtenstein *et al.* [Lic12]. They investigated a thin double layer of deposited SiO_2 on Ru(0001) using

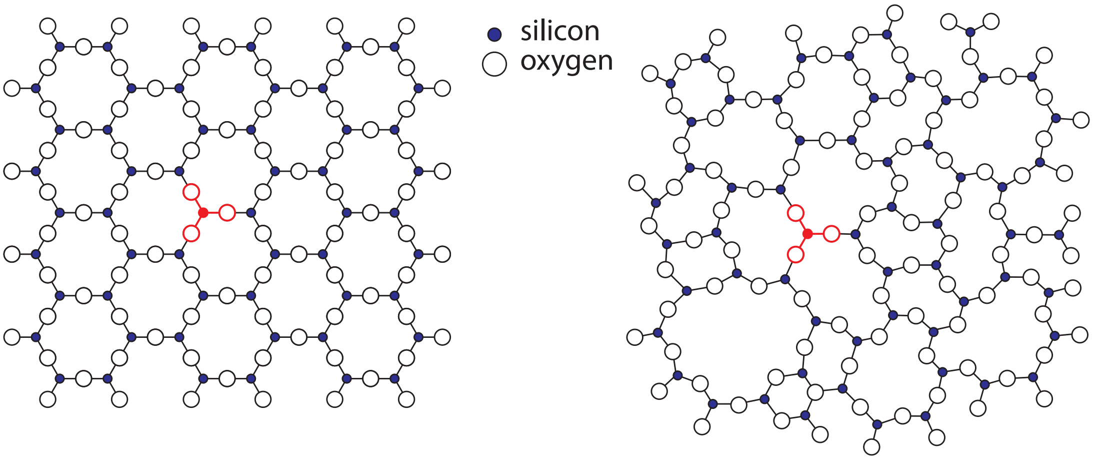

Figure 2.3: Schematic drawing of a two-dimensional projection of crystalline (left) and amorphous SiO_2 (right). Both structures are composed of SiO_4-tetrahedra, whereby the fourth oxygen atom sits below or above the silicon atom and is not shown here. Varying bonding angles lead to a loss of the long-range order in the amorphous modification. Adapted from [Zac32].

noncontact atomic force microscopy (nc-AFM) and scanning tunneling microscopy (STM). By doing this, it was possible to resolve the atomic structure of amorphous SiO_2 (Figure 2.4), which reveals a magnificent agreement with the predicted structure from the random network theory. The crystalline phase is composed out of identical rings with six silicon atoms per ring. In the amorphous modification multiple ring sizes between 4 and 9 exist. Similar observations were made with a thin layer of SiO_2 on top of graphene [Hua12].

So far, the description was restricted to glasses made out of a single oxide. However,

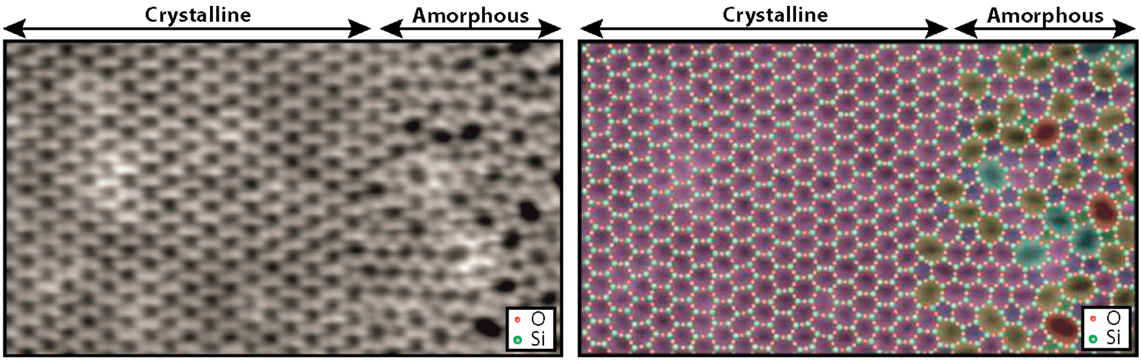

Figure 2.4: Scanning tunneling microscope image of a deposited thin layer of SiO_2 on Ru(0001) (left) and a colorized version with the visualization of the different ring sizes (right). Both the crystalline and the amorphous modification are present in the cutout. Images taken from [Fre17].

the most commonly used glasses are often composed out of several components. As an example, we discuss the adding of an alkali metal oxide like Na_2O to the glass network. In the previous discussed case of pure SiO_2 every oxygen atom is bound to the two neighboring silicon atoms and meshes the network. Such a link is also called bridging oxygen. As it can be seen in Figure 2.5, by incorporating Na_2O into the network, such a connection cracks, and single bound oxygen atoms are created (nonbridging oxygen). The sodium ion chiefly bonds in an ionic way to the oxygen, which is much weaker than the Si-O bonding where also covalent bonding parts exist [Sch91]. Every sodium ion causes one nonbridging oxygen atom. The higher the amount of sodium the stronger the glass network is weakened by the formation of nonbridging oxygen atoms. In general, one differentiates between compounds that lead to the formation of a network (network formers), and the ones that crack or modify it (network modifiers). Typical representatives of a network former are SiO_2, B_2O_3, P_2O_5, As_2S_3, GeO_2, and of a network modifier Na_2O, K_2O, CaO. Moreover, so-called intermediate oxides such as Al_2O_3 may act, depending on the glass composition, both as network former or modifier. A further development of the network theory by Dietzel as explained in [Vog92] considers the appearing electric field strengths in the region of the oxygen atoms and allows a classification of the different glass compounds into network formers, intermediate oxides, and network modifiers. The presented basic picture already allows to understand the fundamental structure of many glasses, and furthermore is able to predict properties of glasses to some extent. The addition of network modifiers weakens the glass network, therefore, the glass components, especially the modifiers, are getting more agile. Hence, a reduced melting point temperature or an increased electric conductivity of such a glass is

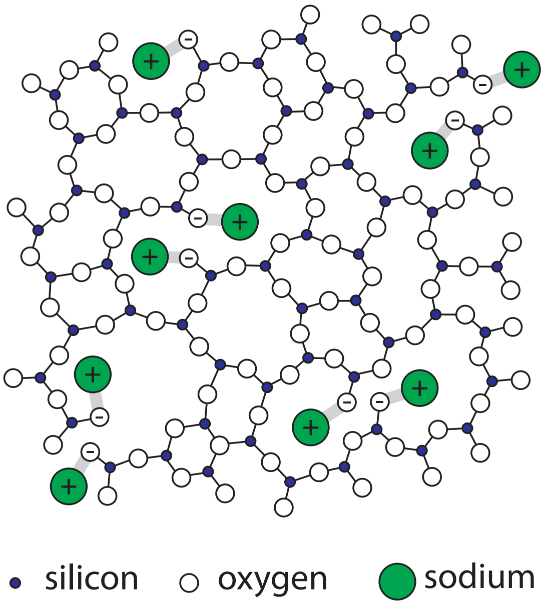

Figure 2.5: Schematic drawing of a two-dimensional projection of a sodium silicate glass. The addition of sodium ions in the form of Na_2O partially breaks the SiO_2 network and forms nonbridging oxygen atoms.

conceivable [Vog92]. The formation of glasses in general, for example multicomponent glasses such as borosilicate glass, as used in this thesis, is quite complex and the understanding often cannot exceed an empirical description. Even binary glasses of certain compositions for example have a tendency for clustering phenomena [Vog92]. Modeling the microscopic structure by means of computer simulations (molecular dynamics) provides an alternative approach for a better understanding of the microscopic glass structure of more complex compositions [Ino12, Ste18, Bø19].

2.2 Low temperature properties of glass

The previous section showed that on a structural level glasses and crystals differ heavily. In which way these differences have an impact on the low temperature properties of glasses, will be discussed in the following, exemplarily on the specific heat capacity, the thermal conductivity, and the ultrasonic absorption.

Specific heat capacity

According to the Debye model [Deb12], the specific heat capacity of dielectric crystals is determined by long-wavelength phonons (collective excitation of the lattice) with linear dispersion relation $\omega = vq$, where we introduced the phonon frequency ω, the speed of sound in the crystal v, and the wavenumber q. The density of states for these phonons and the volume V of the solid is given by

$$D(\omega)\mathrm{d}\omega = \frac{V}{2\pi^2}\frac{\omega^2}{v^3}\mathrm{d}\omega \quad . \tag{2.1}$$

From that, the internal energy U, and therefore the specific heat capacity C_V, can be calculated

$$C_\mathrm{V} = \left(\frac{\partial U}{\partial T}\right)_V = \frac{\partial}{\partial T}\int\limits_0^{\omega_\mathrm{D}} \hbar\omega D(\omega) f(\omega, T)\mathrm{d}\omega \quad , \tag{2.2}$$

by using the Bose-Einstein distribution $f(\omega, T)$ and defining the cutoff frequency ω_D through the total number of atoms N as

$$N = \int\limits_0^{\omega_\mathrm{D}} D(\omega)\mathrm{d}\omega \quad . \tag{2.3}$$

For low temperatures Equation (2.2) can be solved analytically, and for the low temperature specific heat one finds the well-known T^3-dependency

$$C_\mathrm{V} = \frac{12\pi^4}{5} N k_\mathrm{B} \left(\frac{T}{\theta}\right)^3 \quad , \tag{2.4}$$

introducing the Debye temperature $\theta = \hbar\omega_{\mathrm{D}}/k_{\mathrm{B}}$. Long-wavelength phonons, which solely contribute to the heat capacity at low temperatures, are unaffected by the microscopic structural properties of the material. Therefore, they also exist in glasses and determine their low temperature properties as well [Phi87]. Consequently, the above considerations for the specific heat capacity should be applicable for amorphous solids, and one would expect a drop of the specific heat $\propto T^3$ with decreasing temperature as well. Surprisingly, specific heat capacity measurements of glasses revealed a quite different behavior. For quartz glass Zeller and Pohl observed a rather linear temperature dependence of the specific heat at low temperatures [Zel71]. Figure 2.6 shows a measurement of the specific heat capacity of a quartz glass and of a quartz crystal. Below ~0.5 K both curves strongly differentiate. Since the heat capacity is a measure of the number of accessible degrees of freedom, it can be concluded that in glasses there must exist additional low energy excitations which prevent the heat capacity from dropping stronger in temperature. These additional degrees of freedom in glasses at low temperatures were later identified as atomic tunneling systems, originating from the intrinsic disorder of glasses, and will be discussed in the context of the standard tunneling model in detail (Section 2.3).

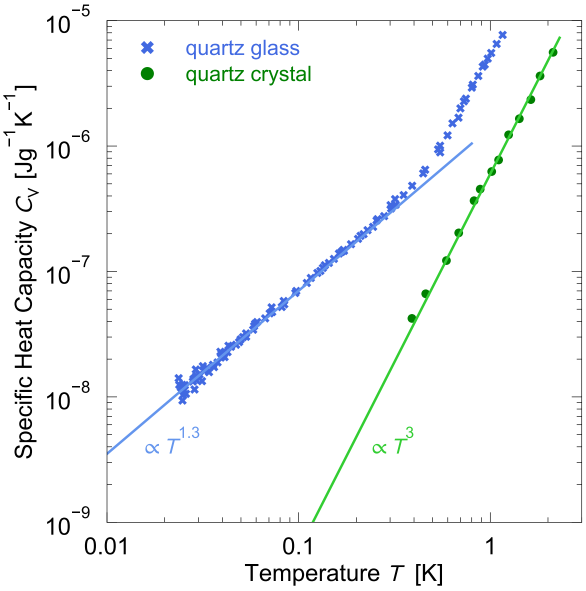

Figure 2.6: Specific heat capacity of quartz glass and quartz crystal at low temperatures. Below ~0.5 K the specific heat capacity of the glass is proportional to $T^{1.3}$, deviating from the Debye model, while the crystal shows the expected T^3-dependency. Data from [Zel71, Las75].

Thermal conductivity

Just as in dielectric crystals at low temperatures, long-wavelength phonons are responsible for the transport of heat in dielectric glasses. In both cases the thermal conductivity κ can be treated within the framework of the kinetic theory of gases considering transport processes of a phonon gas

$$\kappa = \frac{1}{3} C v l \quad , \tag{2.5}$$

whereas C is the specific heat capacity, v the speed of sound, and l the mean free path of the phonons. At low temperatures, the phonon-phonon scattering is negligible. In the case of a crystalline solid the mean free path is limited by the sample's diameter itself $l \approx const.$ (Casimir regime). The T^3-dependence of the phononic heat capacity gives a cubic temperature dependency of the thermal conductivity of crystals at low temperatures. Measurements of glasses, however, showed a fundamentally different behavior [Zel71], see Figure 2.7. On the one hand, across the whole temperature range the absolute values of κ are several orders of magnitude smaller compared to the crystal, and on the other hand, one observes a behavior $\kappa \propto T^2$ at low temperatures. Since for crystals and glasses the thermal conductivity is based on the phonon transport, the phonon mean free path in the glass must be heavily reduced. Again, tunneling systems are responsible for the deviations, which act as additional scattering centers for the phonons through a resonant interaction with them, and therefore drastically modify the thermal conductivity. Deviations above 1 K should be unrelated to tunneling systems, and are discussed in [Ram98, Ens05].

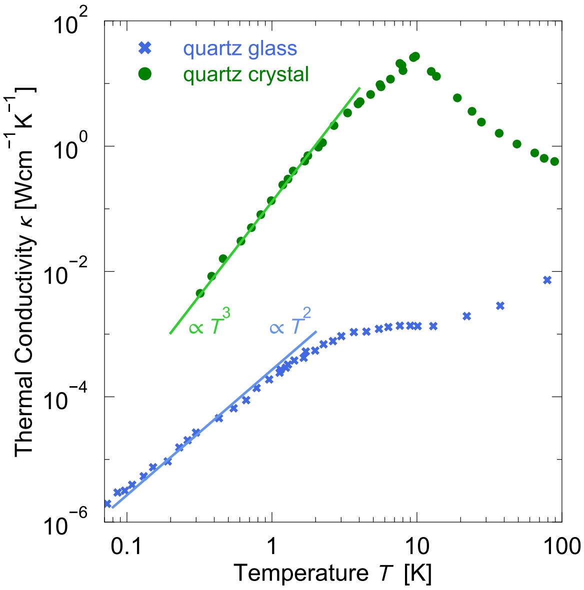

Figure 2.7: Thermal conductivity of quartz glass and quartz crystal at low temperatures. The glass shows a much smaller thermal conductivity and has a different temperature dependency at very low temperatures compared to the crystal. Data from [Zel71].

Ultrasonic absorption

A further evidence for the existence of low-energy excitations with which phonons resonantly interact are given by measurements of the ultrasonic absorption in glasses.

In such measurements it was observed that, in contrast to crystals, a distinct absorption was present at low temperatures [Hun77]. Additionally, a strong dependency of the ultrasonic absorption from the field intensity was found by Hunklinger *et al.* [Hun72].

In anticipation of the following chapter, we reveal that these measurements can be understood by treating the already mentioned tunneling systems as two-level systems with an energy splitting E. Phonons from the ultrasonic field get resonantly absorbed by a two-level system of the same energy if the two-level system is in its ground state. The population difference Δn of such a two-level system with energy E in thermal equilibrium is $\Delta n = \tanh\left(\frac{E}{2k_{\mathrm{B}}T}\right)$. For high temperatures both energy levels are equally populated, and therefore emission and absorption of phonons cancel out each other. For $T \to 0\,\mathrm{K}$ the excited state gets less populated, and phonons can be effectively absorbed. If the intensity of the ultrasonic field J exceeds a critical value J_{c}, the population difference of the ensemble again drops since a growing number of two-level systems is found in their excited state, and the absorption of phonons is hence reduced. A measurement of the ultrasonic absorption as a function of the ultrasonic intensity of a borosilicate glass (BK7) is shown in Figure 2.8. It shows the explained behavior, as the inverse mean free path l^{-1} of the phonons decreases with increasing ultrasonic intensity. One speaks of a saturation of the ultrasonic absorption by the ultrasonic field. According to [Hun76], the data is described with a curve of the form

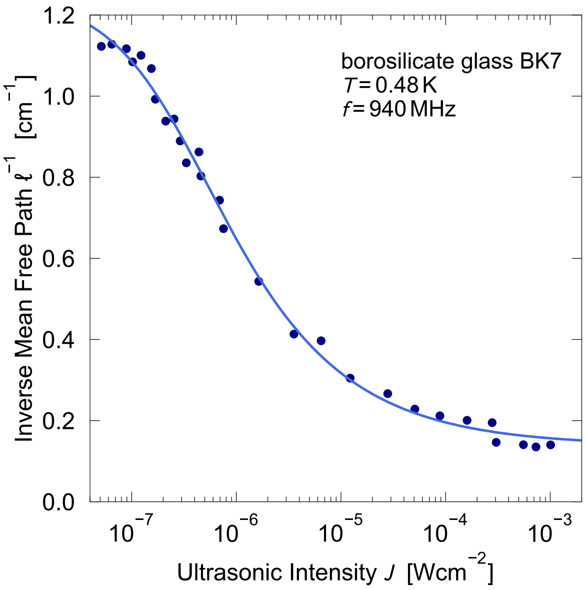

Figure 2.8: Inverse mean free path of the phonons of the ultrasonic field l^{-1} as a function of the ultrasonic field intensity J. For higher field intensities the inverse mean free path decrease, since the absorption of phonons is reduced through a saturation of the tunneling systems by the ultrasonic field. Data from [Hun74].

$$l^{-1} \propto \tanh\left(\frac{E}{2k_{\mathrm{B}}T}\right)\frac{1}{\sqrt{1+\frac{J}{J_{\mathrm{c}}}}} \quad , \tag{2.6}$$

which strongly supports the idea of the existence of two-level systems in glasses at low temperatures. We will return to the discussion of saturated tunneling systems in the context of the interaction of tunneling systems with strong electric microwave fields in Section 2.4.5.

2.3 The standard tunneling model

The previous shown measurements give strong evidence about the existence of low energy two-level states in glasses which determine their low temperature properties. Furthermore, these deviations at low temperatures were found in a variety of different glasses [Ste73, Poh85, Phi87]. There is not only a qualitative agreement between different glasses, but in many cases one finds very similar results even on a quantitative level, which is why one often speaks of the *universality of glasses* when regarding their low temperature properties. Independently from each other, in 1972, Anderson *et al.* [And72] and Phillips [Phi72] suggested a phenomenological model that allowed, without making detailed microscopic assumptions, to explain the low temperature properties of glasses. Their model is based on a broad distribution of atomic tunneling systems forming two-level states, which will be discussed in the following within the framework of the so-called standard tunneling model.

2.3.1 Atomic tunneling systems

The intrinsic disorder of glasses, as discussed in Section 2.1, allows atoms or groups of atoms to occupy several energetically similar equilibrium positions. This is the starting point of the model proposed by Anderson *et al.* and Phillips, also called the standard tunneling model. An illustrative representation is shown in Figure 2.9 (left), where several possible equilibrium positions of atoms in a two-dimensional sodium silicate glass are marked. At very low temperatures ($T \lesssim 1\,\mathrm{K}$) transitions between these positions solely take place through quantum tunneling processes, meaning that even at the lowest temperatures no localization of these atoms occurs. A straightforward approximation of this situation is an asymmetric double well potential as shown in Figure 2.9 (right). The tunneling object might be a single atom or a group of atoms with mass m. The two equilibrium states differ by the energy $\mathit{\Delta}$ and are separated by the potential barrier height V. As illustrated in Figure 2.9, transitions may occur as translations, rotations, or as a combination of both motions, which is why the distance d should be understood as a distance in the configuration space. In order to find the eigenstates of the system one needs to solve the stationary Schrödinger equation

$$\hat{H}\psi(x) = E\psi(x) \quad , \tag{2.7}$$

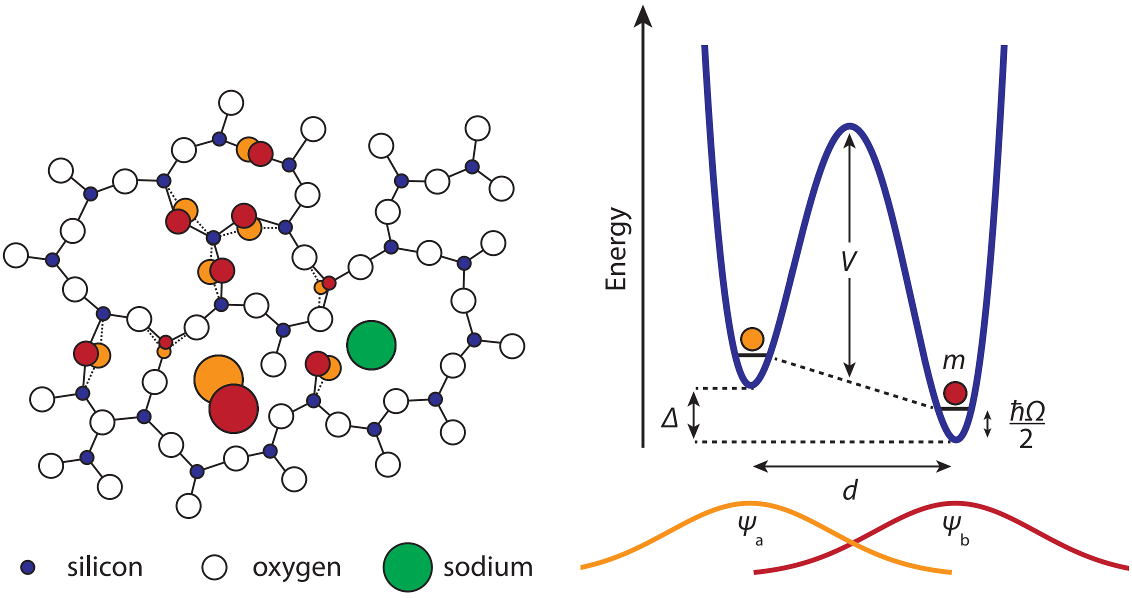

Figure 2.9: Left: Schematic illustration of tunneling systems in a two-dimensional sodium silicate glass. The disorder allows different energetically similar configurations. Possible equilibrium positions of atoms or groups of atoms are marked in orange and red. Right: Drawing of an asymmetric double well potential, with asymmetry energy $\varDelta$ (energy difference between right and left well), the well distance d, and the potential barrier height V. The ground state of the tunneling object with mass m in an isolated single harmonic well is $\psi_{\mathrm{a/b}}$ with the ground state energy $\frac{\hbar\Omega}{2}$.

with the Hamiltonian

$$\hat{H} = -\frac{\hbar^2}{2m}\frac{\mathrm{d}^2}{\mathrm{d}x^2} + V(x) \quad . \tag{2.8}$$

The double well potential $V(x)$ in Figure 2.9 is modeled by a potential of fourth order [Heu98]

$$V(x) = B\left[w_2\left(\frac{x}{a}\right)^2 - w_3\left(\frac{x}{a}\right)^3 + w_4\left(\frac{x}{a}\right)^4\right] \quad , \tag{2.9}$$

originating from the more general soft-potential model, which targets to unify the glass properties below 1 K and the behavior at several kelvin [Kar83, Par93]. The parameters B and a define the scale of energy or length, respectively, while w_i can be regarded as adjustable parameters defining the behavior of the resulting modes. For $w_4 w_2/w_3^2 < 9/32$ the potential forms a double well potential as sketched in Figure 2.9. Otherwise, single anharmonic wells occur that give rise to localized low frequency vibrations (soft modes), which will come into play above 1 K. Since we are only interested in the low temperature properties of glasses, we will not discuss the soft-potential model furthermore and refer to the discussion in [Esq98].

At very low temperatures only the low-lying energy levels of the potential are accessible. Therefore, the cubic and quartic terms are neglected, resulting in two single harmonic potentials described by a single parameter $k = Bw_2/a^2$. Solving the Schrödinger equation for each harmonic potential separately gives the ground states for each isolated well

$$\psi_{\mathrm{a/b}} = \left(\frac{m\Omega}{\pi\hbar}\right)^{\frac{1}{4}} \exp\left(-\frac{1}{2}\frac{m\Omega}{\hbar}\left(x \pm \frac{d}{2}\right)^2\right) \quad , \tag{2.10}$$

and the ground state energy

$$E_0 = \hbar\sqrt{\frac{k}{2m}} := \frac{\hbar\Omega}{2} \quad . \tag{2.11}$$

The binding energies for glasses or crystals of the same composition should be very similar, and therefore, the strength k of the potential as well. Consequently, the ground state energy of the glass should be of the same order if only one atom is involved in the tunneling process, or slightly lower in the case of tunneling of a group, than for the crystal. For a typical oxide glass one expects $\hbar\Omega/k_{\mathrm{B}} \lesssim 100\,\mathrm{K}$ [Phi72, Hun86], which is significantly higher than the maximum energy splittings $E/k_{\mathrm{B}} \sim 1\,\mathrm{K}$ responsible for the low temperature thermal properties. Therefore, neglecting higher energy states of the two single wells in the following calculation is well justified. The overlap between both wave functions ψ_{a} and ψ_{b}, as indicated in Figure 2.9, results in a coupling between the two states due to quantum tunneling. As a result, the two wave functions in Equation (2.10) cannot be the eigenstates of the system anymore. In order to solve the Hamiltonian, we use a superposition of the two single well ground states as an ansatz:

$$\Psi_{\mathrm{tot}} = a\psi_{\mathrm{a}} + b\psi_{\mathrm{b}} \tag{2.12}$$

Inserting Equation (2.12) into (2.7) gives for the eigenvalue E

$$E = \frac{\langle\Psi_{\mathrm{tot}}|\,\hat{H}_{\mathrm{TS}}\,|\Psi_{\mathrm{tot}}\rangle}{\langle\Psi_{\mathrm{tot}}|\Psi_{\mathrm{tot}}\rangle} = \frac{a^2E_{\mathrm{aa}} + b^2E_{\mathrm{bb}} + 2abE_{\mathrm{ab}}}{a^2 + b^2 + 2abS} \quad , \tag{2.13}$$

with the abbreviations $E_{\mathrm{aa}} = \langle\psi_{\mathrm{a}}|\,\hat{H}_{\mathrm{TS}}\,|\psi_{\mathrm{a}}\rangle$, $E_{\mathrm{bb}} = \langle\psi_{\mathrm{b}}|\,\hat{H}_{\mathrm{TS}}\,|\psi_{\mathrm{b}}\rangle$, $E_{\mathrm{ab}} = \langle\psi_{\mathrm{a}}|\,\hat{H}_{\mathrm{TS}}\,|\psi_{\mathrm{b}}\rangle$, and the overlap integral $S = \langle\psi_{\mathrm{a}}|\psi_{\mathrm{b}}\rangle$. The exact solution of the Schrödinger equation must result in the lowest energy value. Therefore, we can approximate the solution by minimizing the total energy, which gives the two conditions $\frac{\partial E}{\partial a} = 0$ and $\frac{\partial E}{\partial b} = 0$ that can be written as

$$(E_{\mathrm{aa}} - E)(E_{\mathrm{bb}} - E) - (E_{\mathrm{ab}} - ES)^2 = 0 \quad . \tag{2.14}$$

Setting the energy zero point between the two minima of the single wells gives $E_{\mathrm{aa}} = \frac{\hbar\Omega + \varDelta}{2}$ and $E_{\mathrm{bb}} = \frac{\hbar\Omega - \varDelta}{2}$. Furthermore, one can neglect the overlap S, and one finally finds the two energy eigenvalues

$$E_{\pm} = \frac{1}{2}\left(\hbar\Omega \pm \sqrt{\varDelta^2 + 4E_{\mathrm{ab}}^2}\right) \quad . \tag{2.15}$$

We hereby see that such a tunneling system, modeled by a double well potential, splits up into two eigenstates, and therefore represents a two-level system with energy splitting

$$E = E_+ - E_- = \sqrt{\varDelta^2 + 4E_{\mathrm{ab}}^2} = \sqrt{\varDelta^2 + \varDelta_0^2} \quad . \tag{2.16}$$

The introduced tunneling splitting $\varDelta_0 = -2E_{\mathrm{ab}}$ describes the coupling energy between the two wells and depends on the specific form of the potential barrier. In the case of the standard tunneling model, one typically uses the expression obtained from the WKB approximation[1]

$$\varDelta_0 = \hbar\varOmega e^{-\lambda} \quad , \tag{2.17}$$

with the tunneling parameter λ being a measure of the ratio between the potential barrier height V and the single well's ground state energy E_0 [Nar70]. The exact numerical factor differs in literature, but is of no further relevance for the overall description. Here, the tunneling parameter given in [And72, Hun00] is used

$$\lambda \approx \frac{d}{2\hbar}\sqrt{2mV} \quad . \tag{2.18}$$

For a clearer notation we use the matrix representation of the Hamiltonian. Within the basis of the single wells $|\psi_{\mathrm{a}}\rangle = \left(\begin{smallmatrix}0\\1\end{smallmatrix}\right)$ and $|\psi_{\mathrm{b}}\rangle = \left(\begin{smallmatrix}1\\0\end{smallmatrix}\right)$ the Hamiltonian of the tunneling system $\hat{H}_{\mathrm{TS}}$ can be written as

$$\hat{H}_{\mathrm{TS}} = \frac{1}{2}\begin{pmatrix} \varDelta & -\varDelta_0 \\ -\varDelta_0 & -\varDelta \end{pmatrix} \quad . \tag{2.19}$$

The matrix elements correspond to the abbreviations introduced in Equation (2.13), and the constant term $\hbar\Omega/2$ was ignored. Switching into the eigenbasis, the Hamiltonian diagonalizes with the eigenvalues (Equation (2.15)) on the diagonal

$$\hat{\mathcal{H}}_{\mathrm{TS}} = \frac{1}{2}\begin{pmatrix} E & 0 \\ 0 & -E \end{pmatrix} \quad . \tag{2.20}$$

A transformation between the two bases can be performed through a rotation by an angle ϕ with the rotation matrices

$$\hat{R}_\phi = \begin{pmatrix} \cos\phi & -\sin\phi \\ \sin\phi & \cos\phi \end{pmatrix} \quad \text{and} \quad \hat{R}_\phi^{-1} = \begin{pmatrix} \cos\phi & \sin\phi \\ -\sin\phi & \cos\phi \end{pmatrix} \quad . \tag{2.21}$$

The requirement $\hat{\mathcal{H}}_{\mathrm{TS}} = \hat{R}_\phi \hat{H}_{\mathrm{TS}} \hat{R}_\phi^{-1}$ sets the rotation angle ϕ as $\tan 2\phi = \varDelta_0/\varDelta$. A backwards rotation of the eigenstates written in the eigenbasis $|\Psi_{\mathrm{g}}\rangle = \left(\begin{smallmatrix}0\\1\end{smallmatrix}\right)$ and

---

[1] named after Wentzel, Kramers, and Brillouin [Wen26, Kra26, Bri26]

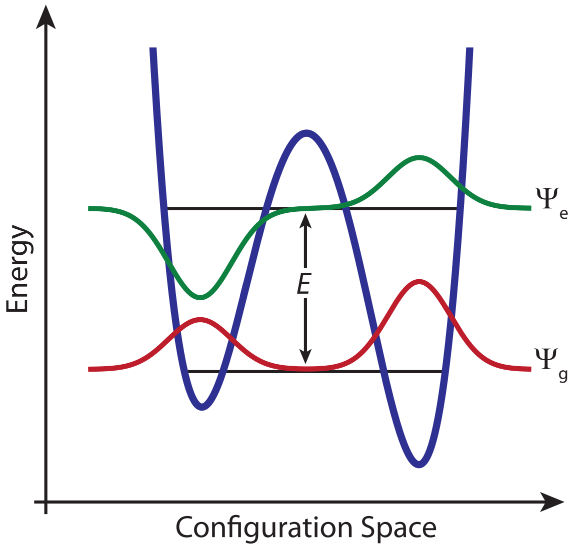

Figure 2.10: Representation of the two eigenstates of a tunneling system. The symmetric wave function Ψ_g corresponds to the ground state, and the asymmetric one Ψ_e to the excited state, which are separated by the energy splitting E. The energy splitting is massively enlarged in relation to the size of the double well potential.

$|\Psi_e\rangle = \left(\begin{smallmatrix}1\\0\end{smallmatrix}\right)$ with $\hat{R}_\phi^{-1}$ into the basis $\psi_{a,b}$, gives the two eigenstates expressed through the wave function of the single well (Equation (2.10))

$$\Psi_g = \quad \cos(\phi)\psi_a + \sin(\phi)\psi_b \tag{2.22}$$

$$\Psi_e = -\sin(\phi)\psi_a + \cos(\phi)\psi_b \quad . \tag{2.23}$$

Figure 2.10 shows the two eigenstates, which are separated by the energy splitting E. The symmetric superposition of the single well wave functions represents the ground state and the asymmetric one the excited state. An asymmetric potential gives a higher probability for a tunneling system in its ground state to be found in the lower well.

2.3.2 Distribution function

So far, the discussion has been restricted to a single tunneling system, which is fully defined by an asymmetry energy Δ and a tunneling parameter λ. However, the disorder leads to a broad distribution of different tunneling systems with varying parameters of the double well potential. This needs to be considered in order to explain the low temperature properties of a glass. A central assumption of the standard tunneling model is that the parameters Δ and λ are independent from each other and are both uniformly distributed. With this assumption the distribution function simply reads

$$P(\Delta, \lambda)\mathrm{d}\Delta\mathrm{d}\lambda = P_0\mathrm{d}\Delta\mathrm{d}\lambda \quad , \tag{2.24}$$

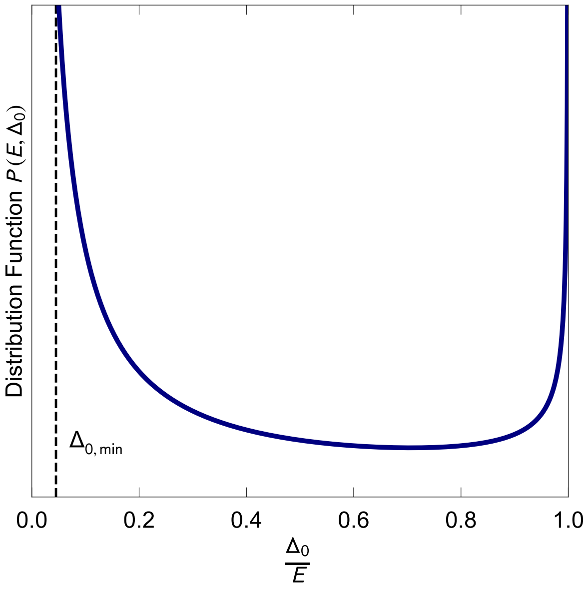

Figure 2.11: Distribution function $P(E, \varDelta_0)$ of the standard tunneling model as function of $\varDelta_0/E$. A cutoff at $\varDelta_{0,\mathrm{min}}$ is needed in order to avoid a non-integrable divergence for $\varDelta_0 \rightarrow 0$.

with a material dependent constant parameter P_0. A variable transformation allows to express the distribution function in terms of the tunneling splitting $\varDelta_0$

$$P(\varDelta, \varDelta_0)\mathrm{d}\varDelta\mathrm{d}\varDelta_0 = P(\varDelta, \lambda)\left|\frac{\partial \lambda}{\partial \varDelta_0}\right|\mathrm{d}\varDelta\mathrm{d}\varDelta_0 = \frac{P_0}{\varDelta_0}\mathrm{d}\varDelta\mathrm{d}\varDelta_0 \tag{2.25}$$

and of the energy splitting E

$$P(E, \varDelta_0)\mathrm{d}E\mathrm{d}\varDelta_0 = P(\varDelta, \varDelta_0)\left|\frac{\partial \varDelta}{\partial E}\right|\mathrm{d}E\mathrm{d}\varDelta_0 = P_0\frac{E}{\varDelta_0}\frac{1}{\sqrt{E^2 - \varDelta_0^2}}\mathrm{d}E\mathrm{d}\varDelta_0 \quad , \tag{2.26}$$

which is useful for subsequent calculations and for the calculation of the density of states. The distribution $P(E, \varDelta_0)$ shown in Figure 2.11 has two poles: $\varDelta_0 = 0$ and $\varDelta_0 = E$. While the latter one is integrable, one needs to confine the distribution for $\varDelta_0 \rightarrow 0$ in order to avoid a non-physical infinite number of tunneling systems. In its simplest form, the confinement is realized with a hard cutoff value $\varDelta_{0,\mathrm{min}}$ below which the distribution is set to zero. Systems with extremely small $\varDelta_0$ would have a vanishing probability for tunneling and are basically isolated in a single well, and therefore observable only on very long timescales. Long time heat-release measurements found cutoff values of $\varDelta_{0,\mathrm{min}}/E < 10^{-6}$ [Nit98].

2.3.3 Outcomes from the standard tunneling model

The standard tunneling model in the form it was discussed above is able to predict the observed linear specific heat capacity of glasses at low temperatures. The fact that tunneling systems appear as two-level systems simplifies the calculation of the internal energy U. Since the thermal population of a two-level system with energy

E is given by $f(E,T) = (\exp(E/k_\mathrm{B}T)+1)^{-1}$, its internal energy reads as $U_\mathrm{TLS} = Ef(E,T)$. In order to obtain the internal energy of the ensemble of tunneling system, one needs to perform an integration over the distribution function. By integrating Equation (2.26) over $\mathit{\Delta}_0$, we obtain the density of states

$$D(E)\mathrm{d}E = \int\limits_{\mathit{\Delta}_{0,\mathrm{min}}}^{E} P(E,\mathit{\Delta}_0)\mathrm{d}E\mathrm{d}\mathit{\Delta}_0 = P_0 \ln\left(\frac{2E}{\mathit{\Delta}_{0,\mathrm{min}}}\right)\mathrm{d}E \approx D_0\mathrm{d}E \quad . \tag{2.27}$$

One finds a weak logarithmic dependency on E, which can be approximated as a constant due to $\mathit{\Delta}_{0,\mathrm{min}} \ll E$. That gives for the internal energy

$$U = \int\limits_0^\infty \frac{D_0 E}{\exp\left(\frac{E}{k_\mathrm{B}T}+1\right)}\mathrm{d}E = \frac{\pi^2 D_0 k_\mathrm{B}^2 T^2}{12} \quad , \tag{2.28}$$

and as a result for the specific heat capacity

$$C_\mathrm{V} = \left(\frac{\partial U}{\partial T}\right)_V = \frac{1}{6}\pi^2 D_0 k_\mathrm{B}^2 T \quad . \tag{2.29}$$

This is in fairly good agreement with the data shown in Figure 2.6. The slight deviation of the measurement from a linear specific heat can be attributed to a non-constant density of states, but more likely to the finite time of observation in experiments. As we will see in Section 2.4.3, the relaxation times of tunneling systems $\tau_1 = \tau_{1,\mathrm{min}}\left(E/\mathit{\Delta}_0\right)^2$ are widely distributed as well, spanning relaxation times over several orders of magnitude. Therefore, not every tunneling system can couple to the experiment within the given perturbation time, and the measurement data does not contain the total specific heat capacity of the ensemble [Hun86]. This time dependency of the specific heat can explain the observed slight deviation from a linear temperature dependency predicted by the standard tunneling model [Nit98].

The thermal conductivity with its T^2-dependency at low temperatures can be explained by the standard tunneling model as well. Interactions between phonons and tunneling systems lead to a reduction of the mean free path of the phonons in glasses. Again, the two-level nature is of importance here since phonons with energy $\hbar\omega_\mathrm{ph} = E$ will get resonantly absorbed by a two-level system of energy E if the two-level system is in its ground state. Thus, the inverse mean free path l^{-1} must scale with the population difference $\Delta n = \tanh\left(\frac{E}{2k_\mathrm{B}T}\right)$ of a two-level system. The inverse mean free path of phonons which scatter at tunneling systems is found to be [Phi87]

$$l^{-1} = \Gamma P_0 \omega_\mathrm{ph} \tanh\left(\frac{E}{2k_\mathrm{B}T}\right) \quad , \tag{2.30}$$

with the factor Γ giving the coupling between phonons and tunneling systems. Since tunneling systems are broadly distributed, there exist scattering centers for basically all phonon energies. It is sufficient to consider only phonons with $\hbar\omega_\mathrm{ph} \approx k_\mathrm{B}T$

(dominant phonons). The population difference Δn is therefore constant, and we find $l^{-1} \propto T$. Together with the cubic specific heat capacity of phonons and Equation (2.5), we thereby find

$$\kappa = \frac{1}{3} C v l \propto T^3 T^0 T^{-1} = T^2 \quad , \tag{2.31}$$

in agreement with the experimental findings.

Although some assumptions of the standard tunneling model seem to be arbitrary and simplified, it is remarkable that the standard tunneling model is, beyond explaining thermal properties, quite successful in describing the low temperature properties of glasses in general. The phenomenological assumptions are justified subsequently by the experimental findings [Phi81, Hun86]. However, neither can the model give an answer about the microscopic origin of these tunneling states, nor does it explain why there seems to be such a broad and uniform distribution for the parameters $\mathit{\Delta}$ and λ. For $\mathit{\Delta}$ it is argued that in glasses typical coupling strength variations lead to a normal distributed $\mathit{\Delta}$ centered at $\mathit{\Delta} = 0\,\mathrm{eV}$ with a width of $\sim 10^{-2}\,\mathrm{eV}$ [Phi72]. Contributing tunneling systems should have a maximum asymmetry energy of $|\mathit{\Delta}_{\mathrm{max}}| = 10^{-4}\,\mathrm{eV} \simeq 1\,\mathrm{K}/k_{\mathrm{B}}$. Hence, the distribution in $\mathit{\Delta}$ is considered to be flat for the relevant tunneling systems. Finding such an argument for λ is harder since it depends on several parameters. The exponential dependence of $\mathit{\Delta}_0$ on λ gives values for $\mathit{\Delta}_0$ over several orders of magnitude for only a limited range of λ, which is why the distribution of λ might be treated as constant.
A convincing microscopic picture is missing, however. Computer simulations of simple glasses were performed that give some principal ideas about the origin of tunneling systems [Heu98, Kho20]. It seems that tunneling systems correspond to collective rearrangements of groups of atoms, which is supported by neutron scattering experiments on quartz glass, where indications for coupled rotations of $\mathrm{SiO_4}$-tetrahedra were found [Buc88]. Moreover, in two pulse polarization echo experiments on partially deuterated glycerol, tunneling processes related to rotational movements were observed as well [Bar13]. In electron transmission microscopy of two-dimensional amorphous $\mathrm{SiO_2}$ the direct observation of structural rearrangements induced by the electron beam was accomplished [Hua12]. Whether these rearrangements have something in common with the tunneling motion at low temperatures is questionable, but it shows that rearrangements as sketched in Figure 2.9 do occur in glasses in principle.

2.4 Dielectric properties of glass at low temperatures

From an experimental point of view novel measurements and techniques are required to give a more specific answer to the microscopic nature of tunneling systems.

Previous measurements, especially acoustic and dielectric measurements, were often performed statically, meaning that the response of the tunneling systems to the driving field is measured, while the tunneling system ensemble itself is passive, which gives certain limitations for observations. Electric fields modify the tunneling system ensemble by changing the asymmetry energy and the population number of the two-level state. A dynamic shift of the tunneling systems' energy splitting allows to study the systems also in non-equilibrium and opens the field for novel experiments investigating tunneling system properties. The goal of this thesis is to demonstrate such a non-equilibrium measurement method on tunneling systems in a bulk glass (N-BK7) by use of a combination of different electric fields (Landau-Zener spectroscopy). Therefore, in the following section the interaction between tunneling systems and electric fields will be thoroughly discussed to understand the impact of tunneling systems on the low temperature dielectric properties of glasses.

2.4.1 Dielectric function

A dielectric solid that is placed in a constant electric field $\boldsymbol{F}$ gets polarized, which means that relocations of charges inside the solid generate dipoles with dipole moment $\boldsymbol{p}$, or already existing (permanent) dipoles reorientate. The resulting polarization $\boldsymbol{P} = \frac{1}{V}\sum \boldsymbol{p}_i$ is proportional to the applied electric field and given by the relation

$$\boldsymbol{P} = \varepsilon_0 \chi \boldsymbol{F} \quad , \tag{2.32}$$

with the electric constant ε_0 and the electric susceptibility χ. The isotropic character of amorphous solids allows us to use χ as a scalar quantity. The electric susceptibility describes the ability of a material to form a polarization in the presence of an electric field and is material specific. Using the electric displacement field $\boldsymbol{D}$

$$\boldsymbol{D} = \varepsilon_0 \boldsymbol{F} + \boldsymbol{P} = \varepsilon_0 (1+\chi) \boldsymbol{F} \quad , \tag{2.33}$$

the dielectric function ε can be defined as $\varepsilon = \varepsilon_0(1+\chi)$. For alternating electric fields, a polarization is formed as well, but it follows the electric field delayed. This phase delay is taken into account by making the dielectric function complex-valued

$$\varepsilon(\omega) = \varepsilon'(\omega) + \mathrm{i}\varepsilon''(\omega) \quad . \tag{2.34}$$

The real part ε' contains the energy storing processes (in phase) and the imaginary part ε'' the dissipating processes (out of phase). The dielectric loss is given as the ratio of imaginary and real part

$$\tan\delta = \frac{\varepsilon''}{\varepsilon'} \tag{2.35}$$

and is called the dissipation factor, with the loss angle δ. The dielectric function is frequency dependent. There do exist several mechanisms that contribute to the dielectric function in solids. Their contribution may disappear with increasing frequency if the applied field is alternating too fast for the underlying processes. In the frequency region of visible and UV light only electronic polarization processes, where the electron shell is shifted with respect to the nucleus due to the electric field, are fast enough to contribute to the dielectric function. For frequencies in the infrared range existing positive and negative ions are shifted against each other and contribute as ionic polarization. At even lower frequencies, in the microwave range, preexisting dipoles reorientate with respect to the applied electric field (orientation polarization). In the thesis at hand, measurements take place at excitation frequencies between $250\,\mathrm{MHz} - 1\,\mathrm{GHz}$. Therefore, ionic and electronic contributions are constant, and only the orientation polarization needs to be taken into account.

2.4.2 Interaction of two-level systems with electric fields

If charges are involved in the tunneling process, the system might possess a dipole moment $\boldsymbol{p}$. Therefore, such a tunneling system couples to electric fields, which leads to modifications of the tunneling splitting $\varDelta_0$ and the asymmetry energy $\varDelta$. For small fields one can use the first order perturbation theory and add the perturbation to the unperturbed Hamiltonian. In the basis of the single well's eigenstates $\psi_{\mathrm{a/b}}$ we can write

$$\hat{H} = \hat{H}_{\mathrm{TS}} + \hat{H}_{\mathrm{pert}} = \frac{1}{2}\begin{pmatrix} \varDelta & -\varDelta_0 \\ -\varDelta_0 & -\varDelta \end{pmatrix} + \frac{1}{2}\begin{pmatrix} \delta\varDelta & -\delta\varDelta_0 \\ -\delta\varDelta_0 & -\delta\varDelta \end{pmatrix} \quad . \tag{2.36}$$

It is assumed that the modification of the barrier height V and the distance d is small compared to the changes in $\varDelta$, and we can neglect the perturbation $\delta\varDelta_0$ in Equation (2.36). Experiments like [Phi81, Lis15, Sar16] strongly support this assumption. The applied electric field changes the asymmetry energy linearly

$$\delta\varDelta = 2\boldsymbol{pF} = 2pF\cos\theta \quad , \tag{2.37}$$

whereby the angle θ defines the relative orientation of the dipole moment with respect to the electric field. We furthermore assumed that all dipole moments have the same absolute value. Equation (2.36) can be transformed into the basis $\Psi_{\mathrm{g/e}}$ through a rotation with the matrices (2.21), and we find for the perturbed Hamiltonian with a periodic excitation $F_{\mathrm{ac}}(t) = F_{\mathrm{ac}}\cos(\omega t)$

$$\hat{\mathcal{H}} = \frac{1}{2}\begin{pmatrix} E & 0 \\ 0 & -E \end{pmatrix} + \frac{1}{E}\begin{pmatrix} \varDelta & \varDelta_0 \\ \varDelta_0 & -\varDelta \end{pmatrix} pF_{\mathrm{ac}}\cos(\omega t)\cos\theta \quad . \tag{2.38}$$

On the one hand the electric field modifies the energy splitting through the additional diagonal elements

$$\delta E = 2\frac{\varDelta}{E} p F_{\mathrm{ac}}(t)\cos\theta \quad , \tag{2.39}$$

and on the other hand the electric field causes off-diagonal elements that couple the states $|\Psi_{\mathrm{g}}\rangle$ and $|\Psi_{\mathrm{e}}\rangle$, and therefore leads to induced transitions between both states.

The Hamiltonian from Equation (2.38) is formally equivalent to the one of a spin-1/2 particle in a magnetic field. We can make use of this analogy for solving the dynamics of a tunneling system perturbed by an alternating electric field. This was first done by [Hun76] for ultrasonic fields, but can be applied to electric fields as well. Here, we follow the derivation described in [Car94, Bur98]. The Hamiltonian for a spin-1/2 particle in a magnetic field $\boldsymbol{B}$ is

$$\hat{H}_{\mathrm{spin}} = -\gamma \boldsymbol{B}\cdot\hat{\boldsymbol{S}} \quad , \tag{2.40}$$

with the spin's gyromagnetic ratio γ and the spin-1/2 operator

$$\hat{\boldsymbol{S}} = (\hat{s}_{\mathrm{x}}, \hat{s}_{\mathrm{y}}, \hat{s}_{\mathrm{z}}) \quad , \tag{2.41}$$

introducing the Pauli spin operators

$$\hat{s}_{\mathrm{x}} = \frac{\hbar}{2}\begin{pmatrix}0 & 1\\ 1 & 0\end{pmatrix} \quad \hat{s}_{\mathrm{y}} = \frac{\hbar}{2}\begin{pmatrix}0 & -\mathrm{i}\\ \mathrm{i} & 0\end{pmatrix} \quad \hat{s}_{\mathrm{z}} = \frac{\hbar}{2}\begin{pmatrix}1 & 0\\ 0 & -1\end{pmatrix} \quad . \tag{2.42}$$

The analogy to the tunneling system Hamiltonian is established by choosing the magnetic field

$$\boldsymbol{B}(t) = \boldsymbol{B}_0 + \boldsymbol{B}_1(t) = \begin{pmatrix} B_{1,\mathrm{x}}\cos(\omega t)\\ 0 \\ B_{0,\mathrm{z}} + B_{1,\mathrm{z}}\cos(\omega t)\end{pmatrix} \quad , \tag{2.43}$$

which results in

$$\hat{H}_{\mathrm{spin}} = -\frac{\gamma\hbar}{2}\left[B_{0,\mathrm{z}}\begin{pmatrix}1 & 0\\ 0 & -1\end{pmatrix} + B_{1,\mathrm{x}}(t)\begin{pmatrix}0 & 1\\ 1 & 0\end{pmatrix} + B_{1,\mathrm{z}}(t)\begin{pmatrix}1 & 0\\ 0 & -1\end{pmatrix}\right] \quad , \tag{2.44}$$

with $B_{1,i}(t) = B_{1,i}\cos(\omega t) \quad (i = [x,z])$, and we can identify

$$\begin{aligned} -\gamma\hbar B_{0,\mathrm{z}} &= E \\ -\gamma\hbar B_{1,\mathrm{x}}(t) &= 2\frac{\varDelta_0}{E} p F_{\mathrm{ac}}(t)\cos\theta \\ -\gamma\hbar B_{1,\mathrm{z}}(t) &= 2\frac{\varDelta}{E} p F_{\mathrm{ac}}(t)\cos\theta \quad . \end{aligned} \tag{2.45}$$

Instead of solving the tunneling system Hamiltonian to receive the system's dynamic response, we make use of the known solutions of the spin-1/2 system, which is treated in terms of the Bloch equations formulated in [Blo46]. Ignoring relaxation processes initially, the equation of motion for the expectation value of the spin $\langle\hat{\boldsymbol{S}}\rangle$ is written as

$$\frac{\mathrm{d}}{\mathrm{d}t}\langle\hat{\boldsymbol{S}}\rangle = \gamma\langle\hat{\boldsymbol{S}}\rangle \times \boldsymbol{B} \quad . \tag{2.46}$$

Adding now the relaxation times τ_1 and τ_2, we end up with the Bloch equations

$$\begin{aligned}
\frac{\mathrm{d}}{\mathrm{d}t}\langle\hat{S}_\mathrm{x}\rangle &= \gamma\left[\langle\hat{S}_\mathrm{y}\rangle B_\mathrm{z}(t) - \langle\hat{S}_\mathrm{z}\rangle B_\mathrm{y}(t)\right] - \frac{1}{\tau_2}\langle\hat{S}_\mathrm{x}\rangle \\
\frac{\mathrm{d}}{\mathrm{d}t}\langle\hat{S}_\mathrm{y}\rangle &= \gamma\left[\langle\hat{S}_\mathrm{z}\rangle B_\mathrm{x}(t) - \langle\hat{S}_\mathrm{x}\rangle B_\mathrm{z}(t)\right] - \frac{1}{\tau_2}\langle\hat{S}_\mathrm{y}\rangle \\
\frac{\mathrm{d}}{\mathrm{d}t}\langle\hat{S}_\mathrm{z}\rangle &= \gamma\left[\langle\hat{S}_\mathrm{x}\rangle B_\mathrm{y}(t) - \langle\hat{S}_\mathrm{y}\rangle B_\mathrm{x}(t)\right] - \frac{1}{\tau_1}\left(\langle\hat{S}_\mathrm{z}\rangle - \langle\hat{S}_\mathrm{z}\rangle_\mathrm{eq}\right) \quad .
\end{aligned} \tag{2.47}$$

Here, $\langle\hat{S}_\mathrm{z}\rangle_\mathrm{eq} = \frac{1}{2}\tanh\left(-\gamma\hbar\frac{B_\mathrm{z}(t)}{2k_\mathrm{B}T}\right)$ gives the thermal equilibrium value of $\langle\hat{S}_\mathrm{z}\rangle$. Using the magnetic field from Equation (2.43) and treating $\boldsymbol{B}_1(t)$ as a small perturbation in $\boldsymbol{B}(t) = \boldsymbol{B}_0 + \boldsymbol{B}_1(t)$ the Bloch equations can be linearized as an approximation around the unperturbed solution $\langle\hat{S}_0(t)\rangle$. We expect a solution of the form $\langle\hat{\boldsymbol{S}}(t)\rangle = \langle\hat{\boldsymbol{S}}_0(t)\rangle + \langle\hat{\boldsymbol{S}}_1(t)\rangle$. We can write the linearized Bloch equations as

$$\begin{aligned}
\frac{\mathrm{d}}{\mathrm{d}t}\langle\hat{S}_{0,\mathrm{z}}\rangle &= -\frac{1}{\tau_1}\left(\langle\hat{S}_{0,\mathrm{z}}\rangle - \langle\hat{S}_\mathrm{z}(B_{0,\mathrm{z}})\rangle_\mathrm{eq}\right) \\
\frac{\mathrm{d}}{\mathrm{d}t}\langle\hat{S}_{1,\mathrm{x}}\rangle &= \gamma\langle\hat{S}_{1,\mathrm{y}}\rangle B_{0,\mathrm{z}} - \frac{1}{\tau_2}\langle\hat{S}_{1,\mathrm{x}}\rangle \\
\frac{\mathrm{d}}{\mathrm{d}t}\langle\hat{S}_{1,\mathrm{y}}\rangle &= \gamma\langle\hat{S}_{0,\mathrm{z}}\rangle B_{1,\mathrm{x}}(t) - \gamma\langle\hat{S}_{1,\mathrm{x}}\rangle B_{0,\mathrm{z}}(t) - \frac{1}{\tau_2}\langle\hat{S}_{1,\mathrm{y}}\rangle \\
\frac{\mathrm{d}}{\mathrm{d}t}\langle\hat{S}_{1,\mathrm{z}}\rangle &= -\frac{1}{\tau_1}\left(\langle\hat{S}_{1,\mathrm{z}}\rangle - B_{1,\mathrm{z}}\left.\frac{\mathrm{d}\langle\hat{S}_\mathrm{z}\rangle_\mathrm{eq}}{\mathrm{d}B_{1,\mathrm{z}}}\right|_{B_{1,\mathrm{z}}=0}\right) \quad ,
\end{aligned} \tag{2.48}$$

with the taylor approximation of $\langle\hat{S}_\mathrm{z}\rangle_\mathrm{eq}$ at $B_{1,\mathrm{z}} = 0$ being

$$B_{1,\mathrm{z}}\left.\frac{\mathrm{d}\langle\hat{S}_\mathrm{z}\rangle_\mathrm{eq}}{\mathrm{d}B_{1,\mathrm{z}}}\right|_{B_{1,\mathrm{z}}=0} = -B_{1,\mathrm{z}}(t)\frac{\gamma\hbar}{4k_\mathrm{B}T}\operatorname{sech}^2\left(-\frac{\gamma\hbar B_{0,\mathrm{z}}}{2k_\mathrm{B}T}\right) \quad . \tag{2.49}$$

In order to decouple $\langle\hat{S}_{1,\mathrm{x}}\rangle$ and $\langle\hat{S}_{1,\mathrm{y}}\rangle$ in Equations (2.48), we introduce the raising and lowering operators $\langle\hat{S}_{1,\pm}\rangle = \langle\hat{S}_{1,\mathrm{x}}\rangle \pm \mathrm{i}\langle\hat{S}_{1,\mathrm{y}}\rangle$. With that, $\langle\hat{S}_{1,\mathrm{x}}\rangle$ and $\langle\hat{S}_{1,\mathrm{y}}\rangle$ in the set of equations is replaced by the two equations

$$\frac{\mathrm{d}}{\mathrm{d}t}\langle\hat{S}_{1,\pm}\rangle = \pm\mathrm{i}\gamma\left(\langle\hat{S}_{1,\pm}\rangle B_{0,\mathrm{z}} + \langle\hat{S}_{0,\mathrm{z}}\rangle B_{1,\mathrm{x}}(t)\right) - \frac{1}{\tau_2}\langle\hat{S}_{1,\pm}\rangle \quad . \tag{2.50}$$

The set of equations can be solved with the solutions given in [Car94]. Here, we are only interested in the equilibrium state for $t \to \infty$, and we ignore all terms that contain the factor $\exp(-t/\tau_1)$.

$$\begin{aligned}
\langle \hat{S}_{0,\mathrm{z}} \rangle &= \langle \hat{S}_{\mathrm{z}}(B_{0,\mathrm{z}}) \rangle_{\mathrm{eq}} \\
\langle \hat{S}_{1,\mathrm{z}} \rangle &= -B_{1,\mathrm{z}} \frac{\gamma \hbar}{4 k_{\mathrm{B}} T} \operatorname{sech}^2 \left(-\frac{\gamma \hbar B_{0,\mathrm{z}}}{2 k_{\mathrm{B}} T} \right) \frac{\cos(\omega t) + \omega \tau_1 \sin(\omega t)}{1 + \omega^2 \tau_1^2} \\
\langle \hat{S}_{1,\pm} \rangle &= \gamma B_{1,\mathrm{x}} \langle \hat{S}_{0,\mathrm{z}} \rangle \frac{\left(-\gamma B_{0,\mathrm{z}} \mp \frac{\mathrm{i}}{\tau_2} \right) \cos(\omega t) \mp \mathrm{i} \omega \sin(\omega t)}{\left(-\gamma B_{0,\mathrm{z}} \mp \frac{\mathrm{i}}{\tau_2} \right)^2 - \omega^2}
\end{aligned} \tag{2.51}$$

These solutions can be transformed back to the case of a tunneling system with Equations (2.45).

$$\begin{aligned}
\langle \hat{S}^{\mathrm{TS}}_{0,\mathrm{z}} \rangle &= \frac{1}{2} \tanh \left(\frac{E}{2 k_{\mathrm{B}} T} \right) \\
\langle \hat{S}^{\mathrm{TS}}_{1,\mathrm{z}} \rangle &= \left(\frac{\varDelta}{E} \right) \frac{p F_{\mathrm{ac}} \cos\theta}{2 k_{\mathrm{B}} T} \operatorname{sech}^2 \left(\frac{E}{2 k_{\mathrm{B}} T} \right) \frac{\cos(\omega t) + \omega \tau_1 \sin(\omega t)}{1 + \omega^2 \tau_1^2} \\
\langle \hat{S}^{\mathrm{TS}}_{1,\pm} \rangle &= -\left(\frac{\varDelta_0}{E} \right) \frac{p F_{\mathrm{ac}} \cos\theta}{\hbar} \tanh \left(\frac{E}{2 k_{\mathrm{B}} T} \right) \frac{\left(\frac{E}{\hbar} \mp \frac{\mathrm{i}}{\tau_2} \right) \cos(\omega t) \mp \mathrm{i} \omega \sin(\omega t)}{\left(\frac{E}{\hbar} \mp \frac{\mathrm{i}}{\tau_2} \right)^2 - \omega^2}
\end{aligned} \tag{2.52}$$

Next, we want to connect these solutions with the electric susceptibility χ. We can make use of the dipole operator, which can be deduced from Equation (2.38) as

$$\hat{\pi} = \left(\frac{\varDelta}{E} \hat{\sigma}_{\mathrm{z}} + \frac{\varDelta_0}{E} \hat{\sigma}_{\mathrm{x}} \right) p \cos\theta \quad , \tag{2.53}$$

with $\hat{\sigma}_i = \frac{2}{\hbar} \hat{s}_i$ being the Pauli matrices. The expectation value of the dipole operator $\langle \hat{\pi} \rangle$ can be expressed through the tunneling system spin expectation values $\langle \hat{S}^{\mathrm{TS}} \rangle$ as

$$\langle \hat{\pi} \rangle = p \cos\theta \left[\frac{2\varDelta}{E} \langle \hat{S}^{\mathrm{TS}}_{1,\mathrm{z}} \rangle - \frac{\varDelta_0}{E} \left(\langle \hat{S}^{\mathrm{TS}}_{1,+} \rangle + \langle \hat{S}^{\mathrm{TS}}_{1,-} \rangle \right) \right] \quad . \tag{2.54}$$

With the relation $\varepsilon_0 \chi = \mathrm{d}\langle \hat{\pi} \rangle / \mathrm{d}F_{\mathrm{ac}}$ we get the contribution of a single tunneling system to the electric susceptibility $\chi = \chi' + \mathrm{i}\chi''$. The terms with a response in phase $\cos(\omega t)$ are attributed to the real part χ', the ones out of phase $\sin(\omega t)$ to the imaginary part χ''. We can differentiate between relaxation and resonant processes, originating from the components $\langle \hat{S}^{\mathrm{TS}}_{1,\mathrm{z}} \rangle$ and $\langle \hat{S}^{\mathrm{TS}}_{1,\mathrm{x}} \rangle$, respectively.

relaxation part:

$$\varepsilon_0 \chi_{\mathrm{z}}(\omega) = \frac{p^2 \cos^2\theta}{k_{\mathrm{B}} T} \left(\frac{\varDelta}{E} \right)^2 \operatorname{sech}^2 \left(\frac{E}{2 k_{\mathrm{B}} T} \right) a(\omega) \tag{2.55}$$

$$\text{with:} \quad a(\omega) = \frac{1 + \mathrm{i}\omega\tau_1}{1 + \omega^2 \tau_1^2} \tag{2.56}$$

resonant part:

$$\varepsilon_0\chi_{\mathrm{x}}(\omega) = \frac{p^2\cos^2\theta}{\hbar}\left(\frac{\Delta_0}{E}\right)^2 \tanh\left(\frac{E}{2k_{\mathrm{B}}T}\right) b(\omega) \tag{2.57}$$

$$\text{with:}\quad b(\omega) = \frac{\frac{E}{\hbar} - \frac{\mathrm{i}}{\tau_2} + \omega}{\left(\frac{E}{\hbar} - \frac{\mathrm{i}}{\tau_2}\right)^2 - \omega^2} + \frac{\frac{E}{\hbar} + \frac{\mathrm{i}}{\tau_2} - \omega}{\left(\frac{E}{\hbar} + \frac{\mathrm{i}}{\tau_2}\right)^2 - \omega^2} \tag{2.58}$$

As it is shown in Figure 2.12 the frequency dependence of $a(\omega)$ in Equation (2.55) shows a typical relaxation behavior and $b(\omega)$ in Equation (2.57) a resonant one. Writing Equation (2.55) and (2.57) as the relative change of the dielectric function's real and imaginary part and defining $\hbar\omega_0 := E$, we finally obtain:

relaxation part:

$$\left(\frac{\delta\varepsilon'_{\mathrm{rel}}}{\varepsilon'}\right)_{\mathrm{TS}} = \frac{p^2\cos^2\theta}{\varepsilon_0\varepsilon_{\mathrm{r}}k_{\mathrm{B}}T}\left(\frac{\Delta}{E}\right)^2 \operatorname{sech}^2\left(\frac{E}{2k_{\mathrm{B}}T}\right) a'(\omega) \tag{2.59}$$

$$\left(\frac{\delta\varepsilon''_{\mathrm{rel}}}{\varepsilon'}\right)_{\mathrm{TS}} = \frac{p^2\cos^2\theta}{\varepsilon_0\varepsilon_{\mathrm{r}}k_{\mathrm{B}}T}\left(\frac{\Delta}{E}\right)^2 \operatorname{sech}^2\left(\frac{E}{2k_{\mathrm{B}}T}\right) a''(\omega) \tag{2.60}$$

$$\text{with:}\quad a'(\omega) = \frac{1}{1+(\omega\tau_1)^2} \quad ; \quad a''(\omega) = \frac{\omega\tau_1}{1+(\omega\tau_1)^2} \tag{2.61}$$

resonant part:

$$\left(\frac{\delta\varepsilon'_{\mathrm{res}}}{\varepsilon'}\right)_{\mathrm{TS}} = \frac{p^2\cos^2\theta}{\varepsilon_0\varepsilon_{\mathrm{r}}\hbar}\left(\frac{\Delta_0}{E}\right)^2 \tanh\left(\frac{E}{2k_{\mathrm{B}}T}\right) b'(\omega) \tag{2.62}$$

$$\left(\frac{\delta\varepsilon''_{\mathrm{res}}}{\varepsilon'}\right)_{\mathrm{TS}} = \frac{p^2\cos^2\theta}{\varepsilon_0\varepsilon_{\mathrm{r}}\hbar}\left(\frac{\Delta_0}{E}\right)^2 \tanh\left(\frac{E}{2k_{\mathrm{B}}T}\right) b''(\omega) \tag{2.63}$$

$$\begin{aligned} \text{with:}\quad b'(\omega) &= -\frac{(\omega-\omega_0)\tau_2^2}{(\omega-\omega_0)^2\tau_2^2+1} + \frac{(\omega+\omega_0)\tau_2^2}{(\omega+\omega_0)^2\tau_2^2+1} \\ b''(\omega) &= \frac{\tau_2}{(\omega-\omega_0)^2\tau_2^2+1} - \frac{\tau_2}{(\omega+\omega_0)^2\tau_2^2+1} \end{aligned} \tag{2.64}$$

Note that this is the contribution of a single tunneling system to the dielectric function. In Figure 2.12 the frequency dependencies of the relaxation (Equation (2.61)) and the resonant part (Equation (2.64)) are plotted.

The frequency dependence of the relaxation part corresponds to the behavior of a Debye relaxation [Deb13], where dipole moments permanently have to reorientate due to the alternating electric field within a specific relaxation time τ_1, given by the underlying relaxation processes. As Equation (2.39) shows, the electric field modulates the energy splitting E of a tunneling system by coupling to its dipole moment, see Figure 2.13 (left). Therefore, the tunneling system has to permanently adapt its population number to the instantaneous equilibrium state. This is done

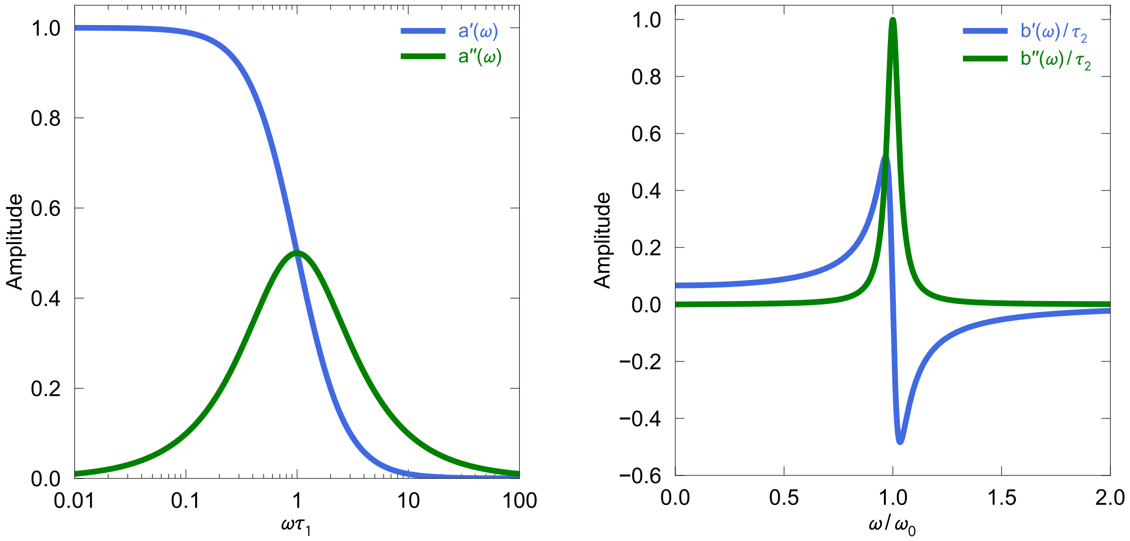

Figure 2.12: Left: Real and imaginary part ($a'(\omega)$, $a''(\omega)$) of the frequency dependence of the relaxation part as a function of $\omega\tau_1$, which shows a Debye relaxation behavior. Right: Real and imaginary part ($b'(\omega)$, $b''(\omega)$) of the frequency dependence of the resonant part as a function of ω/ω_0, scaled with $1/\tau_2$. A relaxation time of $\tau_2 = 30/\omega_0$ was used, with $\hbar\omega_0 = E$ corresponding to the energy splitting E of the tunneling system.

via interactions with the environment – in the case of tunneling systems in dielectric solids through absorption or emission of thermal phonons, as it will be discussed in the next chapter. The functions $a'(\omega)$ and $a''(\omega)$ are plotted as a function of $\omega\tau_1$ in Figure 2.12 (left). For low frequencies $\omega\tau_1 \ll 1$, the relaxation is fast enough to allow the system to follow the electric field in phase. The real part is then maximal, and the imaginary part vanishes. For higher frequencies, the relaxation becomes too slow, and the response lags in phase behind the field. Hence, the real part drops, and the imaginary part has its maximum for $\omega\tau_1 = 1$. At very high frequencies $\omega\tau_1 \gg 1$ the system cannot follow the excitation anymore and real and imaginary part disappear.

On the other hand, as mentioned before, the electric field $F_{\mathrm{ac}}(t)$ causes off-diagonal elements in the Hamiltonian of Equation (2.38), which leads to direct transitions between ground and excited state, see Figure 2.13 (right). This means that a photon from the electric field with energy $\hbar\omega$ gets resonantly absorbed by a tunneling system with energy $E = \hbar\omega_0$ if both energies match $\hbar\omega = E$. Hence, the photon excites the tunneling system from its ground state into the upper state. The frequency dependence of this excitation has the form of a typical resonant behavior, which is shown for the frequency dependent parts $b'(\omega)$ and $b'(\omega)$ of Equation (2.62) and (2.63) in Figure 2.12 (right). At $\omega = \omega_0$ the absorption of photons is maximal, and the imaginary part has its maximum, meaning that energy dissipation is the highest too. The real part changes its sign there. For higher and lower frequencies, the

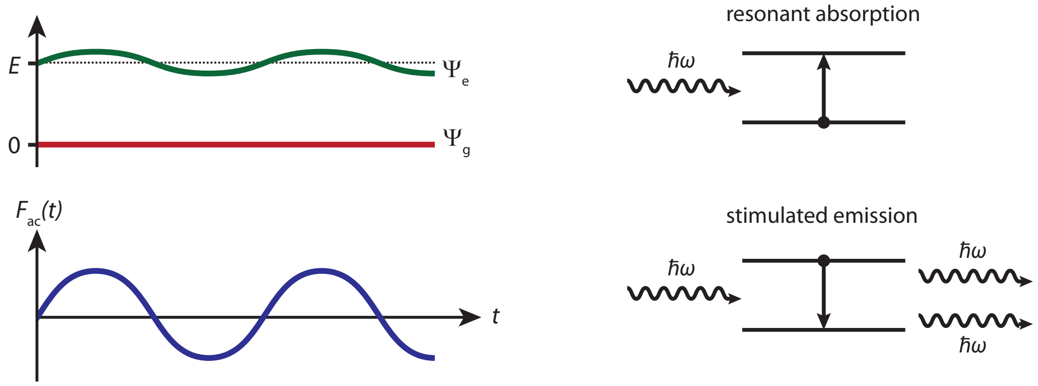

Figure 2.13: Schematic drawing of the effect of an alternating electric field $F_{\mathrm{ac}}(t)$ on the two-level state of the tunneling system. The electric field F_{ac} modulates the energy splitting E of the tunneling system, inducing a relaxation behavior (left). Moreover, the electric field couples both eigenstates of the tunneling system, leading to a resonant interaction between photons of the electric field and the tunneling system with resonant absorption or stimulated emission of photons with energy $\hbar\omega = E$ (right). Adapted from [Ens05].

absorption is suppressed, and the imaginary part disappears. The real part remains greater than zero at low frequencies, while it vanishes at high frequencies. This is the behavior expected from a classical oscillator coupled to a periodic excitation. For low frequencies, the oscillator would slightly follow the excitation in phase, while for high frequencies the response is opposite in phase with vanishing displacement.

2.4.3 Relaxation times of tunneling systems

In order to complete the discussion about the dielectric properties of glasses at low temperatures caused by tunneling systems, we have to specify their relaxation times τ_1 and τ_2, which have already been introduced. For tunneling systems in dielectric solids, the interaction with thermal phonons is the dominant channel for relaxation processes.

One-phonon process

If the energy of a phonon matches the energy splitting of a tunneling system, transitions between the two energy levels of the tunneling system may occur through absorbing or emitting a thermal phonon, similar to the resonant interaction between a photon and the tunneling system discussed before. At temperatures below 1 K the number of phonons is low, and we can restrict the discussion to a process where only a single phonon is involved in the transition (one-phonon process). The relaxation rate $\tau_{1\mathrm{P}}^{-1}$ was calculated in [Jä72]. It is the sum of the transition rates $W_{\mathrm{g}\rightarrow\mathrm{e}}$ and

$W_{\mathrm{e}\to\mathrm{g}}$ between ground and excited state induced by the phonon. Following [Phi87] we can write the relaxation rate as

$$\tau_{1\mathrm{P}}^{-1} = W_{\mathrm{g}\to\mathrm{e}} + W_{\mathrm{e}\to\mathrm{g}} = W_{\mathrm{g}\to\mathrm{e}}\left(1+\exp\left(\frac{E}{k_{\mathrm{B}}T}\right)\right) \quad . \tag{2.65}$$

The probability for a transition from the ground to the excited state $W_{\mathrm{g}\to\mathrm{e}}$ is calculated with Fermi's golden rule

$$W_{\mathrm{g}\to\mathrm{e}} = \sum_{\alpha} \frac{2\pi}{\hbar} \left|\langle\Psi_{\mathrm{e}}|\,\mathcal{H}_{\mathrm{pert}}\,|\Psi_{\mathrm{g}}\rangle\right|^2 D(E) f(E,T) \quad , \tag{2.66}$$

with the phonon density of states from the Debye model $D(E)$ (Equation (2.1)) and the Bose-Einstein distribution $f(E,T)$. The summation is done over all phonon modes α (one longitudinal, two transversal). Using an acoustic wave as perturbation instead of an electric field in $\mathcal{H}_{\mathrm{pert}}$, we can write the term $\langle\Psi_{\mathrm{e}}|\,\mathcal{H}_{\mathrm{pert}}\,|\Psi_{\mathrm{g}}\rangle$ according to [Phi87] as

$$\langle\Psi_{\mathrm{e}}|\,\mathcal{H}_{\mathrm{pert}}\,|\Psi_{\mathrm{g}}\rangle = \frac{\Delta_0}{E}\gamma_\alpha\left(\frac{\hbar\omega}{2\rho V v_\alpha^2}\right)^{1/2} \quad , \tag{2.67}$$

with the sound velocity v_α of the phonon mode and the mass density ρ. The coupling strength between phonon and tunneling system is given by γ_α, which is typically of the order ~1 eV [Hun86]. Putting everything together, we can write for the one-phonon relaxation rate

$$\tau_{1\mathrm{P}}^{-1} = K_1\left(\frac{\Delta_0}{E}\right)^2 E^3 \coth\left(\frac{E}{2k_{\mathrm{B}}T}\right) = \left(\frac{\Delta_0}{E}\right)^2 \tau_{1,\mathrm{min}}^{-1} \quad , \tag{2.68}$$

introducing the factor

$$K_1 = \frac{1}{2\pi\rho\hbar^4}\left(\frac{\gamma_{\mathrm{l}}^2}{v_{\mathrm{l}}^5} + 2\frac{\gamma_{\mathrm{t}}^2}{v_{\mathrm{t}}^5}\right) \quad , \tag{2.69}$$

which contains all material specific parameters and defines the strength of the relaxation. As it was already mentioned in the discussion of the low temperature heat capacity, the relaxation time depends on the tunneling system parameters and is therefore widely distributed. Tunneling systems with a tunneling splitting of $\Delta_{0,\mathrm{min}}$ relax the slowest, and symmetric ones ($\Delta = 0$, $E = \Delta_0$) have the shortest relaxation time $\tau_{1,\mathrm{min}}$.

Two-phonon process

For higher temperatures, the number of phonons increases, and higher order processes may become important. Here, we want to discuss the two-phonon process, where two phonons with energies $\hbar\omega_{1/2}$ induce transitions of the tunneling system state, and the energy condition reads $\hbar\omega_1 = \hbar\omega_2 \pm E$. The energies of the phonons do not match the energy splitting, and a third level is involved in the transition, whose origin can be virtual or real. The relaxation rate for this process was calculated in [Dou80]

$$\tau_{2\mathrm{P}}^{-1} = K_2 \left(\frac{\varDelta_0}{E}\right)^2 T^7 f_1\left(\frac{E}{2k_\mathrm{B}T}\right) \coth\left(\frac{E}{2k_\mathrm{B}T}\right) \quad . \tag{2.70}$$

Again, a material dependent parameter K_2 is introduced which gives the strength of this relaxation process. For comparisons between experimental data and theory, K_1 and K_2 are typically used as free parameters. Expressions for K_2 and the function f_1 are given in [Dou80][2]. The two-phonon process usually becomes important at temperatures above a few kelvin. Therefore, in measurements well below 1 K only the one-phonon relaxation process needs to be considered.

For the total energy relaxation rate τ_1^{-1} one sums over the rates of each process, which gives

$$\tau_1^{-1} = \tau_{1\mathrm{P}}^{-1} + \tau_{2\mathrm{P}}^{-1} + \ldots \quad . \tag{2.71}$$

Relaxation through interactions between tunneling systems

The processes discussed above are both relaxations of the $\hat{S}_\mathrm{z}^{TS}$ tunneling system spin component, which is why they are called longitudinal relaxations. Relaxations in $\hat{S}_\mathrm{x}^{TS}$ lead to dephasing and are called transversal or dephasing relaxations. For the transversal relaxation rate τ_2^{-1} one can write in general [Sli96]

$$\tau_2^{-1} = 2\tau_1^{-1} + \tau_\phi^{-1} \quad , \tag{2.72}$$

where τ_ϕ^{-1} describes pure dephasing processes. Dephasing processes in glasses are caused by interactions between tunneling systems, which will be briefly discussed in the following. We consider a tunneling system in resonance with the driving field. An energy transfer through direct interaction between tunneling systems of similar energy by exchanging a resonant phonon is ineffective because the spatial separation between two resonant tunneling systems is large compared to the $^1/_{R^3}$-dependency of the interaction strength. However, the tunneling system in resonance with the electric field is surrounded by other tunneling systems with different energy splittings. If the tunneling systems' energy splitting is $E \lesssim k_\mathrm{B}T$, those systems will undergo random thermal transitions within a timescale of $\tau_{1\mathrm{T}} = (K_1 k_\mathrm{B}^3 T^3)^{-1}$, given by the phononic relaxation time $\tau_{1\mathrm{P}}$. A transition of a tunneling system changes its local strain field, and thereby couples to neighboring tunneling systems. An interaction

---

[2] $f_1(x) = \frac{x}{70}(x^2+\pi^2)(x^4-\pi^2u^2+\frac{10}{3}\pi^4)$ with $x = {}^E/_{2k_\mathrm{B}T}$

can be elastically, as it was just motivated, or electrically due to dipole-dipole interactions. In either case, the coupling to fluctuating adjacent systems leads to a stochastic change of the energy splitting of the resonant tunneling system. Therefore, its time evolution is disturbed, and the system loses its coherence with other resonant systems, which gives rise to dephasing. This process is called spectral diffusion. Its effect on the dephasing time τ_ϕ was calculated in [Bla77]. The interaction between two tunneling systems mainly effects the $\hat{S}_\mathrm{z}^{TS}$ component. Thus, the change of the energy splitting for a resonant tunneling system i, interacting with neighboring tunneling systems j, can be written as [Bur15]

$$\delta E_i = \frac{\mathit{\Delta}_i}{E_i} \sum_j \frac{\mathit{\Delta}_j}{E_j} U_{ij} \hat{S}_{\mathrm{z},j}^{TS} \quad . \tag{2.73}$$

The average interaction is $\langle U_{ij} \rangle = \pm U_0 / R_{ij}^3$, with the interaction constant $U_0 = U_{0,\mathrm{elastic}} + U_{0,\mathrm{electric}} \simeq \gamma^2/\rho v^2 + p^2/\varepsilon'$. Over the course of time the energy splitting E_i differs from its original value $E = \hbar\omega_0$. The probability of finding the tunneling system i at the time t to have an energy splitting $\hbar\omega$ is approximated with a diffusion kernel of the form [Bla77]

$$D(\omega - \omega_0, t) = \frac{1}{\pi} \frac{\Delta\omega(t)}{(\omega - \omega_0)^2 + [\Delta\omega(t)]^2} \quad . \tag{2.74}$$

It has the shape of a Lorentzian distribution with an increasing width over time. In the short time limit $t < \tau_{1,\mathrm{min}} < \tau_{1\mathrm{T}}$, which was calculated for the phase decoherence in polarization echo measurements, the width is given by $\Delta w(t) = \frac{\Delta}{E} \tau_\phi^{-2}$, and the dephasing rate due to spectral diffusion can be written as [Bur18]

$$\tau_\phi^{-1} = \sqrt{\frac{\pi^6}{24} \frac{P_0 U_0 k_\mathrm{B} T}{\hbar \tau_{1\mathrm{T}}}} \quad . \tag{2.75}$$

The interaction should be weak, and the dephasing rate related to spectral diffusion is often negligible. To what extent spectral diffusion impacts resonant processes at low temperatures is unclear. In Section 2.4.5 we will revisit the concept of spectral diffusion in order to discuss its explicit influence on saturation effects of resonant tunneling systems.

Besides spectral diffusion the interaction between tunneling systems may lead to an additional longitudinal relaxation process, as suggested in [Bur95, Bur04]. It is claimed that due to the interaction, resonant pairs of tunneling systems with similar energy can be formed which perform so-called flip flop transitions, where paired systems alternatingly switch between ground and excited state. These pairs represent a new two-level state, but with a much lower energy splitting than the individual systems had. It can be shown that the distribution function of these resonant pairs is clearly enhanced at low energies compared to the one of the non-interacting standard tunneling model distribution. As a consequence, interactions between such resonant pairs are more likely and finally lead to a delocalization of the tunneling system excitation. A relaxation rate of

$$\tau_{1,\mathrm{int}}^{-1} \propto \left(\frac{\Delta_0}{E}\right)^2 (P_0U_0)^3 T \tag{2.76}$$

is suggested, which should become dominant at very low temperatures when the relaxation through phonons becomes less and less important. For the sake of completeness, it should also be mentioned that interactions between tunneling systems will lead to a modified distribution function of the tunneling systems, as it is stated in [Bur95]. The coupling between tunneling systems leads to collective excitations, and thereby to a reduced number of low-energy tunneling systems. One expects a hole in the distribution function at low energies. The modified distribution function reads as

$$P(E,\Delta_0)\mathrm{d}E\mathrm{d}\Delta_0 = P_{\mathrm{STM}}\left(1-\frac{2\pi}{3}P_0U_0\log\left(\frac{W}{E+k_\mathrm{B}T}\right)\log\left(\frac{W}{\Delta_{0,\mathrm{min}}}\right)\right)\mathrm{d}E\mathrm{d}\Delta_0 \quad , \tag{2.77}$$

where W/k_B gives the crossover temperature from excitations in the form of tunneling states towards thermal excitations or soft localized modes. Typical values for the crossover are found to be between 1 K and 10 K [Ram98].

The dimensionless factor P_0U_0 scales the importance of the mutual interactions. Besides the interaction constant U_0, the factor P_0 occurs, as it gives the density of tunneling systems, and therefore their average distance. Typical values found for P_0U_0 are of the order $\sim 10^{-3}$ [Bur95, Nat98, Nal04].

2.4.4 Temperature dependency

The expressions (2.59), (2.60), (2.62), (2.63) give the contributions of a single tunneling system to the dielectric function. In order to obtain the contribution of the entire ensemble to the dielectric function as a function of temperature, we have to integrate these expressions over the distribution function (2.26) and insert the expressions for the relaxation times.

$$\frac{\delta\varepsilon'}{\varepsilon'} = \int_{\Delta_{0,\mathrm{min}}}^{E_\mathrm{max}} \mathrm{d}E \int_{\Delta_{0,\mathrm{min}}}^{E} \mathrm{d}\Delta_0 \left[\left(\frac{\delta\varepsilon'_\mathrm{rel}}{\varepsilon'}\right)_\mathrm{TS} + \left(\frac{\delta\varepsilon'_\mathrm{res}}{\varepsilon'}\right)_\mathrm{TS}\right] P(E,\Delta_0) \tag{2.78}$$

$$\frac{\delta\varepsilon''}{\varepsilon'} = \int_{\Delta_{0,\mathrm{min}}}^{E_\mathrm{max}} \mathrm{d}E \int_{\Delta_{0,\mathrm{min}}}^{E} \mathrm{d}\Delta_0 \left[\left(\frac{\delta\varepsilon''_\mathrm{rel}}{\varepsilon'}\right)_\mathrm{TS} + \left(\frac{\delta\varepsilon''_\mathrm{res}}{\varepsilon'}\right)_\mathrm{TS}\right] P(E,\Delta_0) \tag{2.79}$$

The integration includes an average over all possible dipole orientations, which are uniformly distributed over the shell of a sphere. In Equations (2.78) and (2.79) the dipole moment appears as $\boldsymbol{p}^2$. The average $\langle \boldsymbol{p}^2(\theta) \rangle$ is calculated as

$$\langle \boldsymbol{p}^2(\theta) \rangle = \frac{\int_0^{2\pi} \mathrm{d}\phi \int_0^{\pi} \sin\theta (p\cos\theta)^2 \mathrm{d}\theta}{\int_0^{2\pi} \mathrm{d}\phi \int_0^{\pi} \sin\theta \mathrm{d}\theta} = \frac{1}{3} p^2 \quad , \tag{2.80}$$

meaning that $p^2 \cos^2\theta$ is replaced by $p^2/3$ in the equations. Besides some limiting cases, which we will discuss later, the double integrals (2.78) and (2.79) need to be solved numerically. Figure 2.14 shows the result of an exemplary numerical integration of the integrals with an excitation frequency of 250 MHz, where only the one-phonon process is used as relaxation process. The transversal relaxation time was held constant at $\tau_2 = 10^{-6}$ s, although it should be temperature-dependent in general. However, no distinct effect on the temperature dependency is observed for relaxation times down to 10^{-8} s. At even lower values a reduction of both the resonant real and imaginary part are observed at very low temperatures. For most glasses, an effect of the transversal relaxation time on the dielectric function should be negligible at these frequencies, see also [Luc16].

In Figure 2.14 the contributions of the relaxation (blue) and resonant part (green) are shown separately. At the lowest temperatures, no relaxation part exists since the phonons die out towards low temperatures, and the relaxation times of tunneling

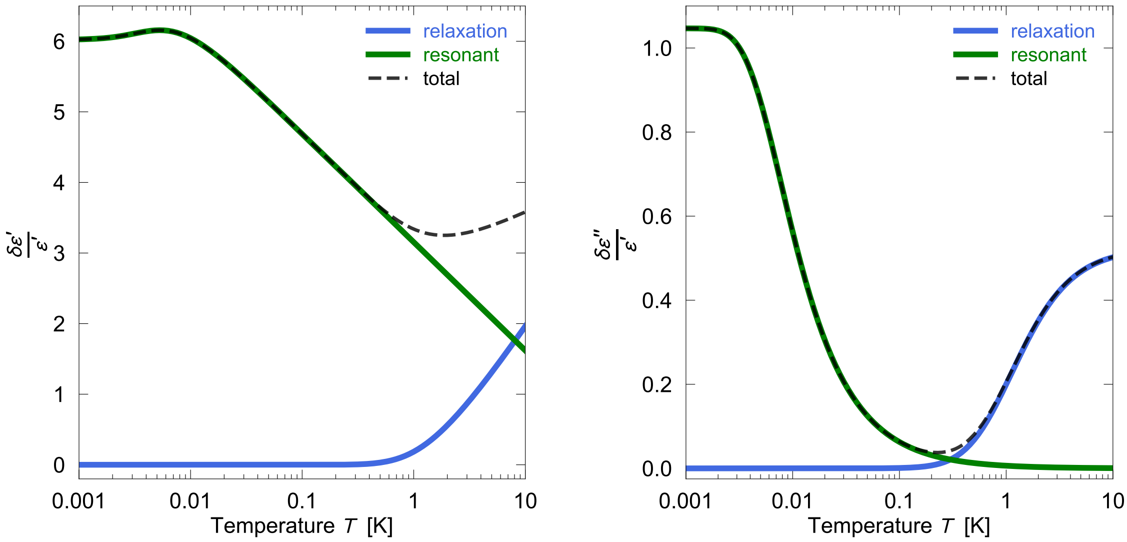

Figure 2.14: Temperature dependency of the relative change of the real (left) and imaginary part (right) of the dielectric function. The sum of relaxation (blue) and resonant processes (green) gives the total contribution of tunneling systems to the dielectric function. Only one-phonon processes were used for the numerical integration. Parameters used: $\omega/2\pi = 250\,\mathrm{MHz}$; $A = P_0 p^2/(\varepsilon_0\varepsilon_\mathrm{r}) = 1$; $K_1 = 2 \times 10^{77}\,\mathrm{J^{-3}s^{-1}}$; $\tau_2 = 1 \times 10^{-6}\,\mathrm{s}$; $E_\mathrm{max}/k_\mathrm{B} = 100\,\mathrm{K}$; $\varDelta_{0,\mathrm{min}}/k_\mathrm{B} = 1 \times 10^{-7}\,\mathrm{K}$.

systems become long. For the given frequency, the relaxation is then too slow to give a contribution to the dielectric function at low temperatures anymore. Only a contribution due to resonant processes exists there. For the imaginary part the dominant contribution comes from resonant tunneling systems with $E = \hbar\omega$, see Figure 2.12. The lower the temperature gets, the stronger their contribution becomes since their upper state is thermally less populated. At very low temperatures all resonant tunneling systems can fully contribute, and one observes a plateau there.
The behavior of the real part is a bit more complex since also off-resonant tunneling systems ($E/\hbar \gg \omega$) contribute, see Figure 2.12. Even at high temperatures the resonant part does not vanish. There, contributions to the real part originate from off-resonant tunneling systems with large energy splittings since these systems are thermally not fully saturated, and therefore perform resonant processes through interactions with the electric field's photons. Towards lower temperatures tunneling systems with smaller energy splittings are able to contribute as well, leading to an increase of the resonant real part. The branching off occurs at temperatures $k_\mathrm{B}T \approx \hbar\omega$, when resonant tunneling systems are thermally accessible too. At resonance the tunneling system's contribution has its change of sign, and some tunneling systems contribute negatively. For even lower temperatures additional contributions can only occur from off-resonant tunneling systems with $E/\hbar \ll \omega$. However, these tunneling systems do not give any contributions, and one observes a plateau in the real part.
At higher temperatures when the relaxation times become small compared to frequency, relaxation processes start to set in. In the real part the increase due to relaxation processes exceeds the decrease of the resonant part, leading to a characteristic minimum of the curve at T_min. For the imaginary part at high temperatures the resonant processes completely vanish, giving a purely relaxation-determined behavior. At high temperatures one observes a plateau in the imaginary part.

Since relaxation and resonant part both depend on the excitation frequency, we expect a strong frequency dependence of the dielectric function as well. A calculation with different frequencies spanning 1 Hz to 1 GHz is shown in Figure 2.15. The calculations include the two-phonon process, which gives a steeper increase of the real part at temperatures $T \gtrsim 4\,\mathrm{K}$. In addition, at temperatures where the two-phonon relaxation becomes important, the rise into the high temperature plateau of the imaginary part becomes faster. The position of the minimum in the real part shifts towards lower temperatures for smaller frequencies. The shift of the minimum is given by the underlying relaxation process. In the case of one-phonon process dominated relaxation this gives the relation $T_\mathrm{min} \propto (K_1\omega)^{1/3}$. For higher frequencies, when the position of the minimum lies in the region where two-phonon processes dominate the relaxation, one finds the dependency $T_\mathrm{min} \propto (K_2\omega)^{1/7}$. Towards lower

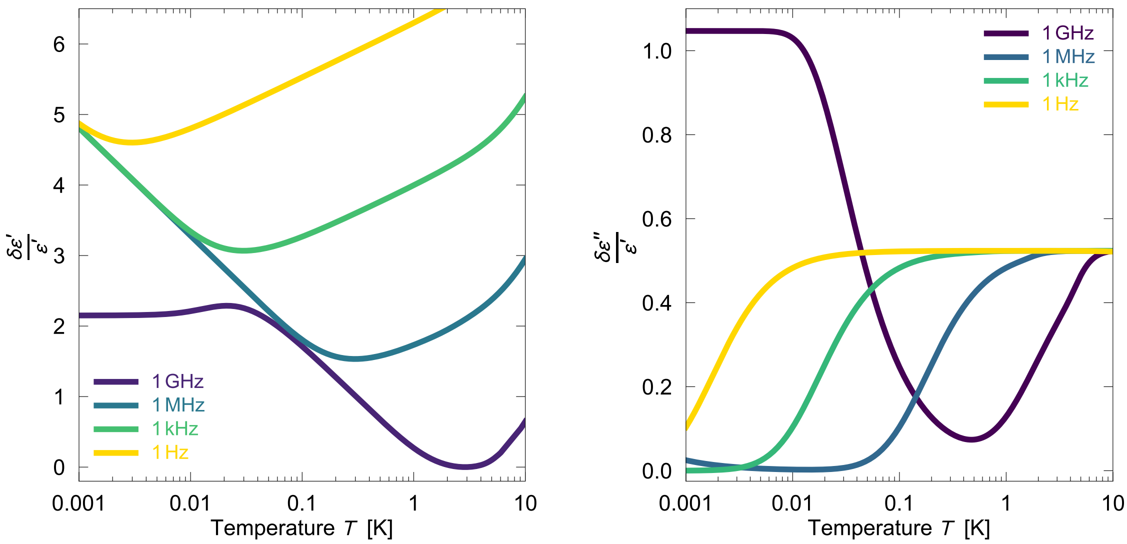

Figure 2.15: Temperature dependency of the relative change of the real (left) and imaginary part (right) of the dielectric function for different excitation frequencies. The same set of parameters as in Figure 2.14 was used besides the adding of a two-phonon relaxation process with $K_2 = 3500\,\mathrm{s^{-1}K^{-7}}$.

frequencies the onset of relaxation processes starts at lower temperatures since slower relaxation times are sufficient to allow tunneling systems to follow the electric field. In the imaginary part resonant processes contribute less for lower frequencies since the resonant tunneling systems have smaller energy splittings and contribute only at lower temperatures. In the real part contributions occur from off-resonant tunneling systems with large energy splittings, giving rise to resonant contributions over the entire temperature and frequency range.

Let us now take a look at analytic solutions of the integrals (2.78) and (2.79) for some limiting cases of the real part. One can give expressions for the slopes of the resonant and relaxation part [Bur98]. We introduce the parameter $A = P_0 p^2/(\varepsilon_0\varepsilon_\mathrm{r})$, which occurs as a prefactor in both integrals. In the limit $\hbar\omega \ll k_\mathrm{B}T$ one finds a logarithmic temperature dependency of the resonant part

$$\frac{\delta\varepsilon'_\mathrm{res}}{\varepsilon'} = -\frac{2}{3} A \ln\left(\frac{T}{T_0}\right) \quad , \tag{2.81}$$

with T_0 being a reference temperature. A similar expression is found for the relaxation part for $\omega\tau_{1,\mathrm{min}} \ll 1$ in the case of the one-phonon process

$$\frac{\delta\varepsilon'_\mathrm{rel}}{\varepsilon'} = A \ln\left(\frac{T}{T_0}\right) \quad . \tag{2.82}$$

Plotting the real part with a logarithmic temperature scale, Equation (2.81) and (2.82) each give straight lines with opposite direction, forming the minimum in the real part. While at low temperatures only resonant processes are visible, at higher temperatures resonant and relaxation parts occur simultaneously, which gives a slope ratio $\delta\varepsilon'_{\mathrm{res}}/\varepsilon' : (\delta\varepsilon'_{\mathrm{res}}/\varepsilon' + \delta\varepsilon'_{\mathrm{rel}}/\varepsilon')$ of $-2 : 1$ in agreement with Figure 2.14 and 2.15. If the relaxation part is dominated by the two-phonon process one finds

$$\frac{\delta\varepsilon'_{\mathrm{rel}}}{\varepsilon'} = \frac{7}{3} A \ln\left(\frac{T}{T_0}\right) \quad , \tag{2.83}$$

resulting in a slope ratio of $-2 : 5$. For the imaginary part one can write down expressions for the plateau values for $T \to 0\,\mathrm{K}$ and $T \to \infty$

$$\left(\frac{\delta\varepsilon''}{\varepsilon'}\right)_{\mathrm{T}\to 0} = \frac{\pi}{3} A \tag{2.84}$$

$$\left(\frac{\delta\varepsilon''}{\varepsilon'}\right)_{\mathrm{T}\to \infty} = \frac{\pi}{6} A \quad . \tag{2.85}$$

In this work, we are dealing with frequencies between 250 MHz and 1 GHz, primarily at very low temperatures. Hence, the temperature dependency of the resonant part is of major importance, which is why it is useful to derive analytic expressions for it (see Appendix A.1)

$$\frac{\delta\varepsilon'_{\mathrm{res}}}{\varepsilon'} = -\frac{2}{3} A \left[\mathrm{Re}\left\{\psi\left(\frac{1}{2} - \mathrm{i}\frac{\hbar\omega}{2\pi k_{\mathrm{B}} T}\right)\right\} - \ln\left(\frac{E_{\mathrm{max}}}{2\pi k_{\mathrm{B}} T}\right)\right] \tag{2.86}$$

$$\frac{\delta\varepsilon''_{\mathrm{res}}}{\varepsilon'} = \frac{\pi}{3} A \tanh\left(\frac{\hbar\omega}{2 k_{\mathrm{B}} T}\right) \quad , \tag{2.87}$$

using the real part of the complex digamma function $\mathrm{Re}\{\psi(z)\}$.

2.4.5 Saturation by a large driving field

As it was mentioned in Section 2.2 for the case of an ultrasonic field as excitation, the strength of the driving field affects resonant absorption processes. The same holds true for an electric excitation $F_{\mathrm{ac}}(t) = F_{\mathrm{ac}} \cos(\omega t)$, where photons can be resonantly absorbed by tunneling systems as discussed in the previous sections. For a high field intensity, the rate of photons interacting resonantly with tunneling systems is high. If this rate exceeds the energy relaxation rate τ_1^{-1}, a tunneling system might still be in its excited state before the next photon interacts resonantly with it. This would then lead to a stimulated emission process, where a transition of the tunneling system back into the ground state takes place by emitting an additional coherent photon. Stimulated emission counteracts the resonant absorption. In the case of a high electric field intensity the population difference of the two-level state becomes zero, and therefore resonant absorption and stimulated emission effectively cancel out each other, see also Figure 2.13 (right). Similar to the case of high temperatures, a high electric field then leads to a vanishing resonant imaginary part since no effective absorption of photons, and with that no dissipation takes place. The glass becomes transparent for photons at large electric fields, and one speaks of a saturation of the tunneling systems by the driving field. For high electric fields the Bloch equations cannot be simplified through a linearization anymore since nonlinearities are essentially for the saturation. A solution of this problem with an ultrasonic excitation is given in [Hun76]. We will make use of these results and transform them into the case of an excitation with an electric field. As ansatz for solving the Bloch equations (2.47) in the steady-state

$$\langle \hat{\boldsymbol{S}}(t) \rangle = \langle \hat{\boldsymbol{S}}_0 \rangle + \sum_{m=-\infty}^{\infty} \langle \hat{\boldsymbol{S}}_\mathrm{m} \rangle \exp(-\mathrm{i}\omega_m t) \quad \text{with} \quad \omega_m = m\omega \tag{2.88}$$

is chosen. It can be shown that $\langle \hat{S}_{1,+} \rangle$, $\langle \hat{S}_{-1,+} \rangle$, $\langle \hat{S}_{1,-} \rangle$, $\langle \hat{S}_{-1,-} \rangle$, and $\langle \hat{S}_{0,\mathrm{z}} \rangle$ are the relevant elements for $\omega\tau_2 \ll 1$. One obtains the same results as before in Equation (2.52), but with a modified $\langle \hat{S}_{0,\mathrm{z}} \rangle$

$$\begin{aligned} \langle \hat{S}_{0,\mathrm{z}} \rangle' &= \langle \hat{S}_{0,\mathrm{z}} \rangle - \frac{\left(\frac{\mathit{\Delta}_0}{E}\frac{pF_\mathrm{ac}\cos\theta}{\hbar}\right)^2 \tau_1\tau_2}{1+\left(\frac{\mathit{\Delta}_0}{E}\frac{pF_\mathrm{ac}\cos\theta}{\hbar}\right)^2 \tau_1\tau_2 + (\omega_0-\omega)^2\tau_2^2} \langle \hat{S}_{0,\mathrm{z}} \rangle \\ &= \frac{1+(\omega_0-\omega)^2\tau_2^2}{1+(\omega_0-\omega)^2\tau_2^2+\Omega_\mathrm{R}^2\tau_1\tau_2} \langle \hat{S}_{0,\mathrm{z}} \rangle \quad , \end{aligned} \tag{2.89}$$

where we introduced the tunneling system Rabi frequency

$$\Omega_\mathrm{R} = \frac{\mathit{\Delta}_0}{E}\frac{pF_\mathrm{ac}}{\hbar}\cos\theta = \frac{\mathit{\Delta}_0}{E}\Omega_\mathrm{R0}\cos\theta \quad . \tag{2.90}$$

For $\Omega_\mathrm{R}^2\tau_1\tau_2 \ll 1$, meaning small excitation or fast relaxations – a relaxation through dephasing counteracts the saturation as well – Equation (2.89) gives the same solution we obtained before from the linearized Bloch equations in the limit of a weak field. In general, the correction factor in $\langle \hat{S}_{0,\mathrm{z}} \rangle' = \alpha(\Omega_\mathrm{R})\langle \hat{S}_{0,\mathrm{z}} \rangle$ needs to be incorporated into the solutions (2.51) and (2.52), respectively. The resonant part can now be rewritten as:

$$\frac{\delta\varepsilon_\mathrm{res}}{\varepsilon'} = \frac{A\cos^2\theta}{\hbar} \int\limits_0^{E_\mathrm{max}} \mathrm{d}E \int\limits_{\mathit{\Delta}_{0,\mathrm{min}}}^{E} \mathrm{d}\mathit{\Delta}_0 P(E,\mathit{\Delta}_0) \left(\frac{\mathit{\Delta}_0}{E}\right)^2 \tanh\left(\frac{E}{2k_\mathrm{B}T}\right) \alpha(\Omega_\mathrm{R}) b(E,\omega) \tag{2.91}$$

Only resonant tunneling systems ($\omega_0 \approx \omega$) are affected by the saturation. Since the resonant imaginary part is mainly sensitive to these tunneling systems, it is expected to show a strong dependence on the field strength. The resonant real part, however, is largely determined by off-resonant tunneling systems, which are unaffected by the saturation. Therefore, for the real part the small field strength approximation (2.86) is applicable. An integration of Equation (2.91) (see Appendix A.2 for details) gives the modified resonant loss, which accounts for the non-zero electric field strength

$$\tan\delta_{\mathrm{res}} = \frac{\pi P_0 p^2 \cos^2\theta}{\varepsilon_0\varepsilon_{\mathrm{r}}} \tanh\left(\frac{\hbar\omega}{2k_{\mathrm{B}}T}\right) \frac{1}{\sqrt{1+\left(\frac{F_{\mathrm{ac}}}{F_{\mathrm{c}}}\right)^2}} \quad , \tag{2.92}$$

where we wrote the imaginary part as the loss tangent. Here, a critical field strength F_{c} is introduced, which defines the field strength where saturation starts to set in, meaning $\Omega_{\mathrm{R}}^2\tau_1\tau_2 = 1$. Thus, the critical field strength reads as

$$F_{\mathrm{c}} = \frac{\hbar}{p\cos\theta}\frac{1}{\sqrt{\tau_{1,\mathrm{min}}\tau_2}} \quad . \tag{2.93}$$

Equation (2.92) needs to be averaged over all dipole orientations. We use a Monte Carlo approach. As it is shown in Section 3.3.1, $\cos\theta$ is uniformly distributed between -1 and 1. Generating a large number of different values for $\cos\theta$, according to its distribution, and summing over all outcomes of Equation (2.92), gives an adequate determination of the mean. The result of this calculation is shown in Figure 2.16, where the result is compared to an approximation solution which uses effective values for the dipole moment of the form

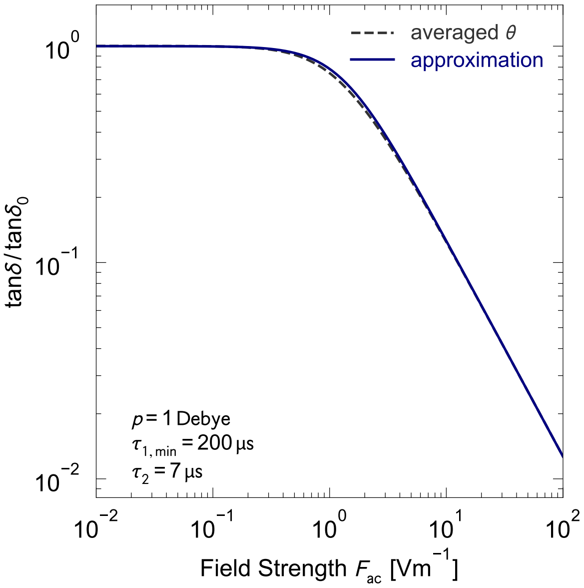

Figure 2.16: Resonant loss as a function of the applied electric field strength. The approximation function (2.94) is compared with the results of an averaged solution of Equation (2.92) over the dipole angle θ. A dipole moment of $p = 1\,\mathrm{Debye} \approx 3.335\times10^{-30}\,\mathrm{C\,m}$ and for the glass N-BK7 typical relaxation times of $\tau_{1,\mathrm{min}} = 200\,\mu\mathrm{s}$ and $\tau_2 = 7\,\mu\mathrm{s}$ [Fic13, Bur13] were used.

$$\tan\delta_{\mathrm{res}} = \frac{\pi}{3}A\tanh\left(\frac{\hbar\omega}{2k_{\mathrm{B}}T}\right)\frac{1}{\sqrt{1+\left(\frac{F_{\mathrm{ac}}}{F_{\mathrm{c}}}\right)^2}} \quad \text{with} \quad F_{\mathrm{c}} = \frac{3\hbar}{2p}\frac{1}{\sqrt{\tau_{1,\mathrm{min}}\tau_2}} \quad . \tag{2.94}$$

The approximation function shows only minor differences around the crossover into the plateau region for small field strengths and can be used instead of the averaged

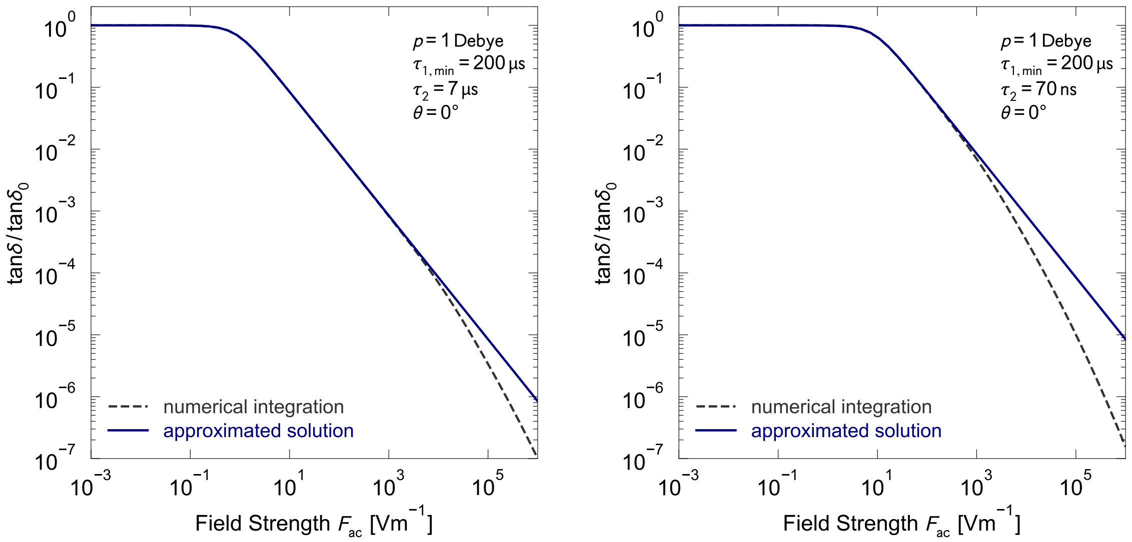

Figure 2.17: Comparison between the approximated analytic solution (2.92) and a numerical calculation of the integral (2.91) for two different values of τ_2. The dipole angle was fixed to $\theta = 0\,°$ for the calculations.

dipole angle calculation. For small electric fields, the loss is independent from F and given by Equation (2.87) as $\tan\delta_0 = \frac{\pi}{3} A \tanh(\frac{\hbar\omega}{2k_\mathrm{B}T})$. If the field strength exceeds the critical field strength, tunneling systems are getting saturated by the field and cannot fully contribute to the loss anymore, which means that the loss decreases. For high fields one expects the resonant loss to drop with $\tan\delta \propto F_\mathrm{ac}^{-1}$.

In order to solve the integral (2.91) analytically, several approximations were needed. Figure 2.17 shows a comparison between the approximated solution (2.92) and a full numerical integration of Equation (2.91) for two different values of τ_2. A value of $\tau_2 = 7\,\mu\mathrm{s}$ should roughly agree with the value in experiment (left). The value $\tau_2 = 70\,\mathrm{ns}$ represents an overestimation and gives an idea about a rather extreme case. The same parameters as in Figure 2.16 are used, besides a fixed dipole orientation, which should not affect the overall statement. In both cases deviations occur at very high field strengths, where the numerical solution deviates from the F^{-1}-dependency. In the experiment maximum values for the field strength are of the order $\sim 10^3\,\mathrm{V\,m^{-1}}$, which means that the presented analytic solution should be appropriate for an accurate description of the experiment.

In Section 2.4.3 we saw that interactions between tunneling systems lead to a fluctuating energy splitting of resonant tunneling systems called spectral diffusion, which is a source for dephasing. Here, we want to discuss the effect of spectral diffusion on the saturation of tunneling systems. A natural way to incorporate spectral diffusion would be to add its relaxation rate τ_ϕ^{-1} from Equation (2.72) to the transversal relaxation rate τ_2 and use this for calculating the critical field strength in Equation (2.94). The effect of spectral diffusion, however, is more subtle, as proposed by [Bur18]. In that work the explicit effect of spectral diffusion on the resonant loss was calculated. As the energy splitting of tunneling systems is not constant in time, different tunneling systems will fulfill the resonant condition over the course of time and interact resonantly with the applied field. Figuratively speaking, on average resonant tunneling systems are exposed to the photons of the electric field for a shorter period of time, which leads to a reduction of saturation, and the loss becomes larger compared to the case of a static tunneling system energy. If the intensity of the driving field gets higher, shorter periods of time in resonance will be sufficient for an excitation and tunneling systems get saturated anyhow. One then expects the spectral diffusion to be insignificant. This effect is similar to the behavior of tunneling systems undergoing Landau-Zener transitions, induced by a dynamic shift of a bias field, which we will discuss in Section 2.4.6.

In [Bur18] it was stated that Equation (2.94) is not valid in the case of a distinct spectral diffusion $\tau_\phi < \tau_{1,\mathrm{min}}$ and should be replaced by an interpolation function, which can be used instead of a full numerical solution of the problem. The interpolation function is given by

$$\tan\delta_{\mathrm{sd}} = \frac{\tan\delta_0}{1 + \frac{\Omega_{\mathrm{R0}}^2 \tau_\phi^2}{\frac{3\pi\Omega_{\mathrm{R0}}\tau_\phi^2}{4\sqrt{2}\tau_{20}} + \ln\left(1+3l_*\right)}} \quad , \tag{2.95}$$

with l_* being defined as

$$l_* = \frac{\ln\left(d_1 + c_1\Omega_{\mathrm{R0}}\tau_\phi\right)}{\ln\left(d_2 + \frac{c_2\tau_{20}}{\Omega_{\mathrm{R0}}\tau_\phi^2}\right)} \quad , \tag{2.96}$$

where $\tau_{20} = 2\tau_{1,\mathrm{min}}$ denotes the minimum phase decoherence time, and τ_ϕ represents the phase relaxation time due to spectral diffusion. The constants c_1, c_2, d_1, d_2 are given as 0.5, 3, 0.55, 1.2, respectively. In Figure 2.18 a comparison between Equation (2.94) and (2.95) is shown. The purple dashed curve shows the loss according to Equation (2.94) without regarding a relaxation through spectral diffusion at all. The adding of the spectral diffusion rate τ_ϕ^{-1} to τ_2^{-1} is presented by the dashed blue curve. The solid green line shows the results of the explicit treatment of spectral diffusion by Equation (2.95). The spectral diffusion relaxation time $\tau_\phi = 20\,\mu\mathrm{s}$ was chosen to be much smaller than $\tau_{1,\mathrm{min}} = 200\,\mu\mathrm{s}$ to ensure its significance.

Figure 2.18 shows that by simply adding the spectral diffusion relaxation time to τ_2 the whole curve shifts towards higher field strengths (dashed blue) since F_c becomes larger. As already explained, the explicit treatment of spectral diffusion (solid green) allows the loss to sustain its plateau value $\tan\delta_0$ at higher field strengths. For very high field strengths the effect of spectral diffusion becomes irrelevant, and the loss converges back to the curve that disregards any spectral diffusion effects (dashed purple).

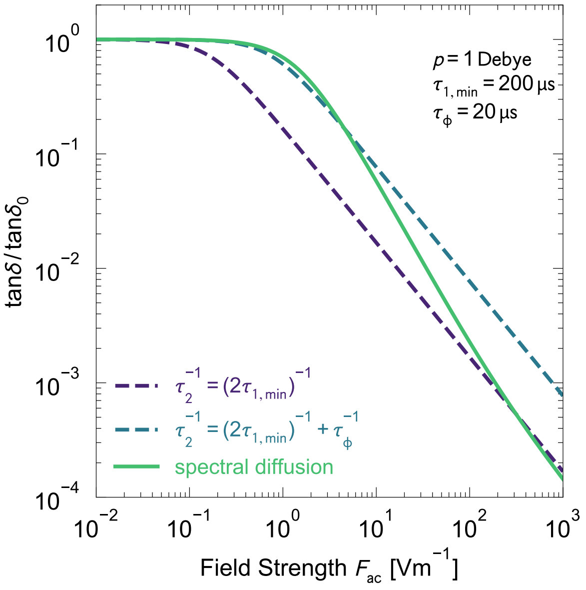

Figure 2.18: Normalized dielectric loss as a function of the field strength for typical tunneling system parameters. The dashed curves show the results of Equation (2.94) without regarding any spectral diffusion (purple), and by adding the spectral diffusion rate to the total transverse relaxation rate τ_2 (blue). The solid green line shows the evaluation of Equation (2.95) with the same set of parameters, which regards the explicit effect of spectral diffusion.

2.4.6 Non-equilibrium loss through Landau-Zener transitions

In earlier dielectric non-equilibrium measurements, where parallel to the electric driving field a large electric DC bias step was applied, a jump of the dielectric function's real part with a subsequent logarithmic relaxation over several hours was observed [Sal94, Nal04]. This behavior was explained through the long-range interaction between tunneling systems leading to a gap in the distribution function (see Equation (2.77)) that originates from the formation of tunneling system pairs. A large DC bias field modifies the energy splittings and leads to the breaking of such pairs. The formation of new pair states, and with that of a new gap, is associated with the observed logarithmic relaxation. For more details see [Bur95, Bur98, Nal04].

Here, we want to focus on a different non-equilibrium phenomenon, which can be explained without any tunneling system interactions. In this section we discuss the non-equilibrium high frequency resonant loss ($\hbar\omega > k_\mathrm{B}T$) of tunneling systems performing Landau-Zener transitions, induced by a rapid dynamic change of an additional electric bias field. In measurements of deposited amorphous thin films, it was observed that during a sweep of the bias field the resonant loss was clearly enhanced compared to the loss with no present bias sweep (steady-state) [Kha14, Mat19]. In the following we want to derive a relation between the resonant loss and the applied bias rate, where we follow [Bur13, Kha13]. The underlying tunneling system dynamic is the foundation for the Landau-Zener spectroscopy of tunneling systems performed in this thesis.

In Section 2.3.1 we found that the energy splitting of a tunneling system is given by $E = \sqrt{\mathit{\Delta}^2 + \mathit{\Delta}_0^2}$. According to Equation (2.37), an electric field modifies the asymmetry energy $\mathit{\Delta}$. Therefore, we can write down the energy splitting in the presence of an applied bias field $F_\mathrm{b}(t)$ that changes in time as

$$E'(t) = \sqrt{(\varDelta + \delta\varDelta(t))^2 + \varDelta_0^2} \quad , \tag{2.97}$$

with $\delta\varDelta(t) = 2pF_\mathrm{b}(t)\cos\theta$. We want to observe the resonant loss, hence, it is sufficient to consider only tunneling systems in resonance with the high frequency driving field ($E \approx \hbar\omega$). This means only slightly detuned systems with $\delta\varDelta \to 0$ are relevant, and we can approximate Equation (2.97)

$$E'(t) \approx \sqrt{\varDelta^2 + \varDelta_0^2} + \frac{\varDelta}{\sqrt{\varDelta^2 + \varDelta_0^2}}\delta\varDelta(t) = \hbar\omega + \sqrt{1 - \left(\frac{\varDelta_0}{\hbar\omega}\right)^2} \cdot \delta\varDelta(t) \quad . \tag{2.98}$$

Next, we write the change of the energy splitting in time as

$$\frac{\mathrm{d}E'(t)}{\mathrm{d}t} = \hbar\nu = \sqrt{1 - \left(\frac{\varDelta_0}{\hbar\omega}\right)^2} \cdot 2p\dot{F}_\mathrm{b}\cos\theta = \hbar\nu_0\sqrt{1 - \left(\frac{\varDelta_0}{\hbar\omega}\right)^2}\cos\theta \quad , \tag{2.99}$$

and define

$$\nu_0 := \frac{2p\dot{F}_\mathrm{b}}{\hbar} \quad . \tag{2.100}$$

With that we can write the time dependence of the energy splitting

$$E'(t) = \hbar\omega + \hbar\nu(t - t_0) \quad , \tag{2.101}$$

while t_0 sets the time when the tunneling system is in exact resonance with the driving field. Since the energy splitting is time-dependent now, we must treat the tunneling system's response as time-dependent too. We use the time-dependent Schrödinger equation $\mathrm{i}\hbar\frac{\partial}{\partial t}\left|\Psi\right\rangle = \hat{\mathcal{H}}\left|\Psi\right\rangle$ with the state $\left|\Psi\right\rangle = c_\mathrm{g}(t)\left|\Psi_\mathrm{g}\right\rangle + c_\mathrm{e}(t)\left|\Psi_\mathrm{e}\right\rangle$ and Equation (2.38) as Hamiltonian. We neglect any relaxation events during the resonance crossing and assume the change of the energy splitting due to the driving field being small $E'/2 \gg \frac{\varDelta}{E}\boldsymbol{pF}_\mathrm{ac}$. Thereby, we receive the two equations

$$\begin{aligned} \mathrm{i}\hbar\dot{c}_\mathrm{e} &= \frac{E'}{2}c_\mathrm{e} + \hbar\Omega_\mathrm{R}\cos(\omega t)c_\mathrm{g} \\ \mathrm{i}\hbar\dot{c}_\mathrm{g} &= -\frac{E'}{2}c_\mathrm{g} + \hbar\Omega_\mathrm{R}\cos(\omega t)c_\mathrm{e} \quad , \end{aligned} \tag{2.102}$$

which are transformed into the rotating frame $(a_\mathrm{e}, a_\mathrm{g}) = (c_\mathrm{e}\exp(\mathrm{i}\omega t/2), c_\mathrm{g}\exp(-\mathrm{i}\omega t/2))$

$$\begin{aligned} \mathrm{i}\hbar\dot{a}_\mathrm{e} &= -\frac{\mathrm{i}\nu}{2}(t - t_0)a_\mathrm{e} - \frac{\mathrm{i}\Omega_\mathrm{R}}{2}a_\mathrm{g} \\ \mathrm{i}\hbar\dot{a}_\mathrm{g} &= \frac{\mathrm{i}\nu}{2}(t - t_0)a_\mathrm{g} - \frac{\mathrm{i}\Omega_\mathrm{R}}{2}a_\mathrm{e} \quad , \end{aligned} \tag{2.103}$$

where Ω_R denotes the Rabi frequency (2.90). The set of equations (2.103) can be identified as the equations of the Landau-Zener problem for a two-level system

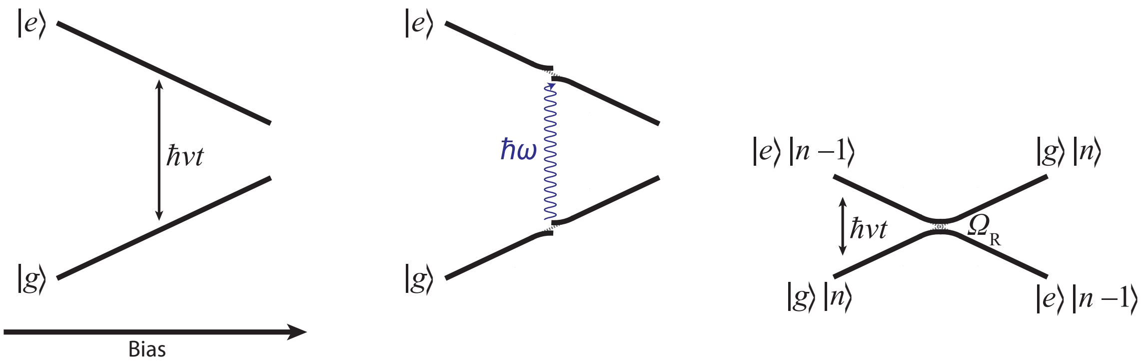

Figure 2.19: Illustration of the Landau-Zener problem for a two-level system. The energy splitting is getting detuned in time by the bias field. The driving field resonantly couples both states at $E = \hbar\omega$, which leads to an avoided level crossing. In the limit of a fast bias sweep no transition between ground and excited state takes place, which is called a Landau-Zener transition.

[Lan32, Zen32, Stü32]. A sketch of the situation is shown in Figure 2.19. The energy states of the two-level system are modified by the bias field, and their energy difference changes with $\hbar\nu t$ in time (left). If the energy difference matches the photon energy of the driving field $\hbar\omega$, a resonant transition may occur (center). One can subtract the photon energy from the upper level, or in other words regard the total energy of tunneling system and photon field. One then ends up with an avoided level crossing (right). Now we want to consider the situation where the tunneling system is in the ground state $|g\rangle\,|n\rangle$ at $t = 0$. If the change of the energy splitting is performed slowly $\nu_0 \ll \Omega_{\mathrm{R0}}^2$ (adiabatic), the system will undergo a transition into the upper state under absorption of one photon from the electric field and ending in the state $|e\rangle\,|n-1\rangle$. On the other hand, a rapid passage $\nu_0 \gg \Omega_{\mathrm{R0}}^2$ results in no excitation since the coupling between the two levels is too weak. The system then stays in the ground state $|g\rangle\,|n\rangle$, which is called a Landau-Zener transition. According to the solution of the Landau-Zener problem, the probability for an adiabatic transition from the ground into the excited state $P_{\mathrm{g}\to\mathrm{e}}$ is found to be

$$P_{\mathrm{g}\to\mathrm{e}} = 1 - \exp\left(-\frac{\pi\Omega_{\mathrm{R}}^2}{2\nu}\right) = 1 - \exp(-\gamma) \quad \text{with} \quad \gamma = \frac{\pi\Omega_{\mathrm{R}}^2}{2\nu} \quad . \tag{2.104}$$

For a system initially in the ground state that crosses the resonance at $t = t_0$, we can write the probability amplitudes $|a_{\mathrm{g}}|^2$ and $|a_{\mathrm{e}}|^2$ at a time $t \gg t_0$ as

$$\begin{aligned} |a_{\mathrm{e}}|^2 &= 1 - \exp\left(-\gamma\right) \\ |a_{\mathrm{g}}|^2 &= \exp\left(-\gamma\right) \quad . \end{aligned} \tag{2.105}$$

Calculating the resulting loss, requires considering the dissipated energy through this process. By absorbing one photon, a photon gets eliminated from the electric field, and therefore leads to dissipation. An eventual following spontaneous photon emission will not compensate the loss of a photon because it would be incoherent and at a different energy. We integrate over the entire dielectric volume and write the total dissipated energy as

$$\mathrm{d}\mathcal{E} = \int \mathrm{d}V \int \mathrm{d}N\hbar\omega|a_\mathrm{e}|^2 \quad . \tag{2.106}$$

The integral over $\mathrm{d}N$ includes all tunneling systems that fulfill the resonance condition during the time interval $\mathrm{d}t$. As it has been done before, we integrate over the distribution function $P(E, \varDelta_0)$. Tunneling systems are homogeneously distributed over the volume, and we can write

$$\mathrm{d}\mathcal{E} = \hbar\omega P_0 V \int\limits_0^1 \mathrm{d}\cos\theta \int\limits_0^{\hbar\omega} \mathrm{d}\varDelta_0 \int\limits_{\hbar\omega-\hbar\nu\mathrm{d}t}^{\hbar\omega+\hbar\nu\mathrm{d}t} \mathrm{d}E \frac{(1-e^{-\gamma})E}{\varDelta_0\sqrt{E^2-\varDelta_0^2}} \quad . \tag{2.107}$$

Note that $\cos\theta$ is only evaluated between 0 and 1 since only half of the dipoles are orientated in the right direction, such that tunneling systems reach the resonance during a bias sweep. The integral over E can be evaluated (see Appendix A.3) because the change in energy $\hbar\nu\mathrm{d}t$ can be assumed to be small. We then find by defining $x = \frac{\varDelta_0}{\hbar\omega}$

$$\begin{aligned} \frac{\mathrm{d}\mathcal{E}}{\mathrm{d}t} &= 2\hbar^2\omega P_0 V \int\limits_0^1 \mathrm{d}\cos\theta \int\limits_0^1 \frac{\pi\Omega_\mathrm{R}^2}{2\gamma}(1-e^{-\gamma})\frac{\mathrm{d}x}{x\sqrt{1-x^2}} \\ &= 2\hbar^2\omega P_0 V \int\limits_0^1 \mathrm{d}\cos\theta \int\limits_0^1 \nu(1-e^{-\gamma})\frac{\mathrm{d}x}{x\sqrt{1-x^2}} \\ &= \pi\omega F_\mathrm{ac}^2 P_0 p^2 V \int\limits_0^1 \mathrm{d}\cos\theta\cos^2\theta \int\limits_0^1 \frac{1-e^{-\gamma}}{\gamma}\frac{x\mathrm{d}x}{\sqrt{1-x^2}} \quad . \end{aligned} \tag{2.108}$$

Defining the dielectric loss $\tan\delta$ as the ratio of the dissipated power per cycle and the stored energy, we can write

$$\tan\delta = \frac{P_\mathrm{dis}}{\omega W_\mathrm{tot}} = \frac{\mathrm{d}\mathcal{E}/\mathrm{d}t}{\omega W_\mathrm{tot}} \quad . \tag{2.109}$$

In the case of an LC-resonator with the maximum field strength in its capacitor being F_ac, the stored energy is $W_\mathrm{tot} = \varepsilon_0\varepsilon_\mathrm{r}F_\mathrm{ac}^2V$ and we find

$$\tan\delta = \frac{\pi P_0 p^2}{\varepsilon_0\varepsilon_\mathrm{r}} \int\limits_0^1 \mathrm{d}\cos\theta\cos^2\theta \int\limits_0^1 \frac{1-e^{-\gamma}}{\gamma}\frac{x\mathrm{d}x}{\sqrt{1-x^2}} \quad . \tag{2.110}$$

For a very fast bias sweep $\nu_0 \gg \Omega_{\mathrm{R0}}^2$, we can approximate $e^{-\gamma} \approx 1-\gamma$ and find the loss to be

$$\tan\delta = \frac{\pi P_0 p^2}{3\varepsilon_0\varepsilon_\mathrm{r}} \quad , \tag{2.111}$$

which corresponds to the steady-state low-power loss $\tan\delta_0$ at very low temperatures. For all other bias rates Equation (2.110) needs to be solved numerically. We furthermore define the dimensionless bias rate

$$\xi = \frac{2\nu_0}{\pi\Omega_{\mathrm{R0}}^2} = \frac{2\nu_0\hbar^2}{\pi p^2 F_{\mathrm{ac}}^2} \tag{2.112}$$

and end up with the expression

$$\tan\delta = \frac{\pi P_0 p^2}{\varepsilon_0\varepsilon_\mathrm{r}}\xi \int\limits_0^1 \mathrm{d}\cos\theta\cos\theta \int\limits_0^1 \left(1-\exp\left(-\frac{\cos\theta}{\xi}\frac{x^2}{\sqrt{1-x^2}}\right)\right)\frac{\mathrm{d}x}{x} \quad . \tag{2.113}$$

Figure 2.20 shows a numerical integration of Equation (2.113), where the non-equilibrium loss is plotted as a function of the dimensionless bias rate ξ. The loss increases towards higher bias rates and converges into a plateau at very high rates, which agrees with the low-power limit $\tan\delta_0$. At first glance this might be unintuitive because the probability for absorbing a photon decreases for rapid bias sweeps, and thus the loss should become smaller. However, as the bias rate increases, the number of tunneling systems crossing the resonance within a time interval $\mathrm{d}t$ becomes higher and more photons potentially get absorbed. Both processes counteract with each other, leading to a plateau at very high bias rates. For the calculation we assumed that no relaxation processes take place during the resonance crossing. Hence, the

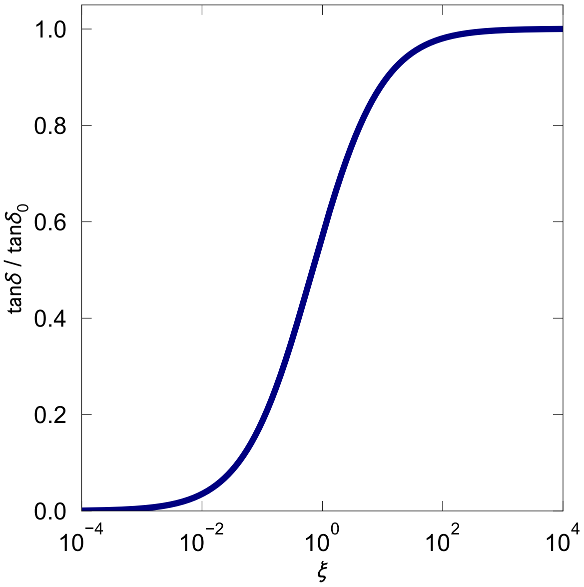

Figure 2.20: Non-equilibrium loss due to tunneling systems performing Landau-Zener transitions induced through a rapid bias sweep. The loss is normalized with the low-power limit $\tan\delta_0$ and plotted as a function of the dimensionless bias rate ξ.

results should only be valid for high bias rates. The assumption of negligible relaxation cannot hold true for small bias rates since relaxations during the resonant passage are more likely to occur then. For $\xi \ll \frac{1}{\Omega_{\mathrm{R0}}\sqrt{\tau_{1,\mathrm{min}}\tau_2}}$ Equation (2.113) must be replaced with the steady-state limit from Equation (2.94). Another approach for calculating the loss over the entire range of bias rates will be discussed in the following chapter, where we numerically solve the full Bloch equations for each tunneling system separately and sum over the tunneling systems in a Monte Carlo approach.

3. Simulation of the tunneling system dynamics

In this thesis we investigate the non-equilibrium dynamics of tunneling systems performing Landau-Zener transitions, which can be used to extract microscopic properties of the involved tunneling systems, like their relaxation times or dipole moment (Landau-Zener spectroscopy). Dynamically shifting the tunneling system energies is furthermore used in pump tone probe tone experiments to invert the tunneling system population through a combination of a tunneling system energy sweep and off-resonant microwave pump tones [Ros16]. This may lead to stimulated emission of photons at the probe tone frequency. The tunneling system ensemble then acts as an amplifying, instead of a dissipative medium for photons in the microwave regime, which will be investigated experimentally in Section 5.4.3. This requires detailed knowledge about the Landau-Zener dynamics of tunneling systems.

The introduced theoretical treatment of the tunneling system's dielectric response within the Landau-Zener dynamics allows a basic understanding of the underlying effects, however, its applicability to more elaborated problems is limited within the treated formalism. For that reason, simulations of the tunneling system dynamics were conducted, which are presented in this chapter. By numerically solving the Bloch equations, the interaction between a single tunneling system and arbitrary electric fields is modeled on the elementary level. The dynamics of the tunneling system ensemble is obtained through Monte Carlo averaging the single system response. This represents a direct imitation of the tunneling system's dynamics. The benefits of using a simulation in this context is twofold. On the one hand, it provides a fundamental understanding of the complex tunneling system dynamics caused by the overlay of several electric fields interacting with the tunneling systems on different time scales. On the other hand its flexible application to numerous problems allows to predict different experimental findings originating from the Landau-Zener spectroscopy, or detect and overcome experimental limitations in advance. Thus, it provides a very useful tool for a detailed examination of the interplay between tunneling systems and electric fields in order to gain deeper insights into tunneling systems in combination with experiments.

This chapter starts with the introduction of the used numerical methods for calculating the dielectric response of tunneling systems interacting with electric fields. Calculations for a single tunneling system are presented in Section 3.2, which allow to validate the proper functionality of the implemented code. The description of the whole tunneling system ensemble through a Monte Carlo simulation is presented in Section 3.3. Whenever it is possible, these results are compared to the predictions of Chapter 2.

3.1 Solving the tunneling system dynamics numerically

For the following calculations, we describe the state of the tunneling system ensemble in terms of the density matrix formalism. This has the advantage of being capable of dealing also with mixed states which occur from the superposition of pure states. Pure states can be described by a single state vector $|\psi\rangle$ and represent points on the surface of the Bloch sphere. Mixed states are statistical ensembles of pure states. Because of decoherence, such a state is located inside the Bloch sphere. The state of the tunneling system ensemble should in general be representable as a mixed state, and the density matrix provides an appropriate statistical description for it. The density matrix is an operator of the form

$$\hat{\rho} = \sum_i p_i \left|\Psi_i\right\rangle \left\langle\Psi_i\right| \quad . \tag{3.1}$$

It gives the probability p_i of finding a mixed state in the pure state Ψ_i. In the case of tunneling systems a possible pure state can be written in terms of the tunneling system's eigenstates $\left|\Psi\right\rangle_i = a\left|\Psi_\mathrm{e}\right\rangle + b\left|\Psi_\mathrm{g}\right\rangle$, with $|a|^2 + |b|^2 = 1$. We can write down the density matrix of a two-level state as

$$\hat{\rho} = \begin{pmatrix} \rho_\mathrm{ee} & \rho_\mathrm{eg} \\ \rho_\mathrm{ge} & \rho_\mathrm{gg} \end{pmatrix} \quad , \tag{3.2}$$

where the diagonal elements ρ_ee and ρ_gg give the probability of finding the state in the excited $\left|\Psi_\mathrm{e}\right\rangle$ or ground state $\left|\Psi_\mathrm{g}\right\rangle$, respectively. The expectation value of an observable $\hat{A}$ is given by $\langle\hat{A}\rangle = \mathrm{tr}(\hat{\rho}\hat{A})$, where tr() denotes the trace of a matrix. We can therefore identify the sum of the off-diagonal elements ρ_eg and ρ_ge as the expectation value of the Pauli matrix $\hat{\sigma}_x$ as $\langle\hat{\sigma}_x\rangle = \rho_\mathrm{eg} + \rho_\mathrm{ge}$. Furthermore, we can write $\langle\hat{\sigma}_y\rangle = \mathrm{i}(\rho_\mathrm{eg} - \rho_\mathrm{ge})$ and $\langle\hat{\sigma}_z\rangle = \rho_\mathrm{ee} - \rho_\mathrm{gg}$. The von Neumann equation gives the time evolution of the density matrix

$$\mathrm{i}\hbar\frac{\partial\hat{\rho}}{\partial t} = [\hat{\mathcal{H}}, \hat{\rho}] = \hat{\mathcal{H}}\hat{\rho} - \hat{\rho}\hat{\mathcal{H}} \quad . \tag{3.3}$$

The Hamiltonian $\hat{\mathcal{H}}$ describes the perturbation of a tunneling system by an electric field, see Equation (2.38). We then end up with a set of four coupled differential equations

$$\begin{aligned}
\dot{\rho}_\mathrm{ee} &= \frac{\varDelta_0}{\mathrm{i}\hbar E}\boldsymbol{p}\boldsymbol{F}_\mathrm{ac}(\rho_\mathrm{ge} - \rho_\mathrm{eg}) - \frac{\rho_\mathrm{ee}}{\tau_1} + \frac{1}{2\tau_1}\left(1 - \tanh\frac{E}{2k_\mathrm{B}T}\right) \\
\dot{\rho}_\mathrm{eg} &= \frac{\varDelta_0}{\mathrm{i}\hbar E}\boldsymbol{p}\boldsymbol{F}_\mathrm{ac}(\rho_\mathrm{gg} - \rho_\mathrm{ee}) + \frac{1}{\mathrm{i}\hbar}\left(E + \frac{2\varDelta}{E}\boldsymbol{p}\boldsymbol{F}_\mathrm{ac}\right)\rho_\mathrm{eg} - \frac{\rho_\mathrm{eg}}{\tau_2} \\
\dot{\rho}_\mathrm{ge} &= \frac{\varDelta_0}{\mathrm{i}\hbar E}\boldsymbol{p}\boldsymbol{F}_\mathrm{ac}(\rho_\mathrm{ee} - \rho_\mathrm{gg}) - \frac{1}{\mathrm{i}\hbar}\left(E + \frac{2\varDelta}{E}\boldsymbol{p}\boldsymbol{F}_\mathrm{ac}\right)\rho_\mathrm{ge} - \frac{\rho_\mathrm{ge}}{\tau_2} \\
\dot{\rho}_\mathrm{gg} &= \frac{\varDelta_0}{\mathrm{i}\hbar E}\boldsymbol{p}\boldsymbol{F}_\mathrm{ac}(\rho_\mathrm{eg} - \rho_\mathrm{ge}) + \frac{\rho_\mathrm{ee}}{\tau_1} - \frac{1}{2\tau_1}\left(1 - \tanh\frac{E}{2k_\mathrm{B}T}\right) \quad ,
\end{aligned} \tag{3.4}$$

where the relaxation times $\tau_{1,2}$ were added subsequently as it was done for the Bloch equations (2.47). An additional electric bias field $F_\mathrm{b}(t)$ modifies the energy splitting $\mathit{\Delta}$, and one can use $\mathit{\Delta}(t) = \mathit{\Delta}(t=0) + 2pF_\mathrm{b}(t)\cos\theta$ in Equation (3.4).
This set of equations needs to be solved in order to receive the density matrix for the system as a function of time. The density matrix contains all the information about the system, and we can extract observables like the polarization from it. A way to solve the set of equations numerically is to rewrite (3.4) as a matrix equation (see [Kha13])

$$\begin{pmatrix} \dot\rho_\mathrm{ee} \\ \dot\rho_\mathrm{eg} \\ \dot\rho_\mathrm{ge} \\ \dot\rho_\mathrm{gg} \end{pmatrix} = \mathcal{M} \begin{pmatrix} \rho_\mathrm{ee} \\ \rho_\mathrm{eg} \\ \rho_\mathrm{ge} \\ \rho_\mathrm{gg} \end{pmatrix} \quad , \tag{3.5}$$

where the matrix $\mathcal{M}$ is determined by (3.4). For the sake of clarity, we set $T \to 0\,\mathrm{K}$. The constant temperature term can in principle be added without loss of generality. Due to the structure of Equation (3.5) we choose an ansatz

$$\boldsymbol{\rho}(t) = e^{t\mathcal{M}}\boldsymbol{c}(t) \quad , \tag{3.6}$$

using the matrix exponential, and a set of time-dependent parameters $\boldsymbol{c}(t)$. We take the initial state $\boldsymbol{\rho}(t_0)$ as the starting point of the numerical solution. From this point we can approximate the state after a small jump in time Δt by assuming $\mathcal{M}$ being constant during this time step. Writing $\boldsymbol{c}(t_0) = \left[e^{t_0\mathcal{M}(t_0)}\right]^{-1}\boldsymbol{\rho}(t_0)$, we can give an expression for $\boldsymbol{\rho}(t_0+\Delta t)$ as

$$\boldsymbol{\rho}(t_0+\Delta t_0) = e^{(t_0+\Delta t)\mathcal{M}(t_0)}\boldsymbol{c}(t_0) = e^{(t_0+\Delta t)\mathcal{M}(t_0)}\left[e^{t_0\mathcal{M}(t_0)}\right]^{-1}\boldsymbol{\rho}(t_0) \quad . \tag{3.7}$$

Starting with an initial state, this pattern allows to calculate the density matrix for each time step iteratively. The matrix exponential needs to be calculated for every time step. This was computed numerically by a script written in Phyton[1].
In another attempt, the set of equations (3.4) was directly solved with the standard SciPy ODE routine[2], which gave the same results, but within shorter computation times. Therefore, all the results which will be presented in the following, were generated with the standard ODE solver routine. We are now able to calculate the time evolution of the density matrix for arbitrary electric fields.

Next, we need to extract observable macroscopic properties from the density matrix, which is in our case the polarization of the tunneling systems. A tunneling

---

[1] Python Software Foundation, 9450 SW Gemini Dr. ECM# 90772 Beaverton, OR 97008 USA, `http://www.python.org`

[2] scipy.integrate.ode, `https://docs.scipy.org/doc/scipy/reference/generated/scipy.integrate.ode.html`, Accessed: 16.11.2020

object with charge q, fully located in one well, represents a dipole moment, and can be expressed as [Phi87]

$$p = q \langle\psi_{\mathrm{b}}| \, x \, |\psi_{\mathrm{b}}\rangle = -q \langle\psi_{\mathrm{a}}| \, x \, |\psi_{\mathrm{a}}\rangle \quad , \tag{3.8}$$

where we used the wave functions of the single wells ψ_{a} and ψ_{b}. In the picture of the Bloch sphere, localizations in single wells are the intersections of the Bloch sphere with the x-axis. Thus, we can write down the density matrices for these states

$$\hat{\rho}_{\mathrm{aa}} = \frac{1}{2}[(|\Psi_{\mathrm{e}}\rangle - |\Psi_{\mathrm{g}}\rangle)(\langle\Psi_{\mathrm{e}}| - \langle\Psi_{\mathrm{g}}|)] = \frac{1}{2}\begin{pmatrix} 1 & -1 \\ -1 & 1 \end{pmatrix} \tag{3.9}$$

$$\hat{\rho}_{\mathrm{bb}} = \frac{1}{2}[(|\Psi_{\mathrm{e}}\rangle + |\Psi_{\mathrm{g}}\rangle)(\langle\Psi_{\mathrm{e}}| + \langle\Psi_{\mathrm{g}}|)] = \frac{1}{2}\begin{pmatrix} 1 & 1 \\ 1 & 1 \end{pmatrix} \quad . \tag{3.10}$$

The polarization operator $\hat{P}$ can then be written as

$$\hat{P} = \frac{1}{V}\left(-p\hat{\rho}_{\mathrm{aa}} + p\hat{\rho}_{\mathrm{bb}}\right) = \frac{p}{V}\hat{\sigma}_x \quad , \tag{3.11}$$

using the Pauli matrix $\hat{\sigma}_x$. The expectation value $\langle\hat{P}\rangle$ gives the polarization of the ensemble, and we find $P(t)$ is given by the sum of the off-diagonal elements of the density matrix (3.2)

$$P(t) = \langle\hat{P}\rangle = \frac{p}{V}\mathrm{tr}(\hat{\rho}(t)\cdot\hat{\sigma}_x) = \frac{p}{V}\left(\rho_{\mathrm{eg}}(t) + \rho_{\mathrm{ge}}(t)\right) \quad . \tag{3.12}$$

According to Equation (2.32), one expects from a sinusoidal driving field $F_{\mathrm{ac}}(t) = F_{\mathrm{ac}}\cos(\omega_{\mathrm{ac}}t)$ with frequency ω_{ac} the polarization

$$\tilde{P}(t) = F_{\mathrm{ac}}\varepsilon_0\chi'(t)\cos(\omega_{\mathrm{ac}}t) + F_{\mathrm{ac}}\varepsilon_0\chi''(t)\sin(\omega_{\mathrm{ac}}t) \quad , \tag{3.13}$$

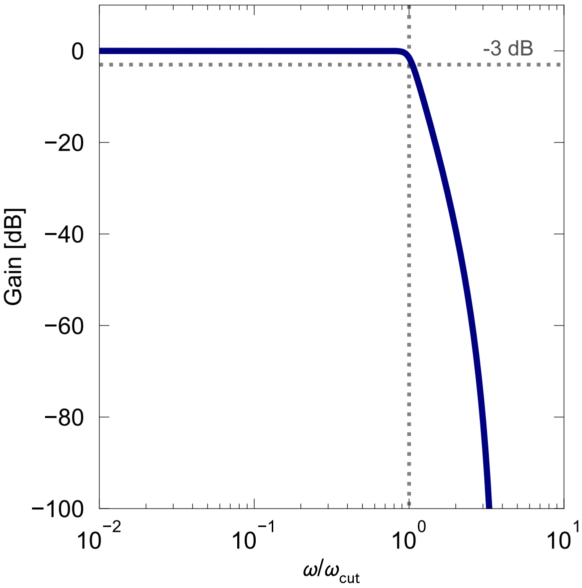

Figure 3.1: Filter characteristic of the used low pass filter to remove the $2\omega_{\mathrm{ac}}$-components from the signal. It is implemented as a digital Butterworth filter of order 15 with a cutoff frequency at $\omega_{\mathrm{cut}} = 1.3\omega_{\mathrm{ac}}$. At $\omega = \omega_{\mathrm{cut}}$ the attenuation by the filter is $-3\,\mathrm{dB}$.

where the polarization is split into a component in phase with the driving field (real part) and a component out of phase (imaginary part). We can extract $\chi'(t)$ and $\chi''(t)$ by multiplying $\tilde{P}$ with $\cos(\omega_{\mathrm{ac}}t)$ or $\sin(\omega_{\mathrm{ac}}t)$, respectively, and we get

$$\tilde{P}(t)\cos(\omega_{\mathrm{ac}}t) = \frac{1}{2}F_{\mathrm{ac}}\varepsilon_0\left[\chi'(t) + \chi'(t)\cos(2\omega_{\mathrm{ac}}t) + \chi''(t)\sin(2\omega_{\mathrm{ac}}t)\right] \tag{3.14}$$

$$\tilde{P}(t)\sin(\omega_{\mathrm{ac}}t) = \frac{1}{2}F_{\mathrm{ac}}\varepsilon_0\left[\chi''(t) + \chi'(t)\sin(2\omega_{\mathrm{ac}}t) - \chi''(t)\cos(2\omega_{\mathrm{ac}}t)\right] \quad . \tag{3.15}$$

The high frequency components $\sin(2\omega_{\mathrm{ac}}t)$ and $\cos(2\omega_{\mathrm{ac}}t)$ are much faster than $\chi'(t)$ and $\chi''(t)$ and can be removed with a low pass filter. The used filter is shown in Figure 3.1, where a sharp cutoff at $\omega_{\mathrm{cut}} = 1.3\omega_{\mathrm{ac}}$ is chosen. This demodulation procedure can be applied to the calculated polarization P, and we end up with

$$\chi'(t) = \frac{2}{\varepsilon_0 F_{\mathrm{ac}}}L\{P(t)\cos(\omega_{\mathrm{ac}}t)\} \tag{3.16}$$

$$\chi''(t) = \frac{2}{\varepsilon_0 F_{\mathrm{ac}}}L\{P(t)\sin(\omega_{\mathrm{ac}}t)\} \quad , \tag{3.17}$$

where $L\{x\}$ denotes the low pass filtering of a signal x. Most of the time we are only interested in the dielectric loss since it gives a good measure for the population of the resonant tunneling systems, and we write down the dielectric loss as $\tan\delta(t) = \frac{1+\chi'(t)}{\chi''(t)}$.

3.2 Single tunneling system calculations

In order to validate the integrity of the implemented code, we performed several calculations of single tunneling systems with and without applied driving or biasing electric fields. As a first test, all electric fields were set to zero ($F_{\mathrm{ac}} = F_{\mathrm{b}} = 0\,\mathrm{V\,m^{-1}}$) as well as the temperature. According to Equations (3.4), the dynamics of the system is then clearly simplified and independent from the tunneling splitting Δ_0. We chose a system with an energy splitting $E/h = 1\,\mathrm{GHz}$ and relaxation times of $\tau_1 = 40\,\mu\mathrm{s}$ and $\tau_2 = 2\tau_1$, meaning that no additional dephasing was assumed. The initial state of the system was chosen such that it starts in the upper level, i.e. $\rho_{\mathrm{ee}} = 1$; $\rho_{\mathrm{gg}} = \rho_{\mathrm{eg}} = \rho_{\mathrm{ge}} = 0$. In the absence of any electric fields, one expects an exponential decay into the ground state. A calculation of the time evolution for this setting shows exactly this behavior, see Figure 3.2. The excited state ρ_{ee} follows a decay $\rho_{\mathrm{ee}}(t) = \exp(-t/40\,\mu\mathrm{s})$ (dashed line), while the sum $\rho_{\mathrm{ee}} + \rho_{\mathrm{gg}}$ always equals 1, as the probability of the ground state exponentially converges towards 1.

Next, we used finite temperatures by applying the same settings as before, but varying the temperature between $T = 0.01\,\mathrm{K}$ and $T = 1\,\mathrm{K}$. The system is initially set to be in its ground state. As Figure 3.3 (left) shows, at finite temperatures ρ_{ee} relaxes within τ_1 towards an equilibrium state larger than zero. This equilibrium value

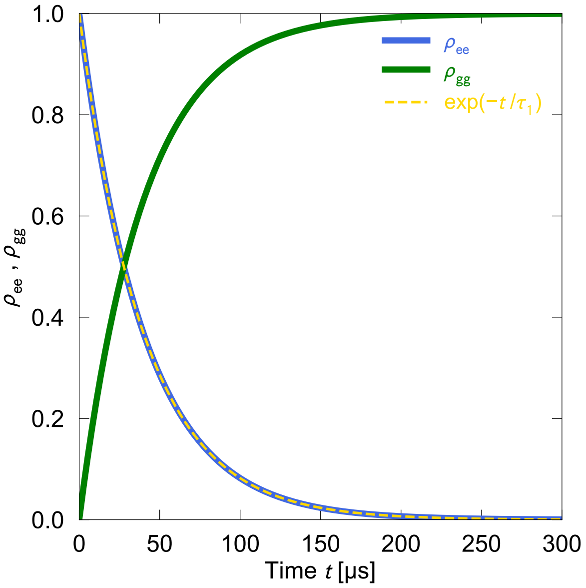

Figure 3.2: Time evolution of the diagonal entries of the system's density matrix in the absence of electric fields and for $T \to 0\,\mathrm{K}$. The initial state of the system was chosen such that it starts in the excited state ($E/h = 1\,\mathrm{GHz}$) with relaxation times of $\tau_1 = 40\,\mathrm{\mu s}$ and $\tau_2 = 2\tau_1$. It then decays exponentially into the ground state with $\rho_{ee}(t) = \exp(-t/40\,\mathrm{\mu s})$ (dashed line), while respecting $\rho_{ee}+\rho_{gg} = 1$.

increases with increasing temperatures as the excited state gets thermally more accessible. It agrees with the expected population number of a two-level system with an energy splitting of $E/h = 1\,\mathrm{GHz}$, which is shown in Figure 3.3 (right). Here, the equilibrium values at several temperatures are compared with $n_e = \frac{1}{2}(1 - \tanh(\frac{E}{2k_B T}))$. The equilibrium values of the simulation were extracted from the calculated time

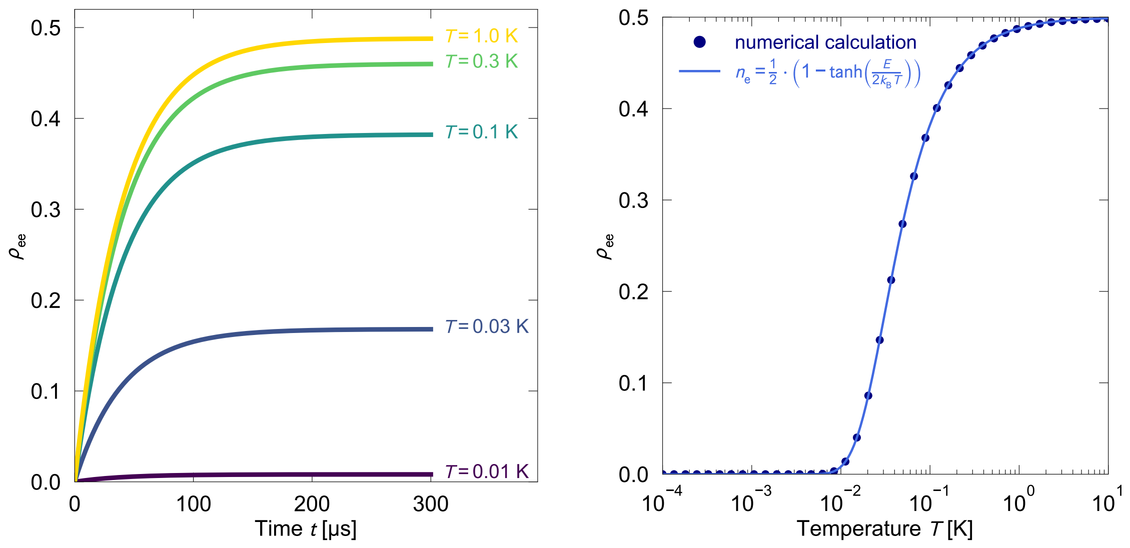

Figure 3.3: Left: Numerical calculation of the time evolution ρ_{ee} for temperatures between $T = 0.01\,\mathrm{K}$ and $T = 1\,\mathrm{K}$. Right: Equilibrium value $\rho_{ee}(t = 300\,\mathrm{\mu s})$ for several temperatures in comparison with the expected temperature dependence of the thermal population of a two-level system. For the tunneling system the same set of parameters as in Figure 3.2 was used.

evolutions at $t = 300\,\mu\mathrm{s}$, where equilibrium has settled in. The good agreement with the expectations shows that both the relaxation mechanism and the temperature are correctly implemented in the differential equations (3.4), and the ODE solver works as expected.

As a next step, we want to look at the effect of an alternating driving field $F_{\mathrm{ac}}(t) = F_{\mathrm{ac}} \cos(\omega_{\mathrm{ac}} t)$. For that, we isolated the effects of the electric driving field, by choosing an arbitrarily long relaxation time and set the temperature to zero. We then calculated the time evolution of ρ_{ee} for different field strengths F_{ac}. We chose $\omega_{\mathrm{ac}}/2\pi = 10\,\mathrm{MHz}$ as frequency for the driving field. The tunneling system is set to be in resonance with the electric field, which demands $\hbar\omega_{\mathrm{ac}} = \sqrt{\Delta^2 + \Delta_0^2}$. This condition is fulfilled by tunneling systems that are found on a half circle with radius $\hbar\omega_{\mathrm{ac}}$ in the Δ_0-Δ-plane and (0,0) as its center, see Figure 3.4 (e). No negative values for Δ_0 are valid. For the calculation we chose a system with $\Delta_0 = \Delta = \frac{\hbar\omega_{\mathrm{ac}}}{\sqrt{2}}$. The result for this setup with different field strengths is shown in Figure 3.4 (a)-(d). The

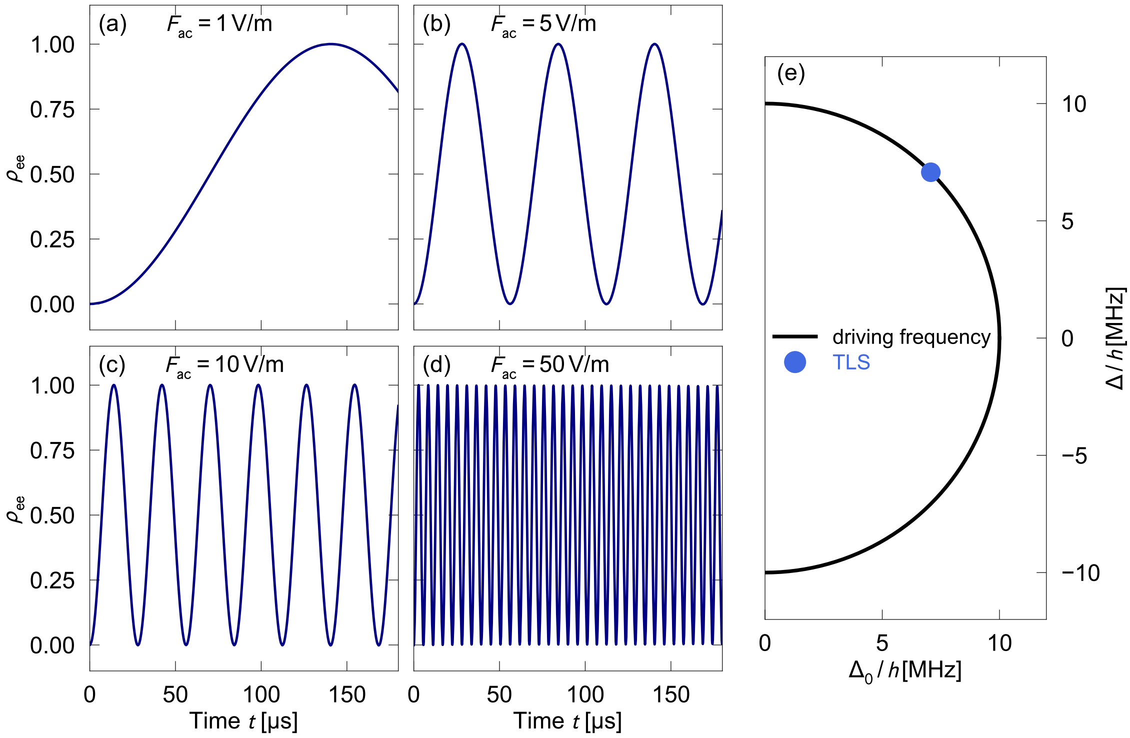

Figure 3.4: Numerical calculation of the time evolution of ρ_{ee} for different driving field strengths ($1\,\mathrm{V\,m^{-1}}$, $5\,\mathrm{V\,m^{-1}}$, $10\,\mathrm{V\,m^{-1}}$, $50\,\mathrm{V\,m^{-1}}$) (a)-(d) in the case of an oscillating driving field. The relaxation times τ_1, τ_2 were chosen to be arbitrarily long, and the temperature was set to zero in order to isolate the effects of the alternating electric field. The tunneling system ($\Delta_0 = \Delta = \frac{\hbar\omega_{\mathrm{ac}}}{\sqrt{2}}$) is in resonance with the frequency of the driving field $\omega_{\mathrm{ac}}/2\pi = 10\,\mathrm{MHz}$ (e).

F_{ac}	$\Omega_{\mathrm{R}}/2\pi$ (predicted)	$\Omega_{\mathrm{R}}/2\pi$ (simulated)
$1\,\mathrm{V\,m^{-1}}$	3.5590 kHz	3.5595 kHz
$5\,\mathrm{V\,m^{-1}}$	17.795 kHz	17.798 kHz
$10\,\mathrm{V\,m^{-1}}$	35.590 kHz	35.595 kHz
$50\,\mathrm{V\,m^{-1}}$	177.95 kHz	177.95 kHz

Table 3.1: Comparison between the predicted Rabi frequencies according to Equation (2.90) and the values from the simulations in Figure 3.4.

simulation reveals an oscillation in ρ_{ee} between 0 and 1, where the system periodically switches between ground and excited state, which is called a Rabi oscillation. The frequency of this oscillation depends on the applied field strength and is given for a tunneling system by Equation (2.90) as its Rabi frequency Ω_{R}. We used a dipole moment of $p = 1\,\mathrm{Debye} \approx 3.335 \times 10^{-30}\,\mathrm{C\,m}$ and set the angle between dipole moment and electric field to $\theta = 0°$. With that, we can compare the simulated values for the Rabi frequencies with the expected values from Equation (2.90). The value in the simulation was obtained by fitting a sinusoidal function to the data. Table 3.1 shows an overview of the results. For all field strengths, one finds an excellent agreement within a few 0.1 ‰. It should be noted that, in order to find these agreements and map the Rabi oscillation properly, one has to choose the time step Δt between two points in the simulation as $\Delta t \lesssim \frac{2\pi}{20\Omega_{\mathrm{R}}}$. Moreover, appropriate values for the internal relative tolerance of the ODE solver should hold the condition $\mathrm{rtol} \lesssim \frac{1}{\text{number of time steps}}$. Otherwise, the inaccuracies add up and lead to deviations for long simulation times. For more details see Appendix A.4.

We can furthermore detune the tunneling system from the electric driving field ($\omega_{\mathrm{ac}}/2\pi = 10\,\mathrm{MHz}$; $F_{\mathrm{ac}} = 10\,\mathrm{V\,m^{-1}}$), which was done in Figure 3.5. The factor $\frac{\Delta_0}{E} = \frac{1}{\sqrt{2}}$ was held constant in order to maintain the same Rabi frequency Ω_{R} for all systems. The detuning in energy $\hbar\delta = \hbar\omega_{\mathrm{ac}} - E$ leads to a modified Rabi oscillation $\Omega'_{\mathrm{R}} = \sqrt{\Omega_{\mathrm{R}}^2 + \delta^2}$ with a reduced maximum value $A_{\mathrm{R}} = \left(\frac{\Omega_{\mathrm{R}}}{\Omega'}\right)^2$ [Mil10]. Hence, the

	predicted		simulated	
δ	Ω'_{R} [kHz]	A_{R}	Ω'_{R} [kHz]	A_{R}
0.1 %	36.958	0.927	36.981	0.928
0.5 %	61.367	0.336	61.399	0.337
1.0 %	106.14	0.112	106.17	0.113
2.0 %	203.14	0.0307	203.17	0.0310

Table 3.2: Comparison between the predicted Rabi frequencies for a detuned tunneling system and the values from the simulations in Figure 3.5.

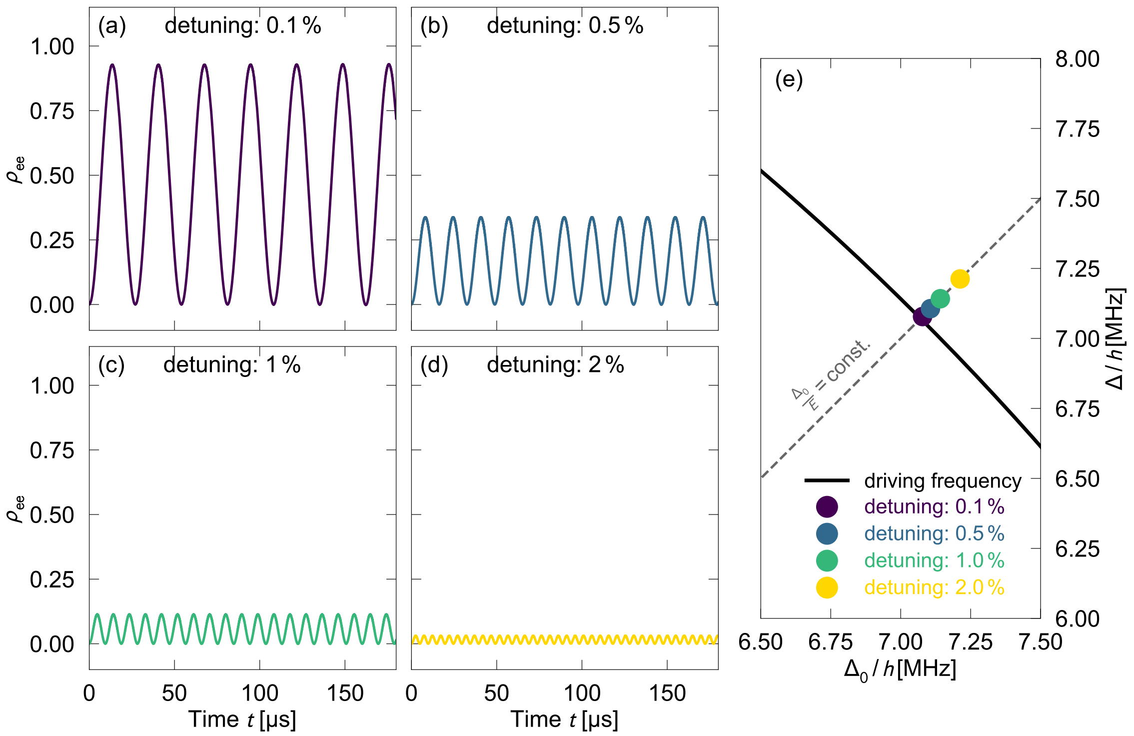

Figure 3.5: Numerical calculation of the time evolution of ρ_{ee} for different detunings from the driving field (0.1 %, 0.5 %, 1.0 %, 2.0 %) (a)-(d). The relaxation times τ_1, τ_2 were chosen to be arbitrarily long, and the temperature was set to zero. Without any energy detuning, the tunneling system parameters are $\varDelta_0 = \varDelta = \frac{\hbar\omega_{\mathrm{ac}}}{\sqrt{2}}$. The detuning in energy holds the factor $\frac{\varDelta_0}{E} = \frac{1}{\sqrt{2}}$ constant (e).

detuning leads to a faster oscillation, while the excited state cannot fully be reached. Again, we can compare the expected values for the oscillation with the behavior obtained from the simulation. The comparison is shown in Table 3.2, where simulated frequency and amplitude are again obtained from a fit of a sinusoidal function. Also for a detuned tunneling system the simulation precisely matches the expectations. The good agreement for these basic calculations shows that the numerical treatment of the driving field in the code works as expected.

Next, we combine the excitation with an electric field with relaxation processes in order to observe saturation effects of the tunneling system. As we have seen in Section 2.4.5, tunneling systems driven by an alternating electric field will get saturated. This means that in equilibrium, excitation and relaxation balance each other, and there remains a probability < 0.5 of finding the tunneling system in its excited state. We can simulate this effect by repeating the calculations from Figure 3.4, but using now shorter relaxation times of $\tau_1 = 20\,\mu\mathrm{s}$ and $\tau_2 = 2\tau_1$. The results are shown in Figure 3.6. In equilibrium, for small driving fields, the probability of finding the

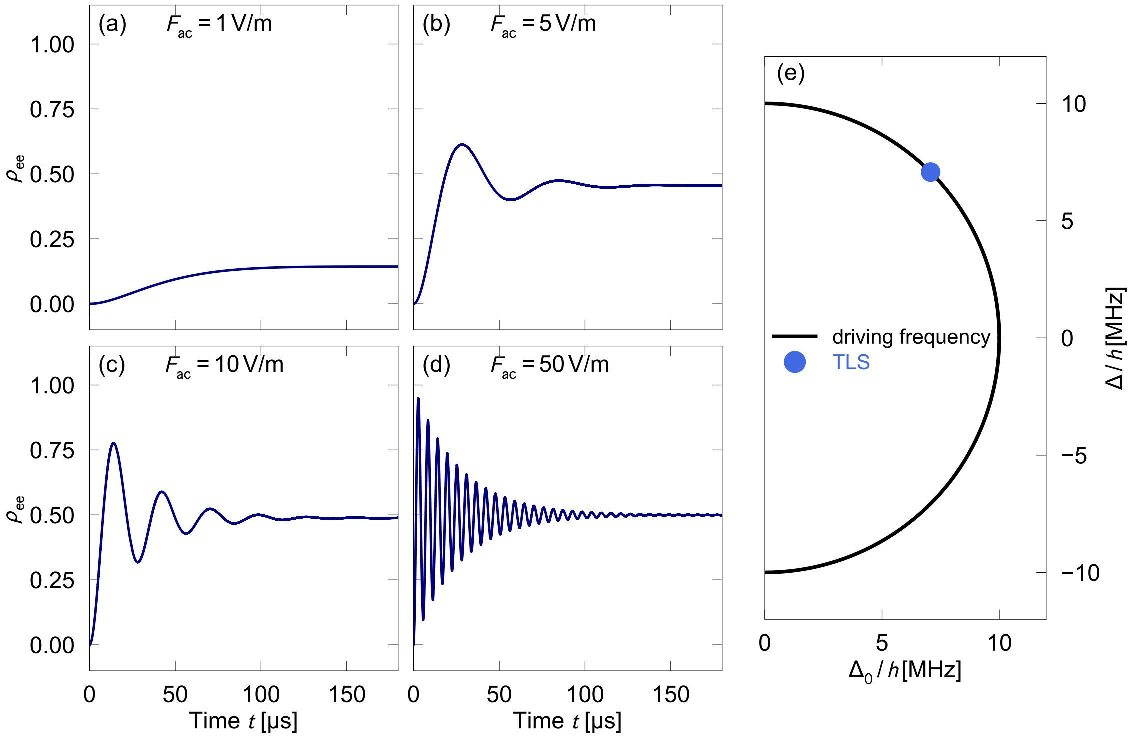

Figure 3.6: Repeating the calculations from Figure 3.4, but applying short relaxation times of $\tau_1 = 20\,\mu s$ and $\tau_2 = 2\tau_1$. The temperature was set to zero.

tunneling system in the excited state ρ_{ee} is close to zero. For higher field strengths, the tunneling system initially performs Rabi oscillations, which are damped by the relaxation. After some multiples of τ_1, the system has equilibrated and ρ_{ee} converges towards its equilibrium value ρ_{ee}^{eq}. A comparison can be drawn with Equation (2.89), which predicts the probability for a resonant tunneling system being in the excited state at very low temperatures as

$$\rho_{ee}^{eq} = \frac{\Omega_R^2 \tau_1 \tau_2}{2(1+\Omega_R^2 \tau_1 \tau_2)} \quad , \tag{3.18}$$

F_{ac}	ρ_{ee}^{eq} (predicted)	ρ_{ee}^{eq} (simulated)
$1\,V\,m^{-1}$	0.1429	0.1432
$5\,V\,m^{-1}$	0.4545	0.4549
$10\,V\,m^{-1}$	0.4878	0.4880
$50\,V\,m^{-1}$	0.4995	0.4995

Table 3.3: Comparison between the predicted equilibrium value ρ_{ee}^{eq} according to Equation (3.18) and the steady-state results from the simulation in Figure 3.6.

where we used $\langle \hat{S}_{0,\mathrm{z}} \rangle' = \frac{1}{2} - \rho_{\mathrm{ee}}^{\mathrm{eq}}$. Table 3.3 compares the results of this equation with the values found in Figure 3.6 after the system reached its equilibrium state. Once again, the numerical results show a very good agreement with the predictions. The maximum value for $\rho_{\mathrm{ee}}^{\mathrm{eq}}$ is 0.5 since a two-level system in equilibrium cannot get population inverted by the driving field. An equilibrium value of 0.5 means a full saturation of the tunneling system, and as a consequence no generation of any loss. From the density operator we can calculate the electric polarization, and from that we determine the dielectric loss $\tan\delta$ by demodulating the dielectric function's real and imaginary part, as explained in Section 3.1. This was done for the time evolutions of Figure 3.6 for $F_{\mathrm{ac}} = 1\,\mathrm{V\,m^{-1}}$ and $F_{\mathrm{ac}} = 10\,\mathrm{V\,m^{-1}}$ and is shown in Figure 3.7. The polarization oscillates with the frequency of the driving field. To make this oscillation visible on the time scale of the plot, the cycle duration was artificially increased, by plotting only every 39th data point (one oscillation in P consists of 10 data points). A normalization volume of $V = 1\,\mathrm{m}^3$ was used for the polarization, which explains the small absolute values for P and $\tan\delta$ as we observe the response of a single tunneling system within the entire volume. The steady-state loss for the smaller

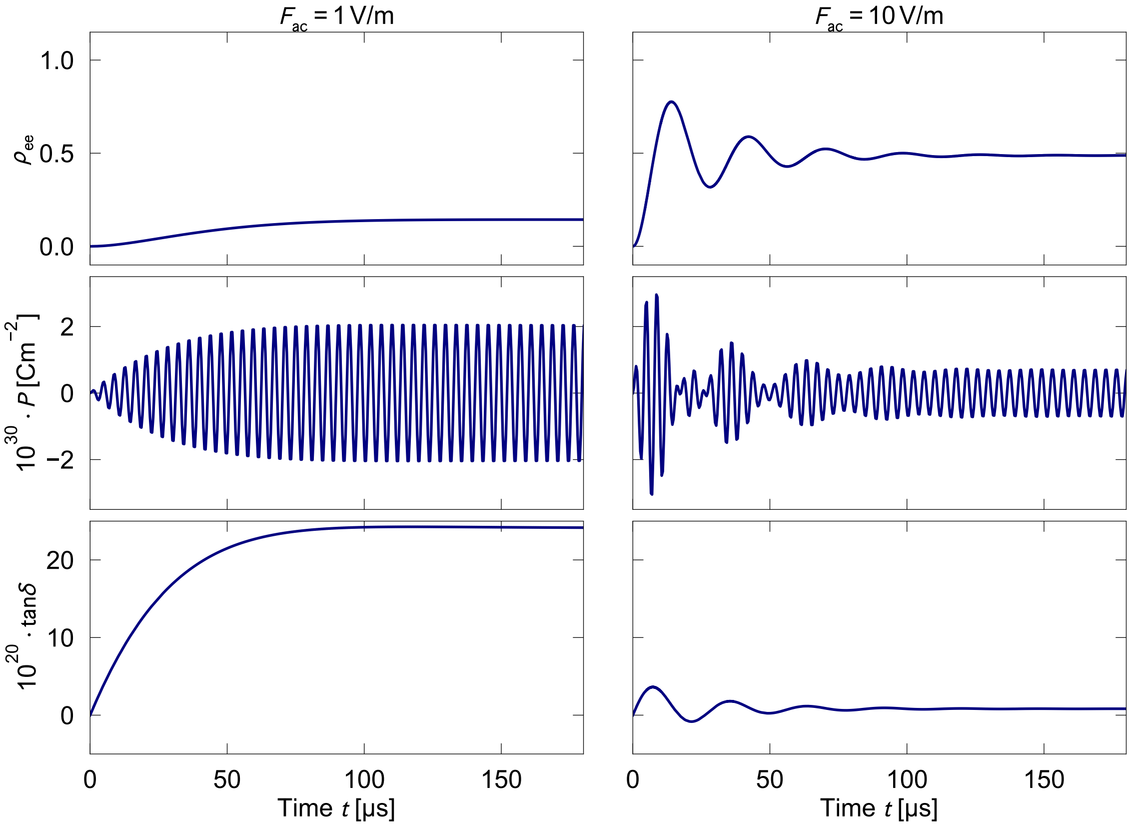

Figure 3.7: Calculated time evolution of the dielectric loss of a tunneling system from the simulations in Figure 3.6, for $F_{\mathrm{ac}} = 1\,\mathrm{V\,m^{-1}}$ (left) and $F_{\mathrm{ac}} = 10\,\mathrm{V\,m^{-1}}$ (right).

driving field is much bigger than the one of the larger field. For $F_{\mathrm{ac}} = 10\,\mathrm{V\,m^{-1}}$ the system can only absorb photons at the beginning when it performs Rabi oscillations. During this initial oscillation, the loss also becomes negative at certain times, where the system tends to emit photons. In equilibrium the loss is close to zero. The driving field almost fully saturates the tunneling system, which then cannot effectively absorb any photons since the probabilities for resonant absorption and stimulated emission are almost the same. For $F_{\mathrm{ac}} = 1\,\mathrm{V\,m^{-1}}$ the relaxation rate exceeds the rate for excitations Ω_{R}, allowing the system to absorb photons also in equilibrium.

As a final test, we applied in parallel to the driving field an additional electric bias field, which shifts the tunneling system in its asymmetry energy $\varDelta$. We chose a system that is initially detuned from the driving field $\varDelta + h \cdot 0.35\,\mathrm{MHz} = \varDelta_0 = \frac{\hbar\omega_{\mathrm{ac}}}{\sqrt{2}}$. The bias field is applied in form of a ramp, starting at 100 µs and reaching its maximum value of $F_{\mathrm{b}} = 150\,\mathrm{V\,m^{-1}}$ after the ramp time t_{b}. Dipole moment and the direction of the bias field are assumed to be aligned. Using as before a dipole moment of $p = 1$ Debye gives a maximum shift in $\varDelta/h$ of about 1.5 MHz, meaning that the tunneling system crosses the resonance which enables Landau-Zener transitions. The simulation of this setup with long relaxation times for different ramp times (10 µs, 50 µs, 100 µs, and 200 µs) is shown in Figure 3.8. At the beginning the system is set into the ground state and performs a suppressed Rabi oscillation because of the detuning. As it was discussed in Section 2.4.6, for a fast resonance crossing, the probability for a transition from the ground into the excited state is reduced, which agrees with numerical calculation. The probability for a transition is given by Equation (2.104) and compared with the value of ρ_{ee} in Figure 3.8 (a)-(d) after crossing the resonance, see Table 3.4. The values obtained from the simulation were averaged over the last 10 µs to cancel out the remaining oscillations. One finds a somewhat good agreement with the expectations, but larger deviations than in the previous simulations occur. A possible explanation for this mismatch might be the fact that the tunneling system is initially energetically too close to the excitation frequency, and not, as demanded by the Landau-Zener problem, clearly detuned from it. There-

t_{b}	$\rho_{\mathrm{ee}}(\infty)$ (predicted)	$\rho_{\mathrm{ee}}(\infty)$ (simulated)
10 µs	0.111	0.075
50 µs	0.443	0.469
100 µs	0.690	0.666
200 µs	0.904	0.883

Table 3.4: Comparison between the predicted probability for a transition into the excited state for a resonance crossing according to Equation (2.104), and the value $\rho_{\mathrm{ee}}^{\mathrm{eq}}$ from the simulations in Figure 3.8 after the tunneling system has passed the resonance.

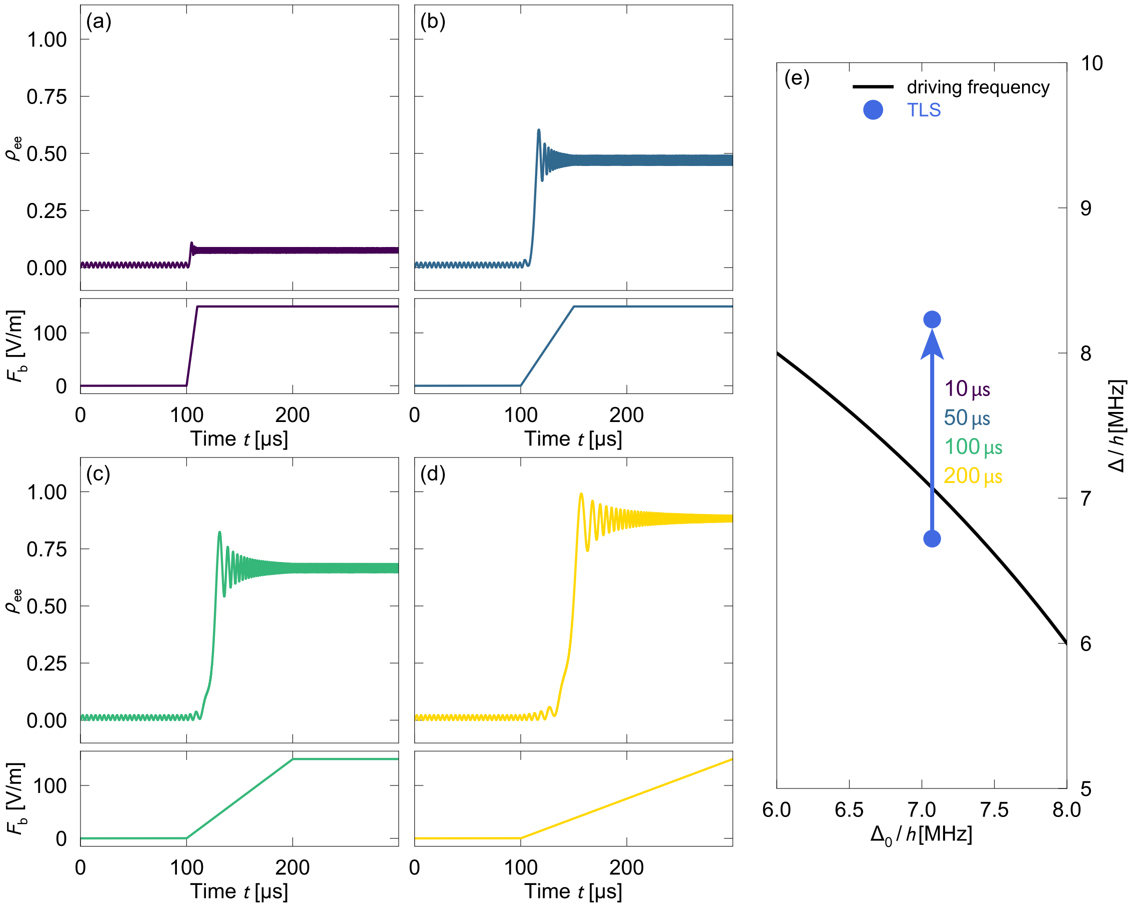

Figure 3.8: Numerical calculation of the time evolution of ρ_{ee} in the presence of a swept electric bias field for different ramp times (10 µs, 50 µs, 100 µs, and 200 µs) (a)-(d). The relaxation times τ_1, τ_2 were chosen to be arbitrarily long, and the temperature was set to zero. The tunneling system is initially detuned by 0.35 MHz in $\Delta/h =$ from the driving field at 10 MHz with a field strength of $10\,\mathrm{V\,m^{-1}}$ and is shifted by the bias field across the resonance (e).

fore, the applicability of Equation (2.104) for this setting might be limited. Indeed, simulations with a larger initial detuning give better agreements with solutions of the Landau-Zener problem, see Appendix A.5. In this case the simulation should be the more accurate description of the given situation.

When we switch to short relaxation times, the Landau-Zener theory completely fails, as it does not consider any relaxation processes during the resonance crossing. The simulation naturally regards relaxation times, and the calculations can be performed also under fast relaxation times without any interference. Results of such calculations are shown in Figure 3.9 for two ramp times 50 µs (left) and 200 µs (center). All settings are identical to Figure 3.8, besides the shorter relaxation times $\tau_1 = 20\,\mu\mathrm{s}$, $\tau_2 = 2\tau_1$. The fast relaxation forces the tunneling system to return to the ground

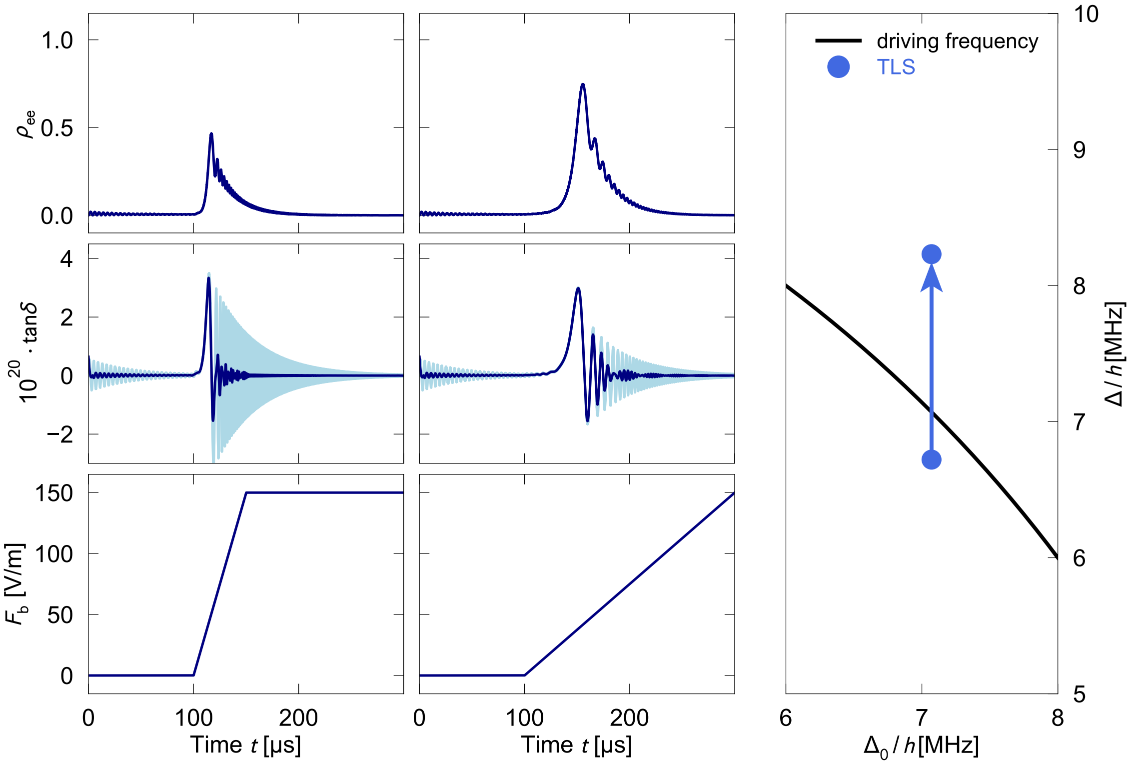

Figure 3.9: Repeating the calculations from Figure 3.8 for two ramp times 50 µs (left) and 200 µs (center), but employing short relaxation times of $\tau_1 = 20\,\mu\text{s}$ and $\tau_2 = 2\tau_1$.

state within τ_1 and does not allow a population inversion over a longer period of time. The loss was slightly smoothed in order to reduce the appearance of fast off-resonant Rabi oscillations (light blue). It shows in both cases a distinct absorption while crossing the resonance, with a subsequent fast oscillation around zero, which averages out when smoothing the data, or by regarding an ensemble of tunneling systems, which we will discuss in the following section.

It can be concluded that the simulation presented above provides excellent agreement with the basic predictions of a single two-level system's dielectric response. In addition to that, it should also provide a reliable description of its response for more complex scenarios, where the predictions by theory are limited.

3.3 Monte Carlo simulation of the tunneling system ensemble

The discussed simulations of a single tunneling system can easily be extended to an ensemble of tunneling systems. First of all, different tunneling systems are randomly generated, whereby their parameters follow the respective distribution. For each system, the time evolution of its density operator $\hat{\rho}$ is then calculated. The polarization of the ensemble is the sum of each system's polarization. Knowing the total polarization, we calculate the ensemble loss from it just in the same way as we did for a single system. Following the law of large numbers, the larger the number of generated tunneling systems is, the better the result corresponds to the true value. Such a Monte Carlo approach should be an appropriate way to map the random nature of the tunneling system ensemble.

3.3.1 Generation of the tunneling system ensemble

A tunneling system driven by electric fields is fully characterized by its asymmetry energy $\varDelta$, its tunneling splitting $\varDelta_0$, and its dipole moment $\boldsymbol{p}$. Equation (2.25) defines the probability density function (PDF) $f(\varDelta, \varDelta_0)$, which gives the probability for finding a tunneling system with certain $\varDelta$ and $\varDelta_0$

$$f(\varDelta, \varDelta_0)\mathrm{d}\varDelta\mathrm{d}\varDelta_0 = \frac{P_0}{\varDelta_0}\mathrm{d}\varDelta\mathrm{d}\varDelta_0 \quad . \tag{3.19}$$

The asymmetry energy $\varDelta$ is uniformly distributed and can be generated with a standard pseudo-random number generator. The distribution in $\varDelta_0$ follows

$$f_{\varDelta_0}(x)\mathrm{d}x = \frac{1}{x}\mathrm{d}x \quad . \tag{3.20}$$

In order to generate values of $\varDelta_0$ which follow this distribution, we make use of the inverse transform sampling. Therefore, we need to find the inverse of the cumulative distribution function (CDF) $F_{\varDelta_0}^{-1}$:

$$F_{\varDelta_0}(x) = \int\limits_{\varDelta_{0,\mathrm{min}}}^{x} f_{\varDelta_0}(x')\mathrm{d}x' = \ln(x) - \ln(\varDelta_{0,\mathrm{min}}) \tag{3.21}$$

$$F_{\varDelta_0}^{-1}(x) = e^{x+\ln(\varDelta_{0,\mathrm{min}})} \tag{3.22}$$

Random numbers for $\varDelta_0$ can now be sampled by generating a random variable u that is uniformly distributed between zero and the scaling parameter a, which then yields $\varDelta_0 = F_{\varDelta_0}^{-1}(u) = e^{u+\ln(\varDelta_{0,\mathrm{min}})}$. With that, we can generate random values for $\varDelta$ and $\varDelta_0$ according to their probability distribution Equation (3.19), while at the same time it is possible to restrict their values to certain ranges. Figure 3.10 shows three exemplary distributions, each composed out of 5000 systems, and tailored for different purposes. In the first case Figure 3.10 (a), $\varDelta/h$ was generated in the interval $[-20\,\mathrm{MHz}, 20\,\mathrm{MHz}]$ and $\varDelta_0/h$ between $[1\,\mathrm{MHz}, 20\,\mathrm{MHz}]$. Calculating the resonant loss with this distribution is rather inefficient because many tunneling systems are generated off-resonantly, whose contributions to the loss are insignificant. The loss

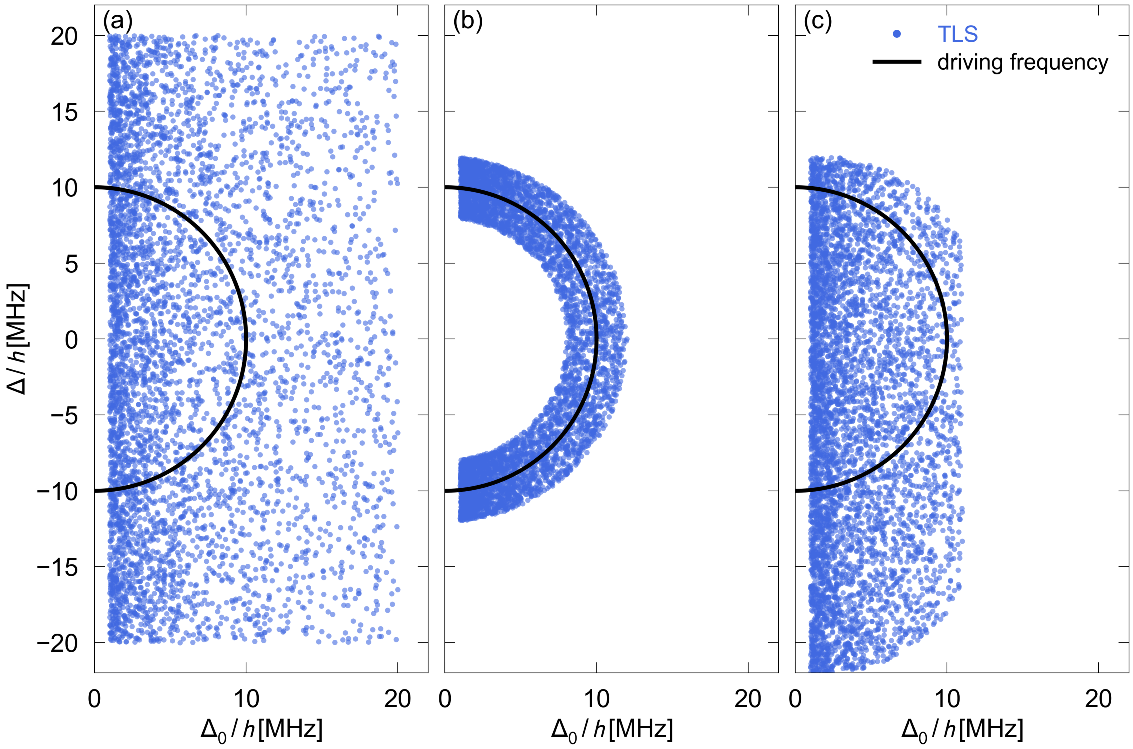

Figure 3.10: Three different ensembles composed out of 5000 tunneling systems which are distributed according to Equation (3.19). Each point represents a tunneling system with the parameters $\varDelta$ and $\varDelta_0$. Systems that lie on the black circle are in resonance with the driving field at 10 MHz. Restricting the parameters to certain energy ranges, allows to tailor the distribution for specific purposes.

would only be dominated by a few systems that fulfill the resonance condition. A better choice is the distribution shown in Figure 3.10 (b), where tunneling system energies are only allowed within a small energy band around the driving field frequency. This gives a higher density of tunneling systems in the relevant energy window. If also a large electric bias field is involved, a distribution as that presented in (c) is favorable since tunneling systems exist that will get pushed into resonance during a bias sweep. The number of generable systems is limited, hence, the divergence at $\varDelta_0 \to 0$ makes it hard to use small values for the cutoff $\varDelta_{0,\mathrm{min}}$ since the density of tunneling systems with $\varDelta_0 \approx \hbar\omega_{\mathrm{ac}}$, which are the most relevant for the resonant loss, becomes very small then. The histograms (3.11) show the distribution of $\varDelta$ and $\varDelta_0$ of the ensemble in Figure 3.10 (a) but with a number of 50,000 tunneling systems. As demanded, $\varDelta$ is uniformly distributed, and the distribution in $\varDelta_0$ shows a $1/x$-dependency.

So far, we have only used a single value for the dipole moment of $p = 1\,\mathrm{Debye}$. However, the dipole angle θ of each system, with regard to the applied electric field, is randomly distributed. One can assume that in disordered solids every dipole ori-

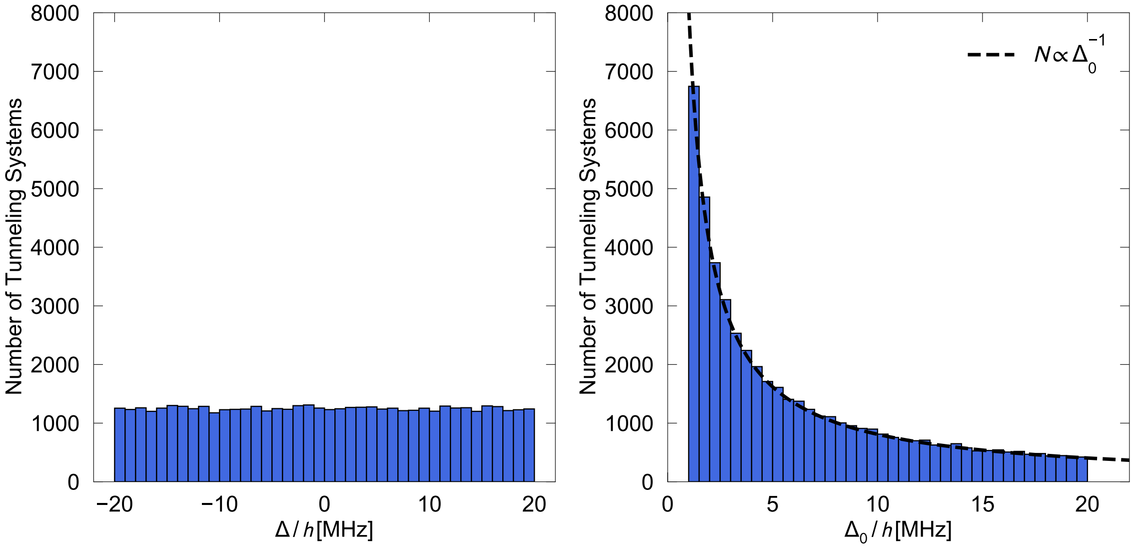

Figure 3.11: Histogram of $\mathit{\Delta}$ and $\mathit{\Delta}_0$ for a tunneling system ensemble alike the one in Figure 3.10 (a) with 50,000 systems in total.

entation has the same probability, and hence, use a dipole moment orientation that is uniformly distributed over the surface of a sphere. The probability of finding a dipole within the surface element $\mathrm{d}A = \sin\theta \mathrm{d}\theta \mathrm{d}\phi$ can then be written as

$$f(\theta,\phi)\mathrm{d}\theta\mathrm{d}\phi = \frac{1}{4\pi}\sin\theta\mathrm{d}\theta\mathrm{d}\phi \quad , \tag{3.23}$$

and thus

$$f(\theta)\mathrm{d}\theta = \frac{1}{2}\sin\theta\mathrm{d}\theta \quad . \tag{3.24}$$

We can write the CDF for this distribution as

$$F(\theta) = \frac{1}{2}(1-\cos\theta) \quad . \tag{3.25}$$

Using again the inverse transform sampling we generate values for θ through

$$\theta = \cos^{-1}(1-2u) \quad u \in [0,1] \tag{3.26}$$

or

$$\theta = \cos^{-1}(u) \quad u \in [-1,1] \quad , \tag{3.27}$$

where u denotes uniformly distributed random numbers in the given interval. Equation (3.27) neglects negative angles of θ, which we include by using the sign function $\mathrm{sgn}(x)$

$$\theta = \mathrm{sgn}(u_1)\cos^{-1}(u_2) \quad u_1, u_2 \in [-1,1] \quad . \tag{3.28}$$

Figure 3.12 (left) shows the distribution of 400,000 generated dipole angle orientations. The angles ±$\pi/2$ have the highest probability since the surface element on

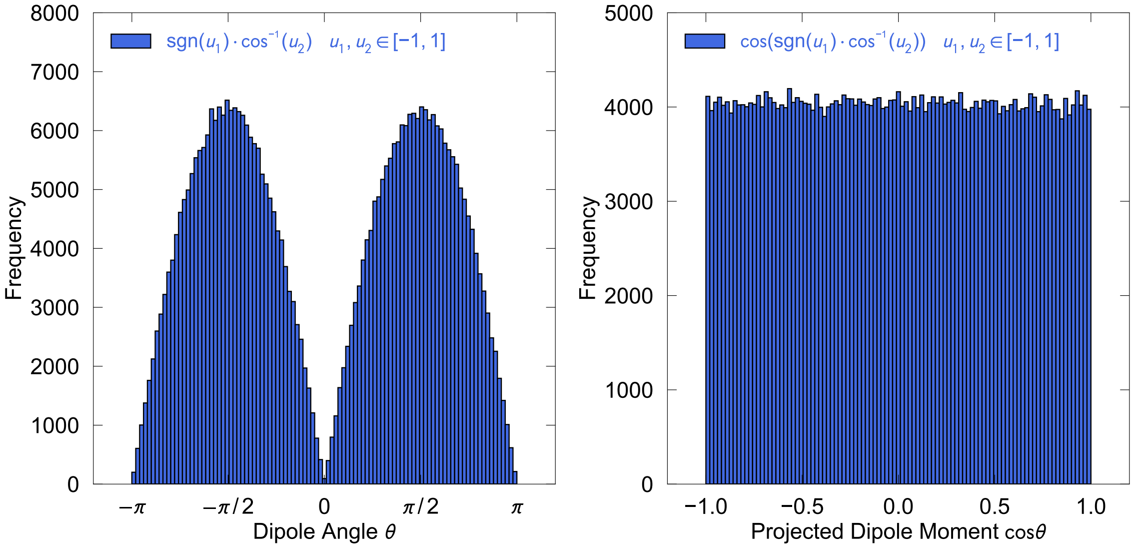

Figure 3.12: Distribution of the dipole angle θ (left), and its projection onto the electric field direction $\cos\theta$ (right) for 400,000 generated angles, according to Equation (3.28).

the sphere for these orientations is the largest. The dipole angle occurs as $\cos\theta$ in all formulae, hence, the distribution of $\cos\theta$ is of major interest, which reveals a uniform distribution in the interval $[-1, 1]$, see Figure 3.12 (right).

In most of the cases that will be presented in the following, we are only interested in the general behavior of the tunneling system ensemble, which is why, in order to simplify the calculations, we neglect the fact that θ follows a probability distribution and choose a fixed value of $\cos\theta = 1$ instead. The same is done for the tunneling system relaxation times τ_1 and τ_2, where we choose constant values for most of the simulations but can in principle also apply the one-phonon relaxation, see Equation (2.68). Whenever the simulation is supposed to map the experiment more closely distributions for these parameters can be directly implemented.

3.3.2 Streamlining the simulation

Computing the time evolution of thousands of single tunneling systems is a rather time consuming process. The computations are performed on an Intel® Core™ i7-8700K CPU. We do not consider any interactions between the tunneling systems and consider them to be independent from each other. Hence, the time evolutions can be regarded separately, and a full parallelization is possible. Calculating the time evolution of several tunneling systems in parallel on different CPU threads massively shortens the computation times.

In order to have the time scale of relaxation processes comparable to those in experiment, we need to simulate the time evolution over a period of several hundred microseconds. An excitation frequency of 1 GHz requires a large number of simulation time steps to resolve the resulting high frequency oscillation of the polarization. The number of time steps then needs to be of the order $\sim 10^6$. A way to reduce this number is by using a lower excitation frequency of 10 MHz, which has already been used in the previous sections. If the temperature can be assumed to be small, the absolute number of the energy splitting E should be irrelevant for the tunneling system's dynamics. The Rabi frequency Ω_R, the change of the energy splitting in the presence of a swept bias field ν, and the therefore the Landau-Zener parameter γ, all depend solely on the ratio $\frac{\Delta_0}{E}$, which is unaffected by the absolute value of E. For this reason, we can rescale the whole system. An excitation with 10 MHz should give equivalent results to faster excitations. Using an even lower excitation frequency eventually leads to a significant modulation of the energy splitting E by strong electric driving fields, which then leads to deviations. Choosing an excitation of 10 MHz allows field strengths of up to $100\,\mathrm{V\,m^{-1}}$, whereby the results were found to be identical to the ones using faster resonant excitations.

The absolute value of E becomes important when the effect of non-negligible temperature comes into play. This involves terms where the thermal population factor $\tanh\left(E/2k_\mathrm{B}T\right)$ occurs. We can artificially boost this factor to the required value by replacing all of these emerging terms with $\tanh\left(\frac{\mathrm{boost}\cdot E}{2k_\mathrm{B}T}\right)$. In the case of an excitation with 10 MHz, we boost all tunneling systems with the factor boost $= 100$, which then gives the same thermal population number of 1 GHz-systems, and thus, should lead to equivalent results.

Another optimization can be made for strong off-resonant tunneling systems. As long as we consider only the resonant loss, tunneling systems with a large detuning are irrelevant. Therefore, we can avoid this very time-consuming calculation by setting the driving field strength for these systems to zero, which has a negligible impact on the evolution anyway. It is found that computing the full Hamiltonian only for tunneling systems within $0.7\hbar\omega_\mathrm{ac} < E < 1.3\hbar\omega_\mathrm{ac}$ significantly shortens the computation time without a loss of any accuracy. This will be of importance for simulations including electric bias fields, where tunneling systems cross a wide energy range, but are in resonance with the driving field only for a short period of time. If short transversal relaxation times $\tau_2 \lesssim 10\,\mathrm{\mu s}$ are used in the simulation, the above limit needs to be chosen wider because the spectral width of tunneling system contributions is broader then, and off-resonant tunneling systems will contribute stronger to the resonant loss.

By applying these refinements to the simulation, the computation of the resonant loss with 15,000 tunneling systems over a time span of 600 µs takes about 2-4 hours, depending on the specific simulation scenario. This gives an acceptable time scale for performing such tunneling system simulations.

3.3.3 Driving field strength dependency

A verification of the simulation can be done by calculating the resonant loss of a tunneling system ensemble as a function of the driving field strength. This is compared to the loss from Equation (2.92), originating from the saturation of tunneling systems by large electric driving fields. We start with an ensemble of 5000 systems, as shown in Figure 3.13, which is driven by an electric field at frequency $\omega_{\mathrm{ac}}/2\pi = 10\,\mathrm{MHz}$ and $F_{\mathrm{ac}} = 3\,\mathrm{V\,m^{-1}}$. The relaxation times are taken to be constant $\tau_1 = 20\,\mathrm{\mu s}$, $\tau_2 = 2\tau_1$, and the dipole moment is set to $p = 1\,\mathrm{Debye}$ with $\cos\theta = 1$. At the beginning, all systems are in the ground state. Therefore, the electric field initially excites all resonant tunneling systems into their upper state, which we have already discussed for the case of a single system in Section 3.2. The initial absorption of photons by resonant tunneling systems is associated with the occurrence of a large dielectric loss. This is in agreement with Figure 3.13 (a), where the color of each point indicates each system's loss. Systems that fulfill the resonance condition (black line) are the ones that generate the highest losses. As the simulation continues, saturation leads to a smaller loss since tunneling systems are already in the excited state and cannot fully absorb photons (b). In equilibrium the rate of excitation and relaxation balance out each other. We then find a reduced loss (c), as tunneling systems are saturated by the excitation. An evaluation of the whole sequence is presented in Figure 3.14.

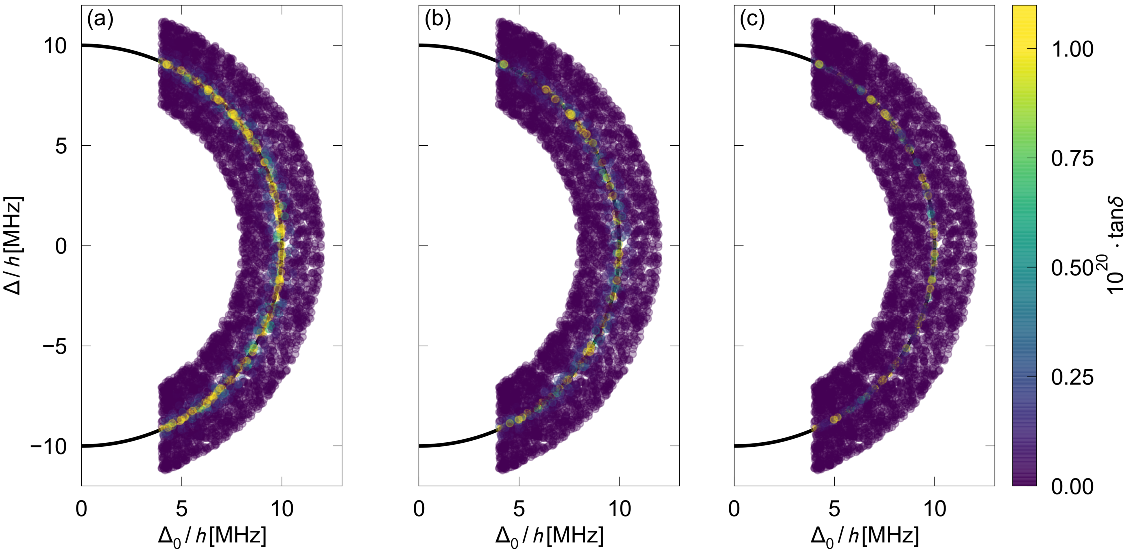

Figure 3.13: Monte Carlo simulation of the dielectric loss for an ensemble of 5000 tunneling systems at three different time steps: (a) t=5 µs, (b) t=25 µs and (c) t=170 µs. Tunneling systems are generated within the relevant energy range with constant parameters $\tau_1 = 20\,\mathrm{\mu s}$, $\tau_2 = 2\tau_1$, $p = 1\,\mathrm{Debye}$, and the temperature set to zero. The ensemble is driven by an electric field of $F_{\mathrm{ac}} = 3\,\mathrm{V\,m^{-1}}$ and $\omega_{\mathrm{ac}}/2\pi = 10\,\mathrm{MHz}$.

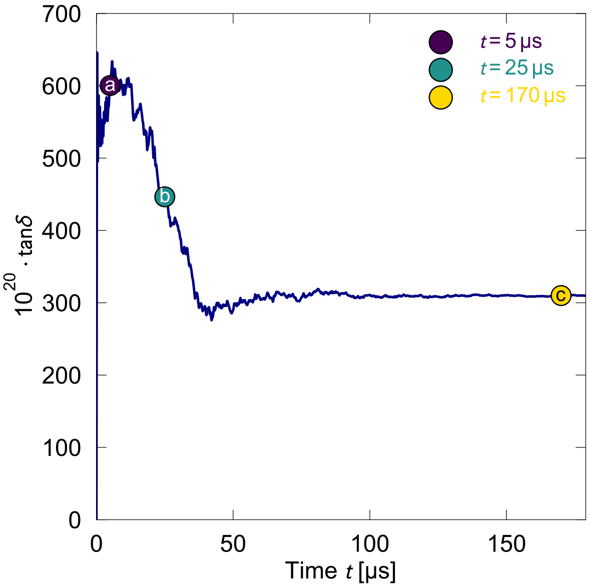

Figure 3.14: Evaluation of the sequence in Figure 3.13. The loss of the ensemble is plotted as a function of time, and the time steps (a), (b), and (c) from above are marked.

It shows the ensemble loss as a function of time, where the three time steps from Figure 3.13 (a), (b), and (c) are marked. One can observe the above-mentioned behavior; an initial increase of the loss with a subsequent relaxation towards the equilibrium loss, which is reduced due to saturation of tunneling systems.

We can repeat this sequence with different field strengths of the driving field. This is done in Figure 3.15 (left) for field strengths between $0.01\,\mathrm{V\,m^{-1}}$ and $100\,\mathrm{V\,m^{-1}}$, with relaxation times of $\tau_1 = 40\,\mathrm{\mu s}$, $\tau_2 = 2\tau_1$. An ensemble with 10,000 tunneling systems and $\varDelta_{0,\mathrm{min}}/h = 4\,\mathrm{MHz}$ was used. All other parameters were chosen as in Figure 3.14. Analogously to the discussion of a single tunneling system, we observe a reduction of the loss in equilibrium with increasing field strengths due to saturation. We obtain the equilibrium loss by averaging over the last $50\,\mathrm{\mu s}$ (grey area) and plot these values as a function of the applied field strength, which was done in Figure 3.15 (right). We find a plateau for small field strengths which goes over into a F^{-1}-dependency above a critical value of the field strength. These data points are compared with Equation (2.92), in which the simulation parameters are plugged in, and we find a critical field strength of $F_\mathrm{c} = 0.559\,\mathrm{V\,m^{-1}}$ (dashed gray curve). This gives a fairly good agreement. However, Equation (2.92) implies a distributed phononic relaxation rate $\tau_{1\mathrm{P}}^{-1}$ which is integrated over a wide energy range. This is not fully compatible with the simulation settings, where we used constant relaxation times and a limited energy range for generated tunneling systems. In order to obtain results that more comparable to those of the simulation, we have to integrate Equation (2.91) with the simulation parameters over the applied energy range of distributed tunneling systems. The result of the numerical integration is shown by the solid blue line in Figure 3.15 (right). The usage of appropriate integration limits gives a better agreement with the results of the simulation. However, the simulation data is still

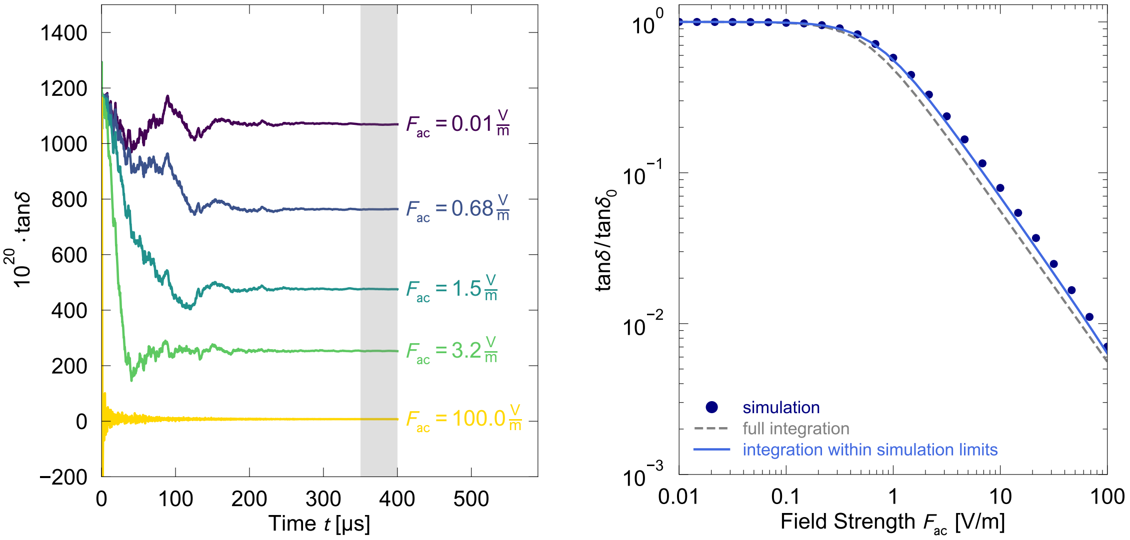

Figure 3.15: Left: Time evolution of the loss for different field strengths. An ensemble of 10,000 tunneling systems and $\varDelta_{0,\mathrm{min}}/h = 4\,\mathrm{MHz}$, with constant relaxation times $\tau_1 = 40\,\mu\mathrm{s}$, $\tau_2 = 2\tau_1$ was used. All other parameters were chosen as in Figure 3.14. The equilibrium loss for each field strength is obtained from an average over the last $50\,\mu\mathrm{s}$ (grey area). Right: Equilibrium loss as a function of the applied field strength. The simulation results are compared with Equation (2.92) (dashed grey curve) and with a loss obtained from an integration adapted to the distribution's energy limits of the simulation (solid blue curve).

slightly shifted towards higher field strengths, indicating an imprecise critical field strength, possibly occurring from the limited number of generated tunneling systems. Nevertheless, the overall behavior follows the expectations.

3.3.4 Temperature dependency

Another test of the simulation can be made by simulating the temperature dependency of the dielectric function's resonant part in equilibrium. For the calculation of the resonant loss, it is sufficient only to regard tunneling systems with energy splittings $E \approx \hbar\omega_{\mathrm{ac}}$. However, this is not appropriate for the resonant real part since also off-resonant tunneling systems give contributions to the dielectric response, see Figure 2.12. Hence, we need to generate tunneling systems over a wider energy range. We chose the energy limits $\varDelta_{0,\mathrm{min}}/h = 1.7\,\mathrm{MHz}$, $E_{\mathrm{max}}/h = 50\,\mathrm{MHz}$ and used a one-phonon relaxation process (2.68) with $K_1 = 5.2 \times 10^{78}\,\mathrm{J}^{-3}\mathrm{s}^{-1}$. The same as before, we calculate the dielectric response to an electric field with field strength $0.1\,\mathrm{V\,m}^{-1}$ and frequency 10 MHz. As discussed in Section 3.3.2 we can emulate the behavior of a 1 GHz excitation by using the thermal population factor $\tanh(\frac{h\cdot 1\,\mathrm{GHz}}{2k_{\mathrm{B}}T})$ in the simulation. Moreover, we need to apply the driving field to all tunneling systems since now we are not only interested in the resonant loss.

Figure 3.16 shows the results of such a simulation with 30,000 generated tunneling systems. The data is compared to the analytic results of the resonant part from Equations (2.86) and (2.87), where we used $A = 142 \times 10^{-20}$ and $\omega_{\mathrm{ac}}/2\pi = 1\,\mathrm{GHz}$ in both cases. For the loss we find a good agreement over the whole temperature range, while in the real part the simulation data is described by theory only up to 200 mK. This is to be expected since in the simulation no tunneling systems above E_{max} exist, which are the ones giving contributions to the real part at higher temperatures. The simulation data then cannot follow the theory anymore. Only at lower temperatures, where tunneling systems with lower energy become thermally accessible, tunneling systems exist which produce the expected behavior. In the resonant loss, the limited energy range of generated tunneling systems is not a problem because only the resonant ones give significant contributions to the loss, which are included in the generated ensemble. At higher temperatures, these systems become thermally more and more populated, and their contribution vanishes. Choosing an even higher cutoff for E_{max} should give better results in the real part for higher temperatures, but requires a larger number of sampled tunneling systems to maintain an appropriate tunneling system density. As we are rather interested in the resonant loss at low

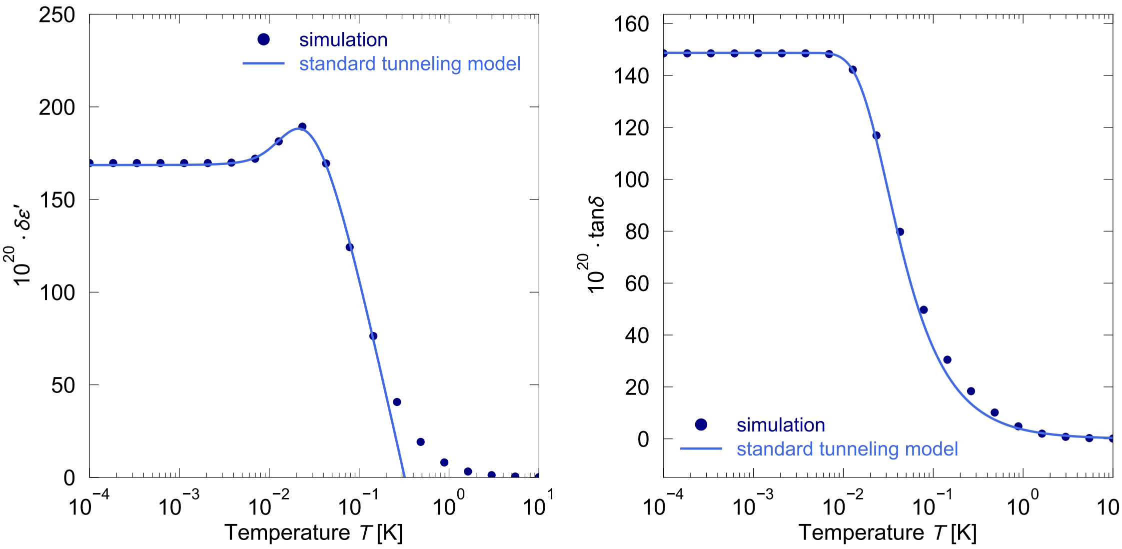

Figure 3.16: Simulation of the real (left) and imaginary part (right) of the dielectric function in equilibrium as a function of temperature. In total 30,000 tunneling systems were generated within a wide energy range of $\Delta_{0,\mathrm{min}}/h = 1.7\,\mathrm{MHz}$, $E_{\mathrm{max}}/h = 50\,\mathrm{MHz}$, applying a one-phonon relaxation process (2.68) with $K_1 = 5.2 \times 10^{78}\,\mathrm{J^{-3}s^{-1}}$. An excitation with field strength $0.1\,\mathrm{V\,m^{-1}}$ and frequency 10 MHz was used. The thermal population was boosted by the factor 100 to emulate the response of tunneling systems to an 1 GHz excitation. The simulation results are compared to Equations (2.86) and (2.87).

temperatures, we will not intensify this topic. We can summarize that the simulation successfully reproduces the expected behavior for these steady-state examples (field and temperature dependency), which underlines the proper operation of the presented Monte Carlo simulation. Already with quite a low number of generated systems, we obtain precise results.

3.3.5 Non-equilibrium loss

We continue with non-equilibrium phenomena and restrict the discussion to the resonant loss, which allows us to confine the distribution of tunneling systems to the resonant ones. We repeated the simulation of Figure 3.13 with an excitation of $F_{\mathrm{ac}} = 10\,\mathrm{V\,m^{-1}}$, $\omega_{\mathrm{ac}}/2\pi = 10\,\mathrm{MHz}$, and constant relaxation times $\tau_1 = 20\,\mathrm{\mu s}$, $\tau_2 = 2\tau_1$. In addition, we applied an electric bias field which is ramped from $0\,\mathrm{V\,m^{-1}}$ to $1\,\mathrm{kV\,m^{-1}}$ within $100\,\mathrm{\mu s}$. Since we use a constant value for the dipole moment of $p = 1\,\mathrm{Debye}$ and a fixed orientation $\cos\theta = 1$, all tunneling systems will be shifted equally in Δ. The maximum shift in Δ is calculated as $\delta\Delta_{\mathrm{max}}/h = 2pF_{\mathrm{b}}/h \approx 10\,\mathrm{MHz}$. Hence, tunneling systems must be generated within this energy range as they cross

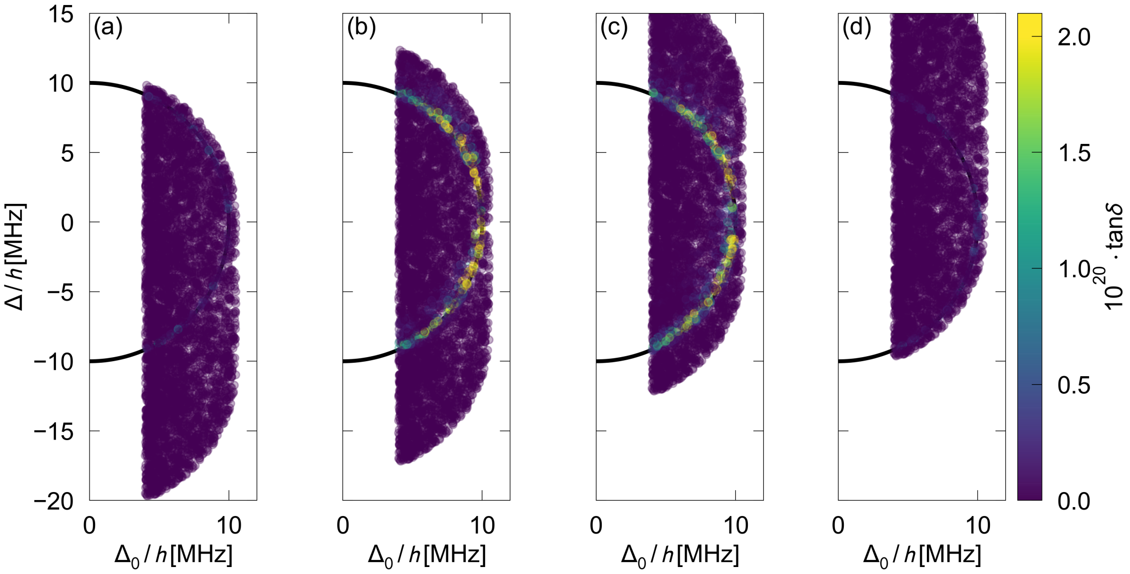

Figure 3.17: Monte Carlo simulation of the dielectric loss for an ensemble of 5000 tunneling systems at four different time steps in the presence of an additional ramped electric bias field: (a) t=5 µs, (b) t=50 µs, (c) t=100 µs, and (d) t=280 µs. Tunneling systems are generated within the relevant energy range with constant parameters $\tau_1 = 20\,\mathrm{\mu s}$, $\tau_2 = 2\tau_1$, $p = 1\,\mathrm{Debye}$, and the temperature was set to zero. The ensemble is driven by an electric field of $F_{\mathrm{ac}} = 10\,\mathrm{V\,m^{-1}}$ and $\omega_{\mathrm{ac}}/2\pi = 10\,\mathrm{MHz}$. The bias field is ramped from $0\,\mathrm{V\,m^{-1}}$ to $1\,\mathrm{kV\,m^{-1}}$ within $100\,\mathrm{\mu s}$, starting at $t = 25\,\mathrm{\mu s}$.

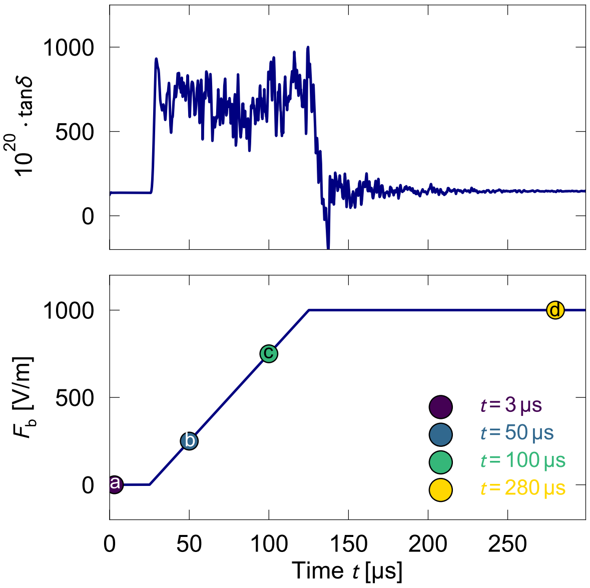

Figure 3.18: Evaluation of the sequence in Figure 3.17. The loss of the ensemble is plotted as a function of time, in the presence of ramped bias field. The time steps (a), (b), (c), and (d) from before are marked.

the resonance during the bias sweep. Figure 3.17 shows the loss of each tunneling system for such a simulation at four steps in time. At the first time step (a), prior to the bias sweep, the ensemble has already equilibrated into its steady-state. The resonant tunneling systems are heavily saturated by the driving field and cannot generate a high loss. When the bias ramp is applied (b) and (c), the asymmetry energy gets strongly modified. Saturated systems are constantly pushed out of resonance, and new sets of tunneling systems become resonant with the driving field. These systems were off-resonantly driven before, and hence, are initially in their ground state. As we have discussed before within the scope of Landau-Zener transitions, by crossing the resonance, they are able to absorb photons from the driving field, which leads to an increased loss, see Sections 2.4.6 and 3.2. This matches the findings shown in Figure 3.17, where the loss of resonant tunneling systems is significantly enhanced during the bias sweep. In (d) the ensemble is shown after the bias sweep when equilibrium is reached again. A different set of tunneling systems is now in resonance with the driving field, but generates the same loss as prior to the bias ramp because the distribution of tunneling systems is flat in Δ.

Figure 3.18 shows the evaluation of the whole sequence, where each time step from Figure 3.17 is marked. Prior to the shown time window, the time evolution of the ensemble was simulated for 300 μs, giving the systems enough time to equilibrate into their steady-state. This is why hardly any time dependence of the loss is found before the bias ramp starts. The result for $\tan\delta$ agrees with the previous explanations. During the bias ramp the ensemble is in non-equilibrium, and the loss is significantly enhanced compared to its equilibrium value before and after the ramp. The noise of the loss during the ramp maps the fluctuations of the sampled tunneling system ensemble, which can be reduced by choosing a larger number of generated

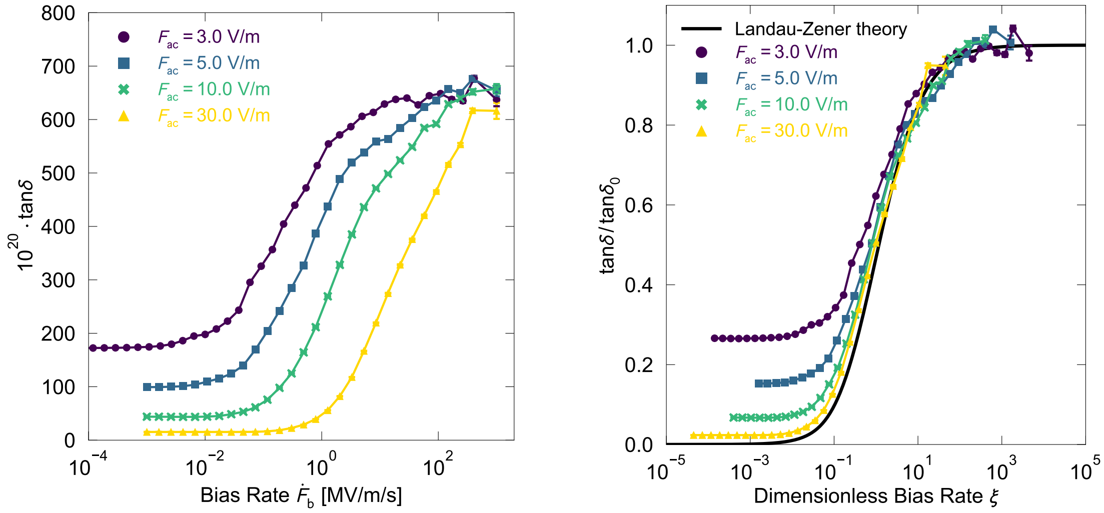

Figure 3.19: Non-equilibrium loss as a function of the applied bias rate $\dot{F}_\mathrm{b}$ (left) and as a function of the dimensionless bias rate ξ (right). The simulation of Figures 3.17 and 3.18 was repeated, with 15,000 generated tunneling systems, and relaxation times of $\tau_1 = 40\,\mu\mathrm{s}$, $\tau_2 = 2\tau_1$, with four different driving field strengths $F_\mathrm{ac} = [3\,\mathrm{V\,m^{-1}}; 5\,\mathrm{V\,m^{-1}}; 10\,\mathrm{V\,m^{-1}}; 30\,\mathrm{V\,m^{-1}}]$. The simulation data is compared to the results of the Landau-Zener theory (solid black line).

tunneling systems in the simulation. The same value of the equilibrium loss before and after the bias ramp reflects the flatness of the tunneling system distribution in Δ.

We can vary the ramp times and extract the non-equilibrium loss through a rapid bias sweep by averaging over the values of the loss during the ramp. Thereby, we obtain the non-equilibrium loss as a function of the bias rate, which is shown in Figure 3.19. We used the same confinements of the distribution as in Figure 3.17, but with 15,000 generated tunneling systems. The relaxation times were extended to $\tau_1 = 40\,\mu\mathrm{s}$, $\tau_2 = 2\tau_1$, and four different driving field strengths F_ac were used. We varied the ramp times over several orders of magnitude to obtain bias rates between $10^{-4}\,\mathrm{MV\,m^{-1}\,s^{-1}}$ and $10^{3}\,\mathrm{MV\,m^{-1}\,s^{-1}}$. All other parameters were chosen as in Figure 3.17. In the plot on the left-hand side, absolute values for the bias rate and loss were plotted. The overall behavior matches the expectations. For small bias rates we observe the equilibrium loss, which decreases with increasing driving field strengths due to saturation. At these rates, the bias sweep is too slow to induce any Landau-Zener transitions, and one observes the steady-state results. With increasing bias rates, the loss increases as well due to the Landau-Zener dynamics of tunneling systems and reaches for all curves the same plateau value at very high rates. The larger the driving field, the faster the bias field needs to be swept to observe an enhanced loss due to Landau-Zener transitions.

A more quantitative comparison with the Landau-Zener theory can be drawn by plotting the normalized loss as a function of the dimensionless bias rate ξ (right). In this case, the simulated loss becomes independent from the applied driving field strength for higher bias rates, where all curves collapse onto a single one. The results from the simulation can be compared to the non-equilibrium loss of tunneling systems predicted by the Landau-Zener theory. We make use of Equation (2.113), but adjust the integration limits to the actual simulation settings. We do not have to perform the integration over the dipole angle θ since it is fixed in the simulation. Moreover, the integration in $x = \frac{\Delta_0}{\hbar\omega_{\mathrm{ac}}}$ is performed between 0.4 and 1, according to the limits of Δ_0. With that, one obtains the black curve in the right plot, which agrees well with the simulation data for high rates ξ. Especially for small driving fields and slow bias rates the Landau-Zener theory fails, as it disregards any relaxations during the resonance crossing. If the relaxation time of tunneling systems becomes comparable to the time of a resonance passage, one expects deviations from the pure Landau-Zener solutions. This becomes in particular relevant for weak driving fields, where small rates are sufficient to induce Landau-Zener transitions. The simulation includes relaxation processes, and therefore provides an adequate description of the non-equilibrium loss over the whole scale of bias rates.

It is interesting to see that if we rescale the loss, by subtracting from each curve its value at small bias rates $\tan\delta_{\mathrm{min}}$ and normalize the loss by the factor $\tan\delta_0 - \tan\delta_{\mathrm{min}}$, we find an agreement with the Landau-Zener theory for all bias rates. This is shown in Figure 3.20, where all curves then entirely collapse onto the theory curve.

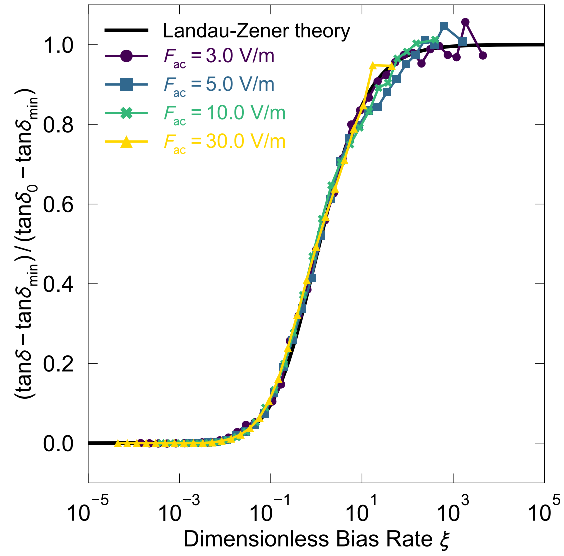

Figure 3.20: Rescaling the non-equilibrium loss by the minimum value as a function of the dimensionless bias rate. All curves then entirely collapse onto a single one.

3.3.6 Noise bias

Besides biasing tunneling systems with ramped fields, we will also be dealing with noise as bias signal in the experimental results chapter. In the following, we will therefore calculate the dielectric loss of the tunneling system ensemble in the presence of a fluctuating bias field. We continued the calculations of Figure 3.15 by applying uniformly distributed random values between $\pm 100\,\mathrm{V\,m^{-1}}$ as bias field after equilibrium was reached. A new value for the bias field is generated every 1 µs, and the points in between are linearly interpolated. This gives an upper limit for the bias rate of $\dot{F}_{\mathrm{b,up}} = 200\,\mathrm{MV\,m^{-1}\,s^{-1}}$. The noise bias field acts as a continuously changing bias rate, and Landau-Zener transitions permanently take place, which on average reduces the population of the upper level. Thus, the loss is enhanced during the noise bias, corresponding to the results of Figure 3.21 (left).

As before, we applied different driving field strengths and calculated the noise-enhanced loss as a function of the driving field strength, see the blue crosses in Figure 3.21 (right). The result is compared to the field strength dependency of Figure 3.15 (purple filled circles). It can be seen that the noise bias helps to prevent the tunneling systems from getting saturated by the driving field, as one can observe the low-power loss even at moderate field strengths. A second data set with reduced

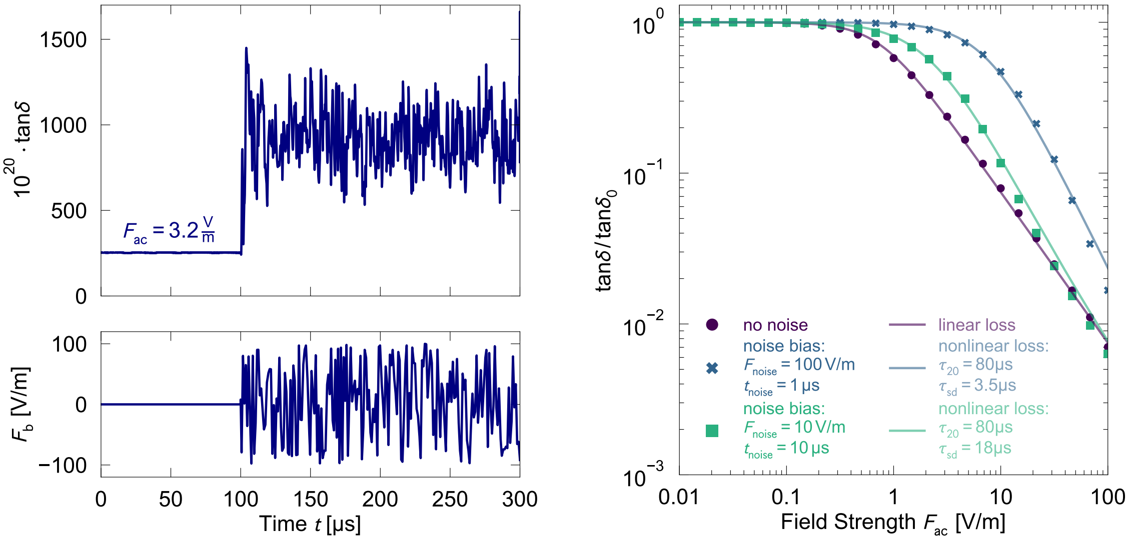

Figure 3.21: Repeating the simulations from Figure 3.15, but applying random noise as bias signal after equilibrium is reached. Left: Time evolution of the loss in the presence of a noise bias with a driving field strength of $F_{\mathrm{ac}} = 3.2\,\mathrm{V\,m^{-1}}$. All other parameters were chosen as in Figure 3.15. The non-equilibrium loss is obtained by averaging over the loss during the noise bias. Right: Loss as a function of the driving field strength with and without applied noise bias. The results with noise bias are compared to a theory of a nonlinear loss in the presence of a distinct spectral diffusion as described by Equation (2.95).

noise level was calculated. There, the bias field fluctuates between $\pm 10\,\mathrm{V\,m^{-1}}$, and new values were generated every $10\,\mathrm{\mu s}$ (green squares). The effect of the noise bias is then reduced, as the plateau at low field strengths cannot be sustained at such high field strengths. For very high field strengths the loss converges back towards the loss without any bias fields. In this regime, the bias rate is too small compared to the rate of excitation, and the probability for Landau-Zener transitions is low, leading to the steady-state results.

The simulation curves are compared to the results of the nonlinear loss in the presence of a distinct spectral diffusion as described by Equation (2.95). Spectral diffusion has a similar effect on tunneling systems as the noise bias has. Both give rise to fluctuations of the tunneling systems' energy splitting, leading to different sets of systems in resonance with the driving field over time. It is therefore reasonable to compare these two cases with each other, despite their different origin and underlying statistics. As Figure 3.21 (right) shows, it is indeed possible to describe the simulated noise bias curve to some extent with the nonlinear loss theory due to spectral diffusion. Defined by the simulation, we used the relaxation time $\tau_{20} = 2\tau_1 = 80\,\mathrm{\mu s}$ and fitted the parameter τ_{sd} such that we find a good agreement between theory and simulation. Besides very high field strengths, the nonlinear loss describes the simulation results even quantitatively well. The spectral diffusion relaxation time τ_{sd} is misused here as a parameter that determines the noise level. Or vice versa, the noise bias can be interpreted as artificial spectral diffusion.

3.3.7 Pump tone probe tone experiments

In equilibrium, the population difference $n_{|\mathrm{g}\rangle} - n_{|\mathrm{e}\rangle}$ of a tunneling systems cannot be smaller than zero. However, in non-equilibrium the Landau-Zener theory allows a population inversion of the tunneling systems under certain circumstances, which we have already seen in Figures 3.8 and 3.9. Due to interactions with the environment, a population inverted tunneling system will always relax back towards its ground state after some time. The population inversion can be revealed by applying an additional high frequency electric field (pump tone), which is slightly detuned from the original driving field (probe tone), see Figure 3.22 (d). The same way as before, a ramped bias field shifts the tunneling system in its asymmetry energy. An initial strongly off-resonant system will first reach resonance with the pump tone. Through an appropriate choice of the pumping field strength and bias rate a Landau-Zener transition may be avoided, and one achieves an adiabatic passage. After passing the pump tone adiabatically the tunneling system should be in the excited state with a high probability, and hence is inverted. The ramped bias field shifts the tunneling system's energy further, such that it becomes resonant with the probe tone after some period of time. If the time between crossing the pump tone and reaching the probe tone is short compared to the relaxation time the tunneling system should still be in the excited state. The probe tone now sees an excited system, instead of a system in the ground state that we discussed in the previous cases above. This results in a stimulated emission process, where a coherent photon with the probe tone frequency is emitted. If one regards the loss at this frequency, one will observe a negative value of the loss, since the driving field is amplified by the emitted photon. There exists an energy transfer from the pump to the probe tone mediated by the tunneling system. In [Bur14a, Ros16], it was stated that such a sequence indeed leads to population inverted tunneling systems, which was observed by means of an appearing negative resonant loss. From an experimental point of view, we will address this topic in Section 5.4.3.

In the following, we want to look at its realization within the introduced simulation framework. For the sake of convenience, we start by considering a single tunneling system. The system is initially detuned towards higher energies from the probe tone at $\omega_{\mathrm{probe}} = 2\pi \cdot 10\,\mathrm{MHz}$ and field strength $F_{\mathrm{probe}} = 20\,\mathrm{V\,m^{-1}}$. An additional high frequency electric field is applied at $\omega_{\mathrm{pump}} = 2\pi \cdot 12\,\mathrm{MHz}$ with $F_{\mathrm{pump}} = 100\,\mathrm{V\,m^{-1}}$. In total we then have the driving field $F_{\mathrm{ac}}(t) = F_{\mathrm{probe}}\cos(\omega_{\mathrm{probe}}t) + F_{\mathrm{pump}}\cos(\omega_{\mathrm{pump}}t)$, which is used in the simulation as excitation. The bias field is ramped within a ramp time t_{b} from $0\,\mathrm{V\,m^{-1}}$ to a negative value $-1\,\mathrm{kV\,m^{-1}}$ since the asymmetry energy $\varDelta$ needs to be shifted towards smaller energies in order to cross both tones. Relaxation times of $\tau_1 = 80\,\mathrm{\mu s}$ and $\tau_2 = 2\tau_1$ were used. All other parameters were chosen as in Figure 3.9.

Figure 3.22 (a)-(c) shows the time evolution of ρ_{ee} and $\tan\delta$ for this scenario with three different ramp times. The points in time when the tunneling system is in resonance with the pump or probe tone are marked by the gray areas. At the fastest bias ramp (a), the used pump tone field strength is too weak to achieve a full excitation. For these parameters the probability for a Landau-Zener transition is enhanced, and the pumping is then not as efficient as for a fully adiabatic transition at slower ramps. At the slowest bias rate (c), the level of excitation is reduced because relaxations during the resonance passage become more relevant, which reduces ρ_{ee}. The pump tone excitation leads to a polarization oscillating at the pump tone frequency, but we observe the response at the frequency of the probe tone. Hence, no significant contribution to the loss is observed for this first resonance crossing. Note that we band pass filtered the polarization here at the probe tone frequency. Otherwise, mixing between pump and probe tone frequency leads to interference and results in parasitic oscillations. Filtering is also done in experiment, where typically a resonator is used for probing the sample. The resonator then acts as band pass filter and filters off-resonant carrier frequencies from the sample's polarization. In the simulation the band pass filter cannot be made arbitrarily narrow since this would heavily slow down the response time, which is why there remains a small response apart from the

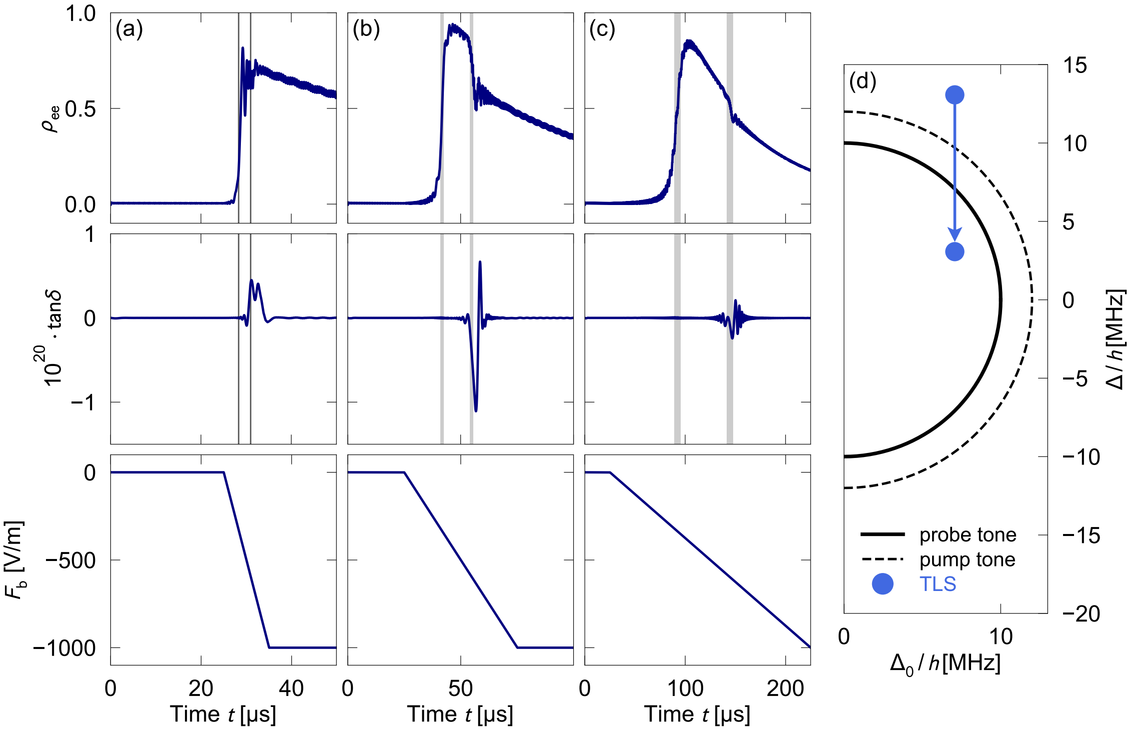

Figure 3.22: Numerical calculations of the time evolution of ρ_{ee} and $\tan\delta$ for different bias ramp times (a)-(c). Besides the probe tone at 10 MHz with field strength $20\,\mathrm{V\,m^{-1}}$, an additional pump tone is applied at 12 MHz and $100\,\mathrm{V\,m^{-1}}$. Relaxation times of $\tau_1 = 80\,\mu\mathrm{s}$ and $\tau_2 = 2\tau_1$ were used, and the temperature was set to zero. The tunneling system is initially detuned and is shifted by the bias field across the two tones (d). The points in time when the tunneling system crosses pump or probe tone are marked by the gray areas.

probe tone frequency. Here, we used a Butterworth filter of order 3 with the cutoffs $f_{\mathrm{c,l}} = 9.7\,\mathrm{MHz}$ and $f_{\mathrm{c,h}} = 10.3\,\mathrm{MHz}$.

After crossing the pump tone, at some point the tunneling system reaches the probe tone. In the case of a fast bias sweep, the time for this transit is small, and hardly any relaxation into the ground state takes place. On the other hand, slow ramping leads to a considerable reduction of ρ_{ee} during the transit due to relaxation. For an even slower bias ramp than in (c), one can easily imagine that the erstwhile population inversion has completely vanished before the tunneling system reaches the probe tone energy, and no stimulated emission process is then possible. A very fast bias ramp can be counterproductive as well. The intensity of the probe tone is typically smaller than the one of the pump tone. The probability for a Landau-Zener transition at the probe tone is therefore higher. Indeed, in (a) one does not observe a change in ρ_{ee} during the second resonance crossing, indicating that a Landau-Zener transition takes place. As no photon is emitted, one cannot observe a negative loss in this case. Only in between these limits, at medium bias rates, the probe tone can effectively induce a stimulated emission process, and the loss measured at this frequency becomes distinctly negative when the tunneling system crosses the probe tone (b).

We can transfer these insights to the tunneling system ensemble. In Figure 3.23 we repeated the simulation of the bias rate dependency with $F_{\text{probe}} = 10\,\mathrm{V\,m^{-1}}$ from Figure 3.19, but included two pump tones detuned by $\delta = \pm 1\,\mathrm{MHz}$ from the probe tone at 10 MHz. The pump tone field strengths were varied between $1\,\mathrm{V\,m^{-1}}$ and $100\,\mathrm{V\,m^{-1}}$. On the left side, the time evolution for a medium fast bias ramp is shown with pump tone intensities of $F_{\text{pump}} = 100\,\mathrm{V\,m^{-1}}$. Analogously to Figure 3.18, the ensemble is initially in equilibrium. When the bias ramp starts at 25 µs, the loss heavily increases at first. This is caused by the systems that initially have energies that sit between pump tone and probe tones. These systems will get into resonance with the probe tone first and have not crossed any pump tones yet. Thus, these systems cause an initial rise in the loss due to the discussed Landau-Zener transitions. As the ramp continues, more tunneling systems reach the probe tone that have already crossed the pump tones and might be inverted. The loss drops and eventually becomes negative. For the second half of the bias sweep, the loss is solely generated by pumped tunneling systems and stabilizes at a constant negative value. Inverted tunneling systems continuously cross the probe tone, and stimulated emission takes

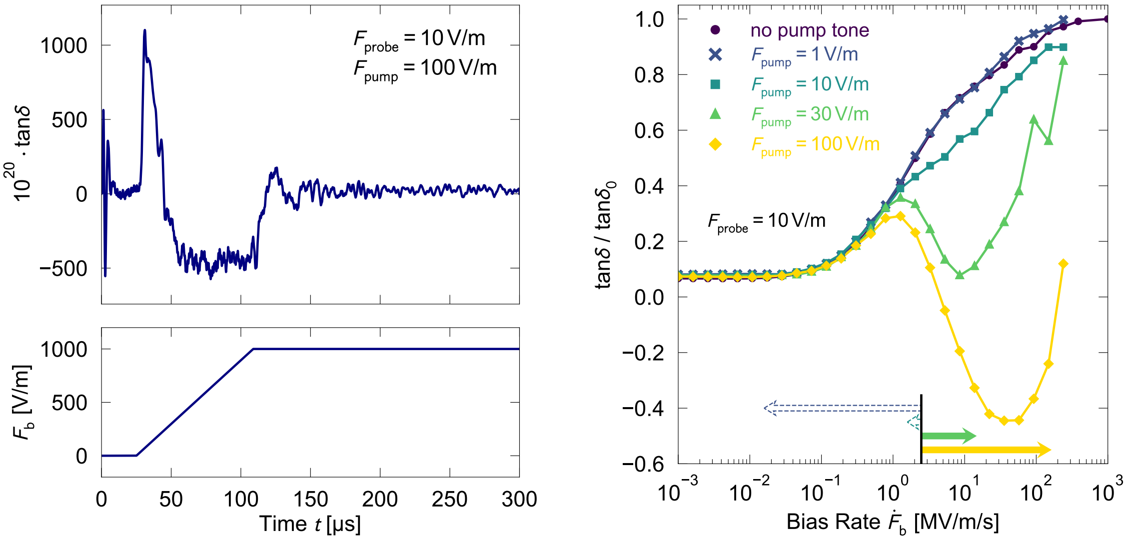

Figure 3.23: Repeating the simulation of the bias rate dependency from Figure 3.19 with a probe tone at 10 MHz and field strength $10\,\mathrm{V\,m^{-1}}$. Two additional pump tones, detuned by ±1 MHz from the probe tone, were used. Left: Time evolution of the loss for a medium bias rate and a strong pump tone. Right: The loss during the second half of the bias ramp is averaged and plotted as a function of the corresponding bias rate for different pump tone intensities. The solid arrows mark the bias rates where a negative loss through tunneling systems performing stimulated emission is expected.

place until the bias ramp stops. We averaged the loss over the second half of the bias sweep and plotted this value as a function of the corresponding bias rate for different pump tone field strengths in Figure 3.23 (right).

We can directly see that the effect of stimulated emission becomes more prominent for higher pump tone intensities. For a weak pump tone $F_{\mathrm{pump}} = 1\,\mathrm{V\,m^{-1}}$, the loss is identical to the non-equilibrium loss without any pump tones. By increasing the pump tone field strength, the loss starts to decrease and becomes negative for strong pumping. This reduction only takes place within certain bias rate limits which we can identify by the conditions we have previously discussed for a single tunneling system. Towards upper bias rates, the probability for population inversion through pumping is limited due to Landau-Zener transitions. Only for an adiabatic resonance crossing at the pump tone frequency, tunneling systems are inverted, which gives the condition $\nu_0 \lesssim \Omega^2_{\mathrm{R0,pump}}$ obtained from Equation (2.104). This can be written as an upper limit for the bias rate, i.e. $\dot{F}_{\mathrm{b}} \lesssim \frac{pF^2_{\mathrm{pump}}}{2\hbar}$. In order to still have inverted tunneling systems at the probe tone frequency, the time interval between pumping and probing must be smaller than the relaxation time. Thus, we can write $\nu_0\tau_1 \gtrsim \delta$, with the detuning δ between pump and probe tone frequency being $\delta = |\omega_{\mathrm{pump}} - \omega_{\mathrm{probe}}|$. We can write this as a lower limit for the stimulated emission $\dot{F}_{\mathrm{b}} \gtrsim \frac{\hbar\delta}{2p\tau_1}$. For the simulation parameters used here, the black vertical line in Figure 3.23 (right) tags this lower limit for the bias rate. Only for the two highest pump tone intensities, this limit lies below the upper limit, which gives rise to a dip in the loss. The region between the two limits is marked by the arrows, which roughly agrees with the occurrence of a negative loss. The dotted arrows indicate that the upper limit for the bias rate lies below the lower one, and hence, no stimulated emission is possible, in agreement with the discussion in [Bur14a].

Solving the dynamics of each tunneling system numerically at its elementary level gives great variability and allows to adopt the simulation directly to various scenarios, where an analytic description of the tunneling system dynamics might be limited or not possible.

4. Experimental Methods

In this chapter detailed information about the experimental methods used within this thesis is given. The chapter starts with a brief introduction about performing measurements at a few millikelvin. We then specify in Section 4.3 on the utilized radio frequency setup for measuring the dielectric response of the glass sample between 250 MHz and 1 GHz at low input powers. Section 4.4 presents the developed superconducting bridge-type resonators that are used for the investigation of tunneling systems performing Landau-Zener transitions in bulk glasses. The measurement principle and the elaborated protocols for the Landau-Zener spectroscopy are explained in Section 4.5. The chapter ends with more specific resonator details that are of importance for the analysis of the experimental results.

4.1 Measurements at very low temperatures

The main part of this thesis deals with tunneling systems that are thermally in their ground state and interact resonantly with the applied electric driving field. Tunneling systems in resonance with an excitation at 1 GHz have a thermal population difference of $\Delta n = \tanh(h \cdot 1\,\mathrm{GHz}/2k_\mathrm{B}T) = 0.24$ at $T = 100\,\mathrm{mK}$ and $\Delta n = 0.98$ at $T = 10\,\mathrm{mK}$. Therefore, temperatures down to a few millikelvin are needed to realize the required experimental conditions. We use a commercial ^{3}He/^{4}He dilution refrigerator Oxford Kelvinox 400[1] with which we were able to perform measurements at stabilized temperatures between 10 mK and 8 K.

Here, we restrict to the basic operating principle of a ^{3}He/^{4}He dilution refrigerator and refer to specialized literature for further reading [Ens05, Pob07, Fro92]. The operation principle is based on a continuous phase transition of the helium isotope ^{3}He from a ^{3}He-rich into a ^{3}He-poor phase whereby heat is taken from the environment. When a mixture of the two helium isotopes ^{3}He and ^{4}He is cooled down below $\approx 800\,\mathrm{mK}$ the liquid mixture separates into two phases: an almost pure ^{3}He phase and a mixed phase where ^{3}He is diluted in ^{4}He. At normal pressure and $T \rightarrow 0\,\mathrm{K}$ about 6.5 % of the ^{3}He is diluted in ^{4}He. Because of its higher mass, ^{4}He possesses a smaller zero-point energy compared to ^{3}He. With that, ^{3}He is more strongly bound to ^{4}He and dilutes into it. Since ^{3}He obeys the Fermi-Dirac statistics, the more ^{3}He is bound to the ^{4}He the higher its energy becomes, which limits the solubility of ^{3}He in ^{4}He. Above a certain concentration the formation of a second phase of almost pure ^{3}He is energetically more favorable. At these temperatures ^{4}He is superfluid

---

[1] Oxford Instruments, Tubney Woods, Abingdon, UK OX13 5QX

and acts as a quasivacuum for the diluted ^{3}He. A transition of ^{3}He from the ^{3}He-rich into the poor phase corresponds to an evaporation process, and energy is taken from the environment. The cooling power for this process is found to be $\dot{Q} = 84\dot{n}_3T^2$ [Pob07], where $\dot{n}_3$ describes the number of ^{3}He performing a transition between the two phases per unit time.

Figure 4.1 shows a schematic drawing of a typical ^{3}He/^{4}He dilution unit which allows to run the phase transition continuously. In the so-called mixing chamber, the coldest part of the cryostat, due to the phase separation the lighter ^{3}He-rich phase

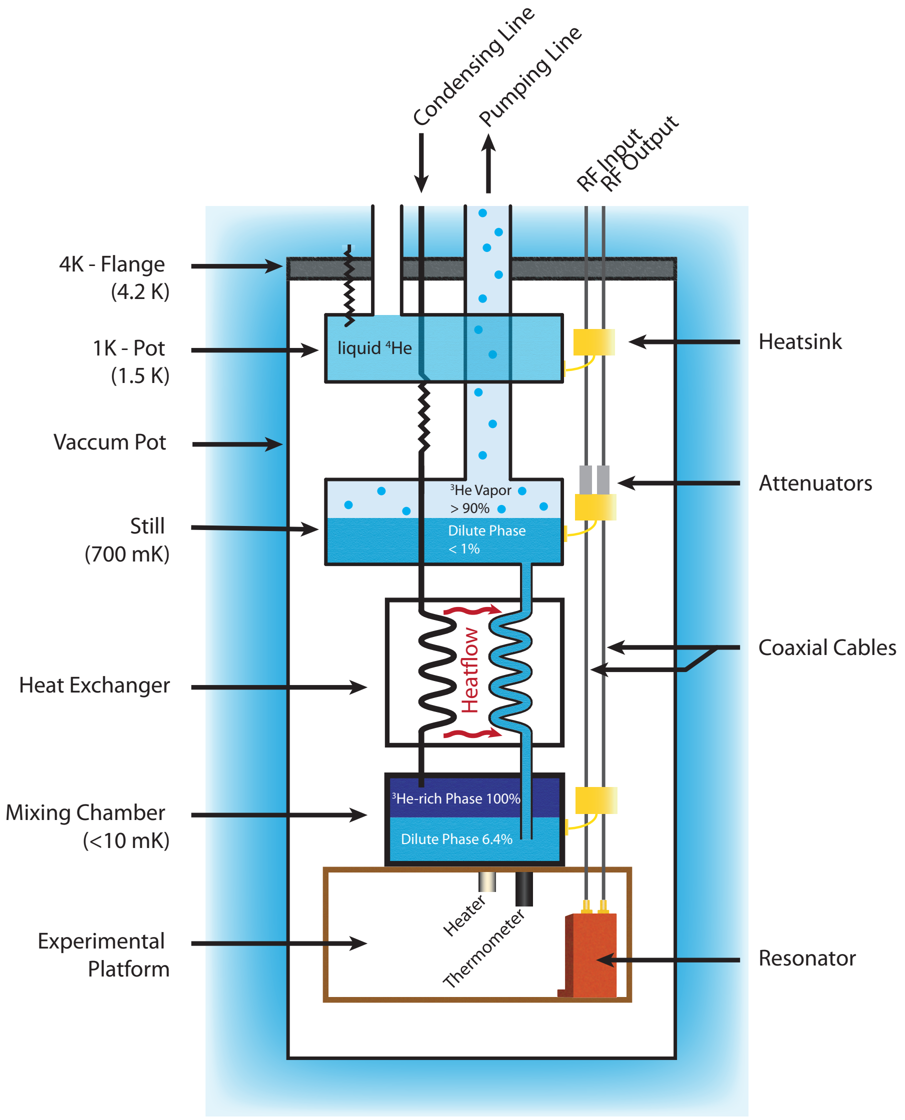

Figure 4.1: Schematic drawing of a ^{3}He/^{4}He dilution refrigerator. The shown dilution unit is placed inside a vacuum pot, which is located inside a bath of liquid ^{4}He. The experiments are placed on the experimental platform at the bottom of the cryostat. Adapted from [Pob07].

swims on top of the diluted ^{3}He-poor phase. The ^{3}He-poor phase is connected to the still which is heated to approximately 700 mK. Due to the ^{3}He's lower boiling temperature, mainly ^{3}He evaporates and is pumped out by a following pumping system. Hence, the ^{3}He concentration in the still is considerably reduced, and a gradient in concentration between still and mixing chamber forms. This results in an osmotic pressure, which causes a flow of ^{3}He from the mixing chamber into the still and drives the phase transition of ^{3}He in the mixing chamber. Collecting and feeding the pumped ^{3}He from the still back into the mixing chamber closes the circulation, and one achieves a continuously operating cooling process.

As illustrated in Figure 4.1 the dilution unit is placed inside an evacuated niobium-shielded metal vessel (vacuum pot) immersed in a bath of liquid ^{4}He. Before the ^{3}He is fed back into the cryostat, the gas runs through cold traps, where it gets cleaned. The gas is then precooled by the surrounding ^{4}He bath to 4.2 K before it enters the vacuum pot, where a second ^{4}He bath (1K-pot) at 1.5 K condenses the incoming ^{3}He gas. The 1K-pot is filled through a capillary from the ^{4}He bath. Pumping the liquid ^{4}He lowers its temperature to about 1.5 K. After passing flow impedances, the still, and heat exchangers the ^{3}He enters the mixing chamber at approximately 10 mK.

Thermally well attached to the mixing chamber, the experimental platform out of copper[2] allows to mount the experiments on it. Moreover, with an attached heater it is possible to regulate the cryostat's temperature above its base temperature. A stable operation of the cryostat with the entire ^{3}He/^{4}He-mixture is possible up to 850 mK. For measurements above this temperature, the cryostat is operated with a fraction of the mixture. We use a carbon resistor thermometer across the entire temperature range, which was calibrated with a noise thermometer. The calibration of the noise thermometer itself was done via a fixed point thermometer that is based on the critical temperature of several superconductors [Rei17]. The temperature-dependent resistance of the carbon resistor is readout through an AC resistance bridge[3], which allows a precise determination of the resistance while using small excitation voltages in order to avoid parasitic heating through the readout. In addition, the resistance bridge provides a control loop. The PID feedback-control gives a stabilization of the temperature of typically less than 0.5 % at the lowest temperatures.

For driving and reading out the resonator's response coaxial cables connect the resonator with the readout electronics at room temperature. In order to reduce the heat load coming from the cables, several heat sinks attached to different temperature stages of the cryostat are used. The type of heat sink used here is shown in Figure 4.2. The coaxial cables are connected to the SMA connectors, whose inner conductors are bonded to a niobium stripline on a sapphire substrate. The dimension

---

[2] Tempered oxygen-free copper, in order to avoid impurities, especially hydrogen, and achieve a high thermal conductivity and low heat load.

[3] LR-700, Linear Research Inc., 5231 Cushman Place, Suite 21, San Diego, CA 92110-3910, USA

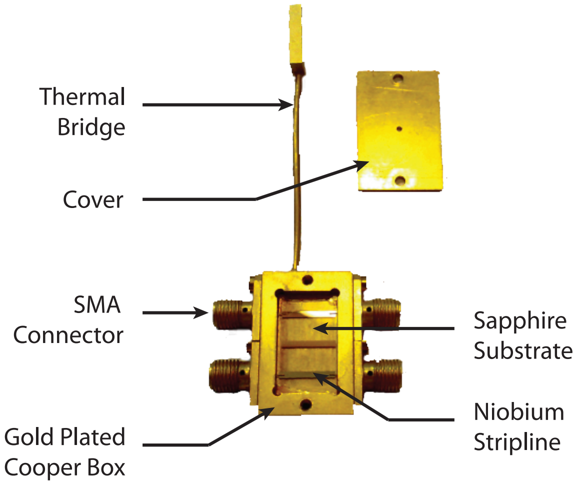

Figure 4.2: Picture of a heat sink for coaxial cables.

of the stripline is chosen to match the 50 Ω impedance of the cable. Because of the good thermal conductivity of sapphire, the inner conductor of the coaxial cable is thermally connected to the gold plated copper box. Through a thermal bridge the heat sink is attached to the cryostat and absorbs the heat coming from the cables.

4.2 Sample

The sample that is used in this thesis is the borosilicate glass N-BK7 from Schott AG[4]. It has a glass transformation temperature of $T_\mathrm{g} = 557\,^\circ\mathrm{C}$, the density $\rho = 2.51\,\mathrm{g\,cm^{-3}}$, and a thermal expansion coefficient of $\alpha = 7.1 \times 10^{-6}\,\mathrm{K^{-1}}$ [Sch14]. The relative permittivity is found to be $\varepsilon_\mathrm{r} = 5.8$ [Fre16] and the sound velocities are $v_\mathrm{l} = 6000\,\mathrm{m\,s^{-1}}$, $v_\mathrm{t} = 3800\,\mathrm{m\,s^{-1}}$ [Hun76]. The main application of this glass is in high quality optical devices for visible light. However, it is also extensively used for investigations of atomic tunneling systems in glasses, e.g. in acoustic measurements [Hun74, Arn75, Nat98] or polarization echoes [Lud03, Bur13]. But also dielectric measurements over a wide frequency range are available [vS75, Ant79, Bec90, Woh01, Fre16]. Because of its good availability, a straightforward processing, and the comparability with previous measurements, the sample is well-suited for a characterization of new devices in general, and therefore for the development of a setup demonstrating the Landau-Zener spectroscopy of bulk glasses.

Table 4.1 shows the chemical composition of N-BK7. The main constituent is SiO_2, which should build the network backbone. Besides the second network former B_2O_3, the other main constituents are the two network modifiers Na_2O and K_2O. The formation of such a multicomponent glass is very complex, and we can only give a rough idea about its microscopic structure as it was sketched in Section 2.1. In

---

[4] Schott AG, Hattenbergstraße 10, 55122 Mainz, Germany

SiO_2	B_2O_3	Al_2O_3	Na_2O	K_2O	BaO
74.8 %	9.6 %	0.03 %	10.1 %	4.7 %	0.74 %

Table 4.1: Chemical composition of the glass N-BK7 in molar percentage [Lud03].

contrast to SiO_2, in pure borate glasses the addition of network modifiers does not weaken the network initially, but leads to strengthening, which is observed up to a content of around 16 % of modifiers. A further increase then weakens the network. This phenomenon is known as the boron anomaly [Vog92]. X-ray diffraction analysis revealed that the addition of Na_2O leads to a modified coordination of boron and oxygen atoms from a triangular into a tetrahedral network [Bis38], which strengthens the network through the higher coordination number. The occurrence of the boron anomaly in borosilicate glasses is known to have a determine influence on their properties like their small thermal expansion [Vog92].

4.3 Radio frequency measurement setup

While measurements of the dielectric function with excitation frequencies up to a few kilohertz are typically performed by directly measuring a capacitor with a capacitance bridge [Rog97, Luc14], for measurements of the dielectric response at higher frequencies LC-resonators are used. As it will be discussed in Section 4.4 the resonance curve of such a resonator allows to extract the dielectric function of the sample, which is used as dielectric material in the capacitor. The utilized resonators possess resonance frequencies between 250 MHz and 1 GHz, see Section 4.4.2. At these frequencies and very low temperatures resonant tunneling systems are thermally mainly in their ground state $k_\mathrm{B}T \sim \hbar\omega$, and we can observe their resonant absorption of photons, provided that the intensity of the driving field is not too high and causes saturated tunneling systems. In order to fulfill these conditions, we need a sensitive setup with the ability to measure resonance curves at high frequencies and low temperatures at very low driving powers. Figure 4.3 shows the schematic of the used radio frequency (rf) measurement setup. The rf-branch is marked in blue, while the optional branch for biasing the resonator with strong electric fields is red-tagged. A vector network analyzer[5] (VNA) connected to a PC generates the rf-signal and detects the transmitted signal's amplitude and phase coming from the device under test. By comparing the generated test signal (port 1) with the response (port 2), the VNA provides the complex-valued scattering parameters S_{11} or S_{21}. The VNA spans a frequency range from 300 kHz to 1.3 GHz and supplies rf-powers between

---

[5] HP 8752C, Hewlett-Packard Company, 3000 Hanover Street, Palo Alto, CA 94304-1185 USA

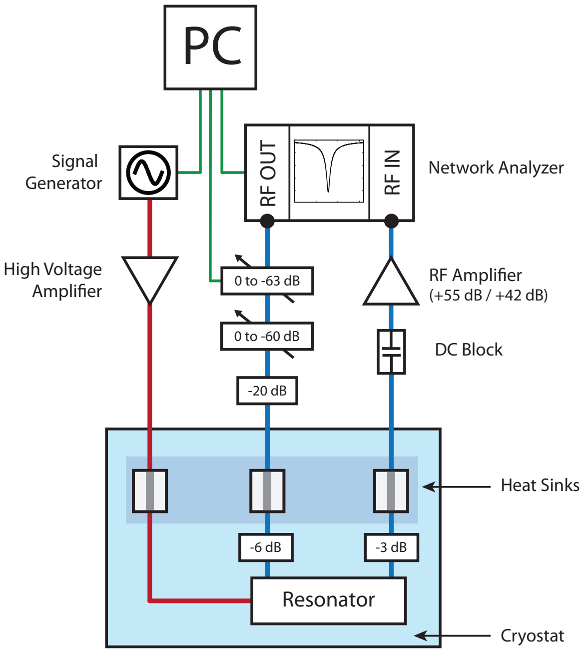

Figure 4.3: Schematic drawing of the electronic setup used in this thesis. The path marked in blue represents the radio frequency readout branch and the one in red the optional biasing branch. All components within the blue box are placed inside the cryostat, while all other parts are located at room temperature. The green lines represent connections to a computer, which allows an automated data acquisition.

5 dBm and −20 dBm. Several attenuators outside and inside the cryostat guarantee measurements at very low input powers and reduce standing waves alongside the cables from possible impedance mismatches. The two attenuators inside the cryostat are located close to the mixing chamber, and therefore reduce the incoming room temperature thermal noise. There are two step attenuators which allow to adjust the demanded excitation power over a wide range. The second step attenuator[6] allows a signal damping from 0 dB to 60 dB in steps of 10 dB. We typically set this attenuator to a fixed value at the beginning of a measurement series and use the first step attenuator[7] to vary the input power. This programmable attenuator is controlled through a microcontroller[8], which is connected to a computer. The programmable attenuator switches up to six single attenuator elements (1 dB, 2 dB, 4 dB, 8 dB, 16 dB, 32 dB) on in addition and is therefore able to regulate the attenuation between 0 dB and 63 dB with 1 dB increment. The attenuator was characterized at all possible attenuations. In Figure 4.4 (left) the data for each attenuation element and as well the pass-through is shown. At low frequencies, the attenuator matches its specifications. For higher frequencies, however, the attenuation is markedly increased, which needs to be considered when calculating the power at the resonator input. As mentioned before, we use several heatsinks within the signal path to provide thermalization of the coaxial cables. Inside the cryostat we mainly use semi-rigid coaxial cables. Only for the part from the last heatsink to the resonator flexible miniature coax-

---

[6] Step Attenuator AE116-60-01-0N, Weinschel, 5305 Spectrum Drive Frederick , MD 21703 USA

[7] Model 50P-1207 Serial 287346, JFW Industries INC, 84 Iron St, Johnstown, PA 15906, USA

[8] Arduino Pro Mini 328 - 5V/16MHz

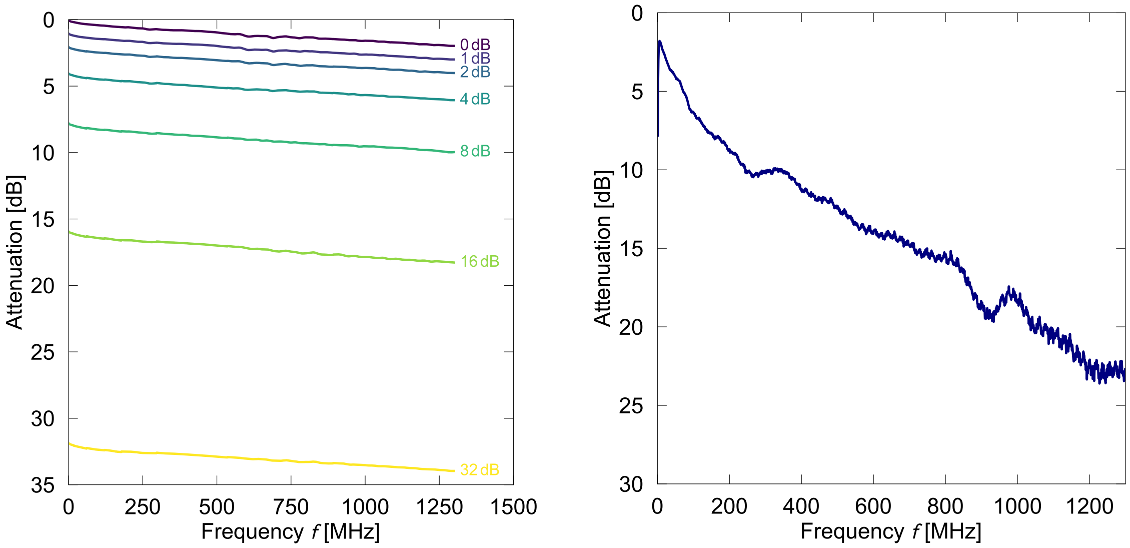

Figure 4.4: Left: Measured attenuation of the programmable attenuator for each individual attenuation element. Right: Attenuation originating from the cable route. Contributions from the attenuators were subtracted.

ial cables were utilized, which have a slightly increased attenuation per meter. We measured the transmission feeding through the resonator without rf-amplifier and subtracted the contributions from the attenuators in order to extract the damping of the cables. The measurements were performed with the 250 MHz-resonator by measuring the transmission through its 50 Ω matched feedline (see Section 4.4.2), while the resonator was cooled down to 12 mK. The result is shown in Figure 4.4 (right). As expected, the attenuation increases with increasing frequency. Presumably, impedance mismatches result in the wobblings, which need to be regarded as non-constant background when we evaluate the resonance curves. We can assume a symmetric cable route for in- and output, and with that, we obtain a cable attenuation for the input line of 5 dB at 250 MHz and 9 dB at 1 GHz.

The output signal from the resonator is typically very small and needs to be amplified before entering the VNA input. For this purpose, we use low-noise room temperature rf-amplifiers. In front of the amplifier a DC block[9] prevents DC and low frequencies currents entering the cryostat or the amplifier, respectively. Depending on the resonance frequency of the resonator, we chose different amplifiers. For frequencies below 500 MHz an amplifier with 55 dB gain[10], and for higher frequencies one with 42 dB gain[11] was used. The measured amplification of both amplifiers as function of

---

[9] Crystek CBLK-300-3, Crystek Corporation, 12730 Commonwealth Drive Fort Myers, Florida 33913, USA

[10] MITEQ AU-4A-0150, L3Harris Narda-MITEQ, 435 Moreland Rd Hauppauge, NY 11788 USA

[11] AFS3-00100200-15-ULN, L3Harris Narda-MITEQ, 435 Moreland Rd Hauppauge, NY 11788 USA

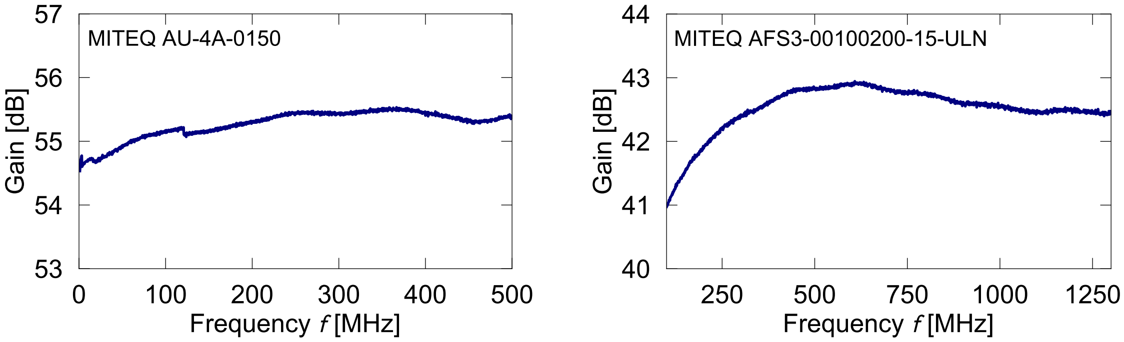

Figure 4.5: Measured gain of the used amplifiers within the specified frequency range. Data from [Fre16].

frequency within the specified frequency range is shown in Figure 4.5. The gain factor is almost constant across the whole frequency range for both amplifiers. Possible non-constant contributions will occur as background in the resonance curves.

The bias signal is generated with a signal generator[12] and amplified with a high-speed power operational amplifier[13]. The amplifier has a high slew rate and is implemented to have a gain of 30 V/V. A step from $0 - 180\,\mathrm{V}$ is performed within 7 µs, which allows to achieve the high bias rates required for the Landau-Zener dynamics.

All programmable components of the setup are connected via GPIB to a PC. A developed LabVIEW[14] program adjusts the parameters of the rf-setup and the temperature of the cryostat. It furthermore reads out the VNA data and enables a fully automated data acquisition.

4.4 Microfabricated superconducting bridge resonators

As it was already mentioned, in the thesis at hand LC-resonators are used to detect the dielectric response of the sample at frequencies between 250 MHz and 1 GHz. Besides the high-frequency driving field, the Landau-Zener dynamics requires a strong perturbing bias field which causes a distinct modification of the tunneling systems' asymmetry energy. In order to apply an additional electric bias field that does not couple into the rf-readout the capacitors of the resonator are arranged in a Wheatstone bridge-type manner. The schematic of such a bridge resonator is shown in Figure 4.6 (left). Four identical capacitors with capacitance C are arranged in a bridge scheme, whereby the sample is used as dielectric material inside of each capacitor. The total capacitance of this arrangement then reads C as well. Together

---

[12] DS340, Stanford Research Systems, 1290-D Reamwood Ave. Sunnyvale, CA 94089, USA

[13] PA15FL, Apex Microtechnology, 5980 N Shannon Rd, Tucson, AZ 85741, USA

[14] LabVIEW 8.5, National Instruments Corporation, 11500 Mopac Expwy, Austin, TX 78759-3504, USA

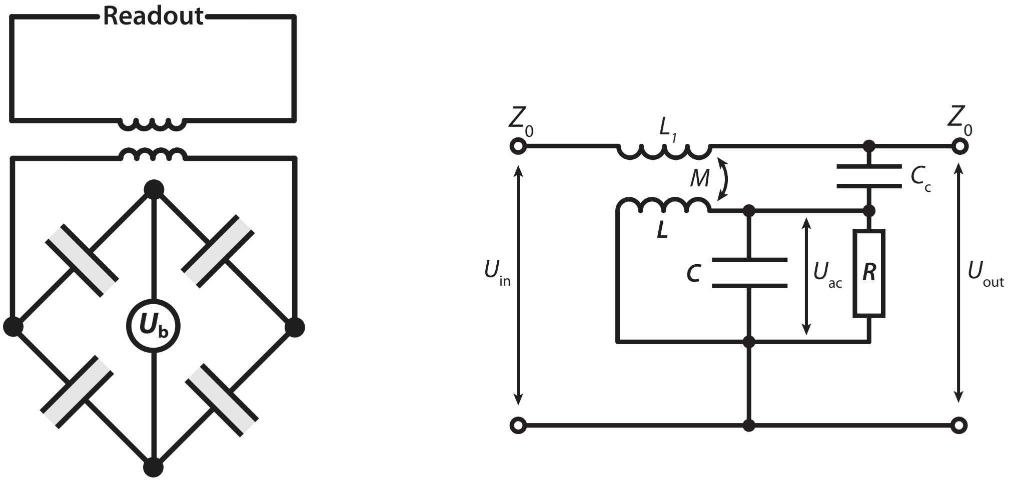

Figure 4.6: Left: Schematic of the LC bridge resonator circuit. Across one diagonal of the bridge the rf-signal is applied and independently from it, over the other diagonal, the bias signal. The resonator is inductively coupled to the readout. The sample is used as dielectric material inside of each capacitor. Right: Circuit diagram of an equivalent parallel RLC-circuit, which is inductively coupled through the coupling parameter M and capacitively coupled through the coupling capacitance C_c to the feedline with impedance $Z_0 = 50\,\Omega$.

with the inductance L parallel to the capacitance this forms an LC-circuit. The circuit is inductively coupled to the readout electronics, and with that, the driving voltage is applied over the horizontal diagonal in Figure 4.6 (left). Across the vertical diagonal the bias signal applied. The voltage drop at a single capacitor corresponds to half of the voltage across the diagonal. Therefore, for the case of plate capacitors with uniform gap d, each sample sees the electric field $F_\mathrm{tot} = \frac{1}{2}(U_\mathrm{ac}/d + U_\mathrm{b}/d)$. The symmetry of the bridge setup prevents a coupling of the bias voltage into the readout branch and vice versa. Hence, this allows to apply an electric driving field and an electric bias field independently from each other to the sample.

An LC-circuit with capacitance C and inductance L shows a resonant behavior at the resonance frequency

$$f_0 = \frac{1}{2\pi\sqrt{LC}} \quad . \tag{4.1}$$

The resonance is damped due to dissipation processes, which is modeled through a resistance parallel to the capacitance. From a high-frequency viewpoint, this setup is equivalent to a parallel RLC-circuit that is inductively M or capacitively coupled C_c to a feedline with a matched impedance of $Z_0 = 50\,\Omega$. The equivalent circuit diagram is shown in Figure 4.6 (right). The dissipated power is given as $P_\mathrm{dis} = U_\mathrm{ac}^2 R/2$, which is mapped by the dimensionless factor

$$Q_\mathrm{i} = \frac{2\pi f_0 W_\mathrm{tot}}{P_\mathrm{dis}} \tag{4.2}$$

called the internal quality factor of the resonator, where W_tot gives the total energy of the resonator. The behavior of an ideal resonator in a hanger mode, as sketched in Figure 4.6 (right), is described by a Lorentzian line shape and can be written as [Kha14]

$$S_{21}^\mathrm{ideal}(f) = \frac{U_\mathrm{out}}{U_\mathrm{in}} = 1 - \frac{Q/Q_\mathrm{c}}{1 + 2\mathrm{i}Q\frac{f-f_0}{f_0}} \quad , \tag{4.3}$$

with the coupling quality factor Q_c, which describes the coupling strength of the resonator to the feedline. The total quality factor Q of the resonator is the inverse sum of the internal quality factor Q_i of the resonator and Q_c

$$\frac{1}{Q} = \frac{1}{Q_\mathrm{i}} + \frac{1}{Q_\mathrm{c}} \quad . \tag{4.4}$$

The internal quality factor Q_i itself is the inverse sum of different contributions. In our case the main contribution comes from the tunneling systems, and we can write $Q_\mathrm{i}^{-1} \approx Q_\mathrm{i,TLS}^{-1}$. Under certain circumstances additional contributions like radiation losses, a finite electric conductivity, or pair-breaking processes in superconductors might contribute as well to Q_i. By comparing Equation (4.2) with Equation (2.109), we can identify $Q_\mathrm{i,TLS}^{-1}$ as the dielectric loss $\tan\delta$ of tunneling systems.
The resonance frequency is directly related to the capacitance, and therefore to the dielectric function's real part ε'. The relative change of the capacitance then reads as

$$\frac{\Delta C}{C} = \frac{C - C^*}{C^*} = \left(\frac{f_0^*}{f_0}\right)^2 - 1 \quad , \tag{4.5}$$

where C^* and f_0^* are some arbitrary reference points, for example, defined by the minimum of the temperature dependency. The inductance is assumed to be constant, and the thermal expansion of the sample should be negligible at low temperatures compared to the relative change of ε', which is of the order 10^{-3} for N-BK7. Thus, we can relate shifts of the resonance frequency f_0 at low temperatures to changes in ε'. However, we have to consider that the capacitance C of the capacitor is composed out of the capacitance of the sample C_x and a parasitic stray capacitance C_p, originating from the electric field that probes the volume outside the sample. We then have

$$C = C_\mathrm{x} + C_\mathrm{p} \quad . \tag{4.6}$$

Because of its proportionality $C_\mathrm{x} \propto \varepsilon'$, we are interested in changes of C_x. The stray capacitance should be constant, and we obtain

$$\frac{\Delta C_\mathrm{x}}{C_\mathrm{x}} = \frac{\Delta C}{C - C_\mathrm{p}} = \frac{\Delta C}{C}\frac{1}{1 - \frac{C_\mathrm{p}}{C}} \quad . \tag{4.7}$$

Together with Equation (4.5) we can write down the relative change of the dielectric function's real part

$$\frac{\delta\varepsilon'}{\varepsilon'} = \frac{\Delta C_\mathrm{x}}{C_\mathrm{x}} = \left[\left(\frac{f_0^*}{f_0}\right)^2 - 1\right] \cdot \frac{1}{\mathcal{F}} \quad , \tag{4.8}$$

where we introduced the filling factor $\mathcal{F} = 1 - \frac{C_\mathrm{p}}{C}$, which compares the amount of electric energy stored in the sample with the total electric energy of the resonator. The filling factor depends on the geometry of the resonator, in particular on the one of capacitor. We will discuss the filling factor of the resonators when we talk about the electric field inside the capacitors in Section 4.6.

Moreover, the stray capacitance modifies the internal quality factor Q_i of the resonator, which we derive from Equation (4.2). We have

$$W_\mathrm{tot} = \frac{1}{2} C U^2 \qquad P_\mathrm{dis} = \frac{U_\mathrm{eff}^2}{R} = \frac{U^2}{2R} \quad , \tag{4.9}$$

where U is the maximum, and U_eff is the effective voltage across the capacitance, which gives us

$$Q_\mathrm{i} = R\sqrt{\frac{C}{L}} \quad . \tag{4.10}$$

With that, we can write down the ratio

$$\frac{Q_\mathrm{i}}{Q_\mathrm{i,x}} = \sqrt{\frac{C}{C_\mathrm{x}}} \quad , \tag{4.11}$$

which leads to

$$\tan\delta = \frac{1}{Q_\mathrm{i,x}} = \frac{1}{Q_\mathrm{i}} \left(1 + \frac{C_\mathrm{p}}{C_\mathrm{x}}\right)^{1/2} = \frac{1}{Q_\mathrm{i}\sqrt{\mathcal{F}}} \quad . \tag{4.12}$$

4.4.1 Determination of the intrinsic resonator parameters

With Equations 4.4, 4.8 and 4.12 we can determine the dielectric function from the intrinsic parameters of the resonator. In this section we will discuss how these parameters are obtained from the resonance data S_{21} measured by the VNA.

Equation (4.3) gives the frequency response of an ideal resonator, which is shown in Figure 4.7. In (a) the resonance curve is plotted in the complex plane $\mathrm{Re}(S_{21})$-$\mathrm{Im}(S_{21})$, where it forms a circle. For $f \to \pm\infty$ the curve converges towards the point $S_{21}^\infty = (1, 0)$. Following the circle clockwise means increasing the frequency. Opposite to the point S_{21}^∞ on the circle lies the resonance frequency f_0 (red point). The amplitude $|S_{21}| = \sqrt{\mathrm{Re}(S_{21})^2 + \mathrm{Im}(S_{21})^2}$ and the phase $\varphi = \arctan\left(\frac{\mathrm{Im}(S_{21})}{\mathrm{Re}(S_{21})}\right)$ are shown in (b) and (c). The resonance frequency f_0 sits at the minimum of $|S_{21}|$, while the phase changes its sign there. The quality factor is a measure of the width of both curves, and the minimum of $|S_{21}|$ is given by $\min(|S_{21}|) = 1 - \frac{Q}{Q_\mathrm{c}}$. In principle,

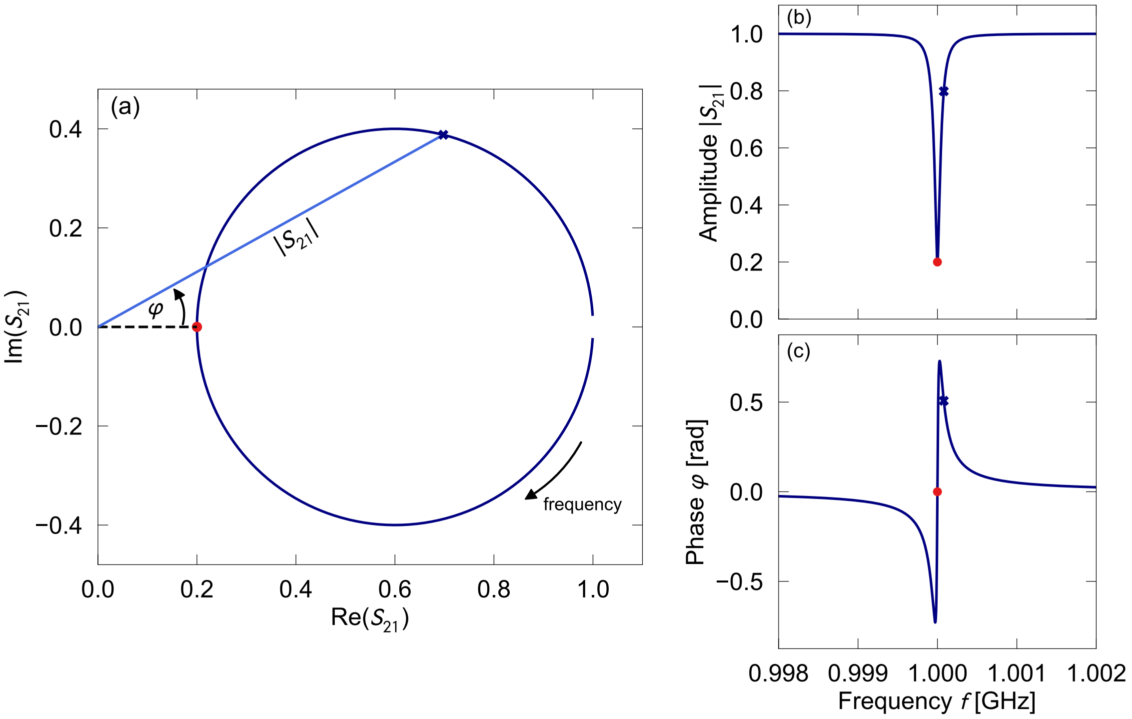

Figure 4.7: Representation of the complex valued scattering parameter S_{21} of an ideal resonator from Equation (4.3) with $f_0 = 1\,\mathrm{GHz}$, $Q = 8000$, and $Q_\mathrm{c} = 10{,}000$. In the complex plane (a) the resonance curve forms a circle, (b) shows the amplitude $|S_{21}|$, and (c) the phase φ. The resonance frequency is marked with the red dot.

fitting Equation (4.3) to the resonance data allows a determination of the intrinsic resonator parameters f_0, Q_i, and Q_c. However, in almost all cases the behavior of a real resonator will deviate from the ideal case, for example due to imbalanced impedances which lead to asymmetries.

The behavior of a non-ideal resonator can be expressed by expanding Equation (4.3) with additional terms [Pro15]:

$$S_{21}(f) = a e^{\mathrm{i}\alpha} e^{-2\pi \mathrm{i} f \tau} \left[1 - \frac{Q/Q_\mathrm{c} e^{\mathrm{i}\phi}}{1 + 2\mathrm{i}Q \frac{f - f_0}{f_0}} \right] \tag{4.13}$$

Attenuation and amplification of the signal lead to the scaling factor a. Additional phase shifts give the factor $e^{\mathrm{i}\alpha}$, and the cable delay τ gives the frequency-dependent factor $\mathrm{e}^{-2\pi\mathrm{i}f\tau}$. An impedance mismatch is modeled by a complex coupling quality factor giving rise to the factor $e^{\mathrm{i}\phi}$ [Kha12]. An example for such a non-ideal resonator is sketched in Figure 4.8. In the complex plane, the non-ideal behavior leads to a distortion of the circle into a rotated spiral. Thus, amplitude and phase are skewed as well, and the position of the resonance frequency is not related to a characteristic point anymore. This makes the determination of the resonator parameters non-trivial because the parameters occurring from the resonator environment are typically

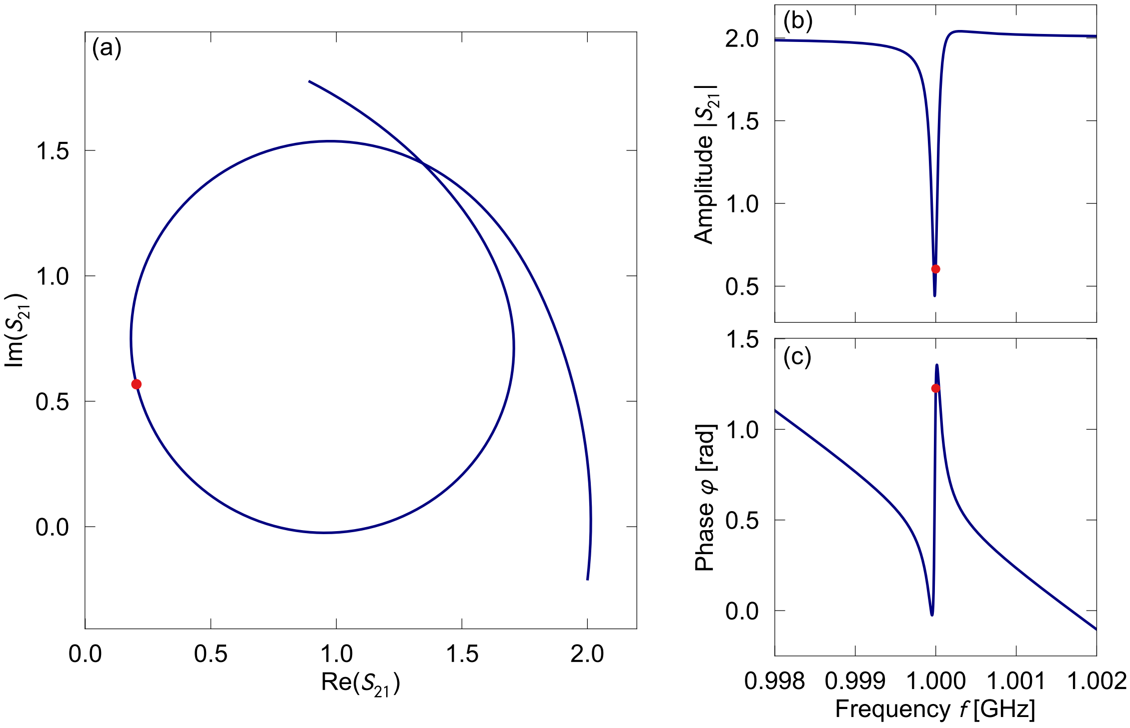

Figure 4.8: Representation of the complex valued scattering parameter S_{21} of a non-ideal resonator from Equation (4.13) with $f_0 = 1\,\mathrm{GHz}$, $Q = 8000$, and $Q_\mathrm{c} = 10,000$, $a = 2$, $\alpha = 0.5$. $\tau = 50\,\mathrm{ns}$, and $\phi = -0.5$. In the complex plane (a) the resonance curve is deformed and rotated compared to the ideal resonator, (b) shows the amplitude $|S_{21}|$, and (c) the phase φ. The resonance frequency is marked with the red dot.

unknown and difficult to quantify precisely. Instead, we eliminate the deviations from an ideal behavior by applying an algorithm described in [Pro15]. The basic idea is to remove the additional terms of the non-ideal resonator by transforming the resonance curve in the complex plane back into its ideal (canonical) form, which is exemplarily shown in Figure 4.9 for different steps.

(a) The cable delay is removed by fitting the data to a circle, whereby τ is the fitting parameter. A multiplication with $e^{-2\pi \mathrm{i} f\tau}$ eliminates the cable delay, and one obtains a circle that is rotated with respect to the origin and to the point S_{21}^{∞}.

(b) The resonance frequency f_0 and its opposite point on the circle S_{21}^{∞} are determined by shifting the center of the circle to (0,0) (not shown here) and performing a fit of the resulting φ-f data. This allows to extract the phase α by rotating the point S_{21}^{∞} to the position where its imaginary component vanishes.

(c) The prefactor a is removed by multiplying the curve with a^{-1}, which shifts the point S_{21}^{∞} to its canonical position (0,1).

(d) In a final step, the phase ϕ is removed by rotating the circle around S_{21}^{∞}, which brings the resonance into its ideal form.

A fit of the corrected curve then gives the intrinsic resonator parameters f_0, Q_i, and Q_c. It turns out that this method works well as long as the signal-noise level is adequate, and the resonance is not affected by a non-constant background. We typically use this method to calibrate our setup by measuring a resonance curve with a good signal-noise ratio, which allows to obtain the coupling quality factor Q_c of the resonator. We do not observe substantial shifts of Q_c when we change the temperature or the driving field strength, and therefore use this value in all following measurements of the cooldown.

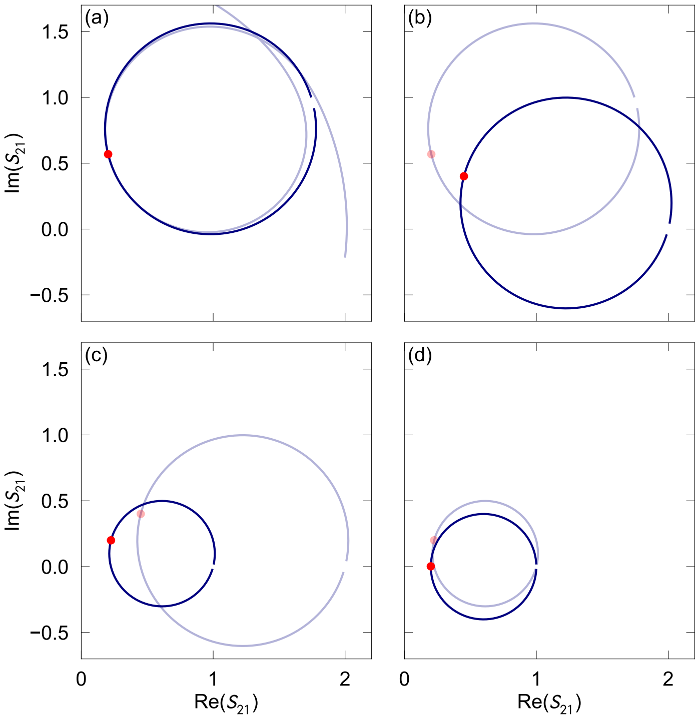

Figure 4.9: Illustration of the transformation of a non-ideal resonator into its ideal form. The transformation steps (a)-(d) are briefly explained in the text and follow the algorithm described in [Pro15]. The resonance frequency is marked by the red point.

In many cases it is more convenient to regard solely the amplitude $|S_{21}|$ and fit an empirical skewed Lorentzian (see Equation (4.14)) which is able to describe also asymmetric line shapes and is more robust at low driving fields, where the signal-noise ratio becomes low. The fit gives us the parameters f_0 and Q. Together with Q_c, obtained from the previous discussed circle fit, Equation (4.4) gives the intrinsic quality factor Q_i. The used skewed Lorentzian has the form [Gao08]

$$|S_{21}(f)|^2 = A_1 + A_2(f - f_0) + \frac{A_3 + A_4(f - f_0)}{1 + 4Q^2\left(\frac{f-f_0}{f_0}\right)^2} \quad , \tag{4.14}$$

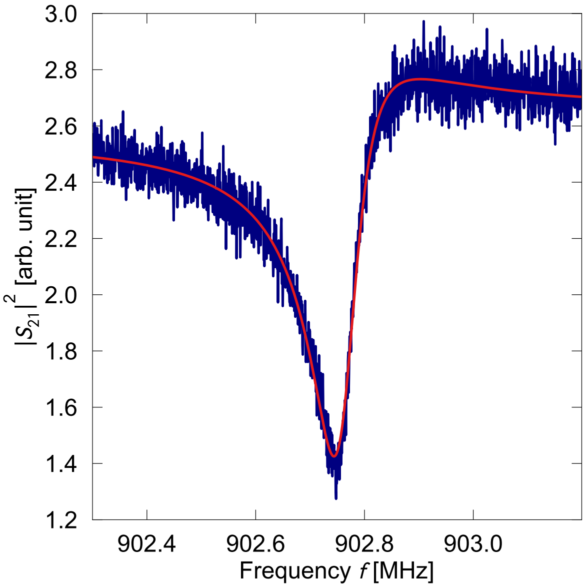

Figure 4.10: Exemplary fit of a resonance curve (blue) with the skewed Lorentzian from Equation (4.14) (red line).

where the parameters A_1 and A_2 determine the background of the resonance, A_3 the resonance amplitude, and A_4 the skewness of the resonance. Figure 4.10 shows an exemplary fit of a fairly asymmetric resonance curve which was fitted with Equation (4.14). The skewed Lorentzian is able to describe the data well and gives the same results as the circle fit procedure [Gao08], which is in agreement with our observations.

Both discussed methods for the determination of the intrinsic resonator parameters assume a constant internal quality factor across the measured frequency range. However, it is not guaranteed that this is fulfilled by the loss originating from tunneling systems. As we have discussed in Section 2.4.5, the tunneling systems are saturated by strong electric fields, and their loss depends on the applied electric field strength. Close to the resonance frequency the electric field inside the capacitor is enhanced due to the resonant characteristic of the resonator. At this frequency, tunneling systems might be stronger saturated compared to frequencies detuned from the resonance, and Q_i may become frequency-dependent. This is especially problematic for resonance curves that are measured at high input powers, where the saturation of tunneling systems becomes stronger. At smaller excitations, the resonant tunneling system loss becomes independent from the field strength, and Q_i should be constant across the whole resonance curve. For minimizing the effect of a non-constant Q_i at strong driving powers, we chose a third approach for determine the quality factor from the resonance curve. In the case of an ideal resonator in a hanger mode, we find for the minimum of the resonance curve $\min(S_{21})$

$$\min(S_{21}) = S_{21}^{\infty}\left(1 - \frac{Q}{Q_\mathrm{c}}\right) \tag{4.15}$$

and thus

$$Q = \left(1 - \frac{\min(S_{21})}{S_{21}^{\infty}}\right) Q_{\mathrm{c}} \quad . \tag{4.16}$$

Both $\min(S_{21})$ and S_{21}^{∞} are real numbers and are extracted from the amplitude $|S_{21}|$. Again, Q_{c} can be used from the circle fit routine. With this approach we detect the quality factor only at a single excitation frequency, and therefore do not average over different values of quality factor, as it is the case for fitting the whole resonance curve with a Lorentzian. Detecting the resonance baseline S_{21}^{∞} might be an erroneous issue for resonance curves as shown in Figure 4.10, especially if the recorded frequency window is small. We detect the baseline $S_{21}^{\infty}(P_0)$ from a measurement over a broad frequency range around f_0 and at a high driving power. The baseline of other resonances, measured at a different input power P, is then calculated from this value by $S_{21}^{\infty}(P) = S_{21}^{\infty}(P_0)\sqrt{10^{(P-P_0)/10}}$, where the powers are measured in dBm. Since we know the used attenuation of the attenuators (see Figure 4.4), we also know the input power P relative to P_0, which gives a reliable determination of the baseline. Fine tuning of $S_{21}^{\infty}(P_0)$ can be realized by demanding an agreement of the hereby detected Q with the other fitting methods at low input powers, where saturation of tunneling systems should not play a role. For an exemplary set of data, a comparison of this method Q_1 with the determination through a Lorentz fit Q_2 is shown in Figure 4.11. The relative deviation $\delta Q^{-1} = 1 - Q_2^{-1}/Q_1^{-1}$ is plotted for different input powers P_{ac}. As expected, at low input powers both methods give the same results, whereby the measurement is noisier due to the smaller excitation. For higher driving powers, when the saturation of tunneling systems becomes relevant, the results start to differentiate significantly. The overall deviations are not too large, but we will prefer the determination of Q through the resonance minimum whenever

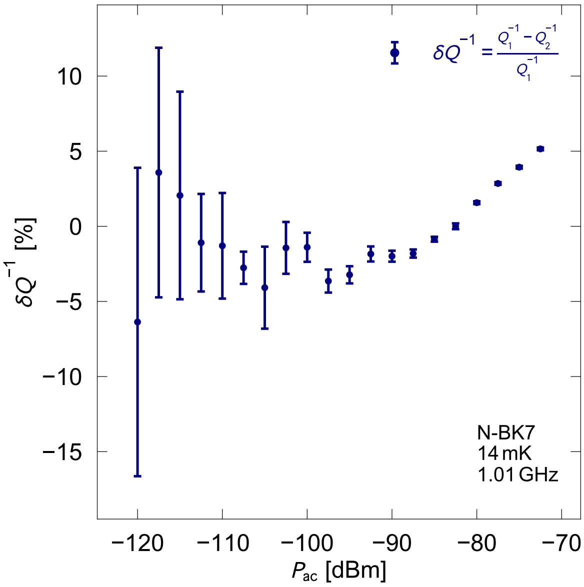

Figure 4.11: Relative deviation of the determined quality factor with two evaluation methods for different input powers. Method 1, Q_1: Determine Q through the resonance minimum, see Equation (4.16). Method 2, Q_2: Determine Q through a Lorentzian fit, see Equation (4.14). In both cases the same set of data was used.

the strength of the driving field matters, and we are not measuring in the low-power limit anyway.

4.4.2 Design

The 250 MHz- and the 1 GHz-resonator share a similar design. As sample we use a window out of N-BK7 of the size 41 mm × 30 mm × 1 mm, which is used as substrate for the microstructure. When cutting the glass into the required size, special care is needed to maintain a smooth surface for the following microfabrication. The sample with the microstructure on top is shown in Figure 4.12. The microstructure is composed out of sputter deposited niobium with a thickness of 400 nm. Niobium becomes superconducting at temperatures below $T_c \approx 9.2\,\mathrm{K}$ [Mat63], which eliminates Ohmic losses and allows high internal quality factors for these resonators. As capacitance we use four identical interdigital capacitors (IDC) and as inductance a meander line inductor. This allows us to implement a planar design, where the electric field of the IDCs penetrates the substrate and therefore probes the tunneling systems inside the sample. Probing the substrate with IDCs enables us to use bulk glasses as samples and does not restrict the sample selection to thin amorphous films when dealing with

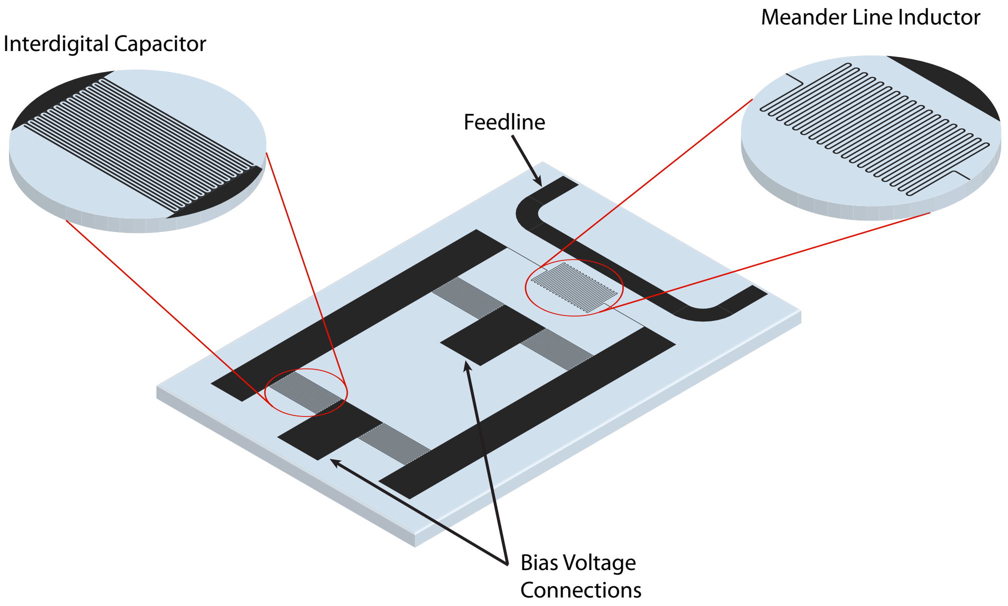

Figure 4.12: Illustration of the glass sample (light blue) with the microstructure (black) on top, representing the 250 MHz-resonator. The planar design enables us to use the substrate as sample.

microstructures. The feedline is connected to the rf-branch, and the bias signal is applied through the bias voltage connection pads (U_b, GND).

In Figure 4.13 the design of the 250 MHz- (left) and the 1 GHz-resonator (right) are shown in more detail. In both cases, appearing edges in the design, especially at the capacitor electrodes, are rounded to avoid strongly enhanced field strengths, which would produce spots with very high couplings to tunneling systems, and therefore possible non-linearities. The capacitors are connected in such a way that they form the bridge geometry from Figure 4.6 (left). In the case of the 250 MHz-setup the finger length of the IDC is 4600 µm, the finger width and spacing are 50 µm, and there are 13 finger pairs per IDC. The meander has a conductor width of 50 µm, a spacing of 100 µm, and has 40 legs in total. The feedline is realized through a microstrip transmission line of width 1.55 mm. Using a dielectric thickness of 1 mm and ground on the bottom of the sample, gives an impedance of about 50 Ω for the microstrip. In the 1 GHz-design the IDCs are reduced to single slits with length 2000 µm and 5 µm width. The inductance is a simple short between the electrodes.

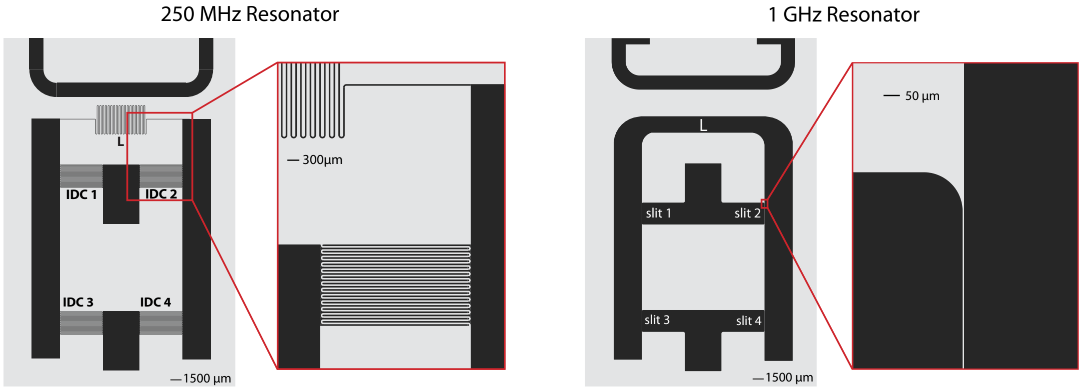

Figure 4.13: Design of the 250 MHz-resonator (left) and the 1 GHz-resonator (right).

Both resonators were designed and simulated with the software Sonnet® [Son18], which allows to adjust the resonator design to match the requirements. In the simulation the dielectric material was set to have a relative permittivity of $\varepsilon_\mathrm{r} = 5.8$, a loss of $\tan\delta = 4 \times 10^{-4}$, and a thickness of 1 mm, which matches the properties of the sample. The metal structure was modeled as being lossless. The bias voltage connections were grounded in the simulation. In Sonnet® the S-parameter of port 1 (input feedline) and port 2 (output feedline) is simulated in the frequency domain. Hence, we receive resonance curves which can be evaluated as explained in Section 4.4.1 and shown in Figure 4.14. We can compare the simulation data with resonance spectra of the resonators that were measured at the base temperature of the cryostat, which is presented in Table 4.2. Since we know the loss of the dielectric material in the simulation, we can write $Q_\mathrm{i} \approx 2500$. The coupling quality factor in

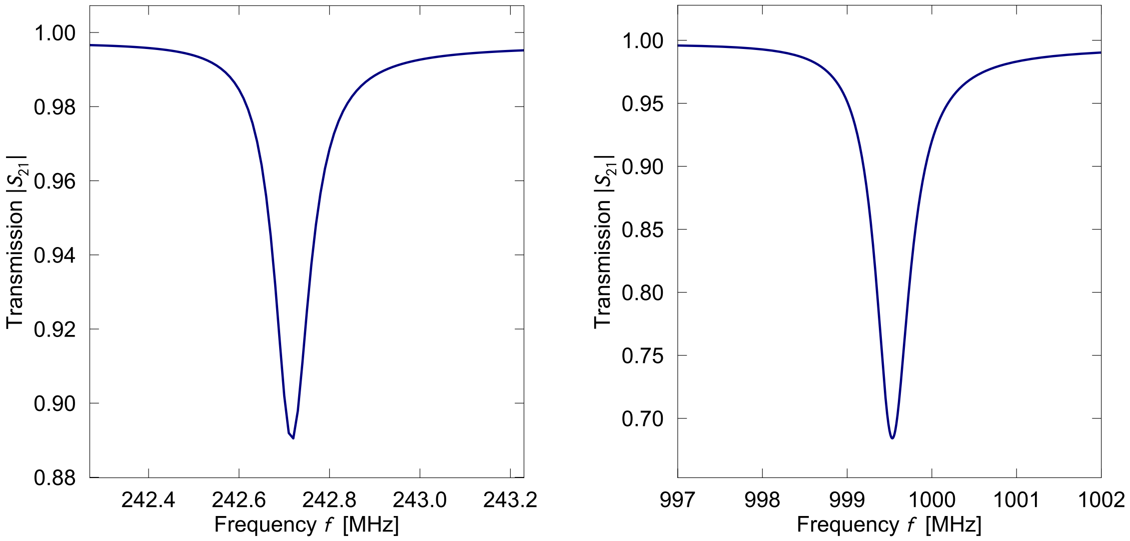

Figure 4.14: Simulated response of the 250 MHz-resonator (left) and the 1 GHz-resonator design with the software Sonnet®.

the simulation $Q_{\mathrm{c,sim}}$ is then calculated by using Equations (4.15) and (4.4) as

$$Q_c = \frac{\min(S_{21})}{1-\min(S_{21})} Q_{\mathrm{i}} \quad . \tag{4.17}$$

The resonance frequency f_0 is accurately predicted through the simulation. It should be noted that the position of the resonance in the experiment typically shifts by a few MHz between different cooldowns. The simulated coupling quality factors fairly agree with the measurements and can provide a rough idea about the expected coupling of the resonator to the feedline during the design procedure. However, details of the experimental realization, like the chip environment by the experimental holder or connections onto the chip, are missing in the simulation and may lead to deviations in Q_{c}.

	$f_{0,\mathrm{sim}}$ [MHz]	$f_{0,\mathrm{exp}}$ [MHz]	$Q_{\mathrm{c,sim}}$	$Q_{\mathrm{c,exp}}$
250 MHz-resonator	242.72	245.3	20300	12000
1 GHz-resonator	999.53	1006.8	5400	1700

Table 4.2: Comparison between simulated (sim) and measured (exp) resonator properties.

4.4.3 Fabrication and sample holder

All microfabrication processes for the chips used in this this were done in-house in a cleanroom. For processing the structure on top of the glass sample a standardized lift-off process was used. Therefore, a photoresist is deposited on the substrate, wherein the negative image of the structure is created through photolithography. On top of the remaining photoresist and the uncovered substrate a layer of 400 nm thick niobium is deposited through a sputtering process with argon as sputtering gas. After that, a solvent removes the photoresist along with the niobium thereon, and the required niobium structure remains on top of the substrate. After the fabrication, the chip is cleaned multiple times within baths of acetone or isopropanol, and ultrasonication in between, which removes possible residuals from the fabrication process.

The cleaned chip is placed into the sample holder box shown in Figure 4.15. A thin film of vacuum grease between the copper box and the backside of the glass holds the chip in place and provides a good thermal contact. The box is made of tempered oxygen-free copper and is coated from the inside with a sputter deposited niobium film (not shown) to reduce radiation losses of the resonator. SMA connectors on the front side allow to connect the coaxial cables for the rf-readout. Thin copper wires are soldered to the inner conductor of the SMA connectors that run into the box. With conductive silver paint[15] the copper wire-ends are glued to the dedicated pads of the feedline. The bias voltage is applied through gold-plated spring-loaded pins[16], which are soldered to the SMA connector at the cover, or directly to the cover and therefore to ground. The cover closes the box and presses the head of the pins on the bias voltage connection pads of the chip and realizes the electric contacting of the bias voltage. Moreover, the resulting vertical force on the chip supports the bonding of the chip to the sample holder. Several holes in the foot of the holder allow to attach the holder mechanically to the experimental platform of the cryostat.

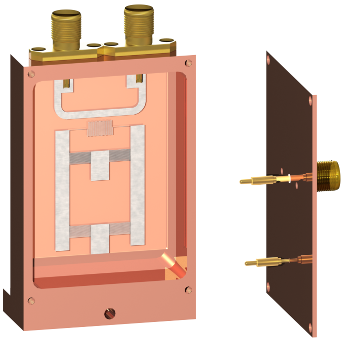

Figure 4.15: Rendering of the sample holder with the mounted chip placed inside of the box. The niobium coating of the inside is not shown here. The cover closes the box and connects the bias voltage through the attached pins.

---

[15] ACHESON Silver DAG 1415, Plano GmbH, Ernst-Befort-Strasse 12, D-35578 Wetzlar, Germany

[16] 0914 Spring-Loaded Pin, Mill-Max Mfg. Corp., 190 Pine Hollow Rd, Oyster Bay, NY 11771, USA

4.4.4 Revised 1 GHz-resonator

In Section 5.3.5 we will see that the presented resonators tend to heat up when we apply strong microwave tones through the transmission line. Therefore, we did a revision of the 1 GHz-resonator design in order to reduce the heat load in two-tone experiments. The main adjustment is to replace the normal conducting connections to the chip with aluminum wire bonds, which become superconducting below 1.2 K [Mat63]. Moreover, the distance between the electrodes of the capacitors were further reduced to 2 µm to reach higher bias field strengths and therefore higher bias rates, which also shrinks the size of the resonator. The substrate is a 50 mm wafer out of N-BK7 with 0.2 mm thickness. The wafer contains in total 12 resonators with different designs, each having the size 10 mm × 10 mm. The design of the resonator used in this thesis is shown in Figure 4.16. Again, we use a planar resonator design out of 400 nm sputter deposited niobium with a meander structure as inductance

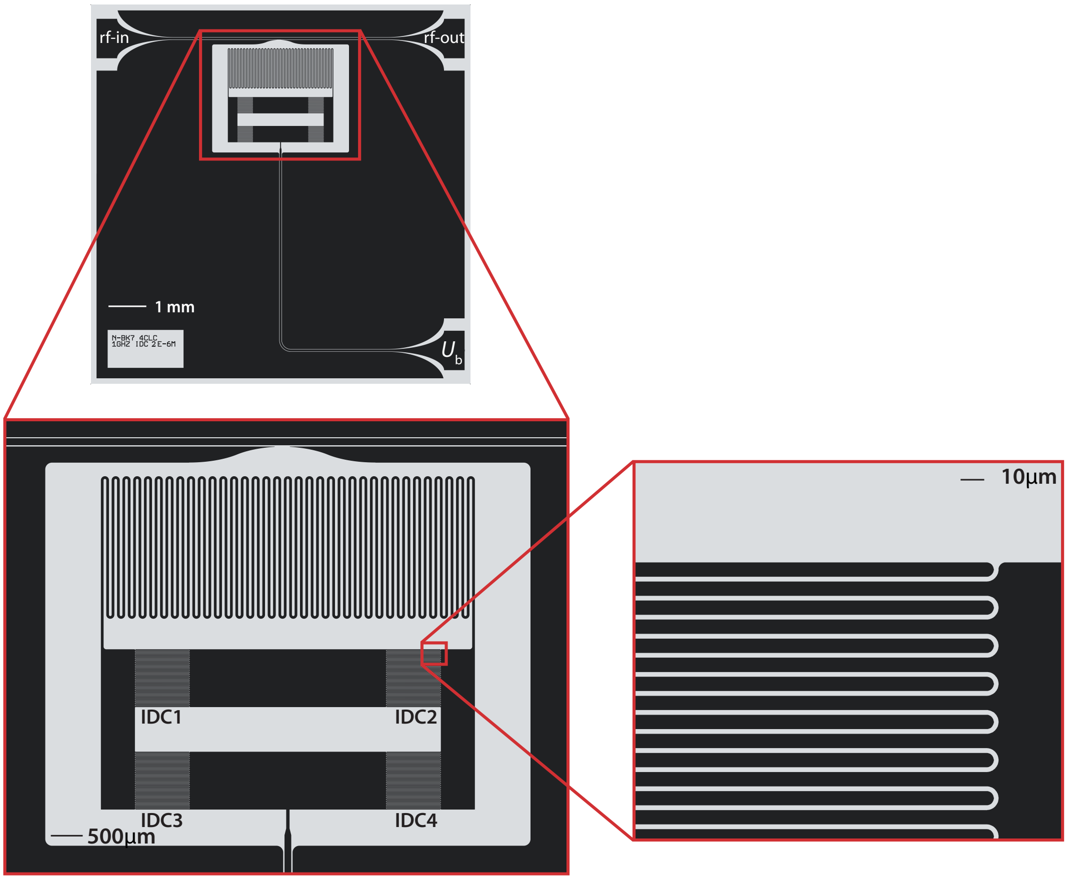

Figure 4.16: Design of the revised 1 GHz-resonator (top). Zoom into the resonator embedded in the ground plane (bottom left). Zoom into the fingers of IDC2 with finger distance 2 µm (bottom right).

and a bridge geometry of four IDCs as capacitance. The resonator is embedded in a niobium ground plane, which is grounded through several Al-bonds to the sample holder box. Three pads in the corners allow to contact the resonator chip with bond wires. The two pads at the top are dedicated for the rf-readout and are connected through a 50 Ω-coplanar waveguide as transmission feedline with each other. The bonding pad at the lower right is used for the bias voltage connection. For the ground reference of the bias voltage, Al-bonds connect the niobium area between IDC1 and IDC2 to the niobium ground plane. The meander is built-up by 70 legs with a conductor width and spacing of 20 µm. The IDCs consist of 27 finger pairs with finger lengths of 400 µm. The finger width is 6 µm and the distance 2 µm.
As before, the design was simulated with Sonnet® and compared to the experimental results, see Table 4.3. The measured resonance frequency of the resonator appears to be 100 MHz smaller than in the simulation. The simulation is known to predict the resonance frequency of these kinds of resonators precisely [Fre16], and we suppose the finger distance of the fabricated IDCs is smaller than the design value. Inspection of the IDC structure with a microscope indicated a slightly reduced finger distance. As it was observed in the simulations before, the coupling quality factor differs from the experimental value.

$f_{0,\mathrm{sim}}$ [MHz]	$f_{0,\mathrm{exp}}$ [MHz]	$Q_{\mathrm{c,sim}}$	$Q_{\mathrm{c,exp}}$
1003.65	902.7	8000	37000

Table 4.3: Comparison between simulated (sim) and measured (exp) resonator properties.

A new sample holder that is suited to fit the resonator chip [Haa20b] was used, which is shown in Figure 4.17. The chip is glued with the low temperature varnish GE 7031[17] to the center of the sample holder. This provides a good thermal contact of the sample and gives a solid mechanical support when bonding to the chip. SMA connectors are attached to the backside of the holder. The end of their inner conductors is filled with tin, and their tip is milled to form a plane surface. This allows direct wire-bonding from the surface of the tip to the bonding pads of the chip and allows a normal-conductor-free contacting of the chip, which should help to avoid Ohmic heating nearby the sample. Only the inner conductor of the SMA connector remains normal conducting. As before, the inside of the holder is coated with a niobium film.

---

[17] Lake Shore Cryotronics, 575 McCorkle Blvd, Westerville OH 43082-8699

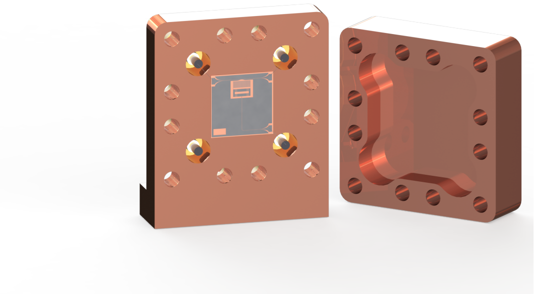

Figure 4.17: Rendering of the sample holder for the revised resonator with the mounted chip. The niobium coating of the inside is not shown here. The cover closes the box.

4.5 Landau-Zener spectroscopy

The presented setup allows to measure the sample's dielectric function with rf-fields at very low temperatures under a simultaneous modification of the tunneling systems' asymmetry energy through an electric bias field. This induces the tunneling systems to perform Landau-Zener transitions, and we can observe the Landau-Zener non-equilibrium dynamics of tunneling systems in bulk glasses, see Section 2.4.6. In this section a measurement protocol is presented which allows to perform a spectroscopy of tunneling systems based on this dynamic.

In the simplest case, in parallel to the recording of resonance curves with the VNA, a continuous bias voltage signal, e.g. a triangle signal, is applied through the bias line. This constantly varies the asymmetry energies of tunneling systems and their resulting modified population reveals in the resonance curve. A drawback of this method is that, due to the continuous ramping, the time between consecutive resonance crossings of tunneling systems becomes short, and thus a tunneling system cannot fully relax back into its ground state in between. Therefore, the assumption of a tunneling system being in its ground state, prior to the resonance crossing, might be violated and multiple coherent Landau-Zener transitions of the same tunneling system occur, which was studied in [Mat19]. Moreover, for this setup at high bias rates due to the continuous switching of high voltages a heating of the sample was observed [Kö19].

Therefore, an alternative protocol was implemented, where the bias is ramped only once. Simultaneously, resonance curves of the resonator are recorded with a high temporal resolution. Before the following ramp, the tunneling systems are given enough time to restore their equilibrium state. This is realized by setting the VNA into its CW time-sweep mode, where the VNA is locked to a single frequency and measures S_{21} as a function of the time. If the internal bandwidth filter of the VNA is set to 3 kHz, the VNA samples 1601 data points within 800.5 ms, which gives a sampling interval of $\Delta t = 0.5\,\mathrm{ms}$. During a time-sweep the bias voltage is ramped. After

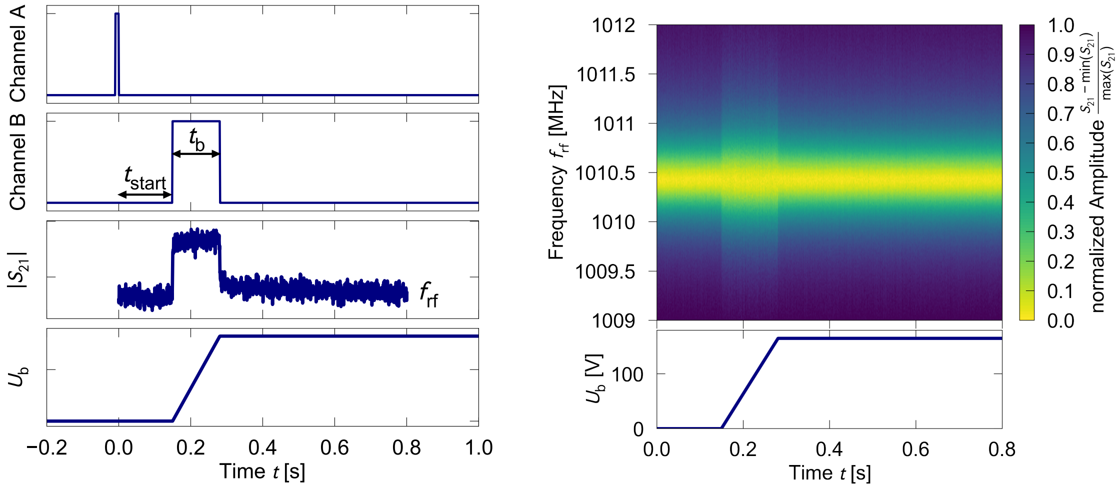

Figure 4.18: Left: Synchronized pulse sequence to record a time trace of $|S_{21}|$, while applying in parallel a bias ramp. Details are explained in the text. Right: By sweeping f_{rf} over the resonance curve, resonance spectra as a function of time in the presence of a bias ramp are reconstructed. For a clearer representation the amplitude $|S_{21}|$ was normalized.

the sequence, the driving frequency is changed, and the bias sequence is repeated. If the onset of the bias ramp is synchronized with the start of the VNA time-sweep, the resonance curve as a function of the time can be reconstructed by successively tuning the driving frequency across the resonance curve. The synchronization is realized with a pulse generator[18] connected to the *sync ports* of both the VNA and the signal generator that generates the bias voltage. The bias ramp with ramp time t_{b} is created by using the Frequency-Shift Keying (FSK) mode of the signal generator, whereby the generator shifts phase-preserved between two preset frequencies. Frequency A is selected when the external TTL (transistor–transistor logic) trigger level is 'LOW', and frequency B is selected when the TTL level is 'HIGH'. For frequency A we use an arbitrarily small frequency $f_{\mathrm{A}} = 1\,\mu\mathrm{Hz}$ and as frequency B $f_{\mathrm{B}} = (2t_{\mathrm{b}})^{-1}$. As waveform we choose a triangle signal with peak-peak amplitude U_{b}. When we set the length of the trigger pulse to t_{b}, the signal generator creates a ramp from zero to U_{b} within t_{b}. On another channel a TTL pulse triggers the VNA which starts a single CW time-sweep on a negative TTL-transition.

The whole sequence is shown in Figure 4.18 (left). The TTL pulse on channel A of the pulse generator starts the VNA time-sweep. After the time t_{start}, a pulse on channel B with length t_{b} triggers the signal generator to perform half of the cycle of a triangle ($f_{\mathrm{b}} = (2t_{\mathrm{b}})^{-1}$). At the end of the pulse, the signal generator puts $f_{\mathrm{A}} = 1\,\mu\mathrm{Hz}$ to the output, which is approximately constant, and we find the ramp shown Figure 4.18. The VNA records a single time trace at the set driving frequency

---

[18] Pulse/Delay Generator PDG 204, SMV Systemelektronik GmbH, Belfortstraße 3, D-81667 München, Germany

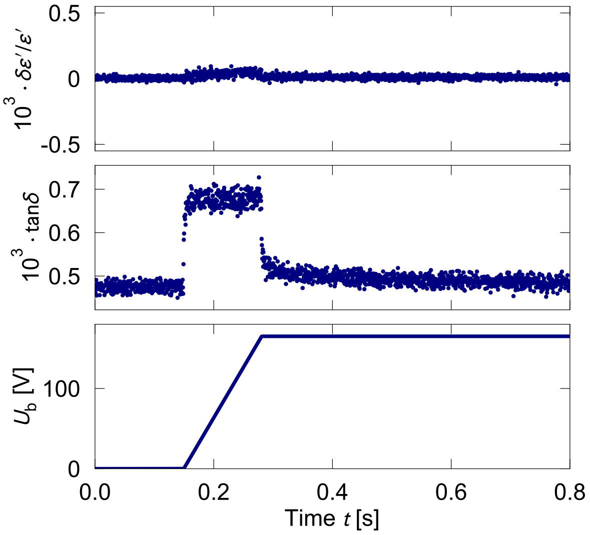

Figure 4.19: Time dependence of $\delta\varepsilon'/\varepsilon'$ and $\tan\delta$ extracted from the data of Figure 4.18 (right) in the presence of a bias ramp.

$f_{\rm rf}$. After completing one sequence, $f_{\rm rf}$ is changed, and a TTL pulse on channel A triggers a new iteration.

Sweeping $f_{\rm rf}$ over the resonance gives the plot shown in Figure 4.18 (right), where the color indicates $|S_{21}|$. A horizontal slice represents a recorded time trace $|S_{21}(t)|$, and vertical slices give resonance curves at different time steps. Typically, a resonance spectrum consists of 200 frequencies, which is sufficient to provide a robust determination of f_0 and Q. From Figure 4.18 (right) one can already see that resonance curves during the bias ramp are broader than ones with constant bias voltage. As explained before, from each resonance curve $\delta\varepsilon'/\varepsilon'$ and $\tan\delta$ can be extracted, which is shown in Figure 4.19. This method allows us to resolve even fast bias ramps of a few milliseconds. The value of the loss during the bias ramp gives the non-equilibrium loss of tunneling systems caused by the Landau-Zener dynamics. By varying the ramp time, one can alter the dynamics and control the population of resonant tunneling systems, which allows to perform a spectroscopy of the involved systems. We will present the results of this Landau-Zener spectroscopy in Section 5.3.

4.6 Electric field inside the capacitors

For a quantitative comparison of the measured dielectric properties with the theory's predictions, we need to know the electric field inside the capacitors to which tunneling systems can couple. As a first step, we calculate the voltage across the capacitor of the LC-resonator resulting from the input power $P_{\rm in}$, which is the root mean square power through the feedline. We will then look at the utilized capacitor geometries to study their inhomogeneous electric fields.

We can write down the power balance for the rf-signal through the feedline at the resonator as

$$P_{\mathrm{in}} = P_{\mathrm{trans}} + P_{\mathrm{refl}} + P_{\mathrm{dis}} \quad , \tag{4.18}$$

with P_{trans} being the transmitted power, P_{refl} the reflected power, and P_{dis} as the dissipated power. We assume that all dissipation processes originate from the dielectric material of the capacitor. By the use of Equation (4.2), we write the stored energy in the resonator as

$$W_{\mathrm{stored}} = \frac{P_{\mathrm{in}} - P_{\mathrm{refl}} - P_{\mathrm{trans}}}{2\pi f_0} Q_{\mathrm{i}} = \frac{1 - |S_{11}|^2 - |S_{21}|^2}{2\pi f_0} Q_{\mathrm{i}} P_{\mathrm{in}} \quad . \tag{4.19}$$

We can use $S_{11} = 1 - S_{21}$ and thus $|S_{11}|^2 = |1 - S_{21}|^2$, which gives together with Equation (4.3) for an ideal resonator at $f = f_0$

$$W_{\mathrm{stored}} = \frac{2Q^2 P_{\mathrm{in}}}{Q_{\mathrm{c}} \omega_0} \quad . \tag{4.20}$$

Writing the stored energy as $W_{\mathrm{stored}} = \langle n \rangle \hbar \omega_0$, where $\langle n \rangle$ is the average number of photons in the resonator, we obtain

$$\langle n \rangle = \frac{2Q^2 P_{\mathrm{in}}}{Q_{\mathrm{c}} \hbar \omega_0^2} \quad . \tag{4.21}$$

Moreover, the total energy of an LC-circuit is given as $W_{\mathrm{LC}} = \frac{1}{2} C U^2$, while U gives the maximum voltage across the capacitance C. Together with Equation (4.20) we can write down the voltage across the capacitor as

$$U = \sqrt{\frac{4Q^2 P_{\mathrm{in}}}{Q_{\mathrm{c}} C \omega_0}} \quad . \tag{4.22}$$

In our case, with four identical capacitors with capacitance C arranged in a bridge geometry which forms a total capacitance of again C, the voltage drop across each capacitor is $U/2$, and we finally arrive at

$$U_{\mathrm{4CLC}} = \sqrt{\frac{Q^2 P_{\mathrm{in}}}{Q_{\mathrm{c}} C \omega_0}} \quad . \tag{4.23}$$

The utilized capacitor geometries cause an inhomogeneous electric field distribution, which we modeled with a finite element simulation in FEMM [Mee20]. Figure 4.20 shows a vertical slice through the capacitor electrodes. The metal structure (thin black lines) lies on top of the glass sample ($\varepsilon_{\mathrm{r}} = 5.8$), and the area above the structure is modeled as vacuum ($\varepsilon_{\mathrm{r}} = 1$). The voltage between the two electrodes was set to 1 V. The left side shows an IDC geometry with finger width and distance of 50 µm, and the right side shows a single slit with 5 µm gap width. FEMM then models the field distribution of the given geometry. In Figure 4.20 the electric displacement

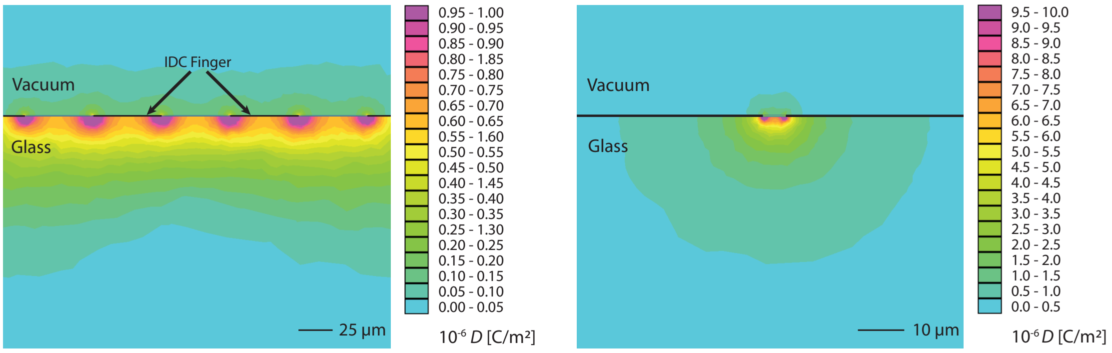

Figure 4.20: Calculated electric displacement of the IDC (left) and the slit geometry (right). The image shows a vertical slice through the structure with the glass below and the vacuum above the metal electrodes (black lines).

field D is shown. The finger and slit lengths in the designs are long compared to the distance between the electrodes so that we can neglect the boundaries of the structure. In both cases, directly at the edge of the electrodes, the field is the largest and penetrates by approximately the electrode distance into the sample. In Figure 4.21 the glass area was evenly rasterized, and histograms for both electric field distributions were created. Especially the areas close to the electrodes, where the highest field strengths occur, are of particular interest, since tunneling systems in these regions couple the strongest to electric fields and give the largest contribution to the dielectric function. In both plots the electric field strength was normalized by the value of a corresponding plate capacitor with the electrode distance of each capacitor as gap size. The histograms reveal the field distribution of the two capacitor geometries. In the case of the IDC, one finds an exponential distribution $f(F)\mathrm{d}F \propto \exp(-F'/\beta)\mathrm{d}F$, with $\beta = 0.25$ and F' being the normalized field strength. For the slit geometry we also find an exponential dependency with a slightly modified value for $\beta = 0.19$.

In the theory predictions homogeneous electric fields are assumed. Knowing the field distribution of the capacitor geometries allows us to incorporate the inhomogeneous field distribution whenever the field strength plays a role. This is in particular of interest for measurements of the resonant dielectric loss as a function of the driving field strength or the bias rate, what we want to calculate in the following. The total energy stored per volume in the capacitor is

$$W_{\mathrm{tot}} = \frac{1}{2}\varepsilon_0\varepsilon' F^2 \quad , \tag{4.24}$$

while the dissipated power is

$$P_{\mathrm{dis}} = \frac{\omega_0}{2}\varepsilon_0\varepsilon'' F^2 \quad . \tag{4.25}$$

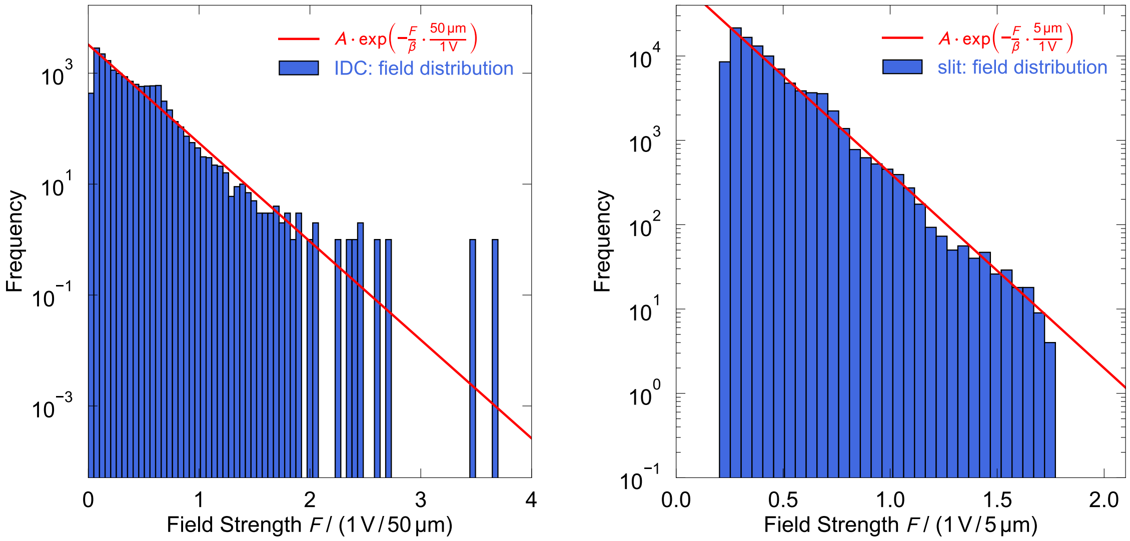

Figure 4.21: Histograms of the simulated field distributions of the IDC (left) and the slit geometry (right) inside the sample. The area of the glass was evenly rasterized in both cases. The field strengths are normalized with the electric field of an equivalent plate capacitor with the electrode distance as gap size.

Equation (4.2) allows to calculate the corresponding loss as the ratio of both of these equations. For a homogeneous field, this leads to the known result $Q_\mathrm{i}^{-1} = \frac{\varepsilon''}{\varepsilon'}$. However, if the field is inhomogeneous, and the imaginary part $\varepsilon''(F(V))$ is field-dependent and therefore becomes a function of the volume, one has to write

$$Q_\mathrm{i}^{-1} = \frac{\int\limits_{V_\mathrm{diel}} \frac{\varepsilon''(F)}{\varepsilon'} F^2 \mathrm{d}V}{\int\limits_{V_\mathrm{tot}} F^2 \mathrm{d}V} \quad . \tag{4.26}$$

Instead of integrating the field strength over the volume, we make use of the obtained field distributions and create random numbers u according to the distribution. The distributed field strengths are then calculated as $F_\mathrm{inhom} = u \cdot F_\mathrm{hom}$, where F_hom is the field strength of a plate capacitor with the electrode distance of the IDC or slit as gap size d. We can sum over all generated field strengths F_inhom, which is equivalent to an integration over the volume, and identify $\varepsilon''/\varepsilon' = \tan\delta$ to find

$$\tan\delta_\mathrm{inhom}(F_\mathrm{hom}) = \frac{\sum\limits_u u^2 \tan\delta(uF_\mathrm{hom})}{\sum\limits_u u^2} \quad . \tag{4.27}$$

This allows us to transform Equation (2.94) or the outcomes from Equation (2.113) into the corresponding results of an inhomogeneous electric field strength distribution. When using the dimensionless bias rate ξ from Equation (2.112) one finds

$\xi \propto u^{-1}$, and thus we can directly write

$$\tan\delta_{\text{inhom}}(\xi_{\text{hom}}) = \frac{\sum\limits_u u^2 \tan\delta(\xi_{\text{hom}}/u)}{\sum\limits_u u^2} \quad . \tag{4.28}$$

In Figure 4.22 the effect of the inhomogeneous field distribution on the loss is shown. The left side shows the loss as a function of the applied driving field voltage at the capacitor and the right side its dependence on the dimensionless bias rate. In both cases the field distribution of an IDC with 50 µm finger distance was used. We compare both curves with the results of an ideal plate capacitor with homogeneous field distribution. When a gap size of twice of the IDC finger distance $d_{\text{eff}} = 100\,\mu\text{m}$ is used, we find the best agreement with the inhomogeneous case. This shows that in the case of an IDC as capacitor in a good approximation the field inside the capacitor can be described by a homogeneous field with an effective field strength of $F_{\text{eff}} = \frac{U}{d_{\text{eff}}} = \frac{U}{2d}$. Instead of performing the full calculation with the inhomogeneous field distribution, this approximation may simplify the comparison with the theory. For the slit as capacitor geometry, we assume the same result, although the found field distribution slightly differs from the IDC case. We attribute this difference to the missing appearance of high field strengths for the slit geometry in the FEMM simulation. Close to the electrodes the field should be the same for the slit and the IDC. Only for larger distances to the slit one expects a difference in the field distribution. However, the field strengths there should be small and have a minor

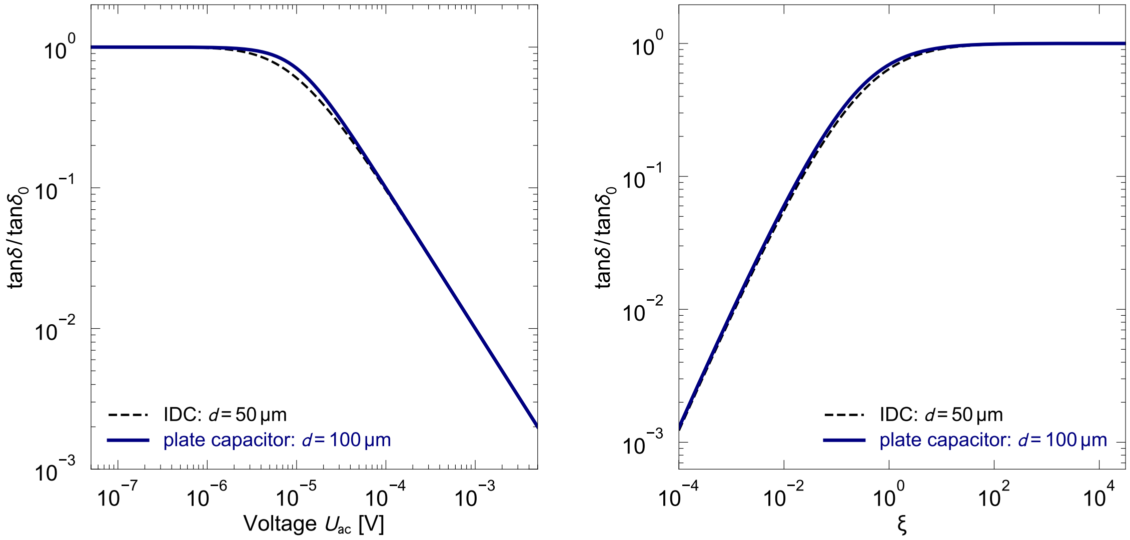

Figure 4.22: Effect of the inhomogeneous field distribution on the driving field dependence and the bias rate dependence of the loss. Instead of using the inhomogeneous field distribution the field of the capacitor geometries can be approximated with the field of a plate capacitor with twice of the electrode distance as gap size.

effect since the coupling to tunneling systems is heavily reduced.

FEMM also allows to determine the filling factor $\mathcal{F}$ of the capacitors. It can calculate the stored energy in the dielectric material and the vacuum, respectively. The ratio of the stored energy in the sample W_x and the total energy gives the filling factor

$$\frac{W_\mathrm{x}}{W_\mathrm{tot}} = \frac{C_\mathrm{x}}{C} = 1 - \frac{C_\mathrm{p}}{C} = \mathcal{F} \quad . \tag{4.29}$$

We find a value of $\mathcal{F} = 0.853$ for both capacitors. Alternatively, we can calculate the filling factor as follows. Due to the symmetry of the planar capacitor geometry, we can write the total capacitance of the capacitor as

$$C = C_\mathrm{x} + C_\mathrm{p} = \varepsilon_\mathrm{r} C_\mathrm{p} + C_\mathrm{p} \quad . \tag{4.30}$$

The parasitic capacitance is given by the electric field through the vacuum layer above the substrate. The electric field inside the sample is identical, but the capacitance is enhanced by the factor ε_r due to the additional polarization of the dielectric material. We calculate the filling factor as

$$\mathcal{F} = 1 - \frac{C_\mathrm{p}}{C} = \frac{\varepsilon_\mathrm{r}}{\varepsilon_\mathrm{r} + 1} = 0.853 \quad , \tag{4.31}$$

with $\varepsilon_\mathrm{r} = 5.8$ for N-BK7, which agrees with the value found in FEMM.

4.7 High frequency properties of superconductors

The appearance of superconductivity in metals can be understood within the BCS-theory [Bar57] where an attractive interaction between electrons, mediated by the lattice of the solid, leads to the formation of so-called Cooper pairs [Coo56]. A Cooper pair consists of two electrons with opposite momentum, which form a composite boson. If the temperature decreases below a critical value T_c, an energy gap in the single-particle density of states is formed at the Fermi energy, which causes eventually the superconductivity. While for a superconductor the DC resistance vanishes below T_c, a superconductor has a finite surface impedance Z_s for high frequency currents with frequency ω. The surface impedance is composed out of a surface resistance R_s and a surface inductance L_s

$$Z_\mathrm{s} = R_\mathrm{s} + \mathrm{i}\omega L_\mathrm{s} \quad . \tag{4.32}$$

Both are ascribed to the complex-valued conductivity of a superconductor $\sigma(\omega, T) = \sigma_1(\omega, T) - \mathrm{i}\sigma_2(\omega, T)$, which is described within the Mattis-Bardeen theory [Mat58]. Here, we want to restrict the discussion only to a qualitative understanding of the occurring surface impedance in superconductors. Magnetic fields and alternating electric fields can penetrate the superconductor only within a thin layer at the surface (London penetration depth). If Cooper pairs get accelerated by such an AC field at the surface, they cannot follow the field instantaneously due to their finite inertia. This motion out-of-phase with the excitation can be explained by introducing a kinetic inductance. The motion of Cooper pairs is free of dissipation, and hence no contribution to the ohmic resistance occurs from the Cooper pairs. However, in a superconductor for $T > 0\,\mathrm{K}$ quasi-particles arise as intrinsic thermal excitations of Cooper pairs. Their scattering mechanism is analogous to the one of electrons, which is why superconductors have a finite ohmic resistance for AC currents. The number of quasi-particles drops exponentially with decreasing temperatures. Therefore, for temperatures well below T_c the surface resistance R_s for superconducting resonators is negligible [McR20]. This is especially true in our case, where the tunneling systems in the substrate give a distinct contribution to the resonator loss at almost all relevant temperatures. Hence, we do not expect major contributions of the superconductor to Q_i. We confine ourselves to the surface inductance in the following. For a thin film of metal one finds [Bar09]

$$L_\mathrm{s} = \mu_0 \lambda \coth\left(\frac{t}{\lambda}\right) \quad , \tag{4.33}$$

where the penetration depth λ is adjusted to the thickness of the film t, and μ_0 describes the vacuum permeability. The penetration depth λ of a superconductor strongly depends on temperature. Within the London model it reads as [Hun07]

$$\lambda_\mathrm{L}(T) = \frac{\lambda_0}{\sqrt{1-\left(\frac{T}{T_\mathrm{c}}\right)^4}} \quad , \tag{4.34}$$

whereby λ_0 is material-dependent. According to [Buc13], for niobium one finds $\lambda_0 = 32 - 44\,\mathrm{nm}$. For higher temperatures, the number of Cooper pairs decreases. With that, they have to move with higher velocity because the current is carried by less pairs, which strongly increases the kinetic inductance for $T \to T_\mathrm{c}$. A temperature-dependent inductance leads to an additional shift of the resonance frequency f_0 that is unrelated to the change due to tunneling systems. When observing the temperature dependency of the dielectric function's real part at temperatures close to the critical temperature of the superconductor, this additional shift needs to be subtracted out from the results. With Sonnet® [Son18] it is possible to include a surface inductance to the simulation of the resonator circuit. This allows to simulate the shift $f_0' = \frac{1}{2\pi\sqrt{(L_0+L_1(T))C}}$ in temperature due to an additional inductance L_1 by applying Equations (4.33) and (4.34) to the simulation. We can determine the ratio

$$\sqrt{\frac{L_0 + L_1(T)}{L_0}} = \frac{f_0}{f_0'(T)} \tag{4.35}$$

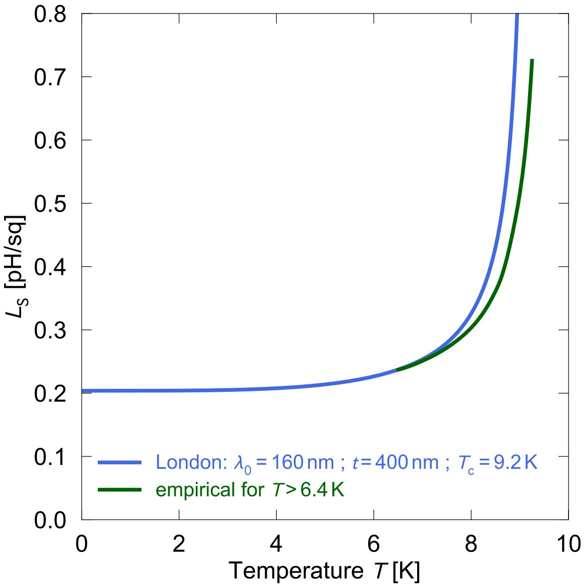

Figure 4.23: Temperature dependence of the used surface inductance L_s for the kinetic inductance correction. For $T < 6.4\,\mathrm{K}$ the penetration depth was calculated with Equation (4.34) and $\lambda_0 = 160\,\mathrm{nm}$, $t = 400\,\mathrm{nm}$, and $T_\mathrm{c} = 9.2\,\mathrm{K}$. For higher temperatures an empirical surface inductance was used (green line) [Fre16].

from the simulation at different temperatures, where f_0' denotes the simulated resonance frequency with, and f_0 without additional surface inductance. Knowing this ratio as a function of temperature allows us to correct the measured resonance frequencies $f_{0,\mathrm{m}}$ in experiment by

$$f_{0,\mathrm{cor}} = \sqrt{\frac{L_0 + L_1(T)}{L_0}} f_{0,\mathrm{m}} \quad , \tag{4.36}$$

which eliminates the shift of the resonance frequency due to the temperature-dependent kinetic inductance of the superconductor. In [Fre16] the temperature dependence of the resonance frequency for similar planar LC-resonators out of sputter deposited niobium with N-BK7 as substrate were compared to normal conducting reference resonators with similar resonance frequencies and N-BK7 as sample as well. A good agreement with the normal conducting resonators up to 9 K was found by applying the correction from above and choosing the surface inductance shown in Figure 4.23. Up to temperatures of $T = 6.4\,\mathrm{K}$ the London penetration depth from Equation (4.34) was used with $\lambda_0 = 160\,\mathrm{nm}$, $t = 400\,\mathrm{nm}$, and $T_\mathrm{c} = 9.2\,\mathrm{K}$. For higher temperatures an empirical dependency with slightly smaller L_s was needed, which is shown by green line. Below 2 K the additional shift of f_0 due to the kinetic inductance was found to be unimportant. We will make use of this correction when measuring the temperature dependency of the dielectric function above 1 K in Section 5.2.1.

5. Experimental Results

This chapter presents the experimental results obtained in this thesis. After a brief look at the thermalization of the resonators, Section 5.2 focuses on dielectric measurements in equilibrium, such as the dependency from the temperature and the driving field strength. In Section 5.3 the non-equilibrium measurements within the scope of Landau-Zener spectroscopy are presented. We end this chapter with two-tone measurements, where additional pump tones are used for driving tunneling systems off-resonantly.

5.1 Thermalization measurements

An important aspect when performing experiments at very low temperatures is the question about the thermalization. It must be ensured that the sample has adapted to the temperature of the cryostat prior to a measurement. This is especially of importance at the lowest temperatures, where the heat flux is small. Amorphous materials are known to be an origin of time-dependent internal heat leaks at cryogenic temperatures, as they release heat over long time scales due to the broadly distributed relaxation times of tunneling systems [Pob07]. Combined with their low thermal conductivity and high heat capacity, in some experiments the thermalization times exceeded several tens of hours [Luc16, Str18]. Although the used sample N-BK7 is known to be good-natured in this regard, it is essential to examine the sample's thermalization behavior in combination with the developed sample holder box.

We did that by exploiting the sample's temperature-dependent dielectric function as thermometer. Measuring the real part or loss as a function of time while lowering the temperature stepwise, allows to trace the sample's temperature. This was done in Figure 5.1 for the 250 MHz- and 1 GHz-resonator at temperatures below 50 mK. The temperature of the cryostat was lowered every 3 h to 4 h, while the temperature was held constant in between. In the case of the 250 MHz-resonator (left) $\delta\varepsilon'/\varepsilon'$ and $\tan\delta$ follow all temperature steps closely. There is no indication for a delayed response or a time-dependent convergence of the dielectric function towards the new equilibrium after a temperature step. Within the time resolution of this measurement, the sample's temperature adopts almost instantaneously to the cryostat temperature. As expected, the thermalization is unproblematic for N-BK7 at these temperatures, and the thermal coupling of the sample to the heat bath seems to be sufficient. Previous measurements of resonators with a similar thermal setup showed a fast thermaliza-

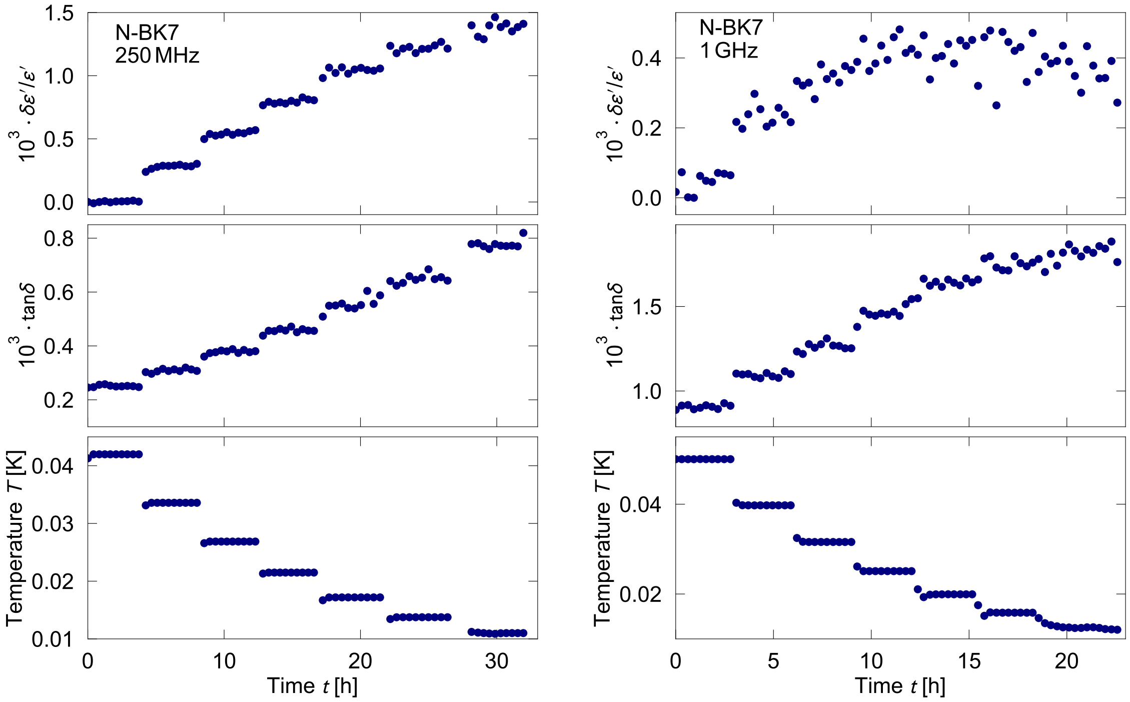

Figure 5.1: Thermalization measurements of the 250 MHz-resonator (left) and 1 GHz-resonator (right) for temperatures below 50 mK. For both setups $\delta\varepsilon'/\varepsilon'$ and $\tan\delta$ were measured, while the temperature of the cryostat was lowered stepwise.

tion of the sample as well [Fre16].

The thermalization time for the 1 GHz-resonator (right) is harder to read off. At the given driving frequency both $\delta\varepsilon'/\varepsilon'$ and $\tan\delta$ become constant at very low temperatures, compare Figure 2.15. Moreover, $\tan\delta$ is large at low temperatures, meaning a rather broad resonance curve, which reduces the resolution of the resonance frequency f_0. Therefore, the steps in temperature are not clearly mapped in $\delta\varepsilon'/\varepsilon'$ and $\tan\delta$, and both curves become more diffuse at low temperatures. However, we do observe steps in $\tan\delta$ to some extent and no complete flattening of both curves occurs which would indicate a thermally decoupled sample. In addition, the setup is equivalent to the 250 MHz-resonator so that we can assume a fast thermalization of the sample and resonator in both cases.

5.2 Dielectric equilibrium measurements

We proceed the discussion of the experimental results with dielectric measurements performed in equilibrium where no bias signal is applied to the resonator. Comparing the measured temperature dependency of the dielectric function with the predictions from the standard tunneling model allows to draw information about the tunneling system distribution function of N-BK7. Another important equilibrium measurement for this thesis is the dependence of $\tan\delta$ on the driving field strength, which we will discuss in Section 5.2.2.

5.2.1 Temperature dependency

We start the discussion of the temperature dependency by comparing the results of the 1 GHz-resonator with the results of a reentrant cavity resonating at 880 MHz [Fre16]. This cavity resonator is made out of gold plated copper, whereby N-BK7 was placed at the position where the electric field of the $\lambda/4$-mode is concentrated. Since no superconducting materials are used, the intrinsic quality factor of this resonator is quite low ($Q_\mathrm{i} < 250$). However, no parasitic contributions from superconductors are existing, which is why this cavity is well-suited as reference resonator for the novel superconducting bridge-type resonators. A comparison of $\delta\varepsilon'/\varepsilon'$ and $\tan\delta$ between both resonators is shown in Figure 5.2. Both curves were measured at the lowest possible excitation strengths to avoid saturation of tunneling systems while maintaining a reasonable signal-noise ratio at the same time. The determination of f_0 and Q was done through a resonance curve fit, see Equation (4.14). For the reentrant cavity a filling factor of $\mathcal{F} = 0.943$ was used. The real part $\delta\varepsilon'/\varepsilon'$ of the bridge resonator was corrected by the superconducting surface inductance as explained in Section 4.7. For $\delta\varepsilon'/\varepsilon'$ one finds an excellent agreement between both curves for almost the entire measured temperature range. Only for temperatures close to the

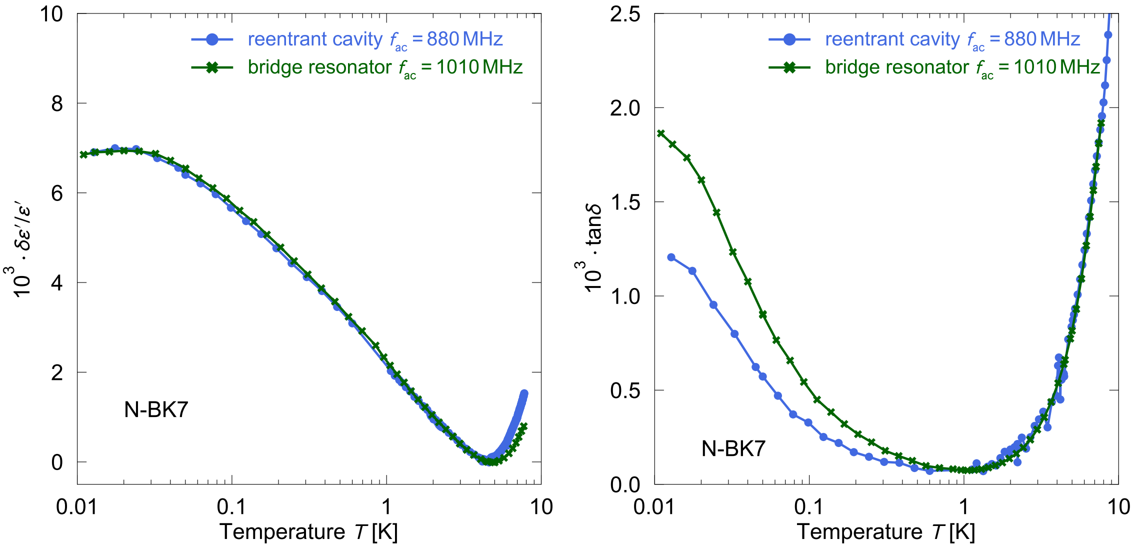

Figure 5.2: Comparison of the temperature dependency of the 1 GHz-bridge-resonator setup with a reference reentrant cavity resonating at 880 MHz with N-BK7 as dielectric material.

critical temperature of niobium small deviations are visible, which should be related to an overestimation of the applied correction of L_s. For temperatures that are most relevant in this thesis – well below 1 K – this should not be an issue.

Because of the reentrant cavity's much higher intrinsic loss, the absolute values in $\tan\delta$ of both curves differ. Therefore, in Figure 5.2 (right) the cavity's loss was shifted by a constant (3.86×10^{-3}) to match the loss of the bridge resonator at 1 K. For the bridge resonator the data were only corrected by the filling factor and the coupling quality factor. At low temperatures, the loss $\tan\delta$ of the reentrant cavity is reduced by a factor ∼1.5 compared to the bridge resonator. As we will see in the next section, in the measurement of the bridge resonator it was possible to reach the low-power limit where no saturation of tunneling systems occurs, and one measures the full tunneling system dissipation. In the case of the reentrant cavity the applied driving field was too high, and due to saturation resonant tunneling systems cannot fully contribute to the loss. Hence, the loss measured with the superconducting bridge resonator is the more adequate measurement of the sample's loss.

For temperatures above 1 K both curves agree quite well, although at these temperatures the loss due to thermally broken Cooper pairs in the superconductor becomes larger. From the nonetheless existing agreement we can conclude that for the bridge resonator the dielectric dissipation of the sample dominates the loss, and the loss caused by the superconductor is negligible, even at 8 K.

The 250 MHz-bridge-resonator can be compared with an LC-resonator which shares a similar design principle, but has only a single IDC as capacitance. This reference

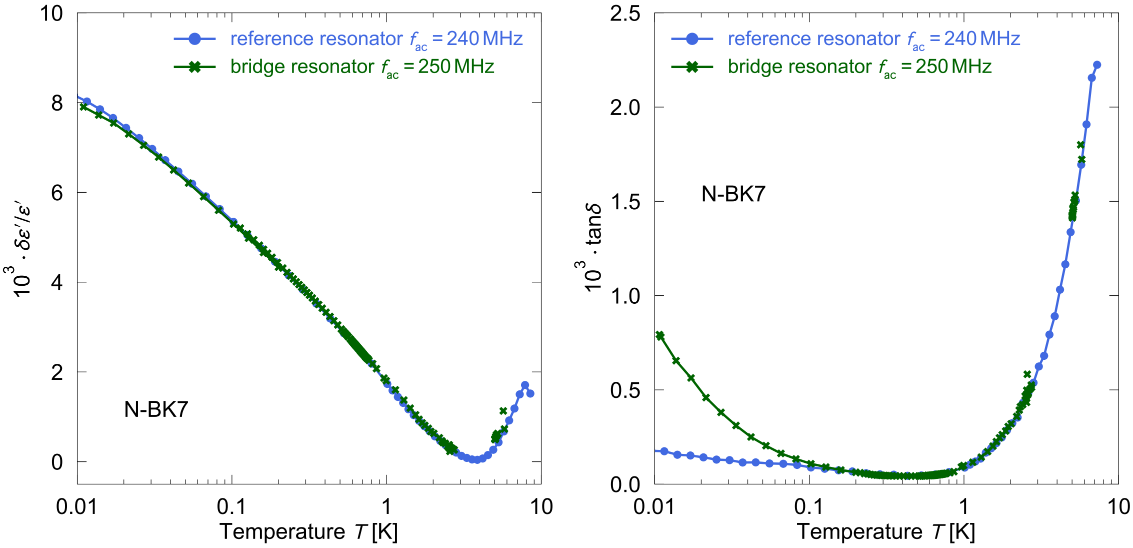

Figure 5.3: Comparison of the temperature dependency between the 250 MHz-bridge-resonator setup and a planar superconducting LC-resonator resonating at 240 MHz with N-BK7 as dielectric material as reference [Fre16].

resonator is also composed out of a planar niobium structure with N-BK7 as substrate and is discussed in [Fre16]. In Figure 5.3 the temperature dependence of $\delta\varepsilon'/\varepsilon'$ and $\tan\delta$ is compared between both resonators. The temperature-dependent surface inductance of niobium was corrected in $\delta\varepsilon'/\varepsilon'$ for both curves. The real part of the bridge resonator agrees well with the reference measurement. In $\tan\delta$ both curves diverge towards low temperatures. Again, the applied driving field was too high in the reference measurement, which lowers the loss through saturation of tunneling systems. For the bridge resonator we were able to measure at low excitations fields to observe the entire resonant loss of tunneling systems.

Next, we can compare the data of the two bridge resonators with the predictions of the standard tunneling model. From Figure 5.2 and 5.3 we can already see that the predicted logarithmic dependency of the resonant real part does not completely coincide with the measurement as the resonant slope is slightly curved when plotted with a logarithmic temperature scale. This indicates that the pure standard tunneling model distribution is not fully capable of describing the data, and the model needs to be modified. Previous measurements of N-BK7 over a wide temperature and frequency range used different modifications of the distribution function in order to attain a more compliant description [Luc16, Fre16], which we can transfer to our discussion. Here, we use the modified distribution from Equation (2.77), which accounts for interactions between tunneling systems and leads to a reduced density of tunneling states at small energies. Instead of using the standard tunneling model distribution, we insert Equation (2.77) into Equations (2.78) and (2.79) when performing the numerical integration. Moreover, we use one-phonon and two-phonon processes for the longitudinal relaxation rate τ_1^{-1}. Dielectric polarization measurements of N-BK7 showed transversal relaxation times τ_2 of several microseconds, which does not impact the temperature dependency of $\delta\varepsilon'/\varepsilon'$ or $\tan\delta$ at all, and we are allowed to use a constant value for τ_2.
Table 5.1 lists the relevant parameters used for the integration, which were applied to all curves. With these parameters we are able to describe $\delta\varepsilon'/\varepsilon'$ and $\tan\delta$ for both frequencies quite well, see Figure 5.4. In $\delta\varepsilon'/\varepsilon'$ the curves were shifted along the y-axis in order to align in the resonant part. For the 250 MHz-measurement the data of the reference resonator from Figure 5.3 was used at high temperatures. As

$A = P_0 p^2/(\varepsilon_0\varepsilon_\mathrm{r})$	$K_1\,[\mathrm{J^{-3}s^{-1}}]$	$K_2\,[\mathrm{s^{-1}K^{-7}}]$	$\tau_2\,[\mathrm{s}]$	P_0U_0	$W\,[\mathrm{K}]$
3.15×10^{-3}	7.14×10^{75}	5	1×10^{-6}	2.3×10^{-3}	5

Table 5.1: Set of parameters used for the calculation of the theory curves in Figure 5.4. The limits for the numerical integration are $E_\mathrm{max}/k_\mathrm{B} = 100\,\mathrm{K}$; $\Delta_{0,\mathrm{min}}/k_\mathrm{B} = 1 \times 10^{-7}\,\mathrm{K}$.

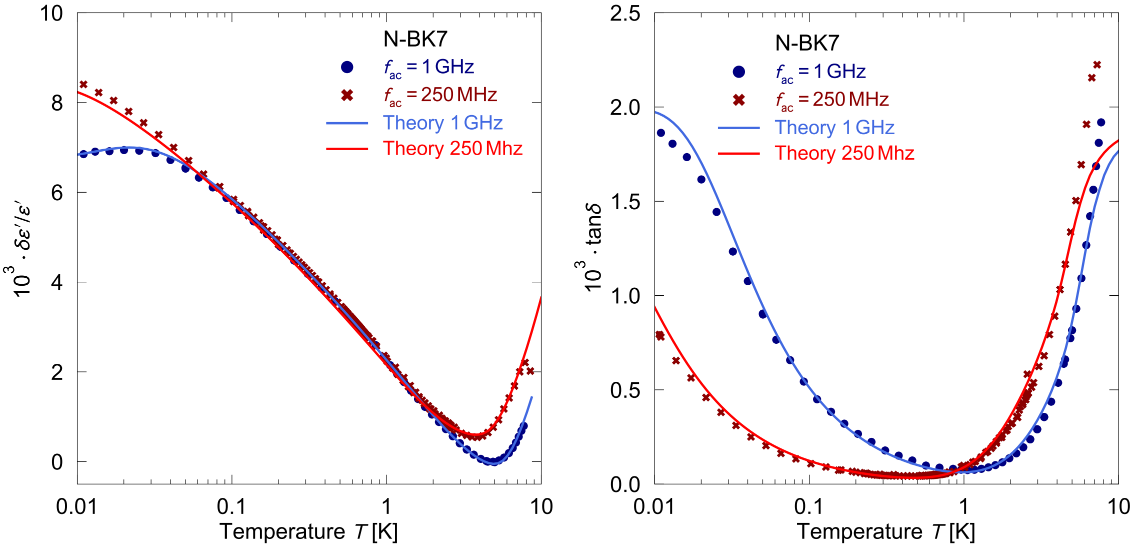

Figure 5.4: Comparison of the temperature dependency of $\delta\varepsilon'/\varepsilon'$ and $\tan\delta$ of N-BK7 with the theory predictions using the parameter set from Table 5.1 with the frequencies 250 MHz and 1 GHz. A modified distribution function, taking interactions between tunneling systems into account, was used for the theory curves.

expected, the minimum of $\delta\varepsilon'/\varepsilon'$ shifts towards higher temperatures with increasing frequency. At these temperatures, the two-phonon process determines the relaxation behavior, which leads to a steeper rise of the slope above the minimum. At high temperatures the loss is underestimated by the theory. As the comparison with the normal conducting resonator in Figure 5.2 showed, the resonator loss at high temperatures is unaffected by losses from the superconductor and should originate from the sample. At these temperatures, the description of the glass properties solely through a two-level system ensemble starts to fail because the thermal energy becomes large and may lead to thermally activated processes. Higher energy states of the underlying potential become thermally accessible too, which gives rise to localized soft modes that might start to contribute in addition to the tunneling systems. Since we are interested in the tunneling system dynamics, we will not discuss the high temperature properties further on and restrict the analysis to low temperatures.

As already mentioned, the resonant part of $\delta\varepsilon'/\varepsilon'$ does not follow a linear slope. The modified distribution due to tunneling system interactions is able to describe the slight bend of the curves for both frequencies. Moreover, the modified distribution results in a reduced resonant loss compared to the pure standard tunneling model predictions, and the ratio of the plateaus in the high and low temperature limit (see Equations 2.84 and 2.85) becomes obsolete.

In general, the resonant part is accurately described by the theory. In contrast to previous measurements the sensitivity of the setup at ultra-low driving powers is sufficient to resolve the resonant loss at very low temperatures entirely. This allows a more profound comparison with the theory predictions. The value for the dimensionless interaction parameter $P_0U_0 = 2.3 \cdot 10^{-3}$ for N-BK7 lies within the range obtained in other measurements $P_0U_0 \approx 10^{-3} - 3 \cdot 10^{-3}$ [Nat98, Lut18].

It should be mentioned that when applying this set of parameters to dielectric measurements performed in the Hz and kHz frequency regime the agreement is considerably worse. However, in the frequency range discussed within this thesis the introduced modification is quite successful in describing the data accurately.

5.2.2 Driving field strength dependency

Another important equilibrium measurement is the measurement of $\tan\delta$ as a function of the driving field strength. This allows the quantification of tunneling system saturation effects, and one can detect the limit where the resonant loss becomes unaffected by the driving field strength. Moreover, the equilibrium loss for different driving fields will later be used to compare the non-equilibrium loss of the Landau-Zener spectroscopy in the high and low bias rate limits.

In order to obtain the field strengths in the capacitor we use Equation (4.23) and apply the effective field strength that was found for the capacitor geometries in Section 4.6, and write

$$F_{\mathrm{ac}} = \sqrt{\frac{Q^2 P_{\mathrm{in}}}{4 Q_{\mathrm{c}} C d^2 \omega_0}} \quad , \tag{5.1}$$

where P_{in} is the root mean square power through the transmission line, and d is the distance between the electrodes: $d = 5\,\mu\mathrm{m}$ (1 GHz-resonator); $d = 50\,\mu\mathrm{m}$ (250 MHz-resonator). The capacitance C of a single resonator's capacitor was simulated with Sonnet® and found to be $C = 8.97\,\mathrm{pF}$ (1 GHz-resonator); $C = 3.59\,\mathrm{pF}$ (250 MHz-resonator). The input power P_{in} was altered by regulating the attenuation of the programmable attenuator. In order to retain a reasonable signal-noise ratio at the lowest driving powers, a stronger averaging, which increases the measurement time significantly, was needed there. The loss $\tan\delta$ was evaluated at the resonance minimum to minimize the effect of a varying saturation strength over the resonance curve, see Section 4.4.1 and Equation (4.16).

In Figure 5.5 $\tan\delta$ is plotted as a function of the driving field strength F_{ac} for both resonators and is compared with the theory predictions from Equation (2.94) (solid lines). Both curves show a plateau at small field strengths which is lower for the 250 MHz-measurement due to a higher thermal population of the upper two-level state. Towards higher field strengths the driving field saturates tunneling systems and the loss drops $\propto F_{\mathrm{ac}}^{-1}$ for both curves as expected from the standard tunneling model. In order to obtain this dependency, besides the coupling quality factor Q_{c}, a constant residual loss of the resonator was subtracted from the data:

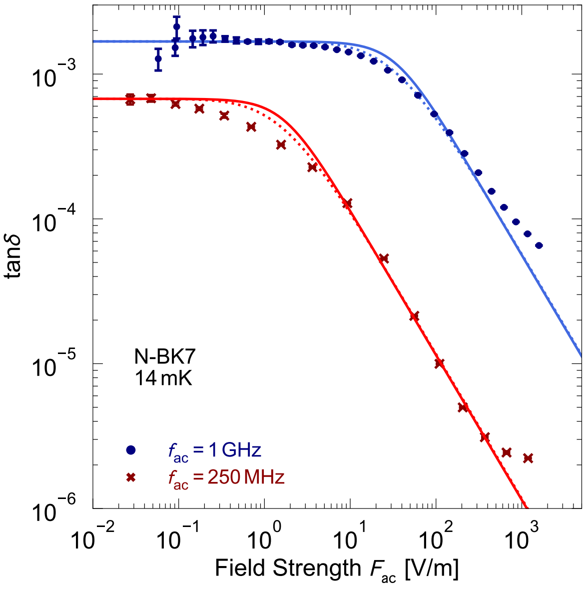

Figure 5.5: Driving field dependency of $\tan\delta$ for excitation frequencies of 1 GHz (blue filled circles) and 250 MHz (red crosses) at 14 mK compared with the predictions of theory. The dotted lines show calculations which include the inhomogeneous field distribution of the capacitor geometries. A residual loss of 4×10^{-5} and 1.35×10^{-5} for 1 GHz and 250 MHz was subtracted, respectively.

$\tan\delta_{\mathrm{res}}(1\,\mathrm{GHz}) = 4 \times 10^{-5}$; $\tan\delta_{\mathrm{res}}(250\,\mathrm{MHz}) = 1.35 \times 10^{-5}$. In addition to tunneling systems, there exist several mechanisms that limit the quality factor of superconducting resonators as reviewed in [McR20]. At low temperatures $T \ll T_{\mathrm{c}}$, as it is the case in this measurement, the loss through thermal quasi-particles is irrelevant. However, quasi-particles may be created through stray infrared light [Bar11] or ionizing particles [Vep20]. These would give a power-independent loss contribution, just the same as vortex and radiative losses [Son09, Sag11]. A mechanism that is dependent on the applied field intensity may rise from microwave induced pair-breaking. Although the microwave photons cannot directly break a Cooper pair ($\hbar\omega < 2\Delta$), the photon flux from a strong driving field can pump a quasi-particle with energy E to higher energy states $E + n\hbar\omega$. As a consequence, relaxations back to much lower energy states can lead to pair-breaking phonons which cause an enhanced density of quasi-particles and thus an enhanced loss [Gol12, dV14]. The expected loss from the mentioned mechanisms are typically of the order 10^{-5} to 10^{-6} [McR20], similar to the values found here. The specific origin for the residual loss observed here cannot be resolved at the moment.

The theory curves describe the data fairly well. As critical field strengths $F_{\mathrm{c}} = 33.5\,\mathrm{V/m}$ (1 GHz) and $F_{\mathrm{c}} = 1.7\,\mathrm{V/m}$ (250 MHz) were used. The temperature dependency measurements of the resonant loss from Section 5.2.1 were all performed at field strengths smaller than F_{c}. The dotted lines in Figure 5.5 show calculations where the effect of the inhomogeneous field distribution was explicitly regarded, which slightly improves the description of the data at the crossover into the plateau. At very high field strengths both curves flatten and do not follow the $\propto F_{\mathrm{ac}}^{-1}$ dependency anymore. At these field strengths we observe a heating of the sample, which we will discuss in the following.

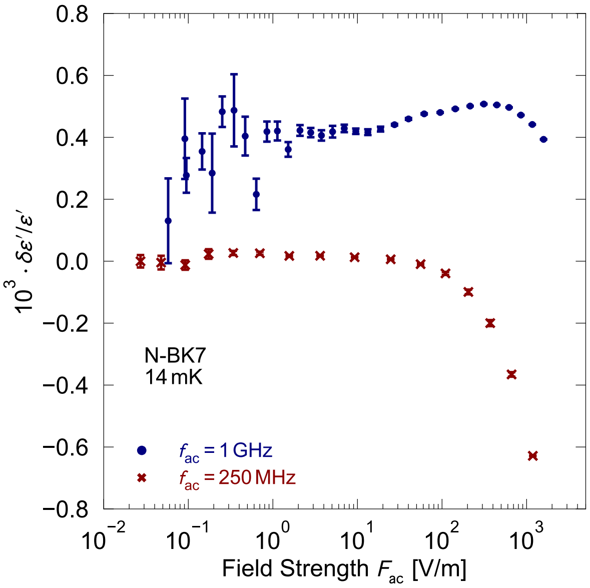

Figure 5.6: Driving field dependency of $\delta\varepsilon'/\varepsilon'$ for excitation frequencies of 1 GHz (blue filled circles) and 250 MHz (red crosses) at 14 mK.

In Figure 5.6 the real part $\delta\varepsilon'/\varepsilon'$ for both excitation frequencies is plotted as a function of the driving field strength. Towards lower field strengths the signal-noise ratio becomes worse, which is why the data starts to scatter more. For the 1 GHz-measurement this effect is enhanced because the higher loss of the sample broadens the resonance curve. In contrast to the loss, the real part should be unaffected by the saturation of resonant tunneling systems as its contributions mainly originate from off-resonant tunneling systems. Hence, $\delta\varepsilon'/\varepsilon'$ should not show a dependence on F_{ac}. However, for $F_{ac} \gtrsim 50\,\mathrm{V\,m^{-1}}$ a considerable drift is noticeable for both curves. We can relate this to an increased sample temperature, which explains the non-monotonic behavior of the 1 GHz-measurement. By comparing the data from Figure 5.6 with the temperature dependency of $\delta\varepsilon'/\varepsilon'$ in Figure 5.4, we can extract the sample's temperature at the given excitation field strength, which was done for a few points in Figure 5.7 (left). At the highest field strengths, the temperature increase is more than 20 mK. The temperature of the cryostat is not affected at these field strengths. However, a reduced heating power of the PID temperature control loop was noticeable. The dependency of the sample temperature on the field strength above $10\,\mathrm{V\,m^{-1}}$ is fitted by a cubic term

$$T_s(F_{ac}) = a \log(b \cdot F_{ac})^3 + 14\,\mathrm{mK} \quad . \tag{5.2}$$

We can use the determined sample temperature to incorporate the effect of a higher temperature into the field strength dependency of $\tan\delta$. As we can see from Equation (2.94) the temperature affects $\tan\delta$ in two ways: Firstly, it changes the thermal population factor $\tanh(\frac{\hbar\omega}{2k_B T})$. On the other hand, it also impacts F_c because the relaxation times τ_1 and τ_2 are temperature-dependent.

In [Fic13] the decay of dielectric polarization echoes was measured at different tem-

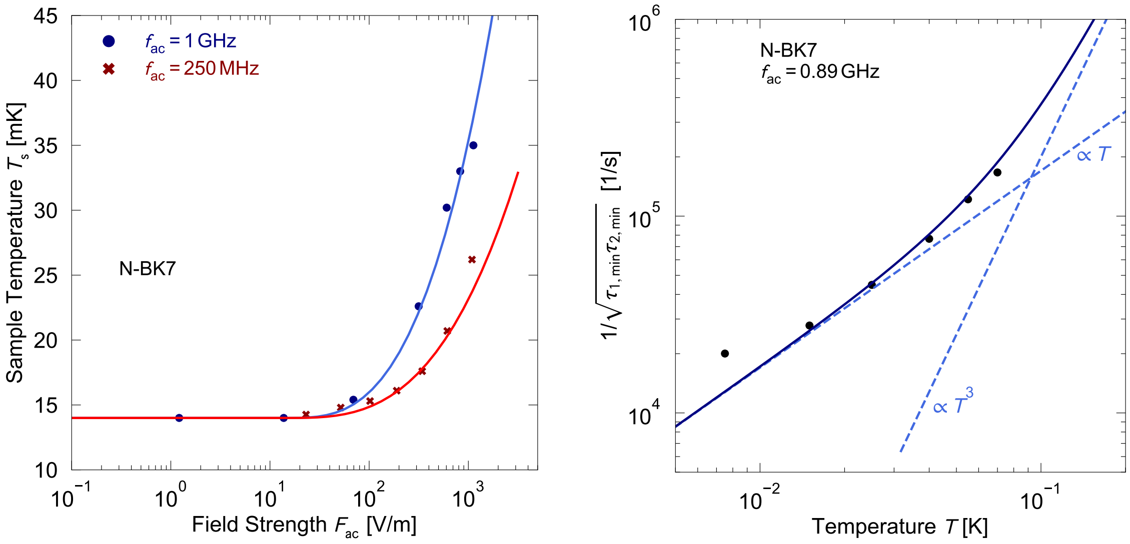

Figure 5.7: Left: Increase of the sample temperature as a function of the driving field strength for 1 GHz (blue filled circles) and 250 MHz (red crosses). Right: Temperature dependency of $F_\mathrm{c} \propto 1/\sqrt{\tau_{1,\mathrm{min}}\tau_{2,\mathrm{min}}}$ of N-BK7 at $f_\mathrm{ac} = 890\,\mathrm{MHz}$. Data from [Fic13].

peratures in N-BK7 at 890 MHz to extract $\tau_{1,\mathrm{min}}$ and $\tau_{2,\mathrm{min}}$ at these temperatures. This data is plotted in Figure 5.7 (right) for temperatures between 7.5 mK and 70 mK. In a phenomenological approach we extract the temperature dependence of F_c by fitting power laws to the data. For an excitation at 250 MHz we do not have the corresponding data, and hence, assume the same temperature dependency for the relaxation times. Combining Figure 5.7 (left) and (right) we find the dependency $F_\mathrm{c}(T_\mathrm{s}(F_\mathrm{ac}))$ which we apply to Equation (2.94) and choose for $F_\mathrm{c}(T_\mathrm{s} = 14\,\mathrm{mK})$ the values used in Figure 5.5. In Figure 5.8 the corrections due to the heated sample were considered in the dotted curves (inhomogeneous field). Although higher temperatures mean an increased thermal population, and therefore a lower loss in first place, the increase of F_c in temperature overcompensates this effect and eventually gives a higher loss. The temperature-corrected curve describes the 1 GHz-data also at strong driving fields well. For the 250 MHz-curve the temperature correction is much less pronounced and cannot explain the stronger bending of the data at high fields. Since the contribution from tunneling systems is heavily reduced there, the residual loss of the resonator plays a more dominant role. The stronger bending of the data compared to the theory at very high driving fields indicates a non-constant residual loss, possibly originating from microwave induced pair-breaking processes.

There remains the question about the origin of sample-heating at strong driving fields. In the following we want to regard this topic with a simple thermal model of the setup. We can calculate the dissipated power due to the resonator's loss with

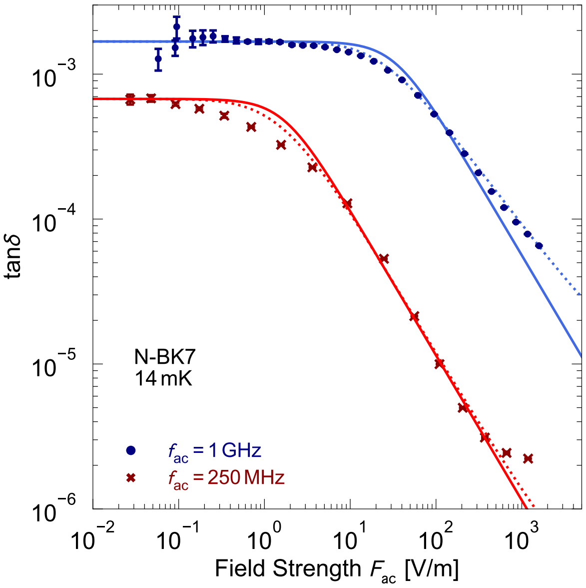

Figure 5.8: Driving field dependency of $\tan\delta$ from Figure 5.5 compared with the theory predictions. The dotted lines show calculations which regard the inhomogeneous field distribution and the temperature increase of the sample at high driving fields.

Equation (4.2). The stored energy in the resonator is given by Equation (4.20). Together with Equation (4.4) we can write down the heat load $\dot{Q}$ at $f = f_0$

$$\dot{Q} = P_{\rm dis} = 2\frac{Q}{Q_{\rm c}^2}(Q_{\rm c} - Q)P_{\rm in} \quad , \tag{5.3}$$

which becomes maximal for $Q = Q_{\rm c}/2$. The dissipated power for the 1 GHz-measurement as a function of the input power at the transmission line is shown in Figure 5.9 (left), where the data points from Figure 5.7 (left) were marked in red. Next, we can calculate the heat transfer from the sample to the cryostat. The heat mainly dissipates at the surface of the sample within the capacitors and is transported to the bottom of the sample, which is thermally connected with the copper of the sample holder box at $T_0 = 14\,\mathrm{mK}$. A rough estimation for the temperature difference ΔT between capacitor and bottom of the sample can be made as

$$\Delta T = \frac{l}{A}\frac{1}{\kappa}\dot{Q} \quad , \tag{5.4}$$

with the sample thickness $l = 1\,\mathrm{mm}$ and the area A of the heat flux cross section. Since the area of the capacitor is small compared to the substrate size, we estimate a heat flow perpendicular through an area of 1 % of the sample's surface (41 mm × 30 mm). Typical values for the thermal conductivity κ of glasses at 100 mK are of the order $\kappa \approx 10^{-6}\,\mathrm{W\,cm^{-1}\,K^{-1}}$ [Pob07]. From the $\kappa \propto T^{-2}$ dependency of glasses at low temperatures we use $\kappa_0(T_0 = 14\,\mathrm{mK}) = 10^{-8}\,\mathrm{W\,cm^{-1}\,K^{-1}}$ and find an equation for the sample temperature $T_{\rm s}$

$$T_{\rm s} - T_0 = \frac{l}{A}\frac{\dot{Q}}{\kappa_0}\left(\frac{T_0}{T_{\rm s}}\right)^2 \quad . \tag{5.5}$$

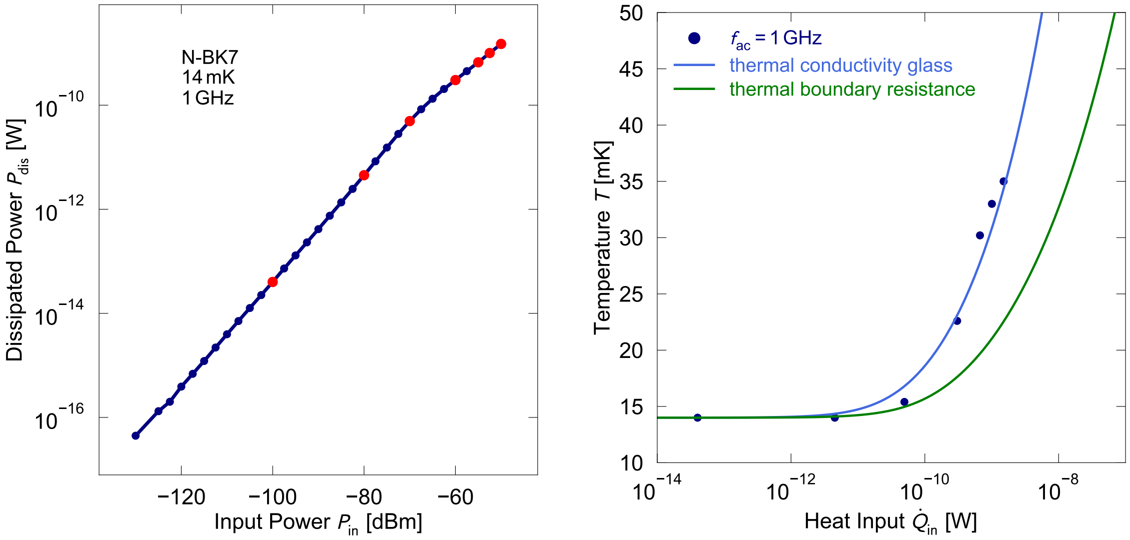

Figure 5.9: Left: Calculation of the dissipated power as a function of the input power through the transmission line at 1 GHz. The data points from Figure 5.7 (left) are marked in red. Right: Temperature increase of the sample as a function of the heat input compared to the calculated temperature increase due to the thermal conductivity of the sample and the thermal boundary resistance between the glass and copper.

This equation is solved for different input powers $\dot{Q}$ and is compared to the detected temperatures of the sample in the experiment with the corresponding dissipated power calculated before. This is shown in Figure 5.9 (right). With these rough assumptions the temperature increase of the sample is reproducible.

Moreover, we can calculate the temperature gradient due to the thermal boundary resistance between the sample and the copper underneath. This thermal resistance is caused by the acoustic mismatch between two materials and is also known as the Kapitza resistance [Pob07]. Phonons, which are responsible for the heat transport in our case, might get reflected at the boundary and reduce the heat flux. Only regarding this effect now, the temperature difference is written as

$$\Delta T = \frac{R_{\mathrm{K}}}{AT^3}\dot{Q} \quad , \tag{5.6}$$

where R_{K} is the Kapitza resistance, which is found to be about $8 \times 10^{-4}\,\mathrm{m^2K^4/W}$ for a boundary between copper and glass [Swa89, Pob07]. The effective area for the heat flux between both materials is not well-defined in our case. As before, we simply assume an area of 1 % of the sample's surface. We can solve the equation

$$T_{\mathrm{s}} - T_0 = \frac{R_{\mathrm{K}}}{AT_0^3}\left(\frac{T_0}{T_{\mathrm{s}}}\right)^3 \dot{Q} \tag{5.7}$$

for different $\dot{Q}$, which is shown in Figure 5.9 (right) as well.

The presented calculations should be understood as a very rough estimation of the expected sample's temperature. Many properties that are needed for the calculation are vague and require a detailed modeling for a more precise analysis of the thermal setup. However, we may conclude that the dissipated heat due to the resonator's loss is able to cause the observed temperature increase, and that the thermal heat flux away from the capacitor might be limited by the thermal conductivity of the glass itself.

5.3 Dielectric non-equilibrium measurements – Landau-Zener Spectroscopy

After we have discussed dielectric equilibrium measurements, we continue with measurements where an additional bias field is applied simultaneously to the rf-driving field. We start with a characterization of the bias branch before non-equilibrium loss measurements with ramped bias fields are presented.

5.3.1 Characterization of the bias signal

As a first test we characterized the crosstalk between the rf-readout branch and the biasing branch. The symmetry of the resonator should reduce the coupling between both branches significantly, which is essential for a parallel application of the bias signal and the rf-readout. In Figure 5.10 we measured the transmission $|S_{21}|$ between bias line (input) and rf-feedline (output) of the 250 MHz-setup at 19 mK. Additional dampings or amplifications due to attenuators or rf-amplifiers in the signal path were subtracted. Besides the resonance frequency at 250 MHz the crosstalk is indeed

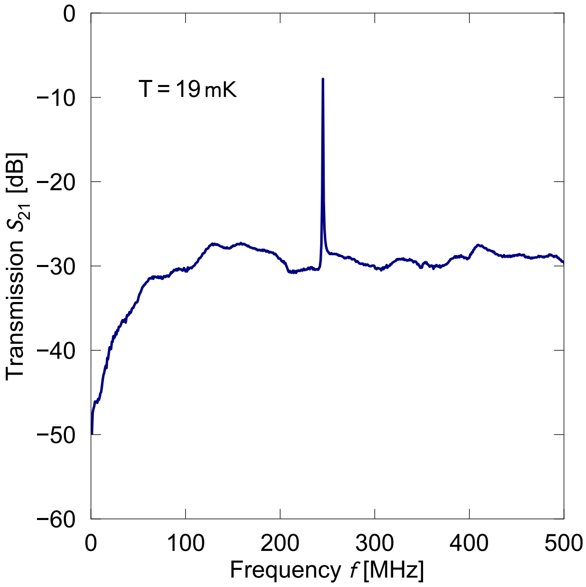

Figure 5.10: Measured transmission $|S_{21}|$ between bias (input) and rf-feedline (output) of the 250 MHz-setup at 19 mK.

heavily reduced by more than three orders of magnitude. Especially at frequencies smaller than 1 MHz, where the bias ramp timescale lies in the experiment, the device provides a very effective decoupling.

Next, we applied constant bias voltages to the resonator and repeated the measurements of the driving field strength dependency. This allows to prove an independent operation of the rf-readout under the application of a large electric DC bias field. Moreover, we are able to scan the tunneling system distribution function in Δ because the bias field leads to a constant shift of the asymmetry energy, and other tunneling systems become resonant with the driving field. Since $\tan\delta$ is mostly sensitive to resonant tunneling systems, measuring its field dependency at a constant bias field probes a different set of tunneling systems. Possible fluctuations in the tunneling system density can then be detected by measuring $\tan\delta$. The real part probes tunneling systems over a wide energy spectrum and therefore should not be substantially altered by shifts in Δ. The data for the following measurements were performed in close collaboration with the bachelor thesis of [Lut20].
In Figure 5.11 the field strength dependency from Figure 5.5 was repeated for the 1 GHz-setup while constant bias voltages were applied to the resonator. As before, Q_i was determined from the minimum of the resonance curve $|S_{21}|$. The maximum applied bias voltage of $U_\mathrm{b} = 165\,\mathrm{V}$ corresponds to a field strength of $F_\mathrm{b} = \frac{U_\mathrm{b}}{4d} = 8.25\,\mathrm{MV\,m^{-1}}$ where one needs to notice that the voltage drop across a capacitor is $U_\mathrm{b}/2$, and we can use an effective field strength of $F_\mathrm{eff} = \frac{U}{2d}$ for the capacitor geometry. Together with Equation (2.37) we calculate the energy shift in

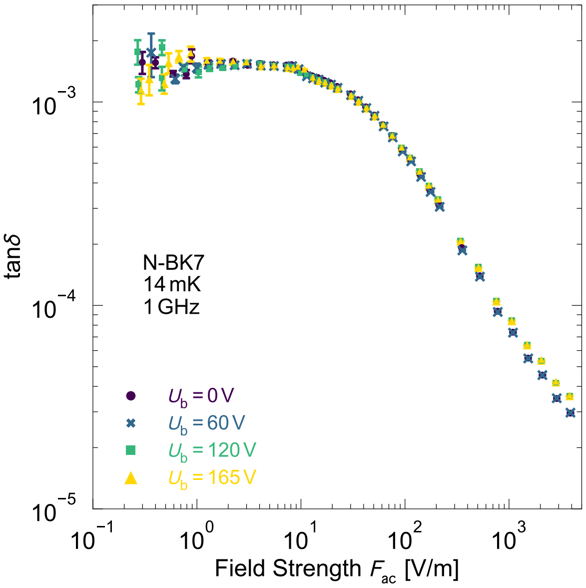

Figure 5.11: Repeating the measurement from Figure 5.5 while applying constant bias voltages U_b to the resonator. The constant bias field brings a different set of tunneling systems in resonance with the electric driving field and allows a scan of the tunneling system distribution function in Δ. Raw data from [Lut20].

$\varDelta$. By integrating over all possible dipole orientations, we obtain the mean $\langle \delta\varDelta \rangle$

$$\langle \delta\varDelta \rangle = 2pF_{\mathrm{b}}\langle \cos\theta \rangle = 2pF_{\mathrm{b}}\frac{\int_0^{2\pi}\mathrm{d}\phi\int_0^{\pi/2}\sin\theta\cos\theta\mathrm{d}\theta}{\int_0^{2\pi}\mathrm{d}\phi\int_0^{\pi/2}\sin\theta\mathrm{d}\theta} = pF_{\mathrm{b}} \quad , \tag{5.8}$$

where we integrate only over half of the sphere because the dipoles can be aligned alongside or opposed to the field direction. We then find a shift of $\langle \delta\varDelta \rangle / h \approx 62\,\mathrm{GHz}$, using a dipole moment of $p = 1.5\,\mathrm{D}$, see Section 5.3.2. Compared to the energy E of resonant tunneling systems without bias field, the bias voltage gives a massive shift in $\varDelta$.

Although a completely different range of the tunneling system distribution is probed by the single measurements in Figure 5.11, all curves align quite well with each other. This observation is in agreement with the standard tunneling model, which postulates a flat distribution in $\varDelta$. At very high driving field strengths the curves split into two subgroups. Between the recordings of both subgroups (0 V, 60 V) and (120 V, 165 V) the cryostat had been warmed up to room temperature. A small rearrangement of the chip environment, for example, may have resulted in a slightly shifted Q_{c} between both cooldowns.

For a more detailed investigation of eventual shifts in the dielectric function under a DC bias, we fixed the driving field strength to $F_{\mathrm{ac}} = 4.13\,\mathrm{V\,m^{-1}}$ and performed sweeps in U_{b}, while holding the bias voltage constant during the recording of resonance curves. Since temporal changes of the bias field lead to an enhanced non-equilibrium loss, which we will discuss later on, after a change of U_{b} we waited several minutes to give the system enough time to reach equilibrium. We chose a low driving field strength which gives a maximum contribution from tunneling systems. Possible fluctuations in the distribution function should be most pronounced there. At this field strength no saturation of tunneling systems is expected, and thus f_0 and Q were obtained by fitting a Lorentzian to the resonance curves, which slightly improves the accuracy in $\delta\varepsilon'/\varepsilon'$ and $\tan\delta$.

In Figure 5.12 $\delta\varepsilon'/\varepsilon'$ and $\tan\delta$ are plotted as a function of the DC bias field strength at 14 mK and 1 GHz. We performed two sweeps, one with increasing DC voltage and the second one in reversed direction. Neither in $\delta\varepsilon'/\varepsilon'$ nor in $\tan\delta$ we can find clear indications for variations of the dielectric function under a DC bias. Small substructures do occur, but they are of the order of the measurement's uncertainties or could not be reproduced with the other sweep. The fact that the dipole orientations are random makes a detection of local variations in the distribution difficult to observe. The shifts $\delta\varDelta = 2pF_{\mathrm{b}}\cos\theta$ due to the bias field are not the same for all elements of a group of tunneling systems initially having the same asymmetry energy $\varDelta$. This leads to a smearing in $\delta\varDelta$ when applying a bias field, and fluctuations at a certain energy would smear out as well.

However, a statement about the overall flatness of the distribution can be made.

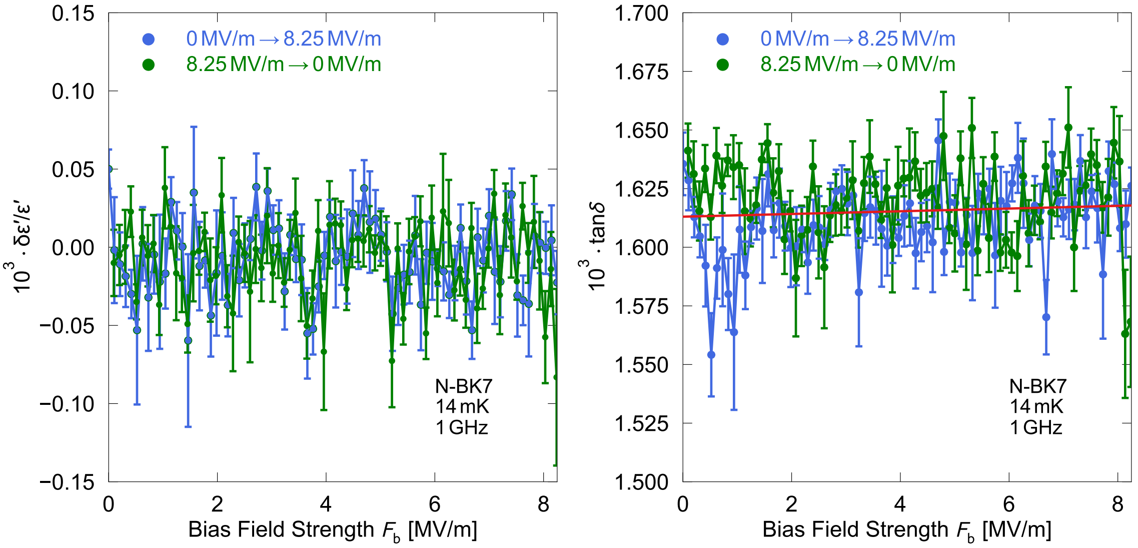

Figure 5.12: Measurement of $\delta\varepsilon'/\varepsilon'$ and $\tan\delta$ at 14 mK with a driving field strength of $F_\mathrm{ac} = 4.13\,\mathrm{V\,m^{-1}}$ at 1 GHz as a function of the DC bias field strength. Two sweeps with increasing (blue) and decreasing (green) DC bias field were performed. The red line shows a linear fit of both sweeps in $\tan\delta$. Data from [Lut20].

Therefore, we fitted the average of both sweeps in $\tan\delta$ linearly (red line) and found the value $m = (5.7 \pm 5.4) \cdot 10^{-7}\,\frac{1}{\mathrm{MV/m}}$ for the slope. According to this, we cannot detect a significant drift in $\varDelta$ when shifting it with a DC bias field. Within the accessible energy range the assumption of a flat distribution in $\varDelta$ seems legitimate. These measurements show that the bias voltage can be applied to the resonator without causing any interferences with the rf-readout of the dielectric function. Moreover, a central assumption of the standard tunneling model – a flat distribution in $\varDelta$ – can be confirmed, which proves the crucial requirement of a constant reservoir of succeeding tunneling systems for the Landau-Zener spectroscopy.

Moreover, we applied time-dependent bias voltages to the resonator in form of a sine function with amplitude $U_\mathrm{b} = 6\,\mathrm{V}$. In parallel to the periodic bias signal, resonance curves were recorded with the VNA (amplitude $|S_{21}|$ and phase φ). The VNA sweeps the driving frequency f_ac from low to high frequencies while it measures $S_{21}(f_\mathrm{ac})$. In Figure 5.13 the VNA was set to record a single resonance spectrum within 6 s. The bias frequency was alternating with $f_\mathrm{b} = 2.5\,\mathrm{Hz}$, 5 Hz, and 10 Hz. With that, during a resonance recording the bias voltage runs through a few cycles. In Figure 5.13 the resonance curves with applied periodic bias signals are compared with a resonance curve measured with disconnected bias signal (green line). We see that the resonance curves are noticeably distorted through the bias voltage as they become modulated by the periodic bias signal. This behavior can be understood by tunneling systems

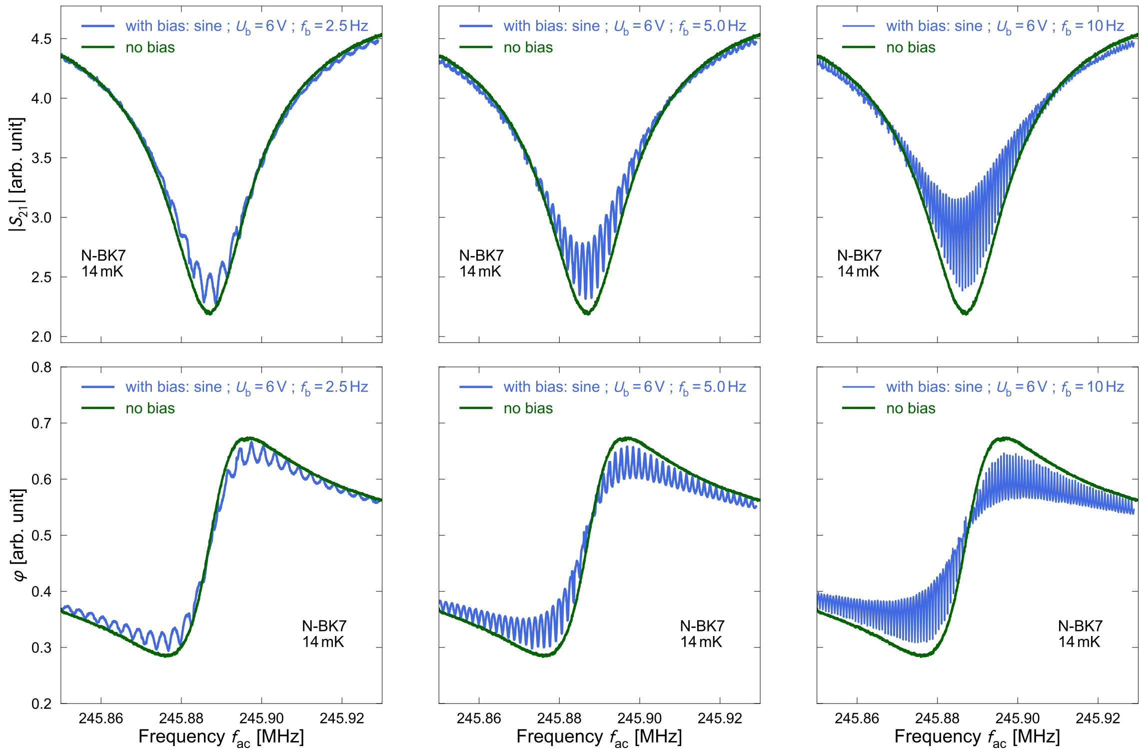

Figure 5.13: Measurement of resonance curves (amplitude $|S_{21}|$ (top); phase φ (bottom)) while biasing the resonator with a sinusoidal voltage. During the recording of the resonance curves the periodic bias leads to a constantly changing bias rate, which modulates Q and therefore leads to a modulation of the amplitude and phase.

performing Landau-Zener transitions induced by the AC bias field, which we will discuss in more detail in the next section. As we saw in Section 2.4.6, the resonant loss is sensitive to temporal changes of the bias field $\dot{F}_\mathrm{b}$. Fast changes increase the loss while for very slow bias rates one observes the steady-state loss. Applying a sine as bias signal leads to a periodic oscillation of the bias rate, and the resonant loss switches periodically between a maximum during the zero-crossings and a minimum during the turning points of the sine. This periodic switching is transferred to the resonator's quality factor Q, which then oscillates during the recording of the resonance curve and causes the modulation. Increasing the frequency of the bias signal leads to a faster modulation but also to higher bias rates during the zero-crossings, and the loss becomes even larger there. The envelopes of the modulated resonance curves correspond to the two extreme cases: maximum bias rate (smallest Q) and steady-state (highest Q). At the higher bias frequencies, the response time of the VNA is too slow to fully resolve the turning points, and the modulation cannot fully reach the no bias curve.

5.3.2 Bias rate dependency of the 1 GHz-setup

In the previous measurement we have already seen that the measured resonant loss of tunneling systems is correlated with the rate of change of an applied bias voltage. In the following we will investigate this correlation systematically by measuring $\tan\delta$ as a function of the bias rate $\dot{F}_\mathrm{b}$ and comparing the results to the predictions of the non-equilibrium loss through Landau-Zener transitions, which we have discussed in Section 2.4.6.

Instead of a continuous bias signal, as used above, the bias is changed now via a single ramp while the resonator's response is measured simultaneously. The implemented protocol for measuring $\tan\delta$ with the required time resolution is explained in Section 4.5.

After the completion of a bias ramp, the system relaxes back into the steady-state. Before the subsequent bias ramp starts, we have to satisfy a sufficient waiting time in order to retain consistent initial equilibrium conditions for the tunneling systems. Figure 5.14 shows an exemplary measurement of $\tan\delta$ under the maximal applied bias rate ($U_\mathrm{b} = 165\,\mathrm{V}$; $t_\mathrm{b} = 5\,\mathrm{ms}$). In this measurement we focused on the relaxation into the steady-state after the end of the bias ramp, which is why we performed the sequence once with a high resolution in time (dark blue curve) and a second time emphasizing longer timescales (light blue curve). The non-equilibrium loss during the bias ramp is not observable on the timescale shown here. A zoom into the bias ramp reveals a value of $\tan\delta_\mathrm{max} = 1.3\times10^{-3}$. In the top left plot one can see that the loss does not instantaneously equilibrate back into the steady-state, but needs a few seconds to do so. For a more detailed analysis of the relaxation, on the right-hand side the data is plotted with a logarithmic time axis, where the end of the bias sweep denotes $t = 0\,\mathrm{s}$. From this representation it becomes clear that the decay is composed out of more than a single time constant. We performed a fit with a decay function of the form

$$\tan\delta(t) = A_1 \exp(-t/\tau_1) + A_2 \exp(-t/\tau_2) + c \quad , \tag{5.9}$$

shown as the green line, which is the sum of two individual decays (dashed blue lines). We find that about 98 % of the total relaxation can be attributed to the first one, for which we determine $\tau_1 = 1.4\,\mathrm{ms}$. The second relaxation has a much longer time constant of $\tau_2 = 0.97\,\mathrm{s}$. A fast relaxation after the bias sweep is expected since the tunneling systems in resonance with the driving field are getting excited and perform damped Rabi oscillations within their relaxation time τ_1 into equilibrium (compare Figure 3.6 and 3.7). Because of $\Omega_\mathrm{R} \propto \frac{\Delta_0}{E}\cos\theta$ the involved Rabi frequencies are widely distributed, and hence should average out each other, and a pure relaxation behavior may remain. From the temperature dependency measurement, we obtained for the one-phonon relaxation the constant $K_1 = 7.14\times10^{75}\,\mathrm{J}^{-3}\,\mathrm{s}^{-1}$. Considering only the resonant tunneling systems $E = \hbar\omega$, we find for the one-phonon relaxation

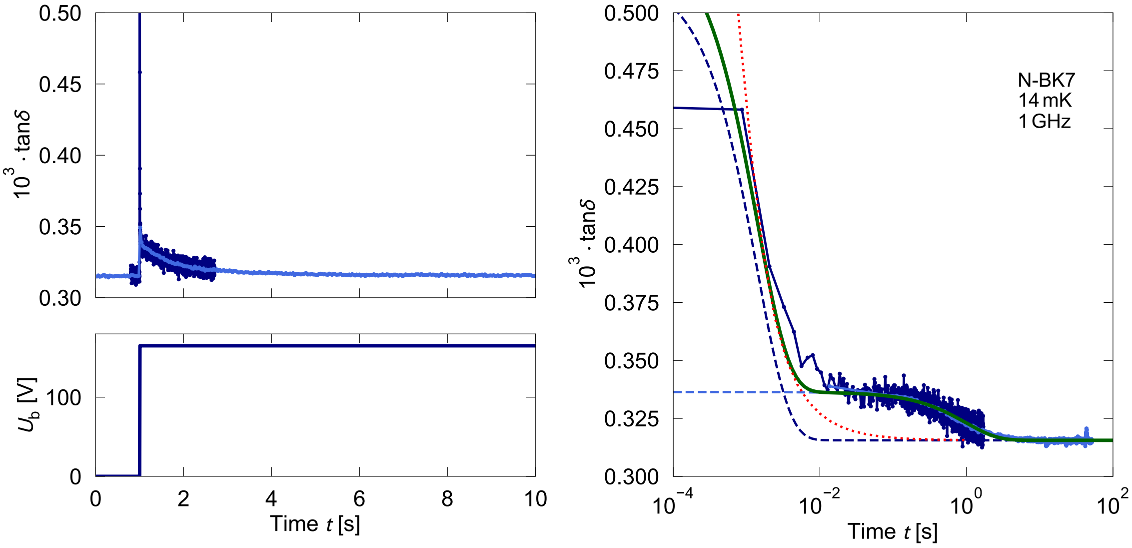

Figure 5.14: Time dependence of $\tan\delta$ during a very fast bias ramp at 14 mK and 1 GHz with a linear (left) and a logarithmic time axis (right). After the end of the bias sweep a relaxation into the steady-state within a few seconds is observed and compared with Equation (5.9) (solid green line) and Equation (5.12) (dotted red line). Data from [Lut20].

time $\tau_{1,\mathrm{min}} = 0.45\,\mathrm{ms}$ (Equation (2.68)), which is of the order of the initial fast relaxation in Figure 5.14. However, tunneling systems with distributed relaxation times are involved, and $\tau_{1,\mathrm{min}} = 0.45\,\mathrm{ms}$ should be the lower limit for a relaxation through a one-phonon process. Moreover, tunneling systems contribute with different strengths to the loss. From Equation (2.63) we find the relation for a single tunneling system $\tan\delta \propto \left(\frac{\varDelta_0}{E}\right)^2$, which means that symmetric ones give a stronger contribution to the loss, compare also Figure 3.17. We can write down the distribution function

$$P(E,\varDelta) = \frac{P_0}{E}\frac{1}{1-\left(\frac{\varDelta}{E}\right)^2}\mathrm{d}E\mathrm{d}\varDelta \quad , \tag{5.10}$$

which we can rewrite into

$$P(E,q) = \frac{P_0}{1-q^2}\mathrm{d}E\mathrm{d}q \quad , \tag{5.11}$$

where we introduced $q = \frac{\varDelta}{E}$. For the resonant loss we can write $E \approx \hbar\omega$. Using the relation $\frac{\varDelta_0}{\hbar\omega} = \sqrt{1-q^2}$, we may write, by integrating over the distribution function, the relaxation into the steady-state after the end of the bias sweep for low temperatures

$$\tan\delta(t) \propto \int_0^1 (1-q^2)e^{-\frac{t}{\tau_{1\mathrm{P}}}}P(q)\mathrm{d}q \propto \int_0^1 e^{-\frac{t(1-q^2)}{\tau_{1,\mathrm{min}}}}\mathrm{d}q \quad . \tag{5.12}$$

Rabi oscillations during the relaxation are neglected. Integrating Equation (5.12) with $\tau_{1,\mathrm{min}} = 0.45\,\mathrm{ms}$ gives a reasonable agreement with the data in Figure 5.14 (dotted red line). A thorough theoretical treatment of the tunneling system dynamics after the bias sweep and more data points at shorter times are required to give a more adequate analysis, but it can be said that the observed fast decay after the end of the bias sweep is consistent with a relaxation of tunneling systems through phonons.

The slow relaxation will also be regarded briefly. The ring-down time of the resonator is $\tau_{\mathrm{rd}} = \frac{Q}{2\pi \cdot f_0} \lesssim \frac{2000}{2\pi \cdot 1\,\mathrm{GHz}} = 0.3\,\mu\mathrm{s}$, the operational amplifier for the bias signal switches high voltages in approximately $7\,\mu\mathrm{s}$, and charging a capacitor with $C = 9\,\mathrm{pF}$ through a bias line with low DC resistance $R \simeq 100\,\Omega$ takes about $\tau = RC \approx 1\,\mathrm{ns}$. All these numbers are much shorter than the observed time constant. A look at the real part $\delta\varepsilon'/\varepsilon'$ during this bias sequence gives more information. In Figure 5.15 we see that immediately after the end of the bias sweep $\delta\varepsilon'/\varepsilon'$ is increased and relaxes back into equilibrium within the time scale of the slow relaxation observed in the loss. This increase is rather small compared to the changes observed in the temperature dependency measurement. An increase of $\delta\varepsilon'/\varepsilon'$ of this size at the given temperature and frequency could arise from a small temperature increase of the sample. As we discussed in Section 5.2.2 due to the temperature dependency of F_{c}, a higher temperature would lead to an increased loss. A slight heating of the sample through the rapid voltage ramp with a subsequent thermalization within a few seconds is a plausible explanation for the observed slow relaxation.

Another explanation is given by experiments that measure the dielectric response under a DC bias step [Sal94, Nal04, Lut18] where jumps in $\delta\varepsilon'/\varepsilon'$ caused by mutual tunneling system interactions were observed and briefly discussed in Section 2.4.6. For N-BK7 the DC steps caused jumps in $\delta\varepsilon'/\varepsilon'$ which were of a similar size as observed here. However, in these experiments a subsequent logarithmic relaxation over several hours was observed. We cannot exclude that this kind of non-equilibrium

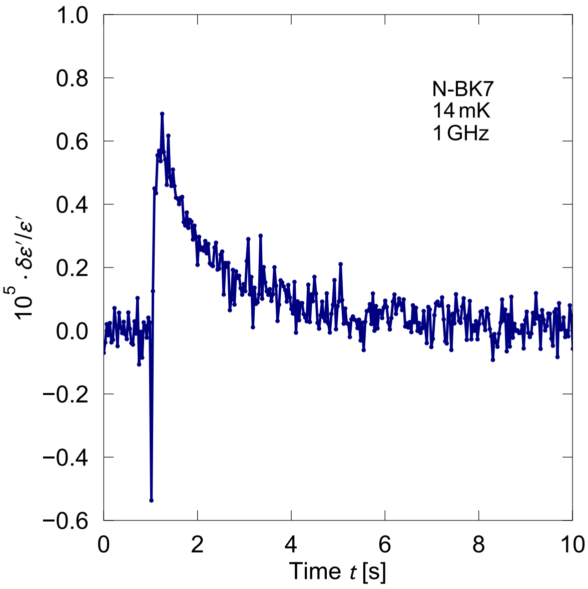

Figure 5.15: Time dependency of $\delta\varepsilon'/\varepsilon'$ for the bias sequence from Figure 5.14. After the end of the bias sweep, $\delta\varepsilon'/\varepsilon'$ jumps up and relaxes back into the steady-state within a few seconds. The increase in $\delta\varepsilon'/\varepsilon'$ is smaller than 1×10^{-5}.

dynamic is also present in this bias sequence, but its contribution to the loss should be quite small and would be dominated by the Landau-Zener dynamics.
Choosing waiting times of more than 10 s are sufficient to eliminate an effect of the slow relaxation on the subsequent bias sequence.

Next, we varied the bias ramp times t_b and measured the loss as a function of time during the bias sweep while keeping the maximal bias voltage fixed. The data for these measurements were recorded in close collaboration with the bachelor thesis of [Kö19]. The results of such a measurement are shown in Figure 5.16, where a medium driving field strength of $122\,\mathrm{V\,m^{-1}}$ was applied. We directly observe a correlation between applied bias rate and the loss. The fastest bias sweep causes an increase from $\tan\delta = 0.5\times10^{-3}$ to approximately $\tan\delta = 1.5\times10^{-3}$, whereas for the slower bias ramps the increase is much less. As discussed before, after the end of the bias ramp the loss relaxes back to equilibrium.

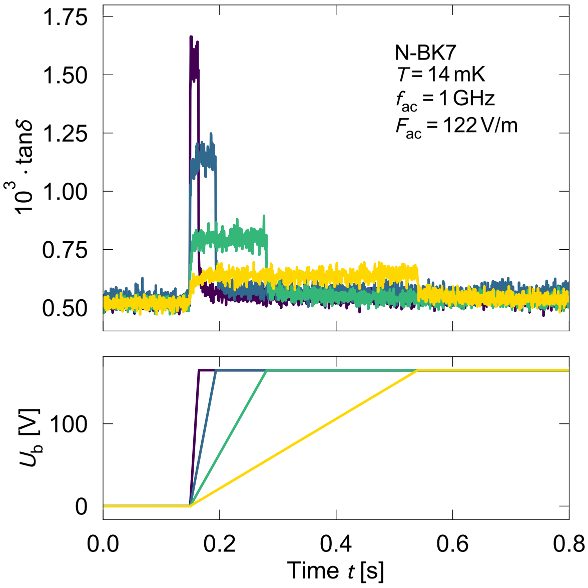

Figure 5.16: Measurement of the loss as a function of time under a bias sweep with different ramp times t_b at $T = 14\,\mathrm{mK}$, $f_\mathrm{ac} = 1\,\mathrm{GHz}$, and $F_\mathrm{ac} = 122\,\mathrm{V\,m^{-1}}$. The non-equilibrium loss during the ramp is clearly correlated with the applied bias rate. Raw data from [Kö19].

Averaging the loss during the bias ramps and calculating the bias rate as $\dot{F}_\mathrm{b} = \frac{U_\mathrm{b}}{4dt_\mathrm{b}}$ allows to plot the non-equilibrium loss due to the Landau-Zener transitions as a function of the bias rate $\dot{F}_\mathrm{b}$, which is shown in Figure 5.17 (left) for different driving field strengths. We observe a behavior as discussed in Section 2.4.6 and as it was obtained in the framework of the Monte Carlo simulation in Section 3.3.5. For very small bias rates the loss is unaffected by the bias field sweep, and we observe the steady-state results defined by the driving field strength, see Figure 5.8. The higher the driving field strength the lower the loss emerges due to saturation. When the bias rate increases, the probability for Landau-Zener transitions is enhanced. At the same time, more and more tunneling systems cross the driving field excitation energy, and the loss converges towards a plateau at very high rates which corresponds

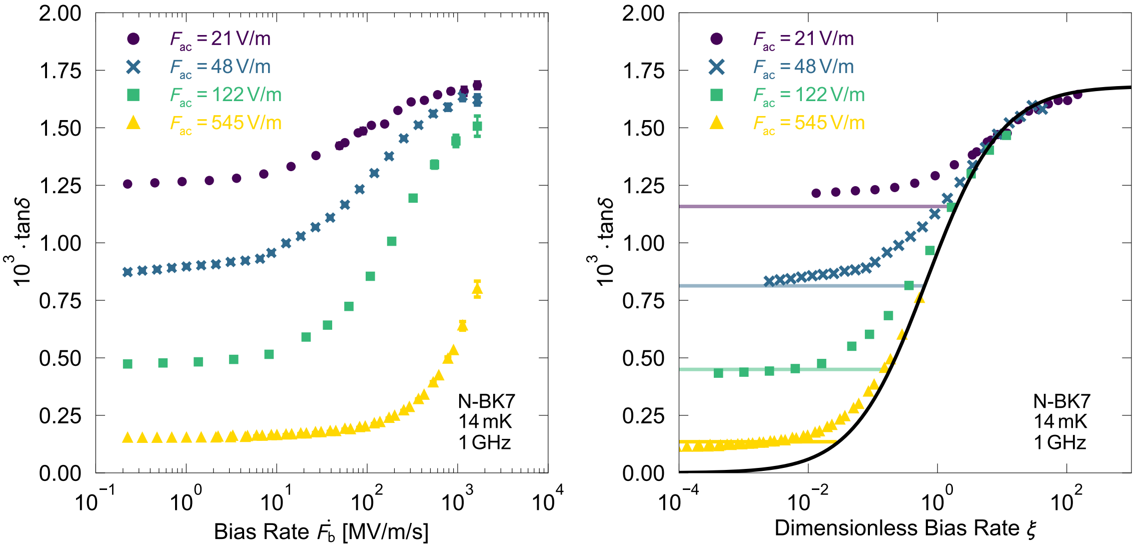

Figure 5.17: Left: Non-equilibrium loss as a function of the bias rate $\dot{F}_{\mathrm{b}}$ for four different driving fields at $T = 14\,\mathrm{mK}$ and $f_{\mathrm{ac}} = 1\,\mathrm{GHz}$. Right: When the non-equilibrium loss is plotted as a function of the dimensionless bias rate ξ, the data collapses onto a single curve for high bias rates. The horizontal lines at low rates represents the steady-state limit obtained from the field strength dependency measurement. For higher rates, the loss can be modeled with Equation (2.112) (black line). Raw data from [Kö19].

to the low-power limit in Figure 5.8. For higher driving field strengths, the bias rate needs to be higher as well in order to find the same probability for a Landau-Zener transition. This is why for $F_{\mathrm{ac}} = 122\,\mathrm{V\,m^{-1}}$ and in particular for $F_{\mathrm{ac}} = 545\,\mathrm{V\,m^{-1}}$ the highest accessible bias rate is not sufficient to reach the low-power limit.

In Figure 5.17 (right) the loss is plotted in terms of the dimensionless bias rate $\xi = \frac{4\hbar}{\pi p}\frac{\dot{F}_{\mathrm{b}}}{F_{\mathrm{ac}}^2}$ (Equation (2.112)), with F_{ac} from Equation (5.1). Note that as Q decreases for higher bias rates, F_{ac} also becomes smaller, which must be considered in the determination of ξ. The given values for the driving field strengths in Figure 5.17 correspond to the steady-state limit $\dot{F}_{\mathrm{b}} \to 0\,\mathrm{V\,m^{-1}\,s^{-1}}$. When the data is plotted in terms of the dimensionless bias rate ξ, the curves collapse onto each other for higher bias rates and can be modeled with Equation (2.113). As a scaling parameter we use the low-power limit obtained from the field strength dependency measurement $\tan\delta_0(14\,\mathrm{mK}) = 1.68 \times 10^{-3}$ at very low driving field strengths. The effect of an inhomogeneous field distribution was calculated in Figure 4.22 and gave only minor differences to the homogeneous case, which is why we used the effective homogeneous field strength $F_{\mathrm{eff}} = \frac{U}{2d}$ in the calculation of the dimensionless bias rate as well. In ξ the only unknown parameter is the average dipole moment p, which we vary in order to obtain an agreement between the data and the theory prediction. Thereby we determine the value

$$p = 1.5\,\mathrm{D} \quad . \tag{5.13}$$

The extracted value for the average dipole moment strongly depends on the field strengths inside the capacitors, and therefore, on a correct estimation of the voltage in the resonator, which requires a thorough calibration of the rf-setup.

We do not have many other predictions for the dipole moment of N-BK7. In [vS75] the product $P_0 p^2$ was obtained from the logarithmic slope of the temperature dependency for N-BK7. By using the density of tunneling systems from heat capacity measurements of vitreous silica, they stated a value of $p = 0.66\,\mathrm{D}$. From dielectric echo experiments on different silica glasses dipole moments of about $p = 0.6\,\mathrm{D}$ were obtained [Gol79]. When OH molecules appeared as impurities in these glasses, a second dipole moment at $p = 3.7\,\mathrm{D}$ was found. Other available values for average dipole moments of non-silicate glasses are $p = 1.8\,\mathrm{D}$ ($\mathrm{As_2S_3}$) [Hun86] or $p = 1.2\,\mathrm{D}$ (Mylar) [Nal04]. Measurements of amorphous thin films indicate higher dipole moments for the tunneling systems in these materials: $p = 7.9\,\mathrm{D}$ ($\mathrm{Si_3N_3}$) [Kha14]; $p = 2.9\,\mathrm{D}$ ($\mathrm{SiN_x}$) [Sar16]; $p = 2.3 - 7.4\,\mathrm{D}$ ($\mathrm{AlO_x}$) [Bre17]. The obtained value of the average dipole moment in our measurement lies within the typical range for bulk glasses. Having obtained a value for the dipole moment, allows to determine the tunneling system density P_0 from the parameter $A = P_0 p^2/(\varepsilon_0 \varepsilon_\mathrm{r}) = 3.15 \times 10^{-3}$ of the temperature dependency (see Table 5.1). Using $\varepsilon_\mathrm{r} = 5.8$ we find $P_0 = 6.46 \times 10^{45}\,\mathrm{J^{-1}\,m^{-3}}$.

In general, we find a good agreement between the data and the predicted Landau-Zener behavior of tunneling systems. Landau-Zener transitions are controllable through the applied bias rate, enabling a targeted manipulation of the population number of resonant tunneling systems, which can be used to perform a spectroscopy of the tunneling systems of the sample. In the thesis at hand, this novel Landau-Zener spectroscopy technique is used for the investigation of bulk glasses for the first time. It allows a determination of intrinsic tunneling system properties like the relaxation time τ_1 or the dipole moment p. In combination with equilibrium measurements, which can also be performed with the setup, this method allows an extensive investigation of the present tunneling systems, employing only a single device. In the further course we will utilize this technique to investigate additional aspects arising from the Landau-Zener dynamics of tunneling systems.

5.3.3 Bias rate dependency of the 250 MHz-setup

Analogously to the 1 GHz-measurement, the bias rate dependency of the loss was measured with the 250 MHz-resonator at 14 mK with an excitation of $F_\mathrm{ac} = 25\,\mathrm{V\,m^{-1}}$, which is shown in Figure 5.18. Just as for the 1 GHz-measurement, we find a good agreement with the steady-state loss at low bias rates. Going to higher bias rates the non-equilibrium loss starts to increase as expected from the Landau-Zener dynam-

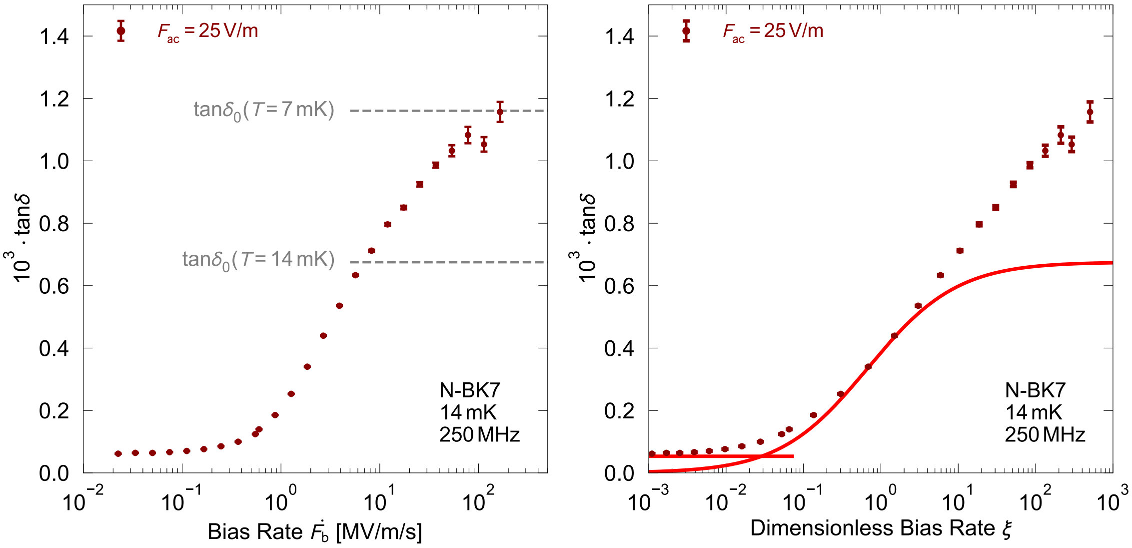

Figure 5.18: Non-equilibrium loss as a function of the bias rate $\dot{F}_b$ (left) and the dimensionless bias rate ξ (right) for a driving field strength of $25\,\mathrm{V\,m^{-1}}$ at 14 mK and 250 MHz. At low bias rates the loss agrees with the steady-state value (red horizontal line), but at higher bias rates the loss clearly exceeds the predictions from Landau-Zener transitions (red curve). The loss found at the highest bias rate corresponds to a loss of resonant tunneling systems being at 7 mK for the given excitation frequency.

ics, but then clearly overshoots the low-power loss limit from Figure 5.8. The loss at the highest applied bias rate corresponds to a resonant low-power loss of tunneling systems with a temperature of 7 mK, which is extrapolated from the low-power limit at 14 mK and applying the relation $\tan\delta \propto \tanh(\frac{\hbar\omega}{2k_BT})$. The measured loss seems to originate from systems that are ‘colder’ than the temperature of the cryostat.

On the right-hand side of Figure 5.18 the loss is plotted as a function of the dimensionless bias rate ξ which was calculated analogously to the 1 GHz-measurement. For the dipole moment we use the value from above: $p = 1.5\,\mathrm{D}$. With that, the initial increase of the data aligns well with the theory predictions (solid line), which demonstrates a consistent evaluation of ξ across the two setups. However, for high bias rates the measured loss significantly overshoots the theory predictions. Tunneling systems at 250 MHz and 14 mK do not fulfill the low temperature condition $k_BT < \hbar\omega$ where the theory of the non-equilibrium loss through Landau-Zener transition is restricted to. The applied bias field generates a maximal shift in the asymmetry energy of $\delta\Delta_{\max} \approx 12\,\mathrm{GHz}$, using the dipole moment from above again. This means that the non-equilibrium loss towards the end of the bias sweep tends to be caused by tunneling systems with an initially much larger energy splitting. If these systems are additionally rapidly swept in their energy, they cannot achieve their instantaneous thermal equilibrium before they reach the energy of the driving field.

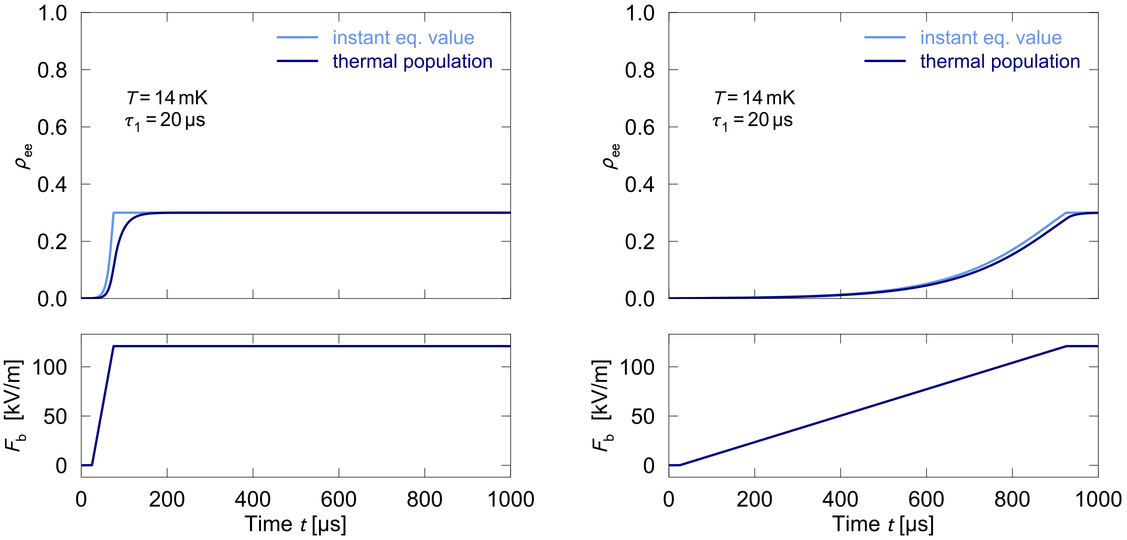

Figure 5.19: Calculation of the thermal occupation number as a function of time (dark blue) for two different ramp times with $T = 14\,\mathrm{mK}$, $\tau_1 = 20\,\mathrm{\mu s}$, $p = 1.5\,\mathrm{D}$ and no applied driving field. A tunneling system with $E/h \approx 2\,\mathrm{GHz}$ is shifted through a bias field to $E/h = 250\,\mathrm{MHz}$. The calculation is compared to the instantaneous equilibrium value (light blue).

We can illustrate this behavior by calculating the thermal occupation number of an initially heavily detuned single tunneling system being swept by the bias field F_b into resonance with the driving field. We use the simulation introduced in Section 3.1 and model a system with $\varDelta_0/h = \frac{1}{\sqrt{2}} \cdot 250\,\mathrm{MHz}$ and $\varDelta/h = -2\,\mathrm{GHz}$. The bias field is ramped from $F_\mathrm{b} = 0 - 121\,\mathrm{kV\,m^{-1}}$, which shifts the tunneling system to $\varDelta/h = -\frac{1}{\sqrt{2}} \cdot 250\,\mathrm{MHz}$ ($p = 1.5\,\mathrm{D}$). Hence, at the end of the bias ramp the tunneling system has an energy splitting of $E/h = 250\,\mathrm{MHz}$. The driving field is turned off because we only want to observe the thermal population. Moreover, we choose $T = 14\,\mathrm{mK}$ and $\tau_1 = 20\,\mathrm{\mu s}$. We then calculate ρ_ee as a function of time, which represents the thermal occupation number of the two-level system. This number is compared to the instantaneous equilibrium value $\rho_\mathrm{ee}^\mathrm{inst} = \frac{1}{2}(1 - \tanh(E(t)/(2k_\mathrm{B}T)))$, with $E(t) = \sqrt{\varDelta_0^2 + (\varDelta(t=0) + 2pF_\mathrm{b}(t))^2}$. This is shown in Figure 5.19 with two different bias ramp times. At the beginning of the sequence the energy splitting E of the tunneling system is large compared to the temperature. Hence, the system is in the ground state. When the bias is ramped, $\varDelta$ shifts towards positive values and E decreases. The upper level then becomes thermally populated. For a fast bias ramp, the relaxation time τ_1 is too slow to adopt to the instantaneous equilibrium value, and ρ_ee turns out to be much smaller than in equilibrium. For the slower ramp it can follow the equilibrium value closer. This means that in the case of fast bias ramps, the non-equilibrium loss can potentially overshoot the value of a thermally equilibrated system. In this case, the thermal population of such systems is smaller (‘colder’) than the one of equilibrated systems at resonance, and the glass can absorb more photons from the driving field, and it is even more lossy than in its steady-state low-power limit, which gives a qualitative explanation of the data.

5.3.4 Noise as bias signal

Instead of using a single ramp for the bias signal, we also applied a continuous signal in form of 1 V_{pp} white noise, generated by the signal generator. The noise was additionally amplified by the power operational amplifier, and therefore low pass filtered at 150 kHz due to the amplifier’s limited response time. As in Section 5.2.2, we measured the loss at 1 GHz as a function of the driving field strength, but applied in parallel a noise-bias signal. In this measurement the two attenuators inside the cryostat were placed from the mixing chamber level towards higher temperatures closer to the still. This slightly reduced the heating at higher field strengths and also gave a higher coupling quality factor of the resonator of $Q_{\mathrm{c}} = 4100$. The measurement in the presence of a noise bias can be compared to the previous one without bias field, see Figure 5.20 (left). In both cases the same plateau value is reached at low field strengths, but the noise-biased measurement is able to sustain this plateau value even at much higher fields, whereas tunneling systems in the steady-state are

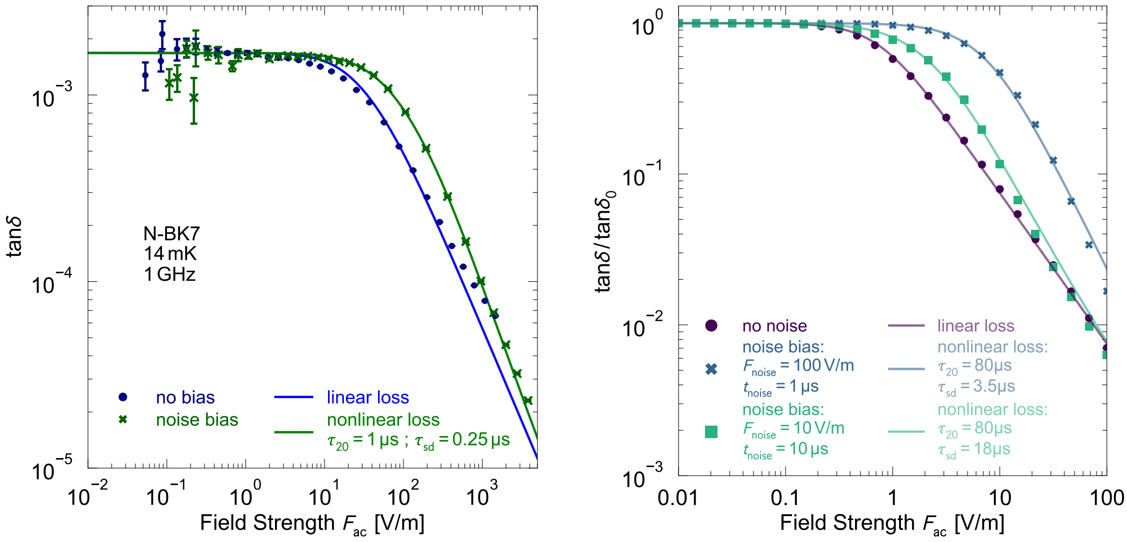

Figure 5.20: Left: Driving field dependency of $\tan\delta$ for an excitation frequency of 1 GHz at 14 mK. The data with no bias field (blue filled circles) is compared to the data with additional noise as bias voltage (green crosses). A comparison with a theory (solid green line) that explicitly considers relaxations through spectral diffusion can be made, see Equation (2.95). The noise bias has a similar effect on the loss as the spectral diffusion and agrees with the predicted behavior from the Monte Carlo simulation (right) from Section 3.3.6.

already distinctly saturated by the driving field. Going to stronger excitations, the noise-biased loss decreases and converges towards the no-bias curve, but remains enhanced.

Qualitatively, this behavior can also be understood within the theory of the non-equilibrium loss caused by tunneling systems performing Landau-Zener transitions. This has already been discussed for the Monte Carlo simulations in Section 3.3.6, which is once more shown in Figure 5.20 (right). Through the noise bias all kinds of bias rates, which continuously induce Landau-Zener transitions, occur. Thus, this counteracts the saturation through the driving field and the resonant loss becomes larger.

As it was done for the simulation, the experimental data is compared with the theory of a nonlinear microwave loss resulting from the decoherence of tunneling systems through spectral diffusion. The no-bias curve is compared with the linear loss from Figure 5.5, where the relation $\tan\delta \propto F_{\mathrm{ac}}^{-1}$ leads to a linear decrease in the log-log plot for strong excitations. In the case of the noise bias, we fit the interpolation function Equation (2.95) to the data by varying the relaxation times τ_{20}, τ_{ϕ}, and using the low-power loss $\tan\delta_0$ from the previous field strength dependency measurement. Both curves were calculated by applying the inhomogeneous field distribution explicitly, see Equation (4.27). The nonlinear loss converges towards the linear loss at high field strengths when we use $\tau_{20} = 2\tau_1 = 1\,\mu\mathrm{s}$, which seems surprisingly small for the sample. This value is in contradiction to a relaxation time only evoked through interactions with phonons, which would lead to a much larger value of about $400\,\mu\mathrm{s}$ [Bur13, Fic13], compatible with the value previously found in this thesis (compare Section 5.3.2). By using a dephasing relaxation time of $\tau_{\phi} = 0.25\,\mu\mathrm{s}$, the nonlinear loss can describe the noise enhanced loss also quantitatively reasonably well. The value of τ_{ϕ} does not have the physical meaning of a relaxation time in this context and only characterizes the artificially induced energy fluctuations of the tunneling systems phenomenologically.

The loss shows the same behavior as it is predicted by the simulation from Section 3.3.6, which underlines the importance of Landau-Zener transitions in this context. Both, for the simulation data and for the experimental data a quantification of the impact of noise on the resonant loss can be made by misusing the spectral diffusion relaxation time τ_{ϕ} as a free parameter. The measurement without applied bias is in agreement with the $\propto F_{\mathrm{ac}}^{-1}$ dependency in the saturation regime, which demonstrates that residual noise or a relaxation through spectral diffusion play a minor part in the steady-state.

This measurement shows that in order to observe the F_{ac}^{-1}-dependency of the loss in the experiment at higher field strengths, leakage of parasitic noise into the resonator must be avoided as this can cause a differing steeper decrease of $\tan\delta$ towards higher field strengths, by stimulating tunneling systems to perform Landau-Zener transitions. On the other hand, artificially applied noise as bias signal might help to detect the low-power loss $\tan\delta_0$ at higher field strengths. This can avoid tedious measurements at ultra-low input powers, which require excessive averaging and therefore time-consuming measurements. The low-power loss $\tan\delta_0$ is an important quantity for characterizing tunneling systems, e.g. their impact on high quality factor resonators or similar superconducting quantum devices. Quite unusual, instead of impairing the measurement, here, the additional noise facilitates the execution of the experiment by enabling to observe $\tan\delta_0$ even at moderate field strengths.

5.3.5 Pump tone probe tone measurements with the 1 GHz-setup

As it has already been discussed in Section 3.3.7, the combination of a dynamic shift of the tunneling system energy through a bias sweep and off-resonant pumping through strong microwave fields (pump tone) detuned from the driving field (probe tone) can cause a population inversion of the involved two-level systems at the probe tone frequency. These inverted systems then may lead to stimulated emission processes, which give rise to a distinct reduction of the resonant loss, instead of resonant absorption measured by the probe tone. Under certain circumstances even an amplification of photons at the probe tone frequency can be realized, which is revealed by a negative loss in the simulation, see Figure 3.23. From an experimental side, by using a resonator with SiN films as dielectric material, such a coherent stimulated emission of tunneling systems was stated and labeled as a random defect laser [Ros16]. In this 'lasing' regime the tunneling system ensemble changes its appearance from a dissipative into an amplifying medium for photons in the microwave regime.

In the following, we want to investigate this two-tone spectroscopy experimentally on the basis of the established Landau-Zener spectroscopy of bulk glasses. Therefore, we used the 1 GHz-resonator and applied additional microwave pump tones through the feedline. The pump tones were generated with two rf-signal generators[1] and were combined with two subsequent power combiners[2], whereby each gives an additional attenuation of 3 dB. Via the rf-branch the combined signal (probe + pump tones) couples into the resonator. Due to the resonant characteristic of the resonator, the coupling of the off-resonant pump tones into the resonator is reduced.

We start the investigation with a single pump tone detuned by $\delta/2\pi \approx 18\,\mathrm{MHz}$ from the probe tone and measured the dielectric response under a bias ramp as a function of the pump tone power. From the discussion in Section 3.3.7 we know that the bias rate should not be too small as this increases the time span between pumping

---

[1] HP 8648A/C Synthesized RF Signal Generator, Agilent Technologies, 5301 Stevens Creek Blvd, Santa Clara, CA 95051, USA

[2] Anaren 41620 Power Splitter/Combiner, Anaren, A TTM Technologies Company Headquarters, 6635 Kirkville Rd., East Syracuse, NY 13057, USA

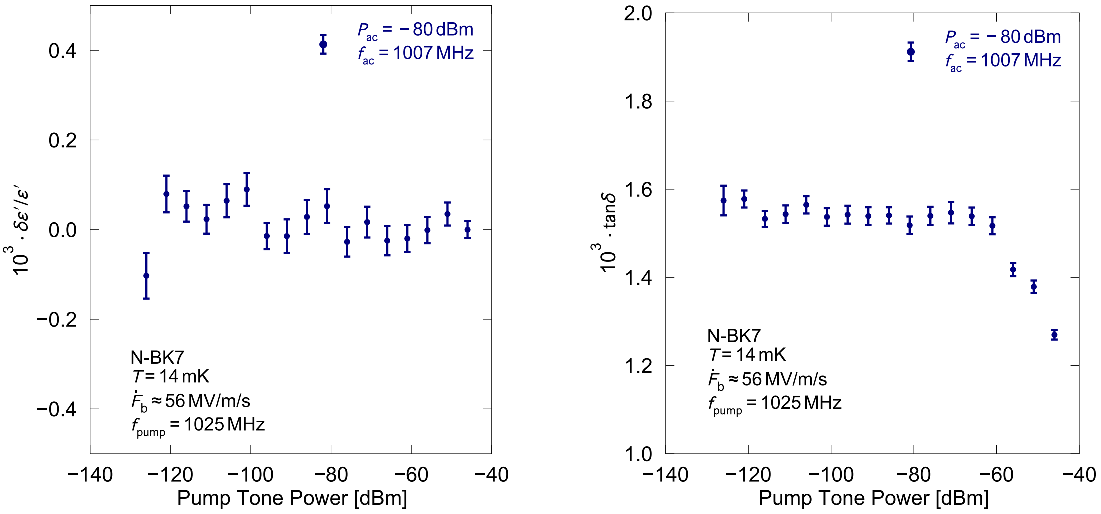

Figure 5.21: $\delta\varepsilon'/\varepsilon'$ (left) and $\tan\delta$ (right) as a function of the pump tone power in the presence of an off-resonant pump tone at $f_{\mathrm{pump}} = 1025\,\mathrm{MHz}$ and a bias ramp with $\dot{F}_{\mathrm{b}} = 56\,\mathrm{MV\,m^{-1}\,s^{-1}}$. The measurement was performed with the 1 GHz-setup at $T = 14\,\mathrm{mK}$.

and probing, and inverted systems may relax back to the ground state in between. This gives us an approximation for the lower limit of $\dot{F}_{\mathrm{b}} \gtrsim \frac{\hbar\delta}{2p\tau_{1,\mathrm{min}}} \approx 6.0\,\mathrm{MV\,m^{-1}\,s^{-1}}$ when we use $p = 1.5\,\mathrm{D}$ and $\tau_{1,\mathrm{min}} = 200\,\mathrm{\mu s}$. On the other hand, the bias rate cannot be made arbitrarily fast because this increases the probability for tunneling systems to perform Landau-Zener transitions at the pump tone frequency, which gives no effective energy transfer from the pump tone to the tunneling system. We set the bias rate to $\dot{F}_{\mathrm{b}} = 56\,\mathrm{MV\,m^{-1}\,s^{-1}}$, which is well above the lower limit. By varying the pump tone power, we change the upper limit for the bias rate $\dot{F}_{\mathrm{b}} \lesssim \frac{pF_{\mathrm{pump}}^2}{2\hbar}$ below which population inversion of tunneling systems should be possible. Thus, above a certain threshold power the condition for the upper limit might be fulfilled, and hence we should observe a reduction of the loss.

Figure 5.21 shows the results of this measurement with the discussed parameters applied. The given numbers for the powers refer to the values provided at the transmission line. The probe tone power of $P_{\mathrm{ac}} = -80\,\mathrm{dBm}$ corresponds to a weak field strength of $F_{\mathrm{ac}} = 21\,\mathrm{V\,m^{-1}}$, which was used in Figure 5.17.

The real part $\delta\varepsilon'/\varepsilon'$ in Figure 5.21 (left) seems to be unaffected by the pump tone power. However, the loss reveals a noticeable reduction above $P_{\mathrm{pump}} \approx -60\,\mathrm{dBm}$. We could not apply much higher pump tone powers as this heated up the cryostat. Having found an indication for a reduction of the loss in the presence of a bias sweep and a pump tone, we fixed the pump tone power at $P_{\mathrm{pump}} = -46\,\mathrm{dBm}$ and measured the loss as a function of the bias rate.

For this measurement we applied two pump tones at $f_{\mathrm{pump1}} = 1000\,\mathrm{MHz}$ and $f_{\mathrm{pump2}} =$

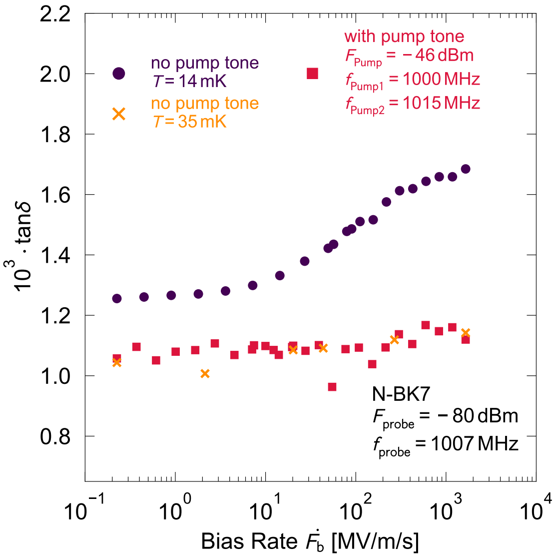

Figure 5.22: Comparison of the bias rate dependency without applied pump tones (purple filled circles) to a measurement with two strong pump tones (red squares). The measurement without applied pump tones was repeated at a higher temperature $T = 35\,\mathrm{mK}$ (orange crosses), which reproduces the data of the pump tone measurement. All curves were measured with a probe tone power of $F_{\mathrm{probe}} = -80\,\mathrm{dBm}$.

1015 MHz, which is shown in Figure 5.22 (red squares). This measurement is compared to the corresponding data without applied pump tones from Figure 5.17 (purple filled circles, $F_{\mathrm{ac}} = 21\,\mathrm{V\,m^{-1}}$). The loss with applied pump tones clearly deviates from the one without pumping. However, this deviation occurs also at bias rates well below the approximated lower limit ($\dot{F}_{\mathrm{b}} = 6.0\,\mathrm{MV\,m^{-1}\,s^{-1}}$), where in principle no reduction of the loss from photon-emitting tunneling systems is expected. This behavior indicates a different origin for the reduced loss.

We could reproduce this reduction when the temperature of the cryostat was increased to $T = 35\,\mathrm{mK}$ and the bias rate dependency was measured without applying any pump tones (orange crosses). The steady-state value is reduced compared to the measurement at lower temperature due to the higher thermal occupation number $\tan\delta \propto \tanh(\frac{E}{2k_{\mathrm{B}}T})$. At this temperature the given probe tone field strength is sufficiently weak and does not cause any tunneling system saturation in the steady-state. One observes the low-power loss already at the lowest bias rates and no increase towards higher bias rates occurs. Apparently, the deviations through applying strong pump tones to the resonator arise from a heated sample.

A potential source for the heating might be the contacting of the transmission line with normal conducting copper wires and its fixation through the conducting silver paint. When strong pump tones run through this connection, heat might dissipate in close vicinity to the sample or directly on top of it and cause the rise in temperature. Other measurements with changed pump and probe tone powers, different pump tone detunings, or an application of the pump tones through the bias line could not reveal a clear evidence for a reduction of $\tan\delta$ besides the occurrence of heating when strong pump tones were applied. Therefore, we did a revision of the resonator setup where basically all normal conducting elements close to the sample were replaced with superconducting ones, see Section 4.4.4. This should reduce the heat load when applying strong pump tones and might enable us to observe changes in the tunneling system population due to the off-resonant pumping in these two-tone spectroscopy measurements.

5.4 Two-tone spectroscopy

The following measurements were all performed with the resonator introduced in Section 4.4.4. We start with a short characterization of the resonator followed by the results of two-tone measurements in combination with sweeps of the bias field.

5.4.1 Characterization of the revised 1 GHz-setup

In Figure 5.23 resonance spectra of the resonator at $T = 14\,\mathrm{mK}$ and different driving powers P_{ac} were recorded. At low driving powers the resonance has a Lorentzian line shape, whereas for higher powers the curves become more asymmetric. At the highest input powers, one observes a discontinuous jump of the amplitude which indicates a nonlinear Duffing oscillator-like behavior. The resonator's coupling quality factor of $Q_{\mathrm{c}} = 37.000$ is much higher than the design value, which leads to large electric currents running at high driving powers for driving frequencies close to the resonance frequency. We suppose a breakdown of the superconductivity at high P_{ac}, causing an abrupt drop of the quality factor and leading to the jump in the resonance curve. Such a breakdown may rise from weak links in the superconductor that become normal conducting under high rf-driving fields. This local heating may drive the surrounding into the normal state, which results in a thermal runaway

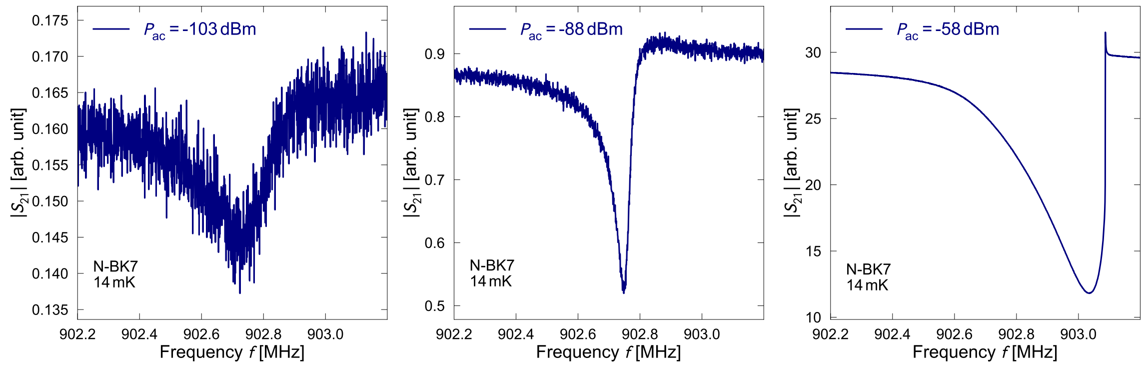

Figure 5.23: Comparison of resonance spectra of the revised 1 GHz-resonator measured at $T = 14\,\mathrm{mK}$ and different driving powers P_{ac}. At high driving powers the resonator shows a nonlinear behavior.

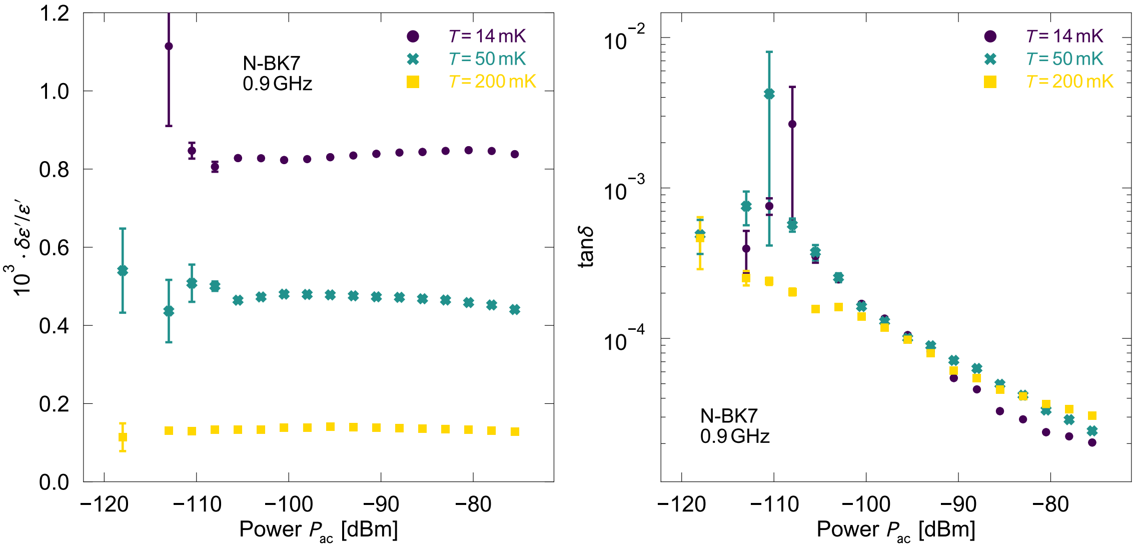

Figure 5.24: Power dependency of $\delta\varepsilon'/\varepsilon'$ and $\tan\delta$ at different temperatures $T = 14\,\mathrm{mK}; 50\,\mathrm{mK}; 200\,\mathrm{mK}$ measured with the revised resonator at $f_{\mathrm{ac}} = 0.9\,\mathrm{GHz}$.

[Gol95, Gur06]. The resonance frequency and the quality factor then cannot be determined unambiguously, and we restrict the further measurements to driving powers below $P_{\mathrm{ac}} \lesssim -75\,\mathrm{dBm}$ where no breakdown is noticeable.

We measured $\delta\varepsilon'/\varepsilon'$ and $\tan\delta$ as a function of the excitation strength. In contrast to Section 5.2.2, $\delta\varepsilon'/\varepsilon'$ and $\tan\delta$ were plotted as a function of the driving power P_{ac} supplied at the feedline of the resonator, which is shown in Figure 5.24 for the temperatures $T = 14\,\mathrm{mK}; 50\,\mathrm{mK}; 200\,\mathrm{mK}$. The maximum driving powers correspond to an effective field strength of $F_{\mathrm{ac}} \approx 2\,\mathrm{kV\,m^{-1}}$ in the capacitor, which is similar to the maximum values found in Figure 5.6. The real part $\delta\varepsilon'/\varepsilon'$ does not show a severe power-dependent behavior. Slight shifts can be observed for all temperatures, which might be related to the appearing asymmetry towards higher driving powers. Heating caused by a strong excitation seems not to be a major issue for this resonator.

The loss $\tan\delta$ shows the expected increase towards lower driving powers for all temperatures. The weak coupling of the resonator to the feedline makes it difficult to achieve a weak driving that is required to observe the unsaturated tunneling system loss $\tan\delta_0$. Hence, the transition into a plateau at low powers cannot be observed in the data. The dependence of $\tan\delta$ on the excitation appears weaker than predicted by the standard tunneling model, as we observe $\tan\delta \propto 1/P_{\mathrm{ac}}$ rather than $\tan\delta \propto 1/\sqrt{P_{\mathrm{ac}}}$. The absence of the plateau at low input powers prevents a more detailed analysis.

The measurement of the temperature dependency allows to compare the resonator with the previous results from Figure 5.4. This was done in Figure 5.25 where the

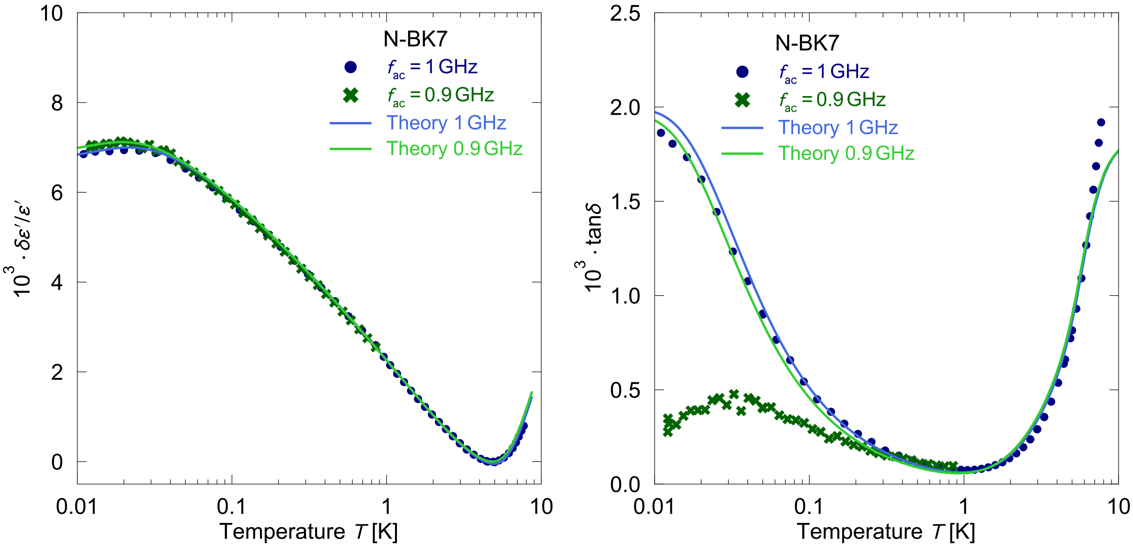

Figure 5.25: Temperature dependency of $\delta\varepsilon'/\varepsilon'$ and $\tan\delta$ measured with the revised resonator at $f_{\mathrm{ac}} = 0.9\,\mathrm{GHz}$ and $P_{\mathrm{ac}} = -105\,\mathrm{dBm}$. The data is compared to the results of the 1 GHz-resonator from Figure 5.4. For the theory predictions the parameters from Table 5.1 were used.

results of the revised setup are compared to the results of the 1 GHz-resonator. The real part $\delta\varepsilon'/\varepsilon'$ agrees well with the previous measurement. Small deviations at the lowest temperatures are related to the smaller excitation frequency f_{ac}, which are also visible in the theory curves. The good agreement proves a proper functionality of the revised setup as it can detect the resonant part of N-BK7 at low temperatures correctly. For the theory predictions we used the parameters from Table 5.1.

The resonant loss on the other hand deviates significantly from the previous measurement with the other resonator ($f_{\mathrm{ac}} = 1\,\mathrm{GHz}$). As we have seen in Figure 5.24, we are unable to perform the measurement of $\tan\delta$ at adequate low driving powers that are necessary to observe the unsaturated resonant loss. Hence, the measured loss for this resonator ($f_{\mathrm{ac}} = 0.9\,\mathrm{GHz}$) is considerably reduced. Moreover, one observes a non-monotonic behavior at lower temperatures. In Section 5.2.2 we have already discussed the effect of temperature on the saturated loss. The critical field strength F_{c} of the tunneling systems depends on their relaxation times and therefore increases towards higher temperatures. For a field strength $F_{\mathrm{ac}} > F_{\mathrm{c}}$ this would lead to an increased loss which counteracts a decreasing loss from the thermal population $\tan\delta \propto \tanh(\frac{\hbar\omega}{2k_{\mathrm{B}}T})$. Depending on the driving power, the temperature dependency of $\tan\delta$ can exhibit a local maximum and one observes a non-monotonic behavior at low temperatures. A measurement of F_{c} as a function of temperature would provide more clarity and at the same time represents a method for measuring the temperature dependency of the relaxation times.

At higher temperatures, the saturation of tunneling systems decreases and $\tan\delta$ converges towards the 1 GHz-result. In order to reach smaller excitations this resonator requires a more sensitive rf-readout. Applying a low temperature amplifier and circulators at low temperatures should provide a considerable reduction of noise. Moreover, the coupling strength of the resonator should be increased, which would increase the signal of the resonance curves. Especially for N-BK7, which possesses a high dielectric loss, a much stronger coupling is feasible without ending in a coupling-dominated total quality factor that would reduce the resolution in $\tan\delta$.

5.4.2 Two-tone measurements

In Section 5.3.5 we could not observe a noticeable impact from off-resonant pump tones to the dielectric response at the probe tone frequency besides heating signatures. When we applied pump tones through the transmission line of the revised resonator – for the moment without a bias sweep – we could observe a characteristic behavior in $\delta\varepsilon'/\varepsilon'$ and $\tan\delta$.

An off-resonant pump tone led to a shift of the resonance frequency into the direction of the pump tone frequency, which means that a pump tone below the resonance frequency shifts the resonance curve to smaller frequencies, while a pump tone above the resonance shifts the curve to higher frequencies. The observed shifts were of the order $10 - 100\,\mathrm{kHz}$. Moreover, when the pump tone was set close to the resonance frequency, the width of the resonance curve significantly decreased. The stronger the pump tones had been, the more pronounced these effects appeared.

Figure 5.26 shows a measurement where the detuning of the pump tone frequency $\delta f_{\mathrm{pump}} = f_{\mathrm{pump}} - f_{\mathrm{probe}}$ was changed with respect to the probe tone frequency at $f_{\mathrm{probe}} = 902\,\mathrm{MHz}$. While the pump tone was held constant, resonance spectra were recorded at $P_{\mathrm{probe}} = -91\,\mathrm{dBm}$, which gives $\delta\varepsilon'/\varepsilon'$ and $\tan\delta$. Then, the pump tone frequency was changed and new resonance spectra were recorded. These scans were repeated for different pump tone powers P_{pump}. We observe the behavior mentioned above. A pump tone below the probe tone frequency leads to an increase in $\delta\varepsilon'/\varepsilon'$ (smaller resonance frequency). This increase is observed until the pump tone is very close to the probe tone, where $\delta\varepsilon'/\varepsilon'$ changes its sign and the characteristic is mirrored. In $\tan\delta$ we observe a distinct drop when the pump tone gets close to the probe tone. This behavior, especially the antisymmetric one in $\delta\varepsilon'/\varepsilon'$, cannot simply be attributed to heating and must have its source elsewhere.

In the following we will see that this behavior can be attributed to the annihilation of discrete tunneling system contributions by the pump tone. Similar results were found in measurements where two identical coplanar wave guide resonators were coupled to each other, which gave two resonance modes (symmetric and antisymmetric) with overlapping electric fields. When one mode was readout with a small probe

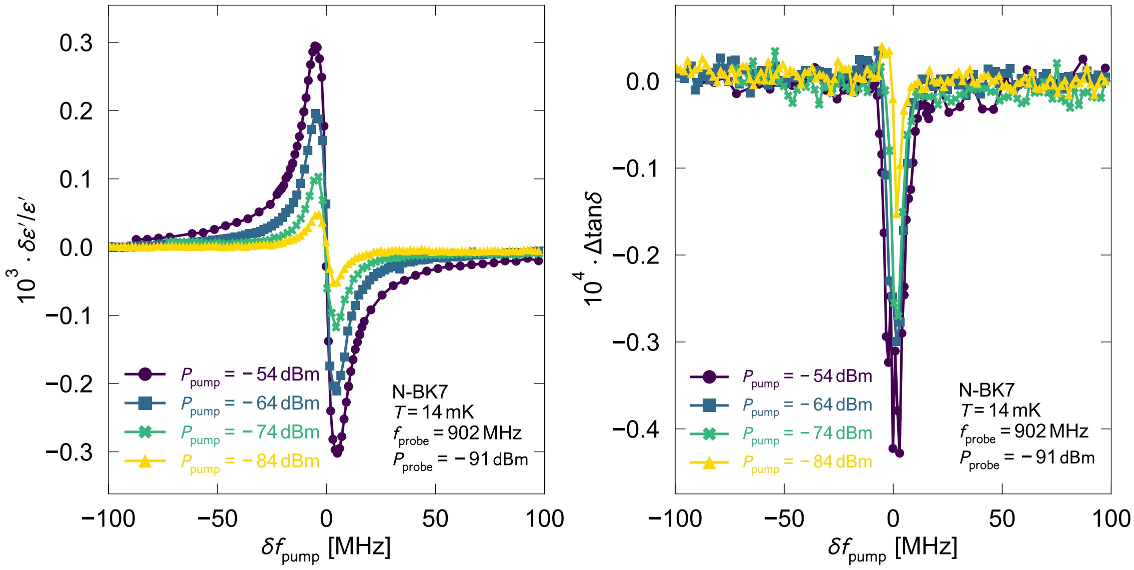

Figure 5.26: Two-tone measurement of $\delta\varepsilon'/\varepsilon'$ (left) and $\tan\delta$ (right). The dielectric response is detected with a probe tone $P_{\mathrm{probe}} = -91$ dBm; $f_{\mathrm{probe}} = 902$ MHz while the pump tone detuning $\delta f_{\mathrm{pump}} = f_{\mathrm{pump}} - f_{\mathrm{probe}}$ is scanned across the probe tone frequency. The measurements were performed with different pump tone powers P_{pump} at 14 mK.

tone while the other mode was driven through a strong pump tone, a shift of the probed resonance towards the pump tone frequency was observed [Kir17]. Recently, in two-tone spectroscopy measurements similar to the ones performed here, the same characteristic modification of the probed resonance was observed when off-resonant pump tones were scanned through the resonance frequency of a lumped-element resonator [Cap20]. In the following we will give a qualitative explanation for this behavior before we introduce a simplified model which allows to analyze the data on a quantitative level.

Figure 5.27 shows a cartoon of the tunneling system contributions originating from tunneling systems in resonance with the probe (blue) or pump tones (red, green). In (a) the situation of vanishing pump tones is shown. This situation corresponds to the dielectric resonant response of tunneling systems in the steady-state being driven at a single frequency f_{probe}. We measure the dielectric response at f_{probe}, which is the sum of tunneling system contributions over a broad energy range. The contributions of single tunneling systems to the dielectric function are given by Equations (2.62) and (2.63) and are shown in Figure 2.12 (right). At very low temperatures also tunneling systems with small energy splittings (red) are thermally in the ground state and can contribute to the dielectric function. The real part ε' primarily consists of off-resonant tunneling system contributions (red and green), while resonant tunneling systems (blue) give the major contribution to the imaginary part ε''. In the case

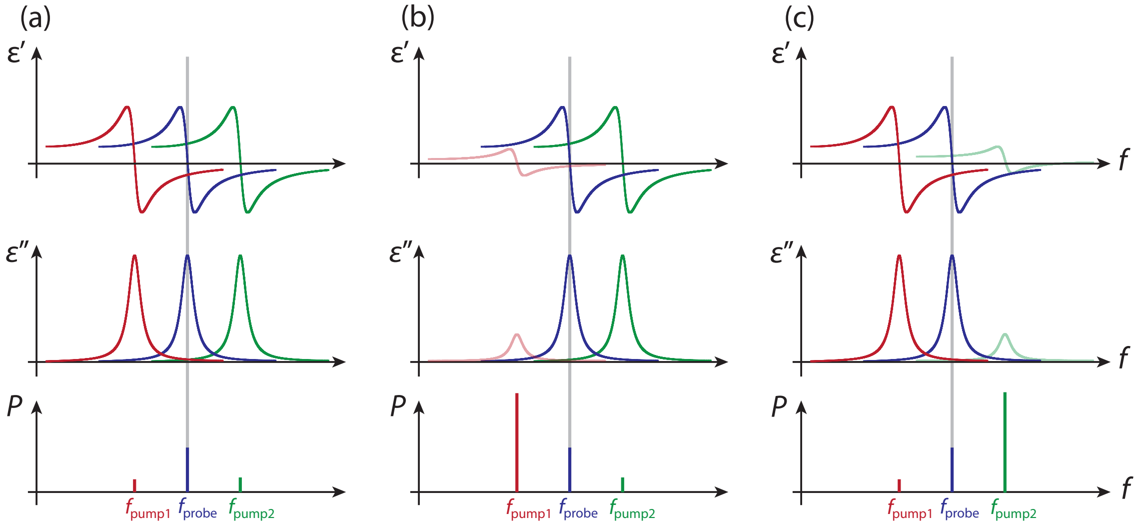

Figure 5.27: Illustration of single tunneling system contributions to the dielectric response at the probe tone frequency. Strong off-resonant pump tones reduce the contributions from off-resonant tunneling systems, which leads to the observed characteristic behavior in $\delta\varepsilon'/\varepsilon'$ and $\tan\delta$.

of a strong probe tone, the saturation of resonant tunneling systems ($E \approx hf_{\text{probe}}$) reduces their contributions to the dielectric function. For the real part, this affects positive and negative contributions evenly, which balance out each other and results in a net change of zero. Only the imaginary part will effectively be reduced, which we have already studied extensively within the saturation of the resonant loss.

The situation changes if we saturate off-resonant tunneling systems with a pump tone (b) and (c). If the pump tone is large, the contribution from off-resonant tunneling systems vanishes. In the case of a pump tone frequency below the probe tone frequency (b), a tunneling system which is in resonance with the pump tone (red) cannot fully contribute, and its negative contribution is missing in the total real part. As a consequence, the real part increases. This tunneling system gives only a small contribution to the resonant imaginary part, and thus, the loss measured at f_{probe} is almost unaffected by a heavily detuned pump tone. Only for small detunings the missing positive contributions to the loss are noticeable and the loss decreases eventually.

A strong pump tone above the probe tone frequency leads to an opposed behavior in the real part as positive contributions from saturated tunneling systems are missing at the probe tone response (c). Changes of the loss are symmetrical with regard to the pump tone detuning. With this qualitative picture we can explain the antisymmetric frequency shift of the resonance frequency for different pump tone detunings, as well as the reduction of the loss for pumping close to probe tone.

Next, we will transfer this illustrative picture into the actual dielectric response of tunneling systems. The total contribution of tunneling systems to $\delta\varepsilon'/\varepsilon'$ and $\tan\delta$ is given by Equations (2.78) and (2.79), where the single tunneling system response is integrated over the distribution function. Since we perform the measurements at low temperatures, we only consider the resonant part and neglect the relaxation processes. The pump tone reduces the contribution from tunneling systems at $E \approx hf_{\mathrm{pump}}$, which can be interpreted as a hole in the distribution function. In acoustic 'hole burning' experiments it was observed that a saturation pulse creates a hole in the tunneling system density that was much broader than the expected line width from the frequency uncertainty or the tunneling systems' finite lifetimes [Arn75, Arn78]. Hole widths of the order of 50 MHz were observed for BK7 at 0.5 K. It has been argued that the broadening occurs from tunneling system interactions which can be treated in terms of spectral diffusion. We will simplify the discussion here by ignoring specific details of spectral diffusion and simply use a Lorentzian at f_{pump} with line width w for the hole in the distribution. The width $w = 2\gamma$ (FWHM) will be treated as a free parameter. We write the hole as

$$p(E, f_{\mathrm{pump}}) = 1 - \frac{|S_{21}^{\mathrm{ideal}}|}{1 + \left(\frac{(E/h - f_{\mathrm{pump}})}{\gamma}\right)^2} \quad . \tag{5.14}$$

Close to the resonance frequency of the resonator the saturation through the pump tone becomes more efficient, which is why we scale the depth of the hole with the resonance shape of an ideal LC-resonator

$$|S_{21}^{\mathrm{ideal}}| = \frac{1}{1 + 4Q^2\left(\frac{\delta f_{\mathrm{pump}}}{f_{\mathrm{probe}}}\right)^2} \quad , \tag{5.15}$$

with $\delta f_{\mathrm{pump}} = f_{\mathrm{pump}} - f_{\mathrm{probe}}$. A stronger pump tone leads to a stronger saturation and therefore results in a deeper hole that should scale with the saturation factor from Section 2.4.5. This would allow to calculate the absolute strength of this effect. Here, we simply use a prefactor that contains the scaling of the whole effect and write

$$\frac{\delta\varepsilon'}{\varepsilon'} \propto \int\limits_{\Delta_{0,\mathrm{min}}}^{E_{\mathrm{max}}} \mathrm{d}E \int\limits_{\Delta_{0,\mathrm{min}}}^{E} \mathrm{d}\Delta_0 \left(\frac{\Delta_0}{E}\right)^2 \tan\left(\frac{E}{2k_{\mathrm{B}}T}\right) b'(E,\tau_2) P(E,\Delta_0) p(E, f_{\mathrm{pump}}) \tag{5.16}$$

$$\tan\delta \propto \int\limits_{\Delta_{0,\mathrm{min}}}^{E_{\mathrm{max}}} \mathrm{d}E \int\limits_{\Delta_{0,\mathrm{min}}}^{E} \mathrm{d}\Delta_0 \left(\frac{\Delta_0}{E}\right)^2 \tan\left(\frac{E}{2k_{\mathrm{B}}T}\right) b''(E,\tau_2) P(E,\Delta_0) p(E, f_{\mathrm{pump}}) \tag{5.17}$$

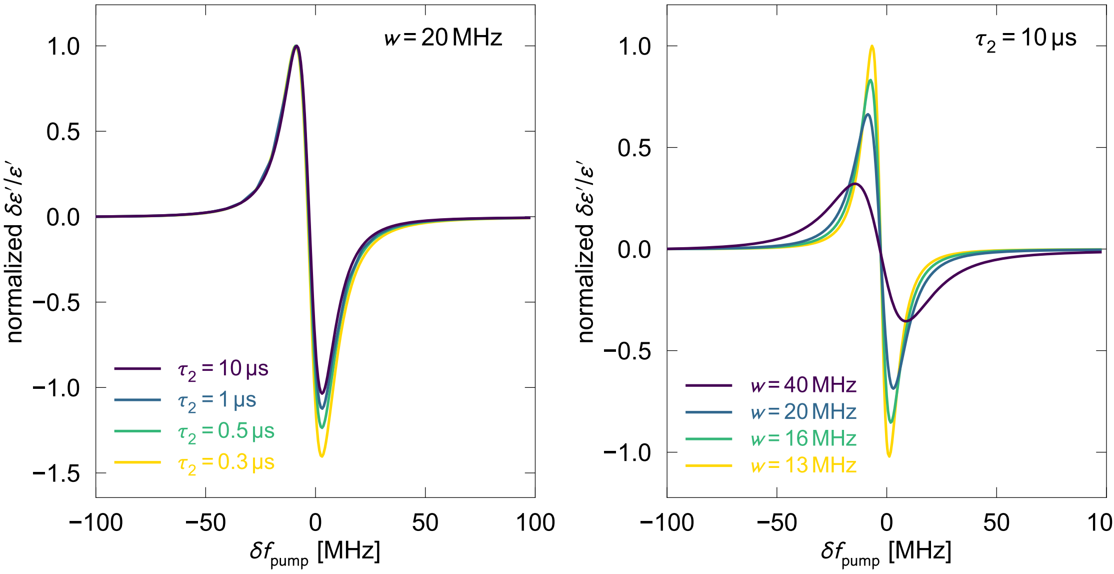

Figure 5.28: Calculation of the shift in $\delta\varepsilon'/\varepsilon'$ with a simplified model where contributions from tunneling systems are missing in the tunneling system density due to a created hole at f_pump by the pump tone. The influence of the dephasing time τ_2 (left) and the width of the hole w (right) on $\delta\varepsilon'/\varepsilon'$ were tested. Details are explained in the text.

In this simplified model we have basically two free parameters: the width of the hole w and the dephasing time τ_2.

In the following, we want to take a short look at the results from the introduced model and see how these two parameters influence the outcomes. In Figure 5.28 (left) Equation (5.16) was numerically integrated as a function of the pump tone detuning for different dephasing times τ_2 and a fixed width $w = 20\,\mathrm{MHz}$. The model reproduces the characteristic shift in $\delta\varepsilon'/\varepsilon'$ for different detunings. The dephasing time τ_2 scales the real part, which we compensated for by normalizing the curves with their maximum value. With that, we see that smaller values for τ_2 lead to an asymmetric line shape, while for $\tau_2 \gtrsim 10\,\mathrm{\mu s}$ the curve becomes antisymmetric.

In Figure 5.28 (right) we kept the dephasing constant ($\tau_2 = 10\,\mathrm{\mu s}$) and varied the hole width. All curves were normalized to the maximum of the $w = 13\,\mathrm{MHz}$ curve. When the hole becomes wider – the hole depth was the same for all curves – the extrema of $\delta\varepsilon'/\varepsilon'$ sit further apart from each other. At the same time the amplitude decreases. This behavior makes sense when we consider the case of a very broad hole. Such a hole annihilates tunneling system contributions below and above the probe tone frequency, and thus, positive and negative contributions are missing almost symmetrically and compensate each other. Hence, the net change in $\delta\varepsilon'/\varepsilon'$ vanishes.

As the next step, we apply these calculations to the data from Figure 5.26, which is shown in Figure 5.29. The data do not show any asymmetry with regard to the

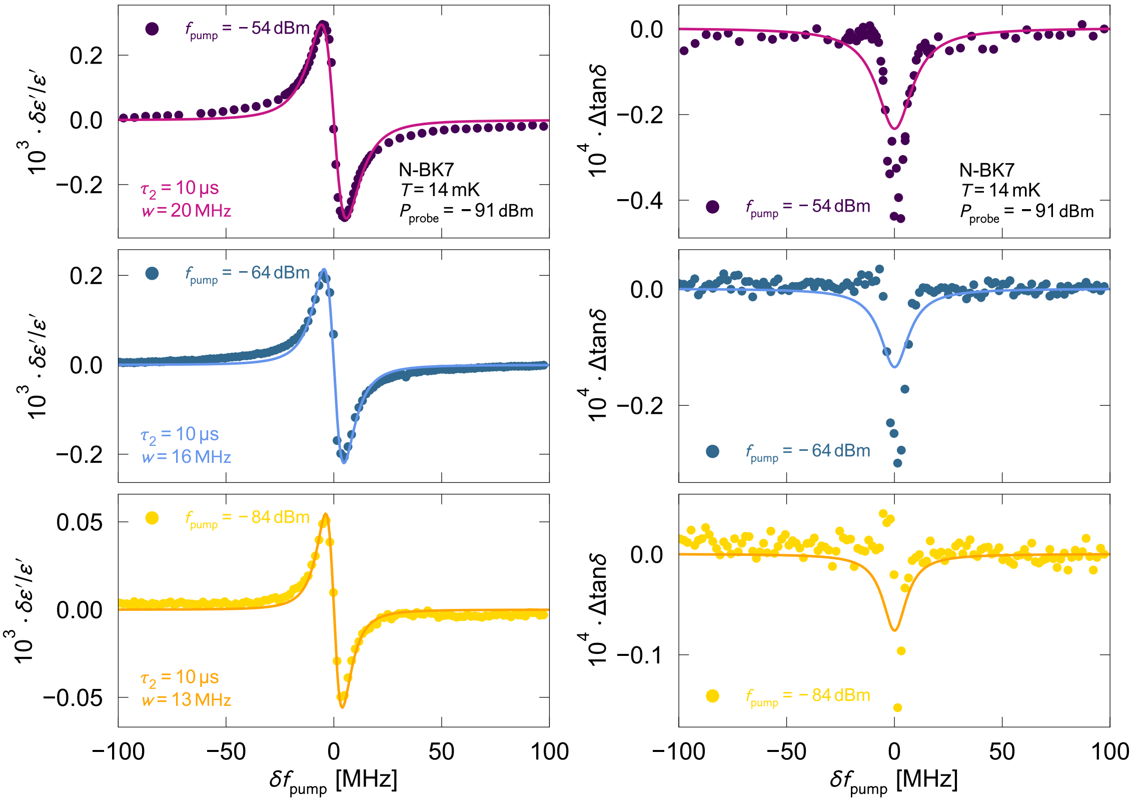

Figure 5.29: Comparison between the data and the calculations from the introduced model. The model is able to explain the observed characteristic in $\delta\varepsilon'/\varepsilon'$ and $\tan\delta$ qualitatively and allows to quantify the dephasing τ_2 and hole w to some extent.

extrema in $\delta\varepsilon'/\varepsilon'$, and we can apply values $\tau_2 > 10\,\mu\text{s}$. Thus, the model gives a lower limit for the average dephasing time that is consistent with the value for N-BK7 found in polarization echo measurements of $\tau_{2,\text{min}} = 6.5\,\mu\text{s}$ at 15 mK [Fic13]. For the description of the data we emphasized the real part, which we are able to describe fairly well with our model when we use a free scaling parameter and fit the width w of the hole to each curve. For the strongest pump tone, the shift in $\delta\varepsilon'/\varepsilon'$ is the largest. Moreover, we find the broadest hole there. For smaller pump tone intensities, the shift decreases and the width of the hole becomes more narrow. We can interpret a more narrow hole for weaker pumping with a spectral diffusion mediated hole-broadening. The energy fluctuation rate of tunneling systems caused by spectral diffusion is the same across all measurements. For a weaker pump tone Landau-Zener transitions, induced by the energy fluctuations, are more likely, which reduces saturation and results in a smaller hole.

The effect on $\tan\delta$ was calculated with the same parameter set. A general description of the data is possible. The observed dip becomes more narrow towards weaker pumping, however, the agreement from the real part cannot be accomplished. For

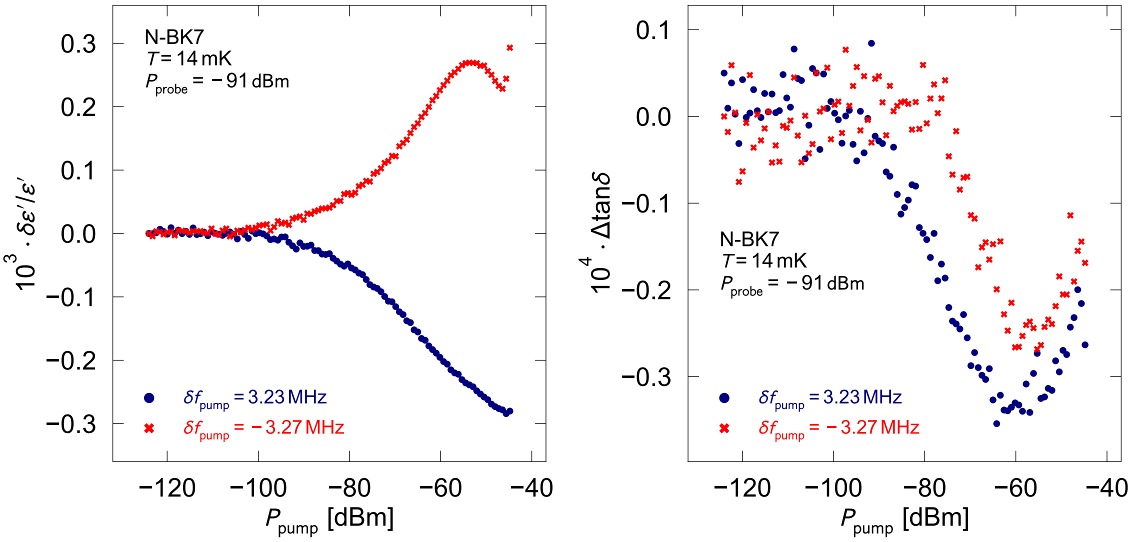

Figure 5.30: Measurement of the shift in $\delta\varepsilon'/\varepsilon'$ and $\tan\delta$ as a function of the pump tone power P_{pump} at fixed pump tone detunings δf_{pump}.

the calculations of the hole, we used a constant quality factor Q, which is obviously not the case across the whole pump tone scan. Pumping close to the probe tone increases the quality factor of the resonator, which reduces the off-resonant pump tone efficiency. This then leads to a reduction of the hole, which again reduces the quality factor, and so on. One needs to implement an iterative procedure to approach this self-regulation of the resonator, which has already been tested [Haa20a].

We took a closer look at the dependence of $\delta\varepsilon'/\varepsilon'$ and $\tan\delta$ on the pump tone power. Therefore, we fixed the detuning of the pump tone and varied its power, see Figure 5.30. We performed two measurements, one with a pump tone below (red) and another one with a pump tone above the probe tone frequency (blue). The pump tone was set close to the probe tone in order to observe an effect also in $\tan\delta$. In accordance with the observations above, the shift in $\delta\varepsilon'/\varepsilon'$ scales with the pump tone power. Depending on the sign of the detuning the shift is in positive or negative direction. The slight asymmetry of the shift might be related to the asymmetric resonance shape and with that to an asymmetric pumping efficiency. Also, the accidental difference of the detuning δf_{pump} should generate an asymmetric shift. For the measurement with $\delta f_{\mathrm{pump}} = -3.27\,\mathrm{MHz}$ we observe a maximum at high pump powers. Such a reversal point is expected because a strong pumping creates a large hole across a wide energy range. This saturates tunneling systems on both sides of the probe tone and the shift in $\delta\varepsilon'/\varepsilon'$ will vanish in the limit of a very strong pumping, which was observed in [Cap20].
The loss drops as expected for higher pump tone powers, and again, a slight asym-

metric behavior is observed. For $P_{\mathrm{pump}} > -60\,\mathrm{dBm}$ the loss increases, which does not match the expectation of the discussed model. When the pump tone hole becomes very large at high powers, all relevant tunneling system contributions to the loss should be saturated and $\tan\delta$ should reach a constant minimum value. Possibly, this turning point marks the onset of heating, which definitely occurred at pump tone powers higher than $-40\,\mathrm{dBm}$.

Additional measurements with modified pump and probe tone settings in combination with a more elaborated modeling of the created hole should give a more stringent determination of τ_2. However, this simplified model already provides a decent analysis of these two-tone measurements. This allows a whole new access to perform tunneling system spectroscopy, as the contributions from off-resonant tunneling systems are projected to the resonant dielectric response. Moreover, the observed pump tone signature proves the realization of an off-resonant tunneling system driving through the pump tones since tunneling systems are getting at least partially saturated through the pumping. In the following, we will combine these two-tone measurements with energy sweeps of the tunneling systems to possibly achieve a population inversion.

5.4.3 Two-tone measurements under dynamic biasing

We repeated the non-equilibrium bias rate dependency measurements from Section 5.3.2 with the revised resonator, first without applied pump tones. In contrast to the previous measurements, this resonator did not show a constant value for $\tan\delta$ during the sweep of large bias voltages, which is shown in Figure 5.31. The bias voltage was ramped from 0 to 90 V within $t_{\mathrm{b}} \approx 100\,\mathrm{ms}$. During the bias sweep, marked by the gray area, $\delta\varepsilon'/\varepsilon'$ and $\tan\delta$ reveal a strong time dependency. The characteristic of the real part indicates a temperature increase of about 60 mK at the end of the bias sweep, where the real part follows the temperature dependency from Figure 5.25 (left). When we decreased the bias voltage to 9 V, the drift in $\delta\varepsilon'/\varepsilon'$ and $\tan\delta$ disappeared, and we could observe constant values for $\delta\varepsilon'/\varepsilon'$ and $\tan\delta$ during the bias sweep. The bias ramp drives the dielectric material at the frequency of the inverse bias ramp time. The dielectric loss of the glass at these frequencies is of the order 10^{-4} [Luc16], which can be converted into an equivalent resistance of $R = \frac{1}{\omega C \tan\delta}$. Together with a simulated capacitance of $C \approx 1\,\mathrm{pF}$ for the resonator we can estimate a dissipated power $P_{\mathrm{dis,bias}} = U^2/R$ of several tens of picowatt. Applying this power over a short period of time in combination with a poor heat conduction may result in a temporary temperature increase of a few millikelvin. Reducing the bias voltage significantly reduces the heat input, which is why we had to go down below 9 V for the bias voltage in the following measurements. Unfortunately, this reduces the maximum accessible bias rates as well.

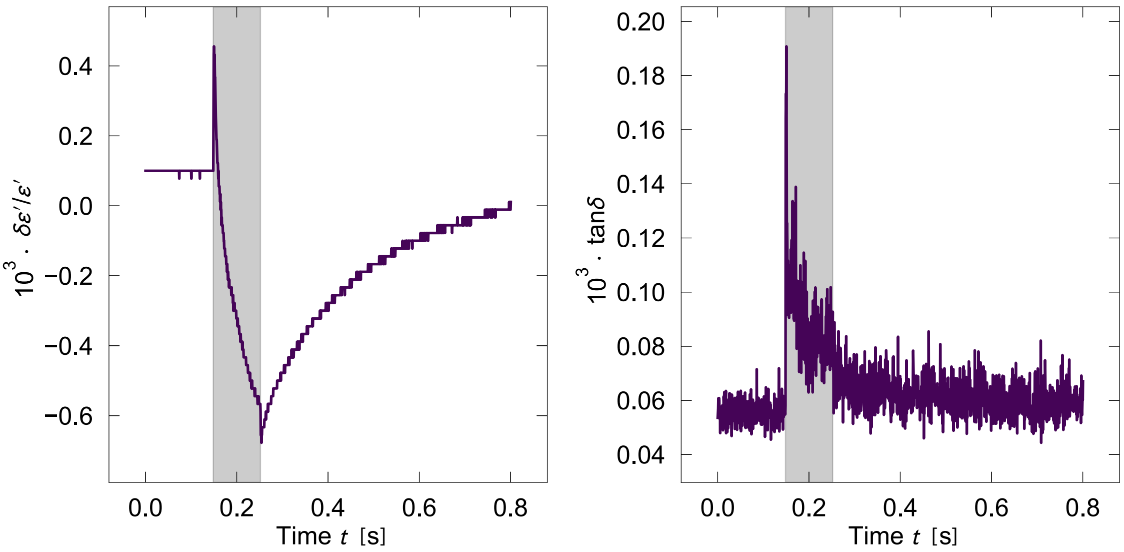

Figure 5.31: Measurement of $\delta\varepsilon'/\varepsilon'$ (left) and $\tan\delta$ (right) as a function of time under a bias sweep. The bias voltage was ramped from 0 to 90 V within $t_\mathrm{b} \approx 100\,\mathrm{ms}$. During the bias ramp (gray area) $\delta\varepsilon'/\varepsilon'$ and $\tan\delta$ show a strong time-dependent drift.

The weak coupling of the resonator to the feedline leads to small signal sizes of the resonance curves. This makes it difficult to measure $\tan\delta$ at small driving powers with a high resolution in time, where the VNA measures S_{21} with a broad internal filter to achieve fast time-sweeps. Especially when $\tan\delta$ increases towards fast bias rates and leads to an even smaller resonance amplitude, the resonance curve is heavily superimposed by noise. Therefore, we performed the following measurements with a continuous triangle signal as bias voltage instead of a single bias ramp. Hence, we cannot detect $\tan\delta$ as function of time, but by slowing down the data acquisition of the VNA, we can use a more narrow bandwidth filtering, which gives a much better signal-noise ratio. Thus, we are able to perform the bias rate dependency measurements at smaller probe tone powers, which allows us to achieve Landau-Zener transitions already at moderate bias rates.

In Figure 5.32, $\delta\varepsilon'/\varepsilon'$ and $\tan\delta$ were measured as a function of the bias rate $\dot{F}_\mathrm{b}$. As waveform for the bias voltage, we used a triangular signal with $3\,V_\mathrm{pp}$ and varied its frequency. The measurements were performed without any pump tones and also with two pump tones symmetrically detuned by 5 MHz from the probe tone. Let us first look at the measurement without pump tones. In $\tan\delta$ we observe the expected increase towards higher bias rates. When the loss becomes larger, the amplitude of the resonance curve decreases, which results in a larger scattering of the data. At very high bias rates we observe a similar value for the loss as we did in Figure 5.17. Unexpectedly, the real part slightly increases towards higher bias rates. The real part should not be very sensitive to the dynamics of resonant tunneling systems at

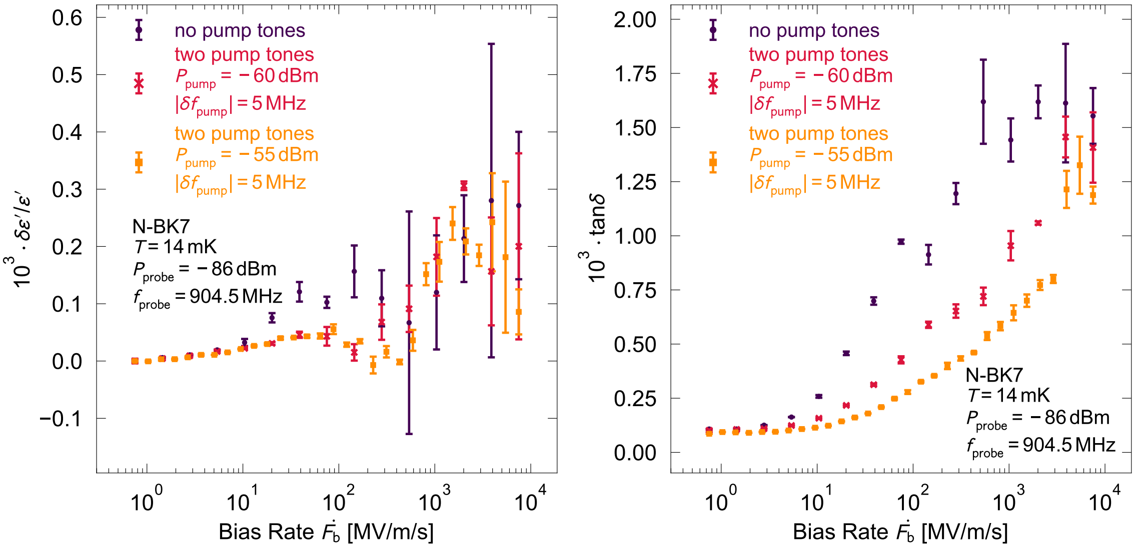

Figure 5.32: Bias rate dependency of $\delta\varepsilon'/\varepsilon'$ (left) and $\tan\delta$ (right) under a continuous triangular bias signal. The measurements were performed without any pump tones (violet) and also with two pump tones symmetrically detuned by 5 MHz from the probe tone frequency for two pump tone powers (red, orange).

all, and in the first place we do not expect a dependence of $\delta\varepsilon'/\varepsilon'$ on the bias rate. An increase could be explained by a temperature rise through the biasing, but other origins are conceivable as well. A theoretical treatment of the real part in the framework of Landau-Zener transitions would be beneficial for a further analysis.

Next, additional pump tones were applied. The detuning was set to 5 MHz to avoid a reduction of $\tan\delta$ in the steady-state through the saturation hole, as it has been discussed in the previous section. For the pump tone powers we used values as large as possible to maximize the off-resonant pumping. At the same time, we avoided very high powers where distinct heating signatures were detected. We observe a clear reduction of the loss when pump tones are applied. This reduction becomes stronger when a higher pump tone power is used. However, an amplification regime with negative values for $\tan\delta$, as observed in the Monte Carlo simulation, cannot be detected here. The real part shows a non-monotonic behavior when pump tones were applied and agrees with the 'no pump tone measurement' only at small and high bias rates.

For a discussion of the reduced loss under pumping it is worth mentioning that $\tan\delta$ converges towards the 'no pump tone measurement' when the detuning δf_pump is increased. This is shown in Figure 5.33. The measurement was performed at a moderate bias rate with a fixed value of $\dot{F}_\mathrm{b} = 525\,\mathrm{MV\,m^{-1}\,s^{-1}}$. Pump and probe tones were chosen as in Figure 5.32 (red curve). When the pump tone frequency is heavily detuned from the probe tone, no reduction of the loss is observed anymore. This

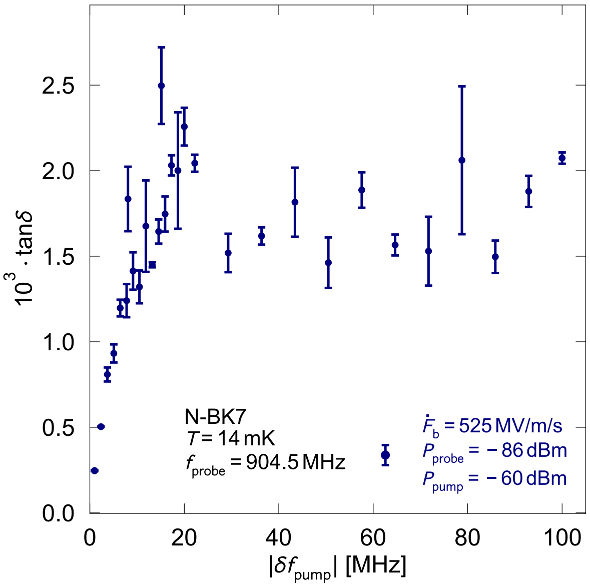

Figure 5.33: Measurement of $\tan\delta$ as a function of the pump tone detuning. The bias rate was held constant at $\dot{F}_{\text{b}} = 525\,\text{MV}\,\text{m}^{-1}\,\text{s}^{-1}$, while two pump tones with $P_{\text{pump}} = -60\,\text{dBm}$ were symmetrically detuned from the probe tone.

excludes a heat input from outside the resonator because this should occur independently from the detuning. Only for small detunings the loss-reduction sets in. As it has been discussed before within the two-tone measurements (see Section 5.4.2), if the pump tones are very close to the probe tone, they can effectively saturate slight off-resonant tunneling systems, which reduces the loss measured at the probe tone frequency. At higher bias rates $\tan\delta$ increase due to the Landau-Zener dynamics, which means a broader resonance curve. This allows a more efficient off-resonant pumping, and thus, $\tan\delta$ might get reduced by the pump tone saturation.

Moreover, it cannot be excluded that the driving of tunneling systems by the pump tones leads to heating through the dielectric dissipation at the pump tone frequency. If the resonance is broadened at higher bias rates, the pump tone couples more strongly into the resonator and the driving becomes more intense. In Section 5.2.2 we have seen that the dissipated heat in the sample from microwave tones of similar power can cause a considerable amount of heating. For larger pump tone detunings the resonator filters these frequencies, and the pump tone excitation becomes inefficient.

These effects may already be responsible for the observed reduction of $\tan\delta$. It cannot be resolved here whether the combination of the bias sweep and pumping also leads to processes where inverted/saturated tunneling systems that get dynamically shifted to the probe tone reduce the loss as well. In the limit of population-inverted tunneling systems the simulation in Figure 3.23 showed a negative loss, which is the domain where amplification through stimulated emission occurs. This limit is obviously not reached here.

5.4.4 Comparison with the Monte Carlo simulations

In the last part of this chapter, by the use of the Monte Carlo simulation, we want to discuss to what extent the observed reduction of the loss in Figure 5.32 can be attributed to the stimulated emission of tunneling systems and which might be the limiting factors for a missing amplification regime in the experiment. Therefore, we repeated the Monte Carlo simulation from Figure 3.23 with simulation parameters closer to the ones of the experiment. The data for these simulations were obtained in collaboration with [Mü21] where the presented simulation framework from Chapter 3 was put in a more user-friendly environment and more experiment-oriented simulation scenarios were conducted.

One main difference to Figure 3.23 is the application of an inhomogeneous field distribution. Therefore, for each tunneling system a random parameter i is sampled which follows an exponential distribution. This parameter is then multiplied with the constant field strength of probe, pump, or bias field, respectively, which represents the inhomogeneous field distribution of an IDC. In addition, a one-phonon relaxation process with $K_1 = 4.2 \times 10^{76}\,\mathrm{J^{-3}\,s^{-1}}$ was applied which gives a minimum relaxation time of $\tau_{1,\mathrm{min}} = 83\,\mathrm{\mu s}$ for $T \to 0\,\mathrm{K}$. Together with a constant transversal relaxation time of $\tau_2 = 5\,\mathrm{\mu s}$ these relaxations are more comparable with the experimental situation. The results are shown in Figure 5.34. In comparison to Figure 3.23 the usage of distributed relaxation times τ_1 and an inhomogeneous field leads to a less pronounced dip in $\tan\delta$. The onset of the dip at medium bias rates occurs approximately at the same position, but it is not as sharp and more washed out compared to the previous simulation. The behavior here is more similar to the observations in the experiment. However, the probe tone field strength in the simulation should

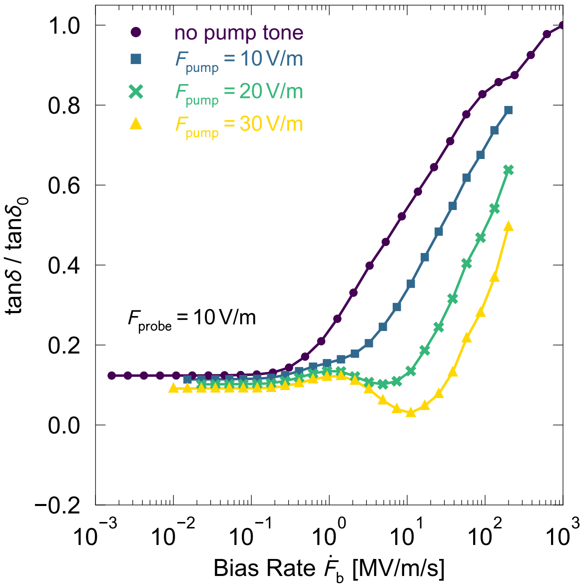

Figure 5.34: Monte Carlo simulation of the bias rate dependency with a probe tone $F_\mathrm{probe} = 10\,\mathrm{V\,m^{-1}}$ and pump tones with different field strengths detuned by 1 MHz from the probe tone. A constant dipole moment of $p = 1\,\mathrm{D}$ and $T \to 0\,\mathrm{K}$ were used. Moreover, a one-phonon relaxation with $K_1 = 4.2 \times 10^{76}\,\mathrm{J^{-3}\,s^{-1}}$, a constant transversal relaxation time of $\tau_2 = 5\,\mathrm{\mu s}$, and an exponential electric field distribution were applied. Data from [Mü21].

be smaller than the one applied in the experiment, which is why the transition into the Landau-Zener enhanced loss occurs at smaller bias rates. With slower relaxation times τ_1 in the simulation, the lower limit for a reduced loss through photon-emitting tunneling systems should appear at smaller bias rates and the dip would be broader. A slower relaxation time τ_1 should match the experimental situation even closer and would result in a behavior more similar to Figure 5.32.

It is interesting to see that in Figure 5.34 the steady-state loss is smaller when larger pump tones are applied, which we did not observe in the simulation from Figure 3.23. We can explain this reduction through missing contributions from pumped off-resonant tunneling systems, as it has been discussed in Section 5.4.2. The smaller value for τ_2 makes the spectral width of a single resonant tunneling system contribution wider, and without any pumping one also observes contributions from off-resonant systems at the probe tone. These off-resonant systems are driven and saturated by the pump tones, and hence, their contribution is missing.

In Figure 5.35 (left) we fixed the pump tones ($F_{\mathrm{pump}} = 20\,\mathrm{V\,m^{-1}}$; $\delta f_{\mathrm{pump}} = 1\,\mathrm{MHz}$) and varied the probe tone field strength. At a small probe tone driving ($F_{\mathrm{probe}} = 3\,\mathrm{V\,m^{-1}}$) the loss at small bias rates is higher, and the onset of the Landau-Zener enhanced loss appears at smaller bias rates. Therefore, the dip due to the photon

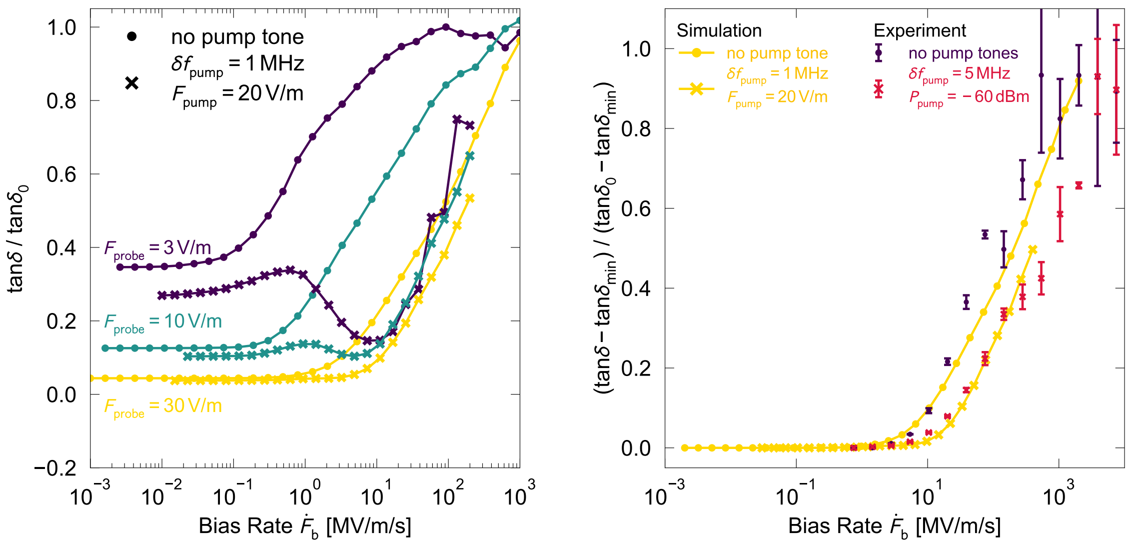

Figure 5.35: Left: Repeating the simulation from Figure 5.34 with fixed pump tones $F_{\mathrm{pump}} = 20\,\mathrm{V\,m^{-1}}$ and $\delta f_{\mathrm{pump}} = 1\,\mathrm{MHz}$ (crosses) for different probe tone field strengths $F_{\mathrm{probe}} = 3\,\mathrm{V\,m^{-1}}$ (purple); $10\,\mathrm{V\,m^{-1}}$ (green); $30\,\mathrm{V\,m^{-1}}$ (yellow). The simulations are compared to the corresponding ones without applied pump tones (filled circles). Data from [Mü21]. Right: Qualitative comparison between the Monte Carlo simulation from the left-hand side ($F_{\mathrm{probe}} = 30\,\mathrm{V\,m^{-1}}$) and the experimental data from Figure 5.32. The loss was normalized, and the bias rate of the Monte Carlo simulation was multiplied by a factor two in order to find an agreement.

emission of pumped tunneling systems becomes more pronounced. The depth of the hole is almost unaffected by the probe tone strength. The upper limit for the appearance of stimulated emission $\dot{F}_{\mathrm{b}} \lesssim \frac{pF_{\mathrm{pump}}^2}{2\hbar}$ is independent from the probe tone field strength, which is why the increase of $\tan\delta$ in the simulation towards higher bias rates is the same for all curves with applied pump tones. If the probe tone becomes stronger than the pump tone ($F_{\mathrm{probe}} = 30\,\mathrm{V\,m^{-1}}$), the dip completely vanishes, and we observe a behavior similar to results of the measurement from Figure 5.32. A comparison between the measurement and simulation is shown in Figure 5.35 (right). In order to compensate the differences of the tunneling system parameters (relaxation times, dipole moment) or of the two-tone setting (pump and probe tone field strengths) between the simulation and experiment qualitatively, the loss was normalized, and the bias rate of the Monte Carlo simulation was multiplied with a factor of two.

The qualitative agreement between experiment and simulations shows that the observed reduction of the non-equilibrium loss in Figure 5.32 in the presence of pump tones could also originate from the stimulated emission of pumped tunneling systems. If this is indeed the case in the experiment, the field strengths of pump and probe tones should have a similar size because we do not observe the characteristic dip. As Figure 5.35 (left) shows, going to smaller probe tones should help to distinguish the reduction through stimulated emission from the effects discussed above since one would expect to observe the dip in $\tan\delta$ then. With the current setup we could not measure $\tan\delta$ with the necessary resolution at low driving powers. Updates to the rf-setup, by applying, for example, a low temperature amplifier or circulators to the read-out branch, are already operating or are planned for the near future.

6. Summary and Outlook

Within the framework of this thesis, Landau-Zener spectroscopy measurements of atomic tunneling systems at very low temperatures were conducted. For the first time, this novel measurement technique was demonstrated and established for tunneling systems in bulk glasses. It consists of a measurement setup which was implemented to perform dielectric equilibrium or non-equilibrium measurements in the microwave regime inside a ^{3}He/^{4}He dilution refrigerator at temperatures between 10 mK and 8 K.

Beyond dielectric equilibrium measurements, extensively conducted in the past, the Landau-Zener spectroscopy also allows to perform measurements in non-equilibrium. Applying only a single device, a comprehensive investigation of various microscopic tunneling system properties, like their dipole moment, relaxation times, saturation effects, or the tunneling system distribution can be performed.

By expanding this method to bulk glasses, a larger range of materials becomes accessible, which also allows to revisit previously studied materials with this new technique to establish a more conclusive picture of tunneling systems in amorphous solids.

The experimental implementation of the Landau-Zener spectroscopy was realized through the combination of a high-frequency driving field and a dynamic shift of the tunneling systems' energy, inducing Landau-Zener transitions, which are measured through the correlated dielectric loss of the sample. The controllable rate of change of the tunneling systems' energy determines the probability of Landau-Zener transitions, and with that, controls the tunneling system population, which allows to perform a spectroscopy of the involved tunneling systems.

The high-frequency driving field was implemented by LC-resonators which were designed to resonate at the demanded excitation frequency (250 MHz and 1 GHz). Therefore, superconducting microfabricated LC-resonators with interdigital capacitors as capacitance and a meander line inductor as inductance were developed. This allowed the realization of a planar resonator geometry, and the resonators could directly be fabricated as a single layer of sputter deposited niobium on the substrate which is the sample itself. The high-frequency electric field inside the capacitors penetrates the substrate/glass and probes the tunneling systems sitting in the bulk sample. By measuring the resonance curve of the resonator, we extracted the dielectric function of the sample. As sample we chose the borosilicate glass N-BK7 since it was well-characterized in previous studies and is therefore well-suited to validate the new setup.

Four identical capacitors arranged in a Wheatstone bridge-type scheme form the capacitance of the LC-resonator. The symmetry of this geometry allows to drive the resonator at its resonance frequency while applying in parallel an independent electric bias voltage across the other diagonal of the capacitance bridge. Thus, the tunneling systems' dielectric response is measured at the high-frequency drive under a simultaneous energy shift of tunneling systems through a bias field sweep, whereby Landau-Zener transitions are induced. By the use of a developed measurement routine, the dielectric function, whereas the dielectric loss $\tan\delta$ was in particular of interest, was fully automatically measured as a function of the bias rate, where bias rates up to $2000\,\mathrm{MV\,m^{-1}\,s^{-1}}$ could be reached.

Detailed numerical simulations of the tunneling system ensemble interacting with arbitrary electric fields were conducted in this thesis by solving the single system's dynamics numerically and averaging the ensemble-response through a Monte Carlo approach. Predictions of the standard tunneling model could be reproduced, but most importantly, the simulations provided solutions to problems where an analytic description was limited or not possible. The implemented simulation framework represents a very valuable tool for a fundamental understanding of the complex tunneling systems dynamics caused by the interactions with several electric fields at once.

By demonstrating the novel Landau-Zener spectroscopy technique of bulk glasses exemplarily for the sample N-BK7, a wide variety of different experiments could be conducted that allowed to study the tunneling systems of the sample under investigation in great detail:
In dielectric measurements, initially performed in equilibrium, a characterization of the bridge resonators was made. Both, the 250 MHz- and the 1 GHz-resonator showed a fast thermalization even at temperatures below 20 mK. Measurements of the temperature dependency of $\delta\varepsilon'/\varepsilon'$ and $\tan\delta$ could reproduce previous results of N-BK7 measured at these excitation frequencies. In contrast to previous measurements, the sensitivity of the new setup at ultra-low driving fields was sufficient to resolve the unsaturated resonant loss entirely. This allowed a more profound comparison with different theory models. As it has previously been reported for N-BK7, the measurement showed deviations from the pure standard tunneling model distribution and could successfully be described with a model where mutual interactions between tunneling systems result in a reduced tunneling system density at low energies.
When we measured $\tan\delta$ at different driving field strengths, we could observe the saturation of tunneling systems at high field strengths, where the loss showed the expected $\tan\delta \propto F_{\mathrm{ac}}^{-1}$ behavior for both devices. At very low field strengths $\tan\delta$ became independent from the field strength, and we observed the unsaturated low-power plateau. Driving the resonators at very high field strengths increased the sample's temperature by more than 20 mK. This heating presumably originates

from the dissipated heat due to the sample's dielectric loss.

Measurements of $\tan\delta$ at different DC bias fields confirmed an unimpeded rf-readout under biasing conditions and also confirmed a flat distribution of the tunneling system asymmetry energy $\varDelta$ within the accessible energy range, as predicted by the standard tunneling model.

In accordance with the Landau-Zener dynamics of tunneling systems, we observed an increased loss under fast changes of the applied bias field, i.e. a bias ramp. After the end of a bias ramp, the loss relaxed back into its equilibrium state. The observed initial fast relaxation was found to be compatible with a relaxation of tunneling systems through one-phonon processes. Measuring $\tan\delta$ at 1 GHz and 14 mK as a function of the bias rate showed the predicted non-equilibrium behavior of tunneling systems undergoing Landau-Zener transitions. For small bias rates, we found the steady-state value for the loss which is only determined by the applied driving field strength. Towards higher bias rates the loss increased and converged into the low-power limit. By replacing the bias rate with the dimensionless bias rate ξ and using an average dipole moment of $p = 1.5\,\mathrm{D}$, the measured non-equilibrium loss agreed well with the predictions of the Landau-Zener dynamics. From the extracted value for the dipole moment and the temperature dependency measurement, we could determine the tunneling system density for N-BK7 as $P_0 = 6.46 \times 10^{45}\,\mathrm{J}^{-1}\,\mathrm{m}^{-3}$.

The non-equilibrium loss measured at 250 MHz and 14 mK heavily overshot the low-power limit when very high bias rates were applied. This arises from initially heavily detuned tunneling systems with much larger energy splittings E than the resonant ones at 250 MHz. These off-resonant tunneling systems are rapidly swept into resonance with the driving field through the bias field. Since they cannot thermally equilibrate fast enough, their excited state is sparsely thermally populated, and these systems absorb more photons than equilibrated ones.

Applying noise as bias signal resulted in an enhanced loss. The noise-bias acts as a continuously changing bias rate, and thus leads to an effective reduction of saturation. Noise should be thoroughly regarded in experiments measuring the resonant tunneling system loss as we could show a strongly deviating field strength dependency when noise was artificially applied through the bias line.

Two-tone spectroscopy measurements were performed with a revised resonator setup at 0.9 GHz, where heating at large driving fields was reduced. An additional strong off-resonant microwave tone (pump tone), applied through the transmission line, saturates off-resonant tunneling systems. Thus, the contributions from these systems are missing in the dielectric response measured at the frequency of the driving field (probe tone), and the single tunneling system contributions are mapped to the resonance curve. As a consequence, a shift of the resonance curve towards the pump tone frequency and a reduction of the quality factor for pump tones close to the probe tone were detected. By describing the data with a simplified model, we were able to extract a lower limit for the tunneling systems' average transversal relaxation time of $\tau_2 \gtrsim 10\,\mu\mathrm{s}$.

The combination of a two-tone measurement scheme with sweeps of the bias field showed a distinct reduction of the non-equilibrium loss. Comparisons with the results obtained from the Monte Carlo simulation give evidence for stimulated emission processes of tunneling systems taking place. However, this effect cannot fully be distinguished from other mechanisms like heating or a pure saturation of off-resonant tunneling systems through the pumping.

The successful application of the Landau-Zener spectroscopy to bulk glasses allows a direct transfer of this characterization technique to numerous other amorphous materials that are suited to serve as substrate for micro-processing the resonators. Applying a flip-chip geometry with a tunneling system poor material as substrate and the sample (e.g. a polymer) lying on top of the interdigital capacitors allows an arbitrary sample choice. In measurements of samples possessing smaller dielectric losses than N-BK7, the observed heating of the sample under strong driving fields might be reduced.

The obtained experimental results and the simulations point the way for future experiments and research.

A further reduction of parasitic heating can be achieved by performing the measurements at higher temperatures, where the thermal coupling of the sample to the heat bath is stronger, and therefore, small heat inputs are less severe. However, in order to find resonant tunneling systems at higher temperatures thermally still in their ground state, the measurements have to be performed at higher driving field frequencies, which would require to update the current rf-setup.

Measuring the non-equilibrium Landau-Zener loss at even higher bias rates might reveal deeper insights about the tunneling system nature. There exist theoretical considerations of a second species of tunneling systems that are scarce but couple much stronger to strain or electric fields than the ones typically observed in the experiment [Sch18]. Under ultra-high bias rates, these strongly coupled tunneling systems may become desaturated and their contribution could become apparent. Achieving much higher bias rates with the current setup is limited by the time resolution of the VNA and the maximum output voltage of the used power operational amplifier. Higher bias field strengths could be realized by further decreasing the electrode spacing of the microfabricated capacitors. For this purpose, parallel plate capacitors with thin amorphous films are more appealing since the thickness of the films is naturally much smaller than the gap size of the interdigital capacitors. However, the dielectric strength of the material might be a limiting factor for achieving ultra-high bias rates. Since tunneling systems are known to couple strongly to strain fields, replacing the

electric bias field with a strain-bias should be a worthwhile strategy for the future. This could give indications to what extent current measurements are suffering from parasitic vibrations. Similar to the observation with an electric noise-bias, present strain fields should have a distinct impact on measurements of the resonant loss.
For the realization of a stimulated emission regime in the two-tone measurements, one should investigate different materials as well since the conditions for stimulated emission might be easier to attain there. Moreover, it should be tested whether applying the pump tones through the bias line to the resonator is more beneficial for pumping tunneling systems. In parts already realized, a higher sensitivity of the rf-setup enables to extend the accessible parameter space to much smaller probe tone powers, allowing to perform measurements also in the single-photon regime, eventually.
A further theoretical modeling of the two-tone spectroscopy, the Landau-Zener dynamics at finite temperatures, or a description of the non-equilibrium dielectric real part under Landau-Zener transitions would allow to interpret the experimental data in a more profound way.

All in all, it could be demonstrated that the performed Landau-Zener spectroscopy method allows a comprehensive investigation of tunneling systems in bulk glasses and provides, in combination with the implemented simulation framework, a new way of systematic characterization of tunneling systems in amorphous materials at very low temperatures.

A. Appendix

A.1 Resonant part for small fields

In order to obtain the total contribution of the resonant part, (2.62) + (2.63) is integrated over the distribution function (2.26), where the mean of the dipole orientation $p^2/3$ was used:

$$\frac{\delta\varepsilon_{\mathrm{res}}}{\varepsilon'} = \frac{P_0 p^2}{3\varepsilon'\hbar} \int\limits_0^{E_{\max}} \mathrm{d}E \int\limits_{\Delta_{0,\min}}^{E} \mathrm{d}\Delta_0 P(E,\Delta_0) \left(\frac{\Delta_0}{E}\right)^2 \tanh\left(\frac{E}{2k_{\mathrm{B}}T}\right) b(E,\omega)$$
$$= \frac{A}{3\hbar} \int\limits_0^{E_{\max}} \mathrm{d}E \int\limits_{\Delta_{0,\min}}^{E} \mathrm{d}\Delta_0 \frac{1}{\Delta_0\sqrt{1-\left(\frac{\Delta_0}{E}\right)^2}} \left(\frac{\Delta_0}{E}\right)^2 \tanh\left(\frac{E}{2k_{\mathrm{B}}T}\right) b(E,\omega) \qquad \text{(A.1)}$$

Doing a variable transformation $x = \frac{\Delta_0}{E}$; $x_{\min} = \frac{\Delta_{0,\min}}{E}$ gives

$$\frac{\delta\varepsilon_{\mathrm{res}}}{\varepsilon'} = \frac{A}{3\hbar} \int\limits_0^{E_{\max}} \mathrm{d}E \int\limits_{x_{\min}}^{1} \mathrm{d}x \frac{x}{\sqrt{1-x^2}} \tanh\left(\frac{E}{2k_{\mathrm{B}}T}\right) b(E,\omega) \quad . \qquad \text{(A.2)}$$

The integral over x can now be executed separately

$$\int\limits_{x_{\min}}^{1} \mathrm{d}x \frac{x}{\sqrt{1-x^2}} = \sqrt{1-x_{\min}^2} \approx 1 \qquad \text{(A.3)}$$

and gives the expression

$$\frac{\delta\varepsilon_{\mathrm{res}}}{\varepsilon'} = \frac{A}{3\hbar} \int\limits_0^{E_{\max}} \mathrm{d}E \tanh\left(\frac{E}{2k_{\mathrm{B}}T}\right) \left[\frac{1}{\omega_0 - \omega - \frac{\mathrm{i}}{\tau_2}} + \frac{1}{\omega_0 + \omega + \frac{\mathrm{i}}{\tau_2}}\right] \quad , \qquad \text{(A.4)}$$

by writing $\omega_0 = E/\hbar$. With another variable transformation $z = \frac{E}{k_{\mathrm{B}}T}$, $a = \hbar(\omega + \frac{\mathrm{i}}{\tau_2})/(k_{\mathrm{B}}T)$, $z_{\max} = \frac{E_{\max}}{k_{\mathrm{B}}T}$, the integral reduces into

$$\frac{\delta\varepsilon_{\mathrm{res}}}{\varepsilon'} = \frac{A}{3} \int\limits_0^{z_{\max}} \mathrm{d}z \tanh\left(\frac{z}{2}\right) \left[\frac{1}{z-a} + \frac{1}{z+a}\right] \quad . \qquad \text{(A.5)}$$

The solution of this integral is given in [Gao08, Phi87]. It can be approximated as

$$\frac{\delta\varepsilon_{\mathrm{res}}}{\varepsilon'} \approx -\frac{2A}{3} \left[\psi\left(\frac{1}{2} + \frac{\hbar}{2\pi k_{\mathrm{B}}T\tau_2} - \mathrm{i}\frac{\hbar\omega}{2\pi k_{\mathrm{B}}T}\right) - \ln\left(\frac{E_{\max}}{2\pi k_{\mathrm{B}}T}\right)\right] \quad , \qquad \text{(A.6)}$$

with $\psi(z)$ as the complex digamma function. The term $\hbar/(2\pi k_\mathrm{B}T\tau_2)$ is small and can be neglected. A separation into real $\mathrm{Re}\{z\}$ and imaginary part $\mathrm{Re}\{z\}$ gives the expressions

$$\frac{\delta\varepsilon'_\mathrm{res}}{\varepsilon'} = -\frac{2A}{3}\left[\mathrm{Re}\left\{\psi\left(\frac{1}{2}-\mathrm{i}\frac{\hbar\omega}{2\pi k_\mathrm{B}T}\right)\right\} - \ln\left(\frac{E_\mathrm{max}}{2\pi k_\mathrm{B}T}\right)\right] \tag{A.7}$$

$$\frac{\delta\varepsilon''_\mathrm{res}}{\varepsilon'} = -\frac{2A}{3}\mathrm{Im}\left\{\psi\left(\frac{1}{2}-\mathrm{i}\frac{\hbar\omega}{2\pi k_\mathrm{B}T}\right)\right\} = \frac{\pi}{3}A\tanh\left(\frac{\hbar\omega}{2k_\mathrm{B}T}\right) \quad . \tag{A.8}$$

The identity $\mathrm{Im}\left\{\psi\left(\frac{1}{2}+\mathrm{i}x\right)\right\} = \frac{\pi}{2}\tanh(\pi x) = -\frac{\pi}{2}\tanh(\pi(-x))$ was used in the last step.

A.2 Resonant loss for large fields

According to Equation (2.91), the imaginary part of the resonant process for a large electric field is

$$\begin{aligned}\frac{\delta\varepsilon''_\mathrm{res}}{\varepsilon'} = \frac{P_0 p^2\cos^2\theta}{\varepsilon_0\varepsilon_\mathrm{r}\hbar}\int\limits_0^{E_\mathrm{max}}\mathrm{d}E\int\limits_{\mathit{\Delta}_{0,\mathrm{min}}}^{E}\mathrm{d}\mathit{\Delta}_0 P(E,\mathit{\Delta}_0)\left(\frac{\mathit{\Delta}_0}{E}\right)^2\tanh\left(\frac{E}{2k_\mathrm{B}T}\right)\\ \times\frac{1+(\omega_0-\omega)^2\tau_2^2}{1+(\omega_0-\omega)^2\tau_2^2+\Omega_\mathrm{R}^2\tau_1\tau_2}\left[\frac{\tau_2}{(\omega-\omega_0)^2\tau_2^2+1}-\frac{\tau_2}{(\omega+\omega_0)^2\tau_2^2+1}\right]\end{aligned} \tag{A.9}$$

In the last term of Equation (A.9) the main contribution comes from the factor

$$\frac{\tau_2}{(\omega-\omega_0)^2\tau_2^2+1} \quad . \tag{A.10}$$

Doing again the variable transformation $x=\frac{\mathit{\Delta}_0}{E}$, $x_\mathrm{min}=\frac{\mathit{\Delta}_{0,\mathrm{min}}}{E}$ we find

$$\begin{aligned}\frac{\delta\varepsilon''_\mathrm{res}}{\varepsilon'} &= \frac{P_0 p^2\cos^2\theta}{\varepsilon_0\varepsilon_\mathrm{r}\hbar}\int\limits_0^{E_\mathrm{max}}\mathrm{d}E\int\limits_{x_\mathrm{min}}^{1}\mathrm{d}x\frac{x}{\sqrt{1-x^2}}\tanh\left(\frac{E}{2k_\mathrm{B}T}\right)\\ &\qquad\times\frac{1+(\omega_0-\omega)^2\tau_2^2}{1+(\omega_0-\omega)^2\tau_2^2+\Omega_\mathrm{R}^2\tau_1\tau_2}\cdot\frac{\tau_2}{(\omega-\omega_0)^2\tau_2^2+1}\\ &= \frac{P_0 p^2\cos^2\theta}{\varepsilon_0\varepsilon_\mathrm{r}\hbar}\int\limits_0^{E_\mathrm{max}}\mathrm{d}E\int\limits_{x_\mathrm{min}}^{1}\mathrm{d}x\frac{x}{\sqrt{1-x^2}}\tanh\left(\frac{E}{2k_\mathrm{B}T}\right)\\ &\qquad\times\frac{\tau_2}{1+(\omega_0-\omega)^2\tau_2^2+\Omega_\mathrm{R}^2\tau_1\tau_2} \quad .\end{aligned} \tag{A.11}$$

The factor $\Omega_{\mathrm{R}}^2\tau_1 = \Omega_{\mathrm{R0}}^2\tau_{1,\min}$ is independent of $x = \frac{\Delta_0}{E}$, and the integration over x can be worked out (see Equation (A.3)) as:

$$\frac{\delta\varepsilon''_{\mathrm{res}}}{\varepsilon'} = \frac{P_0 p^2\cos^2\theta}{\varepsilon_0\varepsilon_{\mathrm{r}}\hbar}\int\limits_0^{E_{\max}} \mathrm{d}E\tanh\left(\frac{E}{2k_{\mathrm{B}}T}\right)\frac{\tau_2}{1+(\omega_0-\omega)^2\tau_2^2+\Omega_{\mathrm{R0}}^2\tau_{1,\min}\tau_2} \tag{A.12}$$

This gets rewritten into

$$\frac{\delta\varepsilon''_{\mathrm{res}}}{\varepsilon'} = \frac{P_0 p^2\cos^2\theta}{\varepsilon_0\varepsilon_{\mathrm{r}}}\int\limits_0^{\omega_{0,\max}} \mathrm{d}\omega_0\tanh\left(\frac{\hbar\omega_0}{2k_{\mathrm{B}}T}\right)\frac{\tau_2^{-1}}{\left(\tau_2^{-1}\sqrt{1+\Omega_{\mathrm{R0}}^2\tau_{1,\min}\tau_2}\right)^2+(\omega_0-\omega)^2} \tag{A.13}$$

The integrand has the form of a Lorentzian with width $\sqrt{1+\Omega_{\mathrm{R0}}^2\tau_{1,\min}\tau_2}$, which can be approximated as a δ-function at ω. Therefore, we end up with the expression

$$\begin{aligned}\frac{\delta\varepsilon''_{\mathrm{res}}}{\varepsilon'} &\approx \frac{\pi P_0 p^2\cos^2\theta}{\varepsilon_0\varepsilon_{\mathrm{r}}}\tanh\left(\frac{\hbar\omega}{2k_{\mathrm{B}}T}\right)\frac{1}{\sqrt{1+\Omega_{\mathrm{R0}}^2\tau_{1,\min}\tau_2}}\\ &= \frac{\pi P_0 p^2\cos^2\theta}{\varepsilon_0\varepsilon_{\mathrm{r}}}\tanh\left(\frac{\hbar\omega}{2k_{\mathrm{B}}T}\right)\frac{1}{\sqrt{1+\left(\frac{F_{\mathrm{ac}}}{F_{\mathrm{c}}}\right)^2}}\quad ,\end{aligned} \tag{A.14}$$

with

$$F_{\mathrm{c}} = \frac{\hbar}{p\cos\theta}\frac{1}{\sqrt{\tau_{1,\min}\tau_2}}\quad . \tag{A.15}$$

A.3 Evaluation of integral (2.107) in E

Since $E \approx \hbar\omega$, we can treat γ as being independent from E and evaluate the integral over the energy splitting E as:

$$\begin{aligned}&\int\limits_{\hbar\omega-\hbar\nu\mathrm{d}t}^{\hbar\omega+\hbar\nu\mathrm{d}t}\mathrm{d}E\frac{E}{\sqrt{E^2-\Delta_0^2}}\\ &\quad=\sqrt{(\hbar\omega+\hbar\nu\mathrm{d}t)^2-\Delta_0^2}-\sqrt{(\hbar\omega-\hbar\nu\mathrm{d}t)^2-\Delta_0^2}\\ &\overset{\hbar\nu\mathrm{d}t\ll\hbar\omega}{\approx}\sqrt{(\hbar\omega)^2+\Delta_0^2}+\frac{\hbar\omega\hbar\nu\mathrm{d}t}{\sqrt{(\hbar\omega)^2-\Delta_0^2}}-\sqrt{(\hbar\omega)^2+\Delta_0^2}+\frac{\hbar\omega\hbar\nu\mathrm{d}t}{\sqrt{(\hbar\omega)^2-\Delta_0^2}}\\ &\quad=\frac{2\hbar\omega\hbar\nu\mathrm{d}t}{\sqrt{(\hbar\omega)^2-\Delta_0^2}}\end{aligned} \tag{A.16}$$

A.4 Short-time and long-time limit for the simulation

The choice of the time interval Δt between two points in the simulation has a significant influence on changes of the density operator $\hat{\rho}$ on a short time scale. Rabi oscillations can reasonably be mapped if more than 20 points per oscillation are available. Figure A.1 shows the Rabi oscillation of a resonant tunneling system for different time intervals Δt. For larger time steps the mapping of the Rabi oscillation becomes inaccurate, and the determined value from the time evolution does not agree with values found from finer samplings, see Table A.1. For the given Rabi frequency $\Delta t = 100\,\mathrm{ns}$ still provides accurate results. As a rule of thumb, we find

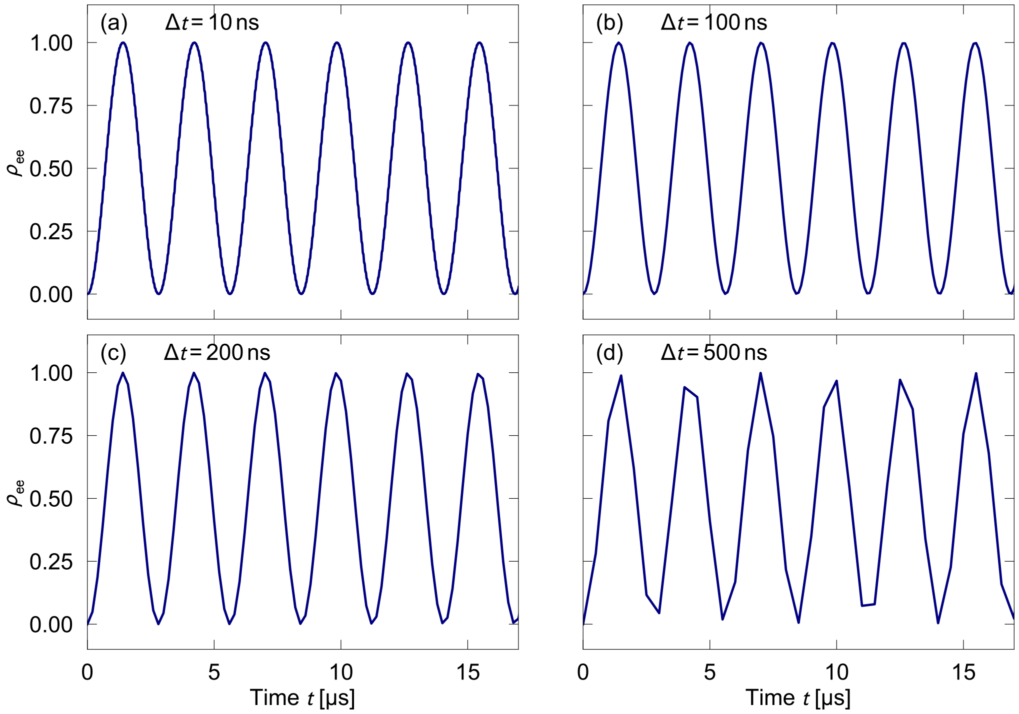

Figure A.1: Time evolution of a tunneling system ($\Delta_0 = \Delta = \frac{\hbar\omega_{\mathrm{ac}}}{\sqrt{2}}$) in resonance with the frequency of the driving field $\omega_{\mathrm{ac}}/2\pi = 10\,\mathrm{MHz}$ and a driving field strength of $100\,\mathrm{V\,m^{-1}}$. The relaxation times τ_1, τ_2 were chosen to be arbitrarily long and the temperature was set to zero. The time interval Δt between two simulation points was varied between 10 ns and 500 ns.

Δt [ns]	10	100	200	500
$\Omega_{\mathrm{R}}/2\pi$ [kHz]	355.74	355.72	356.05	355.69

Table A.1: Comparison between the simulated Rabi frequencies from Figure A.1 for different time step sizes Δt.

that a good choice for the time interval should hold the condition $\Delta t \lesssim \frac{2\pi}{20\Omega_\mathrm{R}}$. For all calculations, Δt was chosen as 10 ns, which allows to represent changes in $\hat{\rho}$ of up to 200 ns. This corresponds to maximum Rabi frequencies of 5 MHz, which means electric driving fields of approximately $1000\,\mathrm{V\,m^{-1}}$.

Another crucial parameter in the simulation is the tolerance of the ODE solver. If the tolerance is set too large, computational uncertainties may add up and lead to deviations on longer time scales. Figure A.2 shows the calculated time evolution of a pure Rabi oscillation for different relative tolerances of the solver with $\Delta t = 10\,\mathrm{ns}$. The time evolution extends over 600 µs, which requires 60,000 simulation points. For larger tolerances (a) and (b), the Rabi oscillation erroneously drops in amplitude, although the used relaxation times are several orders of magnitude longer. For smaller tolerances, the amplitude becomes more stable over the whole time span. In order to obtain precise results even for long simulated time evolutions, one should choose the relative tolerance rtol $\lesssim \frac{1}{\text{number of time steps}}$. We use a tolerance of rtol $= 5 \times 10^{-6}$ for all simulations, which allows for $\Delta t = 10\,\mathrm{ns}$ accurate results for more than 600 µs in simulation time and does not give a substantial penalty in the computation time in comparison to larger tolerances.

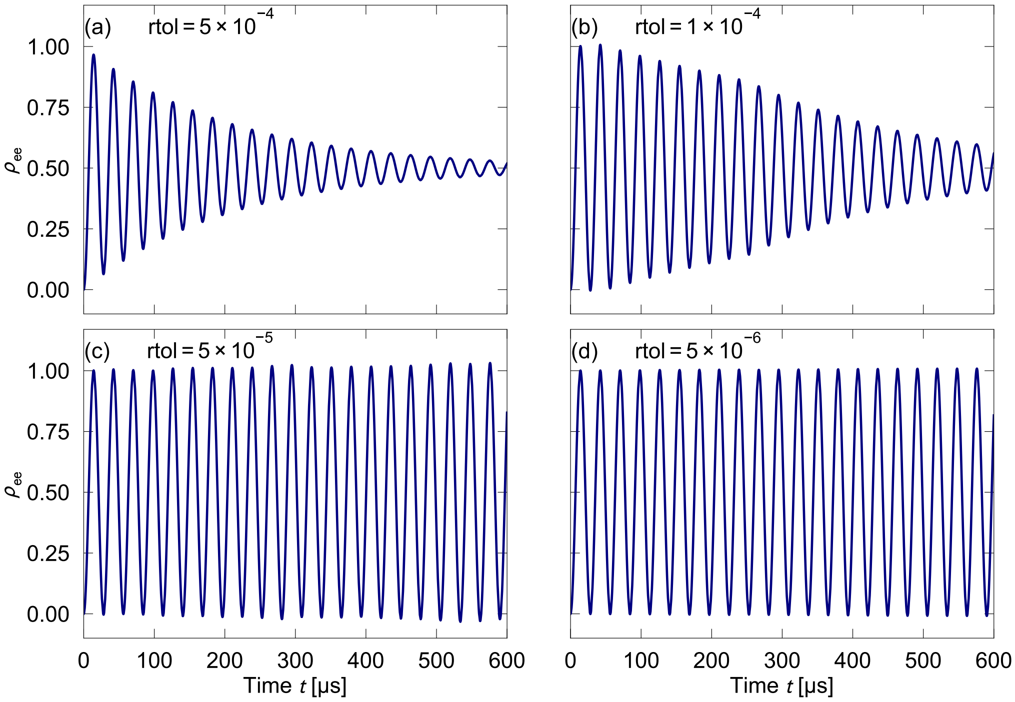

Figure A.2: Time evolution of a tunneling system ($\varDelta_0 = \varDelta = \frac{\hbar\omega_\mathrm{ac}}{\sqrt{2}}$) in resonance with the frequency of the driving field $\omega_\mathrm{ac}/2\pi = 10\,\mathrm{MHz}$ and a driving field strength of $10\,\mathrm{V\,m^{-1}}$. The relaxation times τ_1, τ_2 were chosen to be arbitrarily long and the temperature was set to zero. The internal relative tolerance of the ODE solver rtol was varied between 5×10^{-4} and 5×10^{-6}.

A.5 Landau-Zener transitions for a stronger detuned tunneling systems

The simulations from Figure 3.8 were repeated, but with an initially stronger detuned tunneling system. Therefore, also the maximum bias field is raised to guarantee a crossing over the resonance. The detuning in Δ/h is now 2.5 MHz, and the bias field of $1\,\mathrm{kV\,m^{-1}}$ gives a maximum shift in Δ/h of 10 MHz. The time evolution of ρ_{ee} was calculated for different bias ramp times (10 µs, 100 µs, 300 µs, and 1000 µs), all other parameters were chosen as in Figure 3.8. The results are shown in Figure A.3. The value of ρ_{ee} after the resonance crossing can be compared with the predictions of Equation (2.104), which is presented in Table A.2. In the scenario here, the agree-

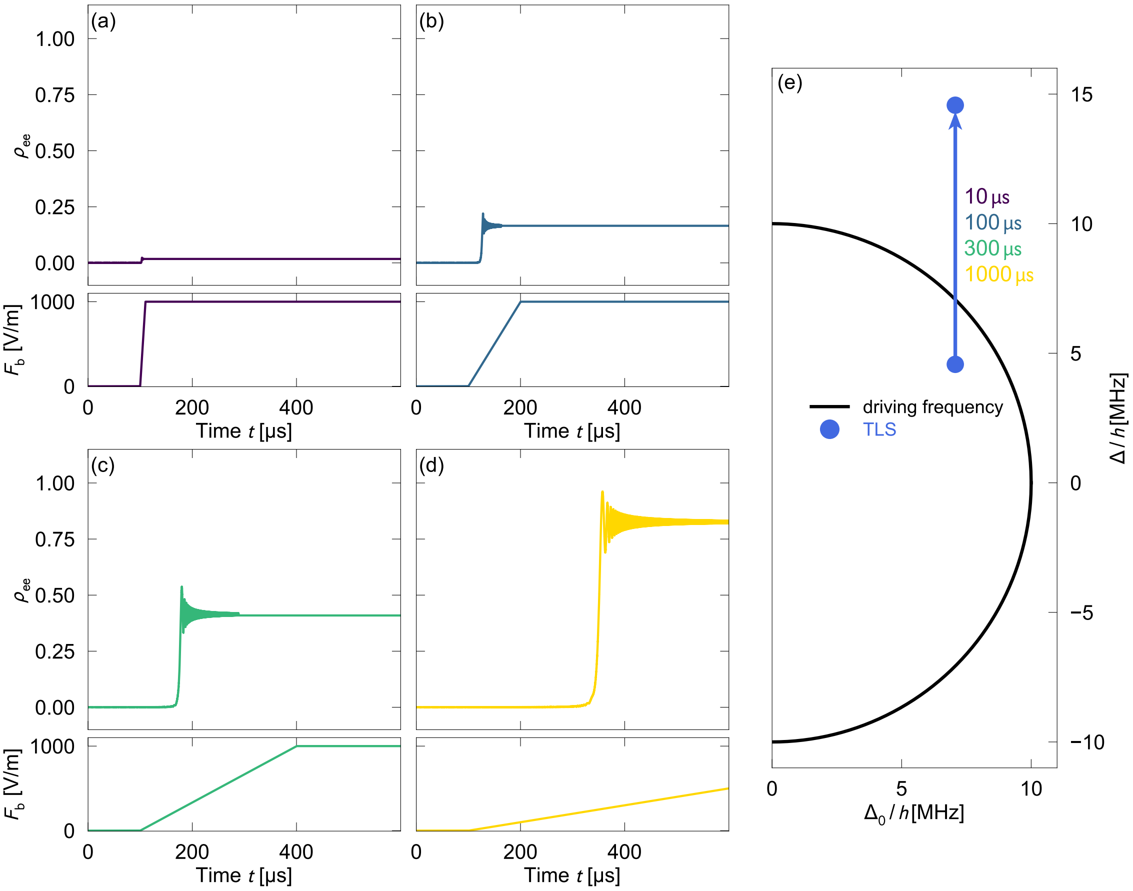

Figure A.3: Numerical calculation of the time evolution of ρ_{ee} in the presence of a swept electric bias field for different ramp times (10 µs, 100 µs, 300 µs, and 1000 µs) (a)-(d). The relaxation times τ_1, τ_2 were chosen to be arbitrarily long, and the temperature was set to zero. The tunneling system is initially detuned by 2.5 MHz in Δ/h from the driving field at 10 MHz with a field strength of $10\,\mathrm{V\,m^{-1}}$ and is shifted by the bias field across the resonance (e).

t_b	$\rho_\mathrm{ee}(\infty)$ (predicted)	$\rho_\mathrm{ee}(\infty)$ (simulated)
10 µs	0.017	0.018
100 µs	0.161	0.165
300 µs	0.410	0.409
1000 µs	0.827	0.826

Table A.2: Comparison between the predicted probability for a transition into the excited state for a resonance crossing according to Equation (2.104) and the value for $\rho_\mathrm{ee}^\mathrm{eq}$ from the simulations in Figure A.3 after the tunneling system has passed the resonance.

ment between simulation and predictions is much better, compared to the results of the simulation in Figure 3.8. The solution of the Landau-Zener problem should be more applicable to the situation presented here, than to the setting of a slightly detuned tunneling system in Figure 3.8. The simulation, however, should in both cases represent the actual description of the tunneling system dynamics.

Bibliography

[And72] P. W. Anderson, B. I. Halperin, and C. M. Varma, Anomalous low-temperature thermal properties of glasses and spin glasses, *Phil. Mag.*, **25**, 1, 1972.

[Ant79] P. J. Anthony and A. C. Anderson, Frequency and temperature dependence of dielectric and ultrasonic dispersion in amorphous materials at low temperatures, *Phys. Rev. B*, **20**, 763–767, 1979.

[Arn75] W. Arnold and S. Hunklinger, Experimental evidence for the direct interaction between two-level systems in glasses at very low temperatures, *Solid State Commun.*, **17**(7), 883 – 886, 1975.

[Arn78] W. Arnold, C. Martinon, and S. Hunklinger, Dircet experimental observation of spectral diffusion in vitreous silica at low temperatures, *J. Phys. Colloques*, **39**, C6–961–C6–962, 1978.

[Bar57] J. Bardeen, L. N. Cooper, and J. R. Schrieffer, Theory of superconductivity, *Phys. Rev.*, **108**, 1175–1204, 1957.

[Bar09] R. Barends, Photon-detecting superconducting resonators, PhD Thesis, Delft University of Technology, 2009.

[Bar11] R. Barends, J. Wenner, M. Lenander, Y. Chen, R. C. Bialczak, J. Kelly, E. Lucero, P. O'Malley, M. Mariantoni, D. Sank, H. Wang, T. C. White, Y. Yin, J. Zhao, A. N. Cleland, J. M. Martinis, and J. J. A. Baselmans, Minimizing quasiparticle generation from stray infrared light in superconducting quantum circuits, *Appl. Phys. Lett.*, **99**(11), 113507, 2011.

[Bar13] M. Bartkowiak, M. Bazrafshan, C. Fischer, A. Fleischmann, and C. Enss, Nuclear quadrupole moments as a microscopic probe to study the motion of atomic tunneling systems in amorphous solids, *Phys. Rev. Lett.*, **110**, 205502, 2013.

[Baz08] M. Bazrafshan, Investigation of the microscopic nature of tunnelling systems in amorphous glycerol by two-pulse polarisation echo experiments, PhD Thesis, Heidelberg University, 2008.

[Bec90] C. Bechinger, Dielektrische Messungen an Silikatgläsern bei Temperaturen unter 1 K, Diploma thesis, Heidelberg University, 1990.

[Bis38] J. Biscoe and B. E. Warren, X-ray diffraction study of soda-boric oxide glass, *J. Am. Ceram. Soc.*, **21**(8), 287–293, 1938.

[Bla77] J. L. Black and B. I. Halperin, Spectral diffusion, phonon echoes, and saturation recovery in glasses at low temperatures, *Phys. Rev. B*, **16**, 2879–2895, 1977.

[Blo46] F. Bloch, Nuclear induction, *Phys. Rev.*, **70**, 460–474, 1946.

[Bre17] J. D. Brehm, A. Bilmes, G. Weiss, A. V. Ustinov, and J. Lisenfeld, Transmission-line resonators for the study of individual two-level tunneling systems, *Appl. Phys. Lett.*, **111**(11), 112601, 2017.

[Bri26] L. Brillouin, La mécanique ondulatoire de Schrödinger: une méthode générale de resolution par approximations successives, *Compt. rend.*, **183**, 24, 1926.

[Buc88] U. Buchenau, H. M. Zhou, N. Nucker, K. S. Gilroy, and W. A. Phillips, Structural relaxation in vitreous silica, *Phys. Rev. Lett.*, **60**, 1318–1321, 1988.

[Buc13] W. Buckel and R. Kleiner, Supraleitung, Wiley-VCH, Weinheim, 7. edition, 2013.

[Bur95] A. L. Burin, Dipole gap effects in low energy excitation spectrum of amorphous solids. theory for dielectric relaxation, *J. Low Temp. Phys.*, **100**(3), 309–337, 1995.

[Bur98] A. L. Burin, D. Natelson, D. D. Osheroff, and Y. Kagan, Interactions between tunneling defects in amorphous solids, in P. Esquinazi (Ed.), *Tunneling Systems in Amorphous and Crystalline Solids*, Volume 1, 223–315, Springer-Verlag Berlin Heidelberg, 1998.

[Bur04] A. L. Burin and I. Y. Polishchuk, The long range interaction and the relaxation in glasses at low temperatures, *J. Low Temp. Phys.*, **137**(3-4), 189–215, 2004.

[Bur13] A. L. Burin, J. M. Leveritt, G. Ruyters, C. Schötz, M. Bazrafshan, P. Fassl, M. von Schickfus, A. Fleischmann, and C. Enss, Low-temperature dipolar echoes in amorphous dielectrics: Significance of relaxation and decoherence free two-level systems, *EPL*, **104**(5), 57006, 2013.

[Bur14a] A. L. Burin, A. O. Maksymov, and K. D. Osborn, Quantum coherent manipulation of two-level systems in superconducting circuits, *Supercond. Sci. Tech.*, **27**(8), 084001, 2014.

[Bur14b] J. Burnett, L. Faoro, I. Wisby, V. Gurtovoi, A. Chernykh, G. Mikhailov, V. Tulin, R. Shaikhaidarov, V. Antonov, P. Meeson, et al., Evidence for interacting two-level systems from the 1/f noise of a superconducting resonator, *Nat. Commun.*, **5**, 4119, 2014.

[Bur15] A. L. Burin, S. Matityahu, and M. Schechter, Low-temperature $1/f$ noise in microwave dielectric constant of amorphous dielectrics in josephson qubits, *Phys. Rev. B*, **92**, 174201, 2015.

[Bur18] A. L. Burin and A. O. Maksymov, Theory of nonlinear microwave absorption by interacting two-level systems, *Phys. Rev. B*, **97**, 214208, 2018.

[Bø19] M. S. Bødker, S. S. Sørensen, J. C. Mauro, and M. M. Smedskjaer, Predicting composition-structure relations in alkali borosilicate glasses using statistical mechanics, *Front. Mater.*, **6**, 175, 2019.

[Cap20] T. Capelle, E. Flurin, E. Ivanov, J. Palomo, M. Rosticher, S. Chua, T. Briant, P.-F. Cohadon, A. Heidmann, T. Jacqmin, and S. Deléglise, Probing a two-level system bath via the frequency shift of an off-resonantly driven cavity, *Phys. Rev. Appl.*, **13**, 034022, 2020.

[Car94] H. M. Carruzzo, E. R. Grannan, and C. C. Yu, Nonequilibrium dielectric behavior in glasses at low temperatures: Evidence for interacting defects, *Phys. Rev. B*, **50**, 6685–6695, 1994.

[Cla94] J. Classen, C. Enss, C. Bechinger, G. Weiss, and S. Hunklinger, Low frequency acoustic and dielectric measurements on glasses, *Ann. Physik*, **3**, 315, 1994.

[Cla00] J. Classen, T. Burkert, C. Enss, and S. Hunklinger, Anomalous frequency dependence of the internal friction of vitreous silica, *Phys. Rev. Lett.*, **84**, 2176–2179, 2000.

[Coo56] L. N. Cooper, Bound electron pairs in a degenerate fermi gas, *Phys. Rev.*, **104**, 1189–1190, 1956.

[Deb12] P. Debye, Zur Theorie der spezifischen Wärmen, *Ann. Physik*, **344**, 789, 1912.

[Deb13] P. Debye, On the theory of anomalous dispersion in the region of long-wave electromagnetic radiation, *Verh. Deut. Phys. Gesell.*, **15**, 777–793, 1913.

[Dou80] P. Doussineau, C. Frénois, R. G. Leisure, A. Levelut, and J.-Y. Prieur, Amorphous-like acoustical properties of Na doped $\beta - \mathrm{Al_2O_3}$, *J. Phys France*, **41**, 1193, 1980.

[dV14] P. J. de Visser, D. J. Goldie, P. Diener, S. Withington, J. J. A. Baselmans, and T. M. Klapwijk, Evidence of a nonequilibrium distribution of quasiparticles in the microwave response of a superconducting aluminum resonator, *Phys. Rev. Lett.*, **112**, 047004, 2014.

[Ell84] S. R. Elliott, Physics of Amorphous Materials, Longman, London, 1984.

[Ens89] C. Enss, C. Bechinger, and M. von Schickfus, Phonons 89, 474, World Scientific, Singapur, 1989.

[Ens97] C. Enss and S. Hunklinger, Incoherent tunneling in glasses at very low temperatures, *Phys. Rev. Lett.*, **79**, 2831–2834, 1997.

[Ens05] C. Enss and S. Hunklinger, Low-Temperature Physics, Springer, Heidelberg, 2005.

[Esq98] P. Esquinazi (Ed.), Tunneling systems in amorphous and crystalline solids, Springer, Heidelberg, 1998.

[Fef08] A. D. Fefferman, R. O. Pohl, A. T. Zehnder, and J. M. Parpia, Acoustic properties of amorphous silica between 1 and 500 mk, *Phys. Rev. Lett.*, **100**, 195501, 2008.

[Fic13] G. Fickenscher, Phasenkohärenz und Energierelaxation von Tunnelsystemen in Gläsern, PhD Thesis, Heidelberg University, 2013.

[Fre16] B. Frey, Entwicklung mikrostrukturierter supraleitender Resonatoren zur breitbandigen Untersuchung dielektrischer Eigenschaften zwischen 37 MHz und 1 GHz bei tiefen Temperaturen, Master Thesis, Heidelberg University, 2016.

[Fre17] H.-J. Freund, Controlling silica in its crystalline and amorphous states: a problem in surface science, *Acc. Chem. Res.*, **50**(3), 446–449, 2017.

[Fro77] G. Frossati, J. le G. Gilchrist, J. C. Lasjaunias, and W. Meyer, Spectrum of low-energy dipolar states in hydrated vitreous silica, *J. Phys. C*, **10**(18), L515–L519, 1977.

[Fro92] G. Frossati, Experimental techniques: Methods for cooling below 300 mk, *J. Low Temp. Phys.*, **87**(3-4), 595–633, 1992.

[Gao08] J. Gao, The physics of superconducting microwave resonators, PhD Thesis, California Institute of Technology, 2008.

[Gol79] B. Golding, M. von Schickfus, S. Hunklinger, and K. Dransfeld, Intrinsic electric dipole moment of tunneling systems in silica glasses, *Phys. Rev. Lett.*, **43**, 1817–1821, 1979.

[Gol95] M. A. Golosovsky, H. J. Snortland, and M. R. Beasley, Nonlinear microwave properties of superconducting nb microstrip resonators, *Phys. Rev. B*, **51**, 6462–6469, 1995.

[Gol12] D. J. Goldie and S. Withington, Non-equilibrium superconductivity in quantum-sensing superconducting resonators, *Supercond. Sci. Technol.*, **26**(1), 015004, 2012.

[Gra12] G. J. Grabovskij, T. Peichl, J. Lisenfeld, G. Weiss, and A. V. Ustinov, Strain tuning of individual atomic tunneling systems detected by a superconducting qubit, *Science*, **338**(6104), 232–234, 2012.

[Gur06] A. Gurevich, Thermal rf breakdown of superconducting cavities, *Beam Dynamics Newsletter*, 34, 2006.

[Haa20a] M. Haas, Private Communication, 2020.

[Haa20b] M. Haas and A. Reiser, Private Communication, 2020.

[Heu98] A. Heuer, Microscopic view of low-temperature anomalies in glasses, in P. Esquinazi (Ed.), *Tunneling Systems in Amorphous and Crystalline Solids*, Volume 1, 459–525, Springer-Verlag Berlin Heidelberg, 1998.

[Hua12] P. Y. Huang, S. Kurasch, A. Srivastava, V. Skakalova, J. Kotakoski, A. V. Krasheninnikov, R. Hovden, Q. Mao, J. C. Meyer, J. Smet, D. A. Muller, and U. Kaiser, Direct imaging of a two-dimensional silica glass on graphene, *Nano Lett.*, **12**(2), 1081–1086, 2012, PMID: 22268818.

[Hun72] S. Hunklinger, W. Arnold, S. Stein, R. Nava, and K. Dransfeld, Saturation of the ultrasonic absorption in vitreous silica at low temperatures, *Phys. Lett. A*, **42**(3), 253 – 255, 1972.

[Hun74] S. Hunklinger, Ultrasonics in amorphous materials, *Proc. Ultrasonic Symp. (IEEE)*, 1974.

[Hun76] S. Hunklinger and W. Arnold, 3 - Ultrasonic properties of glasses at low temperatures, Volume 12 in *Phys. Acoust.*, 155 – 215, Academic Press, 1976.

[Hun77] S. Hunklinger, Acoustic and dielectric properties of glasses at low temperatures, in J. Treusch (Ed.), *Festkörperprobleme 17*, Volume 17 in *Adv. Solid State Phys.*, 1–11, Springer Berlin Heidelberg, 1977.

[Hun86] S. Hunklinger and A. Raychaudhuri, Chapter 3: Thermal and elastic anomalies in glasses at low temperatures, Volume 9 in *Prog. in Low Temp. Phys.*, 265 – 344, Elsevier, 1986.

[Hun00] S. Hunklinger and C. Enss, Tunneling Systems in Crystalline and Amorphous Solids, 499–551, Series of Directions in Condensed Matter Physics Vol. 17, World Scientific, 2000.

[Hun07] S. Hunklinger, Festkörperphysik, Oldenbourg, München, 2007.

[Ino12] H. Inoue, A. Masuno, and Y. Watanabe, Modeling of the structure of sodium borosilicate glasses using pair potentials, *J. Phys. Chem. B*, **116**(40), 12325–12331, 2012.

[Jä72] J. Jäckle, On the ultrasonic attenuation in glasses at low temperatures, *Z. Phys. A*, **257**(3), 212, 1972.

[Kar83] V. G. Karpov, I. Klinger, and F. N. Ignat'Ev, Theory of the low-temperature anomalies in the thermal properties of amorphous structures, *Sov. Phys. JETP*, **57**, 439, 1983.

[Kha12] M. S. Khalil, M. J. A. Stoutimore, F. C. Wellstood, and K. D. Osborn, An analysis method for asymmetric resonator transmission applied to superconducting devices, *J. Appl. Phys.*, **111**(5), 054510, 2012.

[Kha13] M. S. Khalil, A study of two-level system defects in dielectric films using superconducting resonantors, PhD Thesis, University of Maryland, 2013.

[Kha14] M. S. Khalil, S. Gladchenko, M. J. A. Stoutimore, F. C. Wellstood, A. L. Burin, and K. D. Osborn, Landau-Zener population control and dipole measurement of a two-level-system bath, *Phys. Rev. B*, **90**, 100201, 2014.

[Kho20] D. Khomenko, C. Scalliet, L. Berthier, D. R. Reichman, and F. Zamponi, Depletion of two-level systems in ultrastable computer-generated glasses, *Phys. Rev. Lett.*, **124**, 225901, 2020.

[Kir17] N. Kirsh, E. Svetitsky, A. L. Burin, M. Schechter, and N. Katz, Revealing the nonlinear response of a tunneling two-level system ensemble using coupled modes, *Phys. Rev. Materials*, **1**, 012601, 2017.

[Kra26] H. A. Kramers, Wellenmechanik und halbzahlige Quantisierung, *Z. Phys.*, **39**(10), 828, 1926.

[Ku05] L.-C. Ku and C. C. Yu, Decoherence of a josephson qubit due to coupling to two-level systems, *Phys. Rev. B*, **72**, 024526, 2005.

[Kö19] D. Körner, Nichtgleichgewichtsdynamik von Tunnelsystemen im Bor-Kronglas N-BK7 bei 1 GHz und tiefen Temperaturen, Bachelor Thesis, Heidelberg University, 2019.

[Laf15] B. Lafuente, R. T. Downs, H. Yang, and N. Stone, 1. The power of databases: The RRUFF project, 1 – 30, De Gruyter, Berlin, 2015.

[Lan32] L. Landau, On the theory of transfer of energy at collisions ii, *Phys. Z. Sowjetunion*, **2**(46), 118, 1932.

[Las75] J. C. Lasjaunias, A. Ravex, M. Vandorpe, and S. Hunklinger, The density of low energy states in vitreous silica: specific heat and thermal conductivity down to 25 mk, *Solid State Commun.*, **17**(9), 1045–1049, 1975.

[Lic12] L. Lichtenstein, M. Heyde, and H.-J. Freund, Atomic arrangement in two-dimensional silica: From crystalline to vitreous structures, *J. Phys. Chem. C*, **116**(38), 20426–20432, 2012.

[Lis15] J. Lisenfeld, G. J. Grabovskij, C. Müller, J. H. Cole, G. Weiss, and A. V. Ustinov, Observation of directly interacting coherent two-level systems in an amorphous material, *Nat. Commun.*, **6**, 2015.

[Lis19] J. Lisenfeld, A. Bilmes, A. Megrant, R. Barends, J. Kelly, P. Klimov, G. Weiss, J. M. Martinis, and A. V. Ustinov, Electric field spectroscopy of material defects in transmon qubits, *npj Quantum Inf.*, **5**(1), 1–6, 2019.

[Luc14] A. Luck, A. Fleischmann, A. Reiser, and C. Enss, Effects of large nuclear quadrupoles on dielectric properties of glasses at very low temperatures, *J. Phys.: Conf. Ser.*, **568**(3), 032013, 2014.

[Luc16] A. Luck, Nuclear spin dominated relaxation of atomic tunneling systems in glasses, PhD Thesis, Heidelberg University, 2016.

[Lud02] S. Ludwig, C. Enss, P. Strehlow, and S. Hunklinger, Direct coupling of magnetic fields to tunneling systems in glasses, *Phys. Rev. Lett.*, **88**, 075501, 2002.

[Lud03] S. Ludwig, P. Nagel, S. Hunklinger, and C. Enss, Magnetic field dependent coherent polarization echoes in glasses, *J. Low Temp. Phys.*, **131**, 89–111, 2003.

[Lut18] S. Lutter, Dielektrische Messungen der Nichtgleichgewichtsdynamik wechselwirkender Tunnelsysteme in Gläsern bei tiefen Temperaturen, Master Thesis, Heidelberg University, 2018.

[Lut20] M. Lutz, Dielektrische Eigenschaften von N-BK7 bei 1 GHz unter Einfluss einer großen statischen Polarisation bei sehr tiefen Temperaturen, Bachelor Thesis, Heidelberg University, 2020.

[Mar05] J. M. Martinis, K. B. Cooper, R. McDermott, M. Steffen, M. Ansmann, K. D. Osborn, K. Cicak, S. Oh, D. P. Pappas, R. W. Simmonds, and C. C. Yu, Decoherence in josephson qubits from dielectric loss, *Phys. Rev. Lett.*, **95**, 210503, 2005.

[Mat58] D. C. Mattis and J. Bardeen, Theory of the anomalous skin effect in normal and superconducting metals, *Phys. Rev.*, **111**, 412–417, 1958.

[Mat63] B. T. Matthias, T. H. Geballe, and V. B. Compton, Superconductivity, *Rev. Mod. Phys.*, **35**, 1–22, 1963.

[Mat19] S. Matityahu, H. Schmidt, A. Bilmes, A. Shnirman, G. Weiss, A. V. Ustinov, M. Schechter, and J. Lisenfeld, Dynamical decoupling of quantum two-level systems by coherent multiple landau–zener transitions, *npj Quantum Inf.*, **5**, 114, 2019.

[McR20] C. R. H. McRae, H. Wang, J. Gao, M. R. Vissers, T. Brecht, A. Dunsworth, D. P. Pappas, and J. Mutus, Materials loss measurements using superconducting microwave resonators, *Rev. Sci. Instrum.*, **91**(9), 091101, 2020.

[Mee20] D. Meeker, Finite Element Method Magnetics Version 4.2 User's Manual, https://www.femm.info/wiki/HomePage, 2020.

[Mei18] S. M. Meißner, A. Seiler, J. Lisenfeld, A. V. Ustinov, and G. Weiss, Probing individual tunneling fluctuators with coherently controlled tunneling systems, *Phys. Rev. B*, **97**, 180505, 2018.

[Mil10] P. W. Milonni and J. H. Eberly, Coherence in Atom-Field Interactions, Chapter 9, 401–455, John Wiley & Sons, Inc., 2010.

[Mü19] C. Müller, J. H. Cole, and J. Lisenfeld, Towards understanding two-level-systems in amorphous solids: insights from quantum circuits, *Rep. Prog. Phys.*, **82**(12), 124501, 2019.

[Mü21] L. Münch, Master Thesis, Heidelberg University, 2021, in preparation.

[Nal04] P. Nalbach, D. Osheroff, and S. Ludwig, Non-equilibrium dynamics of interacting tunneling states in glasses, *J. Low Temp. Phys.*, **137**(3-4), 395–452, 2004.

[Nar70] V. Narayanamurti and R. O. Pohl, Tunneling states of defects in solids, *Rev. Mod. Phys.*, **42**, 201–236, 1970.

[Nat98] D. Natelson, D. E. Rosenberg, and D. D. Osheroff, Evidence for growth of collective excitations in glasses at low temperatures, *Phys. Rev. Lett.*, **80**, 4689–4692, 1998.

[Nei13] C. Neill, A. Megrant, R. Barends, Y. Chen, B. Chiaro, J. Kelly, J. Y. Mutus, P. J. J. O'Malley, D. Sank, J. Wenner, T. C. White, Y. Yin, A. N. Cleland, and J. M. Martinis, Fluctuations from edge defects in superconducting resonators, *Appl. Phys. Lett.*, **103**(7), 072601, 2013.

[Nit98] A. Nittke, S. Sahling, and P. Esquinazi, Heat release in solids, in P. Esquinazi (Ed.), *Tunneling Systems in Amorphous and Crystalline Solids*, Volume 1, 9–56, Springer-Verlag Berlin Heidelberg, 1998.

[Pal14] E. Paladino, Y. M. Galperin, G. Falci, and B. L. Altshuler, 1/f noise: Implications for solid-state quantum information, *Rev. Mod. Phys.*, **86**, 361–418, 2014.

[Par93] D. A. Parshin, Soft potential model and universal properties of glasses, *Phys. Scr.*, **T49A**, 180–185, 1993.

[Phi72] W. A. Phillips, Tunneling states in amorphous solids, *J. Low Temp. Phys.*, **7**, 351–360, 1972.

[Phi81] W. A. Phillips (Ed.), Amorphous solids, Volume 24 in *Topics in current physics*, Springer, Heidelberg, 1981.

[Phi87] W. A. Phillips, Two-level states in glasses, *Rep. Prog. Phys.*, **50**(12), 1657–1708, 1987.

[Pob07] F. Pobell, Matter and methods at low temperatures, Springer, Berlin ; Heidelberg, 3. edition, 2007.

[Poh85] R. O. Pohl, Some facts, old and new, about the low temperature thermal properties of noncrystalline solids, *Phase Trans.*, **5**(4), 239–259, 1985.

[Pro15] S. Probst, F. B. Song, P. A. Bushev, A. V. Ustinov, and M. Weides, Efficient and robust analysis of complex scattering data under noise in microwave resonators, *Rev. Sci. Instrum.*, **86**(2), 024706, 2015.

[Ram98] M. A. Ramos and U. Buchenau, Beyond the standard tunneling model: The soft-potential model, in P. Esquinazi (Ed.), *Tunneling Systems in Amorphous and Crystalline Solids*, Volume 1, 527–569, Springer-Verlag Berlin Heidelberg, 1998.

[Rau95] S. Rau, C. Enss, S. Hunklinger, P. Neu, and A. Würger, Acoustic properties of oxide glasses at low temperatures, *Phys. Rev. B*, **52**, 7179–7194, 1995.

[Rei17] A. Reifenberger, Spezifische Wärme von supraleitenden metallischen Gläsern bei tiefen Temperaturen, PhD Thesis, Heidelberg University, 2017.

[Rog97] S. Rogge, D. Natelson, B. Tigner, and D. D. Osheroff, Nonlinear dielectric response of glasses at low temperature, *Phys. Rev. B*, **55**(17), 11256, 1997.

[Ros16] Y. J. Rosen, M. S. Khalil, A. L. Burin, and K. D. Osborn, Random-defect laser: Manipulating lossy two-level systems to produce a circuit with coherent gain, *Phys. Rev. Lett.*, **116**, 163601, 2016.

[Sag11] J. M. Sage, V. Bolkhovsky, W. D. Oliver, B. Turek, and P. B. Welander, Study of loss in superconducting coplanar waveguide resonators, *J. Appl. Phys.*, **109**(6), 063915, 2011.

[Sal94] D. J. Salvino, S. Rogge, B. Tigner, and D. D. Osheroff, Low temperature ac dielectric response of glasses to high dc electric fields, *Phys. Rev. Lett.*, **73**, 268–271, 1994.

[Sar16] B. Sarabi, A. N. Ramanayaka, A. L. Burin, F. C. Wellstood, and K. D. Osborn, Projected dipole moments of individual two-level defects extracted using circuit quantum electrodynamics, *Phys. Rev. Lett.*, **116**, 167002, 2016.

[Sch91] H. Scholze, Glass, Springer, New York, 1991.

[Sch14] Schott AG, Data Sheet Schott N-BK7 517642.251, 2014.

[Sch18] M. Schechter, P. Nalbach, and A. L. Burin, Nonuniversality and strongly interacting two-level systems in glasses at low temperatures, *New J. Phys.*, **20**(6), 063048, 2018.

[Sel25] N. Seljakow, L. Strutinski, and A. Krasnikow, Zur Frage nach der Struktur des Glases, *Z. Phys.*, **33**, 53–62, 1925.

[Sli96] C. P. Slichter, Principles of Magnetic Resonance, Volume 1, Springer, Berlin, Heidelberg, 1996.

[Son09] C. Song, T. W. Heitmann, M. P. DeFeo, K. Yu, R. McDermott, M. Neeley, J. M. Martinis, and B. L. T. Plourde, Microwave response of vortices in superconducting thin films of Re and Al, *Phys. Rev. B*, **79**, 174512, 2009.

[Son18] Sonnet Software, Inc., 126 N. Salina St., Syracuse, NY 13202, Sonnet® User's Guide, 2018.

[Ste73] R. B. Stephens, Low-temperature specific heat and thermal conductivity of noncrystalline dielectric solids, *Phys. Rev. B*, **8**, 2896–2905, 1973.

[Ste76] R. B. Stephens, Intrinsic low-temperature thermal properties of glasses, *Phys. Rev. B*, **13**, 852–865, 1976.

[Ste18] B. Stevensson, Y. Yu, and M. Edén, Structure–composition trends in multicomponent borosilicate-based glasses deduced from molecular dynamics simulations with improved B–O and P–O force fields, *Phys. Chem. Chem. Phys.*, **20**, 8192–8209, 2018.

[Str98] P. Strehlow, C. Enss, and S. Hunklinger, Evidence for a phase transition in glasses at very low temperature: A macroscopic quantum state of tunneling systems?, *Phys. Rev. Lett.*, **80**(24), 5361, 1998.

[Str18] M. R. Strohmaier, Thermalisierungsverhalten von amorphem Polyvinylacetat und Polyvinylchlorid bei tiefen Temperaturen, Bachelor Thesis, Heidelberg University, 2018.

[Stü32] J. Stückelberg, Theorie der unelastischen Stösse zwischen Atomen, *Helv. Phys. Acta*, **5**, 369, 1932.

[Swa89] E. T. Swartz and R. O. Pohl, Thermal boundary resistance, *Rev. Mod. Phys.*, **61**, 605–668, 1989.

[Vep20] A. P. Vepsäläinen, A. H. Karamlou, J. L. Orrell, A. S. Dogra, B. Loer, F. Vasconcelos, D. K. Kim, A. J. Melville, B. M. Niedzielski, J. L. Yoder, S. Gustavsson, J. A. Formaggio, B. A. VanDevender, and W. D. Oliver, Impact of ionizing radiation on superconducting qubit coherence, *Nature*, **584**(7822), 551–556, 2020.

[Vog92] W. Vogel, Glaschemie, Springer, Berlin ; Heidelberg [u.a.], 1992.

[VR98] R. Van Rooijen, A. Marchenkov, H. Akimoto, R. Jochemsen, and G. Frossati, Dielectric properties of vitreous silica with various hydroxyl concentrations, *J. Low Temp. Phys.*, **110**(1), 269–274, 1998.

[vS75] M. von Schickfus, S. Hunklinger, and L. Piché, Anomalous dielectric dispersion in glasses at low temperatures, *Phys. Rev. Lett.*, **35**, 876–878, 1975.

[vS77] M. von Schickfus and S. Hunklinger, Saturation of the dielectric absorption of vitreous silica at low temperatures, *Phys. Lett.*, **64 A**(1), 144, 1977.

[Wan04] W. Wang, C. Dong, and C. Shek, Bulk metallic glasses, *Mater. Sci. Eng. R Rep.*, **44**(2), 45 – 89, 2004.

[War34] B. E. Warren, The diffraction of x-rays in glass, *Phys. Rev.*, **45**, 657–661, 1934.

[Wen26] G. Wentzel, Eine Verallgemeinerung der Quantenbedingungen für die Zwecke der Wellenmechanik, *Z. Phys.*, **38**(6-7), 518, 1926.

[Woh01] M. Wohlfahrt, Untersuchung der dielektrischen Tieftemperaturanomalien von Mehrkomponentengläsern in Magnetfeldern, PhD Thesis, Heidelberg University, 2001.

[Wür02] A. Würger, A. Fleischmann, and C. Enss, Dephasing of atomic tunneling by nuclear quadrupoles, *Phys. Rev. Lett.*, **89**, 237601, 2002.

[Zac32] W. H. Zachariasen, The atomic arrangement in glass, *J. Am. Chem. Soc.*, **54**(10), 3841–3851, 1932.

[Zel71] R. C. Zeller and R. O. Pohl, Thermal conductivity and specific heat of noncrystalline solids, *Phys. Rev. B*, **4**(6), 2029, 1971.

[Zen32] C. Zener and R. H. Fowler, Non-adiabatic crossing of energy levels, *Proc. R. Soc. London*, **137**(833), 696–702, 1932.

Acknowledgments

Abschließend möchte ich mich herzlich bei all denen bedanken, die auf verschiedenste Art und Weise zum Gelingen dieser Arbeit beigetragen haben und deren Unterstützung ich über die letzten Jahre genießen durfte. Dankbarkeit lässt sich bekanntlich nur schwer durch Worte ausdrücken, ich versuche mich dennoch daran und tue dies ausgesprochen gerne. Mein besonderer Dank gilt:

Prof. Dr. Christian Enss für die Möglichkeit, dass ich mich die vergangenen Jahre sorgenfrei diesem spannenden Forschungsthema widmen durfte, für die Freiheiten und die Motivation zahlreiche Ideen im Labor umsetzen zu können, für das stetige Interesse an der Arbeit und die Diskussion der Ergebnisse, sowie für die Chance und das Vertrauen die Forschungsergebnissen auf zahlreichen Tagungen und Seminaren präsentieren zu dürfen,

Prof. Dr. Heinz Horner für die freundliche Übernahme des Zweitgutachtens, sowie des großen Interesses an der Arbeit,

Dr. Andreas Reiser dafür, dass die Bürotür für Anliegen und Diskussionen immer offen steht, dass Probleme nicht umgangen sondern gelöst werden, für das immer sehr angenehme und konstruktive Arbeitsgruppenklima, die Unterstützung bei diversen Labortätigkeiten, die vielen Gesprächen über physikalische und nicht-so-physikalische Themen, für den/das ein oder anderen/andere Rat/Rad, sowie für das Aufrechterhalten des Blutzuckerspiegels (zumindest meistens) durch die vielen "Leckereien",

Dr. Andreas Fleischmann für seine zahlreichen kreativen und verblüffender Weise eigentlich immer zutreffenden Analysen zum Experiment, die allgemeine Begeisterung für die Physik und dafür, dass ich die Frage "Und, lasert es schon?" immer verneinen durfte,

Andreas Schaller für die unkomplizierte und reibungslose Zusammenarbeit, für die vielen Lacher oder die aufmunternden Sprüche, womit die letzten Jahre auch in stressigen Phasen zu einer reinen Freude wurden,

Dr. Andreas Reifenberger und Dr. Annina Luck von denen ich eine sofort nutzbare Labor-Infrastruktur erben durfte und mir mit zahlreichen Tipps den Einstieg wesentlich erleichtert haben,

den aktuellen und ehemaligen Bürokollegen 00.311 insbesondere ANDREAS SCHALLER, MARCEL HAAS und CHRISTIAN STÄNDER für die wunderbare und auch unterhaltsame gemeinsame Zeit im Büro, welche ich das letzte Jahr aufgrund des pandemiebedingten Homeoffice besonders vermisst habe, sowie für den “Büroausflug” nach Klosters,

sowie allen weiteren aktuellen und ehemaligen Mitgliedern der Arbeitsgruppen F3, F4 und F5 für das kollegiale Arbeitsklima, der allgemeinen Hilfsbereitschaft und der schönen gemeinsamen Zeit auf diversen Frühjahrstagungen,

dem REINRAUMTEAM und HERRN WOLF für die stets schnelle Herstellung der Resonatoren und der problemlosen Zusammenarbeit,

RUDOLF EITEL für die ununterbrochene Versorgung mit flüssigem Helium, auch wenn sich spontan doch einmal etwas an den Plänen ändert, sowie den immer kurzweiligen Mittagstischrunden,

den Bachelor:innen und Master:innen SVEN LUTTER, TIMOTHY HERBST, NICOLE ASSMANN, ALEXANDER WERNER, ERIK WEERDA, ALJOSCHA AUER, LUKAS MÜNCH, DIANA KÖRNER, ALEXANDER MÜLLER, MARIUS LUTZ und ANDREAS RALL, die zum Teil direkt aber auch indirekt zu den Ergebnissen dieser Arbeit beitragen konnten und durch ihr neugieriges Nachfragen immer wieder neue Denkanstöße lieferten,

den Mitarbeiter:innen der gesamten SERVICEABTEILUNG des KIPs, welche Ideen stets kompetent umsetzen und bei verwaltungs- oder computertechnischen Problemen immer schnelle Unterstützung leisten,

den fleißigen “externen” Korrekturleser:innen ALEXANDRA FREY, JOHANNES SCHWINN, WERNER GULDEN und ELISABETH GULDEN, die sich die Mühe gemacht haben sich mit Tunnelsystemen, Landau-Zener Übergängen und der dazwischen versteckten Sprache auseinanderzusetzen,

den Mitgliedern der HEIDELBERG PHYSIK STEILKURS GRUPPE, die das Physik Studium so viel angenehmer gemacht haben und durch die zahlreichen gemeinsamen Unternehmungen in Heidelberg oder in sonstigen Ecken Europas in schöner Erinnerung bleiben, auf dass noch zahlreiche “Frühjahrskongresse” folgen werden,

meiner FAMILIE und insbesondere meinen GESCHWISTERN und ELTERN, für deren unermüdliche Unterstützung und deren Vertrauen während der gesamten Zeit,

und zu guter Letzt, aber dafür umso herzlicher, gilt mein Dank meiner “Homeoffice-Kollegin” JANA für das Verständnis und die Geduld vor allem in der Endphase der Arbeit, aber auch für die Wärme, die es beim Experimentieren nahe des absoluten Nullpunkts so dringend braucht.